

**Photogrammetric and Stereo Vision
Techniques for Evaluating Material
Properties in Timber and Timber-Based
Composite Structures**

A thesis submitted in partial fulfilment of the
requirements for the award of
Doctor of Philosophy

By

Ahmed S. Mohamed
BSc, MSc (Civil Engineering)

School of Engineering and the Built
Environment

Edinburgh Napier University, UK

2016

ABSTRACT

A fundamental requirement for efficient use of a glulam beam is an accurate knowledge of its mechanical behaviour and the material properties characterising that behaviour. It becomes extremely important to obtain accurate measurements of material properties of glulam, but this can be challengeable, especially for commonly used properties, such as the modulus of elasticity and shear modulus. Experiment testing is the way to determine elastic properties, however, the problem of experimentally determining appropriate values of these properties for timber-based composite is not as simple and straightforward as in isotropic materials, and care must be taken in the experimental methods used in determining their values. There is a need to develop an appropriate method in order to evaluate these properties. Unlike the traditional methods in which contact devices such as inclinometers or linear variable differential transducers are used to identify the material properties of glulam by utilizing their measurements of displacements and rotations at specific points, the optical methods provide an efficient and accurate approach for measuring these properties at multi-location so that more regions of interest can be monitored simultaneously without contact. Moreover, the traditional devices are limited to give measurements in one or two dimensions whereas the optical methods can be used to gain measurements in three dimensions. Although the optical techniques were successfully applied to different structural applications, little work has been done on the area of evaluating material properties of timber, especially modulus of elasticity and shear modulus. Therefore, the primary motivation of this project will be allocated to evaluate those properties utilizing the stereo vision approach.

This thesis describes the research work in which a stereo camera system combined with a photogrammetric approach was proposed to evaluate material properties of timber and timber-based composite joists. A series of experiments were conducted to investigate the applicability of the approach to evaluate different material properties of glulam beams under different types of tests, including the torsion and the compression. Remarkable findings were obtained which might help for developing an outline for a

future research programme in the field of evaluating material properties of glulam, allowing investigating the relationship between these properties. The results also showed that the optical system not only allowed assessing performance and reliability of the traditional sensors, but also allowed monitoring the deformation of the samples at various locations by providing more information which would not be possible to obtain using the traditional techniques.

DECLARATION

I hereby declare that this thesis together with work contained herein was produced entirely by myself, and contains no materials that have been accepted for the award of any other degree or diploma in any university. To the best of my knowledge and belief, this thesis contains no material previously published or written by another person except where due acknowledgment to others has been made.

Signature:

Ahmed S. Mohamed

DEDICATION

I will always remember my father, Saleh Mohamed Alsughair, who sadly passed away in September 8, 2008. He always gave me endless love, invaluable advice, and support, and for this I am extremely grateful and I am forever indebted to him.

This thesis is dedicated to my father's spirit.

The author
A. Mohamed

ACKNOWLEDGEMENT

I would like to express my sincere gratitude to my supervision team: Dr. Hexin Zhang and Prof. Abdy Kermani for their kind encouragement and invaluable advice. In particular, a very big thank you to Dr. Zhang for his constructive guidance and support throughout this research programme.

Thanks are also due to Stefan Lehneke and Dhonju Roshan, who were always available to give a hand during the conducted tests. Moreover, I wish to express special gratitude to Remi Caudoux for all his assistance and co-operation during the preparation of the test specimens, and the setup of the experimental tests.

Deep gratitude is expressed to my wife, Gada; without her patience, love, encouragement and invaluable assistance, I would not have finished this thesis. I thank my daughter, Munira, and my sons Aseel and Suhail for all the happy times they have given to me. I would like to thank my mother, brothers and sisters, who have always encouraged me and given me a firm spiritual support during the whole of my research.

TABLE OF CONTENTS

ABSTRACT.....	ii
DECLARATION.....	iv
DEDICATION.....	v
ACKNOWLEDGEMENT.....	vi
LIST OF FIGURES	xi
LIST OF TABLES	xviii
1. INTRODUCTION	1
1.1 Introduction.....	1
1.2 Research Objectives and Plan.....	6
1.3 Significance of the Study.....	11
1.4 Outline of the thesis	12
2. LITERATURE REIEW	14
2.1 Timber and Glued-laminated Timber.....	14
2.2 Mechanical Properties of Timber and Timber-based Composite Materials.....	15
2.2.1 Wood as an Orthotropic Material.....	16
2.2.2 The Elastic Properties.....	18
2.3 Current Methods for Measuring Displacement and Deformation in Structures	19
2.4 Photogrammetry and Stereo Vision	21
2.4.1 Historical Background of Photogrammetry.....	21
2.4.2 Review of Close-Range Photogrammetric Methods to Wood Properties.....	22
2.4.3 Application of the Photogrammetric Techniques to Materials Other than Timber	26
2.4.4 Application of the Photogrammetric Techniques to Industry	27

2.5	Standard Test Methods for Elastic and Shear Properties	28
2.5.1	Testing Methods for Shear Modulus	28
2.5.2	Testing Methods for Modulus of Elasticity	33
3.	STEREO VISION SYSTEM.....	43
3.1	Introduction.....	43
3.2	Image Acquisition Hardware	43
3.2.1	Cameras and Lenses	44
3.2.2	Frame-grabber Card.....	48
3.2.3	Lighting Units.....	49
3.2.4	The Control Computer (PC).....	49
3.3	Image Processing Software.....	49
3.3.1	HDevelop.....	50
3.3.2	The Development of Applications with HALCON.....	51
3.4	Camera Calibration	52
3.4.1	Camera Models.....	52
3.4.2	Perspective Projection Model for Area Scan Cameras.....	53
3.4.3	The HALCON Calibration Plate	58
3.4.4	Camera Calibration Process	59
3.5	Stereo Vision	61
3.5.1	Binocular Stereo Vision	61
3.5.2	Binocular Stereo Calibration	62
3.5.3	Stereo Reconstruction.....	63
3.6	Software Implementation.....	68
3.6.1	The Microsoft Visual Studio	68
3.6.2	The Microsoft Foundation Classes (MFC).....	68
3.6.3	The Implemented Graphical User Interfaces.....	69
3.6.4	The Implemented Algorithms.....	72
4.	VALIDATION AND EVALUATION OF THE PROPOSED STEREO CAMERA SYSTEM.....	76
4.1	Introduction.....	76

4.2	Experimental Evaluation of the Parameters of the Stereo Camera System	77
4.2.1	Materials and Testing Equipment.....	77
4.2.2	Experimental Setup and Procedure	79
4.2.3	Calculation Methods.....	84
4.2.4	Results and Discussions	88
4.3	Experimental Validation of the Stereo Camera System	97
4.3.1	Materials and Methods	97
4.3.2	Experimental Setup and Procedure	100
4.3.3	Calculation Methods.....	103
4.3.4	Validation of Test Results	104
4.4	Experimental Investigation of Different Target Techniques	108
4.4.1	Materials and Testing Equipment.....	109
4.4.2	Experimental Setup and Procedure	110
4.4.3	Results and Discussions	113
4.5	Summary.....	115
5.	EVALUATION OF TORSIONAL BEHAVIOUR AND SHEAR MODULUS OF GLULAM TIMBER BEAMS.....	116
5.1	Introduction.....	116
5.2	The Applicability of the Photogrammetric Approach on the Torsion Test	118
5.2.1	Materials and Methods	118
5.2.2	Results and Discussions	131
5.3	The Validation of the Photogrammetric Approach	138
5.3.1	Materials and Methods	138
5.3.2	Results and Discussion	142
5.4	Evaluation of Torsional Behaviour and the Variations of Shear Modulus of Glulam Timber Beams	150
5.4.1	Materials and Methods	151
5.4.2	Experimental Setup and Procedure	156
5.4.3	Calculation Methods.....	159
5.4.4	Experimental Results and Discussion	162

5.5	Summary.....	195
6.	APPLICATION OF THE PROPOSED PHOTOGRAMMETRIC APPROACH TO STUDY THE PERFORMANCE OF DISPLACEMENT TRANSDUCERS.....	197
6.1	Introduction.....	198
6.2	Experimental Validation of the Approach	200
6.2.1	Materials and Methods	200
6.3	Performance Study of the Displacement Transducers	207
6.3.1	Materials and Methods	207
6.3.2	Experimental Set-up and Procedure	208
6.3.3	The Algorithm Developed for the Photogrammetric Deflection Measurements	212
6.4	Validation Test Results	216
6.5	Evaluation Test Results	218
6.5.1	Comparison of the Test Results between the Photogrammetric Approach and the LVDT	218
6.5.2	Investigation of the LVDT Mounting System.....	220
6.6	Summary.....	226
7.	CONCLUSIONS AND RECOMMENDATIONS.....	227
7.1	Summary.....	227
7.2	CONCLUSIONS	229
7.3	RECOMMENDATIONS.....	234
	REFERENCES.....	237

LIST OF FIGURES

Figure 1-1: The research work being carried out in this thesis.....	8
Figure 1-2: Schematic diagram for developing the binocular stereo vision system.	11
Figure 2-1: The prescene of some defects in wood.....	15
Figure 2-2: The three principal axes of wood with respect to grain direction and growth rings (Miller, R.B., 1999).....	17
Figure 2-3: Example of test configuration with requirements of specific locations for the gauges (BS EN 408:2010).....	29
Figure 2-4: Torque versus relative rotation (BS EN 408:2010).....	30
Figure 2-5: Test arrangement for shear field test (BS EN 408:2010).....	31
Figure 2-6: Example of the shear field test apparatus fixed on one of both sides (BS EN 408:2010).	32
Figure 2-7: Deformation of the square with diagonals (BS EN 408:2010).	32
Figure 2-8: Test configuration for measuring local modulus of elasticity in bending (BS EN 408:2010).....	34
Figure 2-9: The graph of load-deformation within the elastic range of deformation (BS EN 408:2010).....	35
Figure 2-10: Test configuration for measuring global modulus of elasticity in bending (BS EN 408:2010).....	36
Figure 2-11: Structural timber test specimen (BS EN 408:2010).....	38
Figure 2-12: Glued laminated timber test specimen (BS EN 408:2010).	38
Figure 2-13: Typical compression test configuration in accordance with CEN (EN408:2010, 2010).....	40
Figure 2-14: The graph of load-deformation of an EN 408(2010) perpendicular to the grain in compression.	42
Figure 3-1: Relationship between the parameters of the lens.	45
Figure 3-2: Development of application with HALCON (MVTec Software GmbH, 2011b).	51

Figure 3-3: Perspective projections using a pinhole camera model (Steger et al., 2008).	54
Figure 3-4: Image plane and virtual image plane (Steger et al., 2008).....	54
Figure 3-5: Effects of radial distortion with $k>0$ (left), $k=0$ (middle), and $k<0$ (right) (Steger et al., 2008).	57
Figure 3-6: The HALCON calibration plate (Steger et al., 2008).	59
Figure 3-7: Flowchart of 3D reconstruction process.....	62
Figure 3-8: Geometry of a two-camera system.....	64
Figure 3-9: Epipolar geometry of a two-camera system.....	66
Figure 3-10: Geometry of Binocular Stereo (adapted from (Jain et al., 1995)).....	67
Figure 3-11: Developed graphical user interface used during the torsion tests.	71
Figure 3-12: Developed graphical user interface used during the compression tests. ...	71
Figure 3-13: A part of the implemented C++ calibration code for calibrating the stereo camera system.	72
Figure 3-14: A diagram of the basic steps for stereo camera calibration.....	73
Figure 3-15: Flowchart of the stereo reconstruction algorithm based on HALCON....	75
Figure 4-1: Images of the employed targets for a) the first investigation, and b) the second investigation.	78
Figure 4-2: Stereo camera system mounted on a tripod.....	78
Figure 4-3: Flowchart of the experimental tests conducted in this investigation.	79
Figure 4-4: Schematic plot of the test set-up with instrumentation of the first study ...	81
Figure 4-5: Test set-up and instrumentation of the second investigation.	82
Figure 4-6: Five image pairs of the calibration plate acquired at different positions and orientations.....	83
Figure 4-7: Flow diagram of the 3D reconstruction Algorithm.....	86
Figure 4-8: a) The initial part of the algorithm showing the HALCON operators used to open windows and read the calibration parameters, and b) the last part of the algorithm showing the operators used to reconstruct the 3D coordinates of the targets.	87
Figure 4-9: The influence of the number of the calibration images on the results of test 1 (top), and test 2 (bottom).....	90

Figure 4-10: The influence of the number of the calibration images in the stability of the results of test 1 (top), and test 2 (bottom).	91
Figure 4-11: Snapshot of the HALCON interface showing the detection of the circular marks.	92
Figure 4-12: The calibration target with the defined coordinate system.	93
Figure 4-13: The maximum differences between the exact and measured 3D coordinates of the targets.	96
Figure 4-14: The image of the target monitored by the stereo cameras.....	97
Figure 4-15: Image of the LVDT transducer.	98
Figure 4-16: The image of the digital micrometre.	99
Figure 4-17: The Basler stereo cameras.....	100
Figure 4-18: The photogrammetric set-up and instruments used during the accuracy evaluation test.	101
Figure 4-19: Screen shot of the implemented GUI showing the stereo camera calibration process.....	102
Figure 4-20: Comparison of the relative displacement results measured by the three sensors (a) Test 1, (b) Test 2 and (c) Test 3.	105
Figure 4-21: The correlation between the vertical displacements measured by a) the photogrammetric approach and the digital micrometre, b) the photogrammetric approach and the LVDT sensor.	106
Figure 4-22: Different type of targets used in the tests.....	109
Figure 4-23: A Schematic diagram of the test specimen with its dimensions.	109
Figure 4-24: Examples of different experimental setups a) the photogrammetric system monitoring the targets glued to the specimen, and b) the LVDT transducer monitoring the relative displacements over the gauge length.....	111
Figure 4-25: The setup and location of the photogrammetric marks and the LVDT on the surface of the glulam specimen.....	112
Figure 4-26: Displacement measurements according to the marking type and the used LVDT.....	114
Figure 4-27: Standard error according to marking type.....	114

Figure 5-1: Glulam timber specimens for torsion tests.....	119
Figure 5-2: Torsion specimens after applying targets to their surfaces (left) and details of the applied targets (right).....	119
Figure 5-3: Torsion testing machine.	120
Figure 5-4: The drive unit with the rotating loading chuck.	121
Figure 5-5: The fixed weighing chuck of the machine.	121
Figure 5-6: Clamps of the torsion tester at the fixed end (left) and at the rotating end (right).	122
Figure 5-7: Dual-axis inclinometers.....	123
Figure 5-8: Dual-axis inclinometer attached to a wooden mount.....	124
Figure 5-9: Data log system for inclinometers.....	125
Figure 5-10: The implemented photogrammetric software for torsional tests.....	126
Figure 5-11: Schematic torsional experimental setup with instrumentation.....	128
Figure 5-12: Image of the test setup of the specimen on the torsion machine with instrumentation.....	128
Figure 5-13: The selected section of the beam to be monitored (left) and details of the calibration plate and target points (right).....	129
Figure 5-14: Comparison between the measurements of inclinometers and the photogrammetric system for sample 1 (top) and sample 2 (bottom).	133
Figure 5-15: a) Displacements of the longer side of the cross-section b) original and deformed cross-section.	136
Figure 5-16: Comparison of rotation of the short side and long side.....	137
Figure 5-17: Image of the stereo camera system (left) and inclinometer (right).	139
Figure 5-18: Image of test arrangement for torsion test.....	140
Figure 5-19: Image of the developed GUI during stereo camera calibration.	141
Figure 5-20: The implemented HALCON algorithm for extracting the targets.	144
Figure 5-21: Comparison between the inclinometer and optical measurements for a) sample 1, and b) sample 2 under a speed rate of 2 degrees per minute.	146
Figure 5-22: Relationship between measurements of the inclinometer and the optical system (R^2 Values) measured in a) sample 1 and b) sample 2.....	147

Figure 5-23: Comparison between inclinometers and optical measurements for sample 2 under a speed rate of a) 4°/min, and b) 6°/min.	149
Figure 5-24: Workflow diagram of the experimental torsion test.....	150
Figure 5-25: Glulam samples for torsion test.....	151
Figure 5-26: The process of creating the photogrammetric pattern on the torsion specimens.	153
Figure 5-27: The glulam samples after being painted with the photogrammetric patterns.	153
Figure 5-28: Dual-axis inclinometer (left) and the developed data log interface for recording the readings of inclinometers (right).....	155
Figure 5-29: The binocular stereo camera systems (left) and the implemented photogrammetric software for image acquisition and camera calibration (right).....	156
Figure 5-30: Torsion test arrangement and equipment.	157
Figure 5-31: Image of experimental setup of the torsion test (left) and a detail of the photogrammetric pattern (right).....	158
Figure 5-32 : Image of the stereo camera system 1 during the calibration process.	158
Figure 5-33: Schematic of the angular deformation sensors.....	161
Figure 5-34: Responses of the sample HT002 to torques during the four phases of loading in trail test 1.....	163
Figure 5-35: Torque versus relative angle of twist recorded by inclinometers for specimen HT002.	164
Figure 5-36: Torque versus relative angle of twist recorded by stereo camera systems for specimen HT002.....	164
Figure 5-37: Torque versus angle of twist for all torsion specimens.	165
Figure 5-38: Determination of torsional stiffness of specimen HT002 (top) and specimen HT003 (bottom).	167
Figure 5-39: The average shear modulus of the torsion specimens calculated from each trial torsion test.....	170
Figure 5-40: The average shear modulus of the torsion specimens.	172

Figure 5-41: The correlation between the values of shear modulus measured in clockwise and anticlockwise directions under torque loading (top) and unloading (bottom) phases.	174
Figure 5-42: A screen shot of the calibration parameters of the left camera generated by the calibration procedure of HALCON.....	177
Figure 5-43: A screen shot of the developed GUI during stereo camera calibration..	178
Figure 5-44: The image processing steps for extracting the targets.....	179
Figure 5-45: Comparison between inclinometers and optical measurements for a) sample HT005 in the first trial torsion test, and b) sample HT009 in the first trial torsion test.	181
Figure 5-46: Comparison of the rotations measured in specimen HT004 between a) between inclinometer B and the stereo camera systems 1 and b) inclinometer C and the stereo camera systems 2.....	182
Figure 5-47: Illustration of targets arrangement in the torsion specimen.	183
Figure 5-48: Deformations of points located on line L6 of the left pattern at different loading and unloading phases.	185
Figure 5-49: Deformations of points located on line L6 of the right pattern at different loading and unloading phases.	186
Figure 5-50: Diagram of different shear spans used to determine the shear modulus of various segments.	187
Figure 5-51: Variations of shear modulus at different shear spans.....	190
Figure 5-52: Illustration of the regions selected to evaluate their shear modulus.	191
Figure 5-53: Rotations of Line L6 and its segments during maximum loading in a clockwise direction for a) the left photogrammetric pattern b) the right photogrammetric pattern.....	192
Figure 5-54: Variations of shear modulus along the long side of the cross section....	194
Figure 6-1: Workflow diagram of the experimental work.....	200
Figure 6-2: A Schematic diagram of a compression specimen with its dimensions...201	
Figure 6-3: The LVDT transducer with its mounting system.....	202
Figure 6-4: The image of the used Basler cameras.....	202

Figure 6-5: The test configuration for the validation of the photogrammetric approach.	204
Figure 6-6: Stereo camera calibration	206
Figure 6-7: Materials used in the study	207
Figure 6-8: Schematic view of the test sample with LVDT instrumentation	209
Figure 6-9: Image of experimental setup of compression test.	210
Figure 6-10: Schematic plot of the experimental setup of compression test with instrumentation (top), and more details of the specimen (bottom).	211
Figure 6-11: Screenshot of the implemented HALCON algorithm during stereo processing of the captured images.	213
Figure 6-12: Flowchart of the algorithm.	214
Figure 6-13: The image processing steps for extracting the targets.	215
Figure 6-14: Comparison of measurements between the LVDT and the photogrammetric approach for trial test 2 (top) and trial test 3 (bottom).	217
Figure 6-15: The selected targets to evaluate the performance of the LVDT.	219
Figure 6-16: Comparison of the measurement results for sample 1.	219
Figure 6-17: Comparison of the measurement results for sample 2.	220
Figure 6-18: The setup used to investigate the mounting system of the LVDT.	221
Figure 6-19: Comparison of the LVDT and the Photogrammetric measurements.	222
Figure 6-20: The test results for evaluating the LVDT mounting system.	223
Figure 6-21: Screenshot of the target detection, showing the locations of the targets monitored with different gauge lengths.	224
Figure 6-22: Comparison of the displacement results at the middle of sample 1 (top) and sample 9 (bottom).	225

LIST OF TABLES

Table 2-1: Shape factor values for torsion test (BS EN 408:2010)	30
Table 2-2: Dimension of structural timber or glued laminated timber test pieces (BS EN 408:2010).	37
Table 5-1: The camera parameters of the stereo camera system.	131
Table 5-2: 3D pose parameters (rotation and translation).....	131
Table 5-3: Internal camera parameters of the stereo camera system.	142
Table 5-4: 3D pose parameters (rotation and translation).....	143
Table 5-5: Dimensions of the timber samples.....	152
Table 5-6: Shear modulus of the torsion samples in clockwise and anti-clockwise directions.	169
Table 5-7: Average shear modulus of each of the torsion samples in all trial tests.	171
Table 5-8: Relative characteristics properties for homogenous and combined glulam(BS EN 14080 (2009))......	172
Table 5-9: The average shear modulus of specimen HT010 calculated in different ways.	175
Table 5-10: Internal camera parameters of the first stereo camera system.....	176
Table 5-11: 3D pose parameters (rotation and translation).....	177
Table 5-12: The shear modulus values of three spans of torsion specimens.	189
Table 5-13: Shear modulus of torsion samples at each line segment.	193

1. INTRODUCTION

1.1 Introduction

Timber is a natural and valuable environmentally friendly structural material which is not only a material for the future, but it is also one of the earliest building materials used for construction purposes. Because of its attractive features, high strength-to-weight ratio and ease of construction, the demand for timber as an important building material is considerably high. Timber has become increasingly popular structural material in commercial and industrial applications and especially for residential constructions where beams and columns are required. Timber sections can be obtained easily with a simple process in order to be used in construction. The dimensions of their cross sections and length, however, are limited by the size of the trees to produce the particular type of wood. The use of normal sawn timber may become impractical when the applied loads become large or the span of the structure is long. Timber is also limited by the strength of the particular type of wood. Moreover, the presence of natural defects of various kinds such as, knots and grain deviation cause the variability or variation in strength and stiffness properties of timber, making it difficult for engineers to predict their behaviour under loading. In these circumstances, engineered wood products (EWP) can be used to overcome these dimensional limitations of sawn lumber and can also be used to reduce or control the natural variations and defects in such a way that each defect has minimal influence.

Glued-laminated timber, commonly referred to as glulam, is one of the oldest known EWP and is still highly competitive in modern, large-scale constructions. Glulam products have grown in popularity because of the ability to produce long lengths and large cross-sections whose dimensions are no longer restricted by the limited dimensions of the trees. These types of materials have the advantage of providing lightweight, high strength, considerable stiffness and the ability to make long and complex shapes. Compared to solid wood, the material properties of glulam can be controlled to lie within desirable limits. This can be achieved by the

production process in which strength-reducing characteristics can be adjusted. For example, natural wood defects, such as knots, can either be removed or more uniformly distributed throughout a glulam section, which increases the uniformity of their strength properties. This results in a structural product in which defects are generally reduced and relatively high strength is achieved.

The above mentioned advantages make glulam an ideal and more attractive structural material in modern construction. Glulam finds its way in a wide range of structural applications ranging from residential buildings to commercial buildings to industrial products. Due to its flexibility and adaptability, glulam can be manufactured in almost any size and shape with a variety of structural forms, such as beams, columns, curved sections, trusses and girders. Among these different elements of timber, timber beams are the most common elements of glulam structures. Timber beams, also referred to as “joists”, have been traditionally used as solid sawn lumber. Advancement in engineering wood products has resulted in increasing the use of these products, including wood I-joists, open web trusses and glued laminated timber joists.

For the purpose of designing glulam joists, it is essential that these types of glulam sections should be designed in such a way that they meet the specific requirements of strength and stiffness for a given application. There are a wide range of engineering properties that affect the strength and performance of produced timber and timber-based composite joists and these properties should be taken into account. The mechanical properties, especially the elastic and strength properties are of considerable importance as they are the more essential criteria to select materials or to establish design or product specifications. Known as elastic constants, the elastic properties include the basic and fundamental properties such as modulus of elasticity (MOE) and shear modulus (G). Although these properties can be determined experimentally, the way to get the value of these properties is more comprehensive and the understanding of glulam properties remains insufficient to allow an assessment of these properties. Therefore, there is a need for more knowledge of these mechanical properties of glulam joists in order to evaluate their behaviour.

The shear modulus (G), also called modulus of rigidity, is a material constant, expressing the relation between shear stress and shear strain, which indicates the resistance to shear deformation. It is a fundamental mechanical property of wood that is used in the design of timber and engineered wood products. Shear modulus of timber materials plays a very significant role in structural modelling, such as lateral torsional stability of joists (EN 1995-1-1, 2004), and designing serviceability of wood-joist floors (Foschi, 1982). The shear modulus is also an important input for setting up analytical and finite element models (Chui, 2002, Jiang et al., 2004).

Shear testing of composite materials has proven to be one of the most difficult areas of mechanical property testing (Schwartz, M.M., 1984). The difficulty in measuring pure shear has probably led to the different approaches and methods to determine this property. Although there have been a variety of shear test methods developed and used to estimate the shear modulus of timber joists, there have been no standardization of widely accepted test methods that can be referenced for use. CEN (EN 408:2003, 2003) and ASTM (ASTM-D198-94, 1994) provided an analytical approach to obtain the shear modulus incorporating the modulus of elasticity of joists obtained from three and four point bending tests. The analytical approach has been rarely used due to its complex procedure and a fraction of the modulus of elasticity (MOE) from the bending test has been adopted for decades. Therefore, the shear modulus is often calculated from modulus of elasticity using E to G ratio of 16:1, which was given by Bodig and Goodman (Bodig and Goodman, 1973). The published design values of shear modulus in Wood hand book (USDA, 1999) and BS (EN 338:2009, 2009) are also determined based on this assumption. However, recent researches (Burdzik and Nkwera, 2003, Hindman et al., 2005a, Hindman et al., 2005b, Harrison, 2006, Khokhar et al., 2010, Zhang et al., 2011) have indicated that there is little evidence of a correlation between the shear modulus and modulus of elasticity for solid timber beams and therefore the shear modulus should be measured independently.

Despite being gradually accepted that shear modulus should be independently measured, the knowledge and technologies developed so far to evaluate the shear modulus is far from mature. Bending test (EN 408:2003, 2003, ASTM-D143-94,

1994) is generally the most common approach to evaluate the shear modulus of timber and glulam materials. Full-size structural joists can be tested under bending to take the possible influence defects and orthotropic behaviour into account. However, the bending test creates a combination of flexural and shear stresses which leads to difficulties in obtaining the true value of shear stiffness (Vafai and Pincus, 1973, Riyanto and Gupta, 1998). The most recently updated British Standard, BS EN 408:2010+A1:2012 suggested two new approaches including the torsion method to evaluate the shear modulus. This method creates a pure shear state, which is ideal for measuring the shear modulus. More and more researchers including (Khokhar et al., 2010, Zhang et al., 2011, Zhang et al., 2012) have also suggested the torsion method to measure the shear modulus of structural size timber and glulam beams.

A fundamental requirement for the efficient use of a glulam beam as a structural element is accurate knowledge of its mechanical behaviour and the material properties characterising that behaviour. Measuring the elastic properties of a timber joist effectively during testing is the key to evaluating the shear modulus and its variations. Many different test methods have been developed and adopted by different researchers to evaluate these properties of timber joists. These tests, including torsion, bending, compression and tension tests require standard testing devices for measuring the rotations or the displacements of the timber samples at specific locations.

The inclinometer, for example, is one of the most commonly used instruments in the torsion test for measuring the rotation of the timber samples. It is an accurate and reliable device for measuring the rotation at the point where it is installed. Although this mechanical device have proven to be accurate and flexible for measuring displacements, they sometimes reveal significant problems. This sensor tend to be time-consuming and labour intensive. Moreover, the size and the nature of the surface contact measuring of this mechanical device has prevented it to be used in measuring more details of the shear deformations, which might help to understand the relation between the MOE and G for timber and glulam beams. In addition, this sensor can be damaged or destroyed during destructive testing.

The linear variable differential transducer (LVDT) is commonly used for assessing the deformation or displacement measurements on timber during the bending and compression tests. In accordance to the EN408 standard, the LVDT transducer is required to be installed to the middle of the compression glulam samples to provide a local displacement measurement which can be used to determine the MOE of the specimen. LVDT is an accurate and reliable device for measuring the linear displacement in applications where linear displacement measurements are required. However, little information exists concerning the setup of the LVDT sensor, especially when being attached to timber specimens. Limited research has been conducted to verify the accuracy of the devices used during the above-mentioned tests. Moreover, the use of this traditional instrument has also been limited by giving only one-dimensional measurements, meaning that the results are not fully applicable to real structural systems. Furthermore, the measuring instrument can also be damaged during the experiment and it is not suited for tasks requiring measuring displacements at a large number of object points.

Photogrammetry, a non-contact technique for extracting reliable measurements of physical objects from photographs, provides a good alternative technique for structural measurements. Compared with the more traditional means of measuring deformations of structures, photogrammetry, on the other hand, offers a number of remarkable advantages including:

- It is a 3D and non-contact measurement system.
- It can be used to undertake measurement of objects with difficult or restricted access.
- It can be used for monitoring a large number of points on a structure with minimal time, enabling much more information to be extracted and making this system ideal for applications require detailed displacement and rotation measurements.
- It offers low cost and flexibility.

- It provides a permanent visual and measurement record for further assessment, meaning that the measurements of the images need not to be carried out immediately.

Optical methods that give displacements or strain fields are now widely used in used to evaluate material properties of timber-based composite but most of these methods have been extremely limited to give in-plane measurements, meaning that the results are not fully applicable to real structural systems. In this research, however, a photogrammetric method based on a binocular stereo vision system that uses two cameras to measure 3D displacements on any 3D object is proposed. The goal of developing this system was for the purpose of evaluating material properties of timber and timber-based composite beams. The torsion test and shear field test during standardized four-point bending test are recommended as standard approaches to determine the shear modulus of structural-size timber and glulam beams, according to CEN (EN408:2010, 2010) standard. Evaluation of shear modulus from shear field test during four-point bending test may not be an appropriate approach. Since the torsion test provide a state of pure shear stress distribution in the specimen, allowing measurement of the pure shear properties, this method might be a suitable approach for determining the shear properties of timber and timber-based composite materials. Therefore, the photogrammetric approach was mainly proposed for the torsion test. In contrast to the traditional techniques, the photogrammetric approach could provide more details of angular deformation which are necessary for providing more details of shear deformation of torsion specimens.

1.2 Research Objectives and Plan

The aim of this research that will be discussed in this thesis is to provide an effective alternative method for evaluating material properties of timber and timber-based composite structures in order to avoid the limitation of the conventional and contact methods. The other research aims of the work are to:

1. Implement a photogrammetric approach based on a binocular stereo camera system for deformation measurements in timber and timber-based composite materials.
2. Develop a customized software that is used to automate recording and processing the image data for the laboratory tests using the binocular stereo system.
3. Evaluate the influence of several camera parameters on the efficiency of the stereo camera system and validate the stereo system by conducting experimental tests and comparing test results of the photogrammetric approach with those obtained from the different traditional devices.
4. Investigate the performance of the optical system on evaluating material properties in timber and timber-based materials by conducting a series of different tests including torsion and compression.
5. Investigate the influence of inducing torque in a clockwise or an anticlockwise direction on the torsional behaviour and the shear modulus of the glulam timber specimens.
6. Evaluate the values and variations of the shear modulus of the glulam specimens under the torsion test.
7. Evaluate the performance of the LVDT displacement transducer on monitoring the deformation of the glulam timber samples during the compression test.

To achieve these objectives, a research plan was made to help in fulfilling the requirements of the research. As shown schematically in Figure 1-1, this research can be divided into four main stages. In the first stage, the main goal was to find an efficient alternative approach for evaluating material properties of timber and timber-based composite materials. Therefore a literature review was conducted and it was concluded that the photogrammetric approach based on the binocular stereo camera system reveals significance and remarkable advantages over the traditional methods. Therefore, we focused on developing a photogrammetric and a stereo camera system as well as implementing this system in a software package in order to automate recording and processing the image data for the laboratory testing.

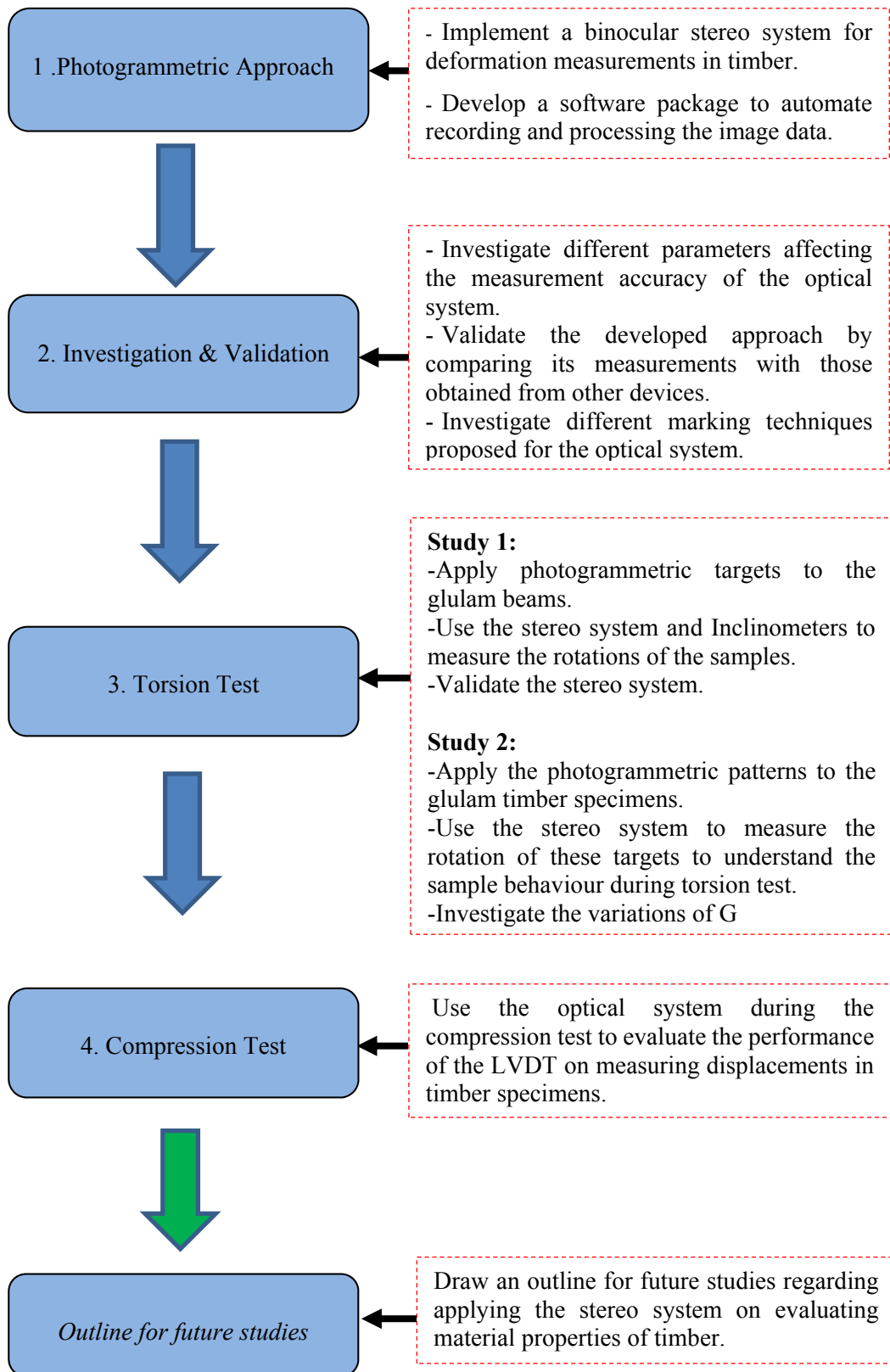


Figure 1-1: The research work being carried out in this thesis.

To obtain accurate three-dimensional information from the stereo cameras, the geometric parameters of the stereo camera system need to be known. This can be achieved by calibrating the stereo cameras. There are many different calibration methods which can be used to calibrate the cameras and find their calibration parameters. For instance, Matlab Camera Calibration Toolbox (Bouguet, 2004) by Jean-Yves Bouguet and camera calibration based on HALCON (MVTec Software GmbH, 2010) are two examples of the calibration methods which are well-known and used to determine the camera parameters known as internal parameters as well as the pose, known as external parameters, taking into account lens distortion. The two methods require the user to use a calibration object, which is a planar pattern, shown at different orientations. However, the manual and interactive method of corner extraction of the calibration plate in Matlab Toolbox are extremely time-consuming. On the other hand, camera calibration in HALCON offers a full three-dimensional (3D) camera calibration as well as hardware independence by providing interfaces to hundreds of industrial cameras and frame grabbers, also for standards like GenICam, GigE Vision. Additionally, HALCON also includes an extensive library of more than 1300 operators with outstanding performance for complex tasks including pattern matching, measuring, camera calibration, and binocular stereo vision. Moreover, the library of this software provides efficient implementations of various image processing methods, which can be integrated easily into customised software development based on C, C++ or Visual Basic. Therefore, the stereo system was implemented and developed based on this software. Figure 1-2 shows a schematic drawing of the proposed stereo camera system for 3D measurements.

In the second stage of this research the stereo camera system was validated through experimental studies. Several factors affecting the accuracy of the system including the number of calibration images, the camera model and the baseline length of the stereo camera system were considered during this investigation. Three different types of photogrammetric targets have been proposed by the authors to evaluate the efficiency of the stereo camera system to investigate the displacement measurement of the samples during the compression tests. The applicability of these targets when

attached to timber has been evaluated and compared with each other as well as with transducer sensor.

In the third stage of this research, the stereo system was used during the torsion test to evaluate shear modulus of a structural-size beam of timber. Two main studies were considered for torsional experiments. The first study was conducted to employ the optical system for proper use of the torsion test in order to evaluate the shear modulus and the torsional behaviour of timber glulam beams. In the second study, extensive experimental torsion tests were conducted on twelve glulam beams. A photogrammetric pattern consisting of circular black targets on a white background was proposed by the authors of this research to be employed together with the stereo camera system. The potential of using the photogrammetric approach to evaluate the variation of the shear modulus along the cross sectional depth of the torsion specimens was also considered in this study. In addition, the effect of using different shear spans on the shear modulus (G) was also investigated.

Finally, in the last stage, the photogrammetric approach was proposed to be used in the compression test. The goal of this investigation was to evaluate the performance of the LVDT displacement transducer on monitoring the deformation of the glulam timber samples during the compression test. Before being employed to evaluate the setup and the measurements of the LVDT, the photogrammetric method was validated through experimental tests conducted on the compression specimens. The setup of the mounting system used to attach it to the glulam specimen was also investigated. Experimental studies were carried out on the timber samples and the optical system was validated by comparing displacement values measured by the photogrammetric approach with those obtained from different traditional devices.

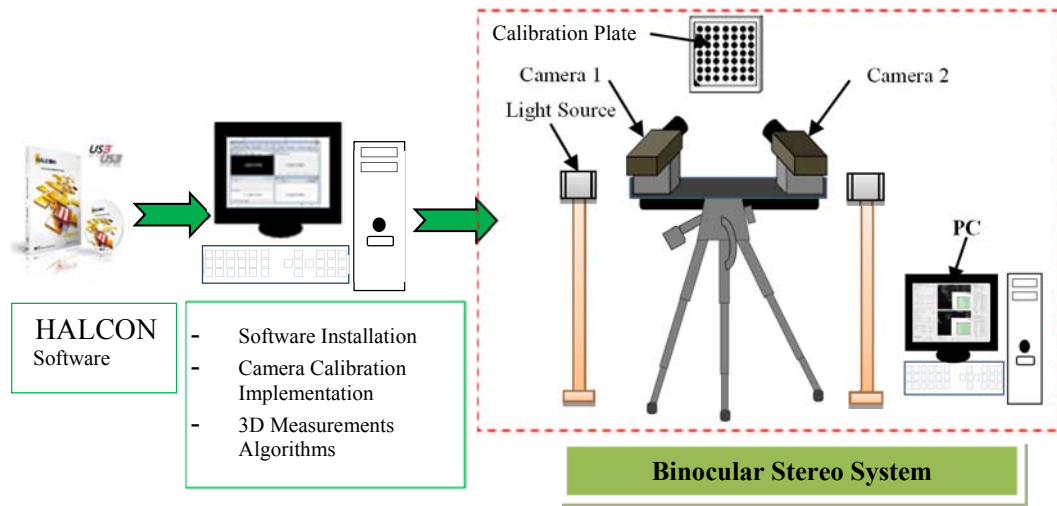


Figure 1-2: Schematic diagram for developing the binocular stereo vision system.

1.3 Significance of the Study

Photogrammetry is an alternative technique to evaluate material properties of timber-based composite materials under different testing including torsion and compression. Although this method was applied to glulam beams, it can also be applicable to other types of materials and engineered wood products. This research will provide a better understanding and proper use of the torsion test which is used to evaluate the elastic and shear properties and will assist further research on these tests for engineered wood beams. The outcome of this study will contribute to the recommendations provided by the EN 408 standard for adopting the torsion as standardized test to determine the shear modulus values of the glulam timber beams. The proposed photogrammetric approach by the authors of this research provides the possibility of investigating the shear deformation at different locations, which cannot be achieved utilizing the traditional measurement devices. This investigation will also allow assessing performance and reliability of displacement transducers (LVDTs) when mounted on timber during compressive tests as well as monitoring the deformation of the samples at various locations by providing more information which would not be possible to obtain using the traditional techniques. These evaluations will also assess the development of an outline for a future research

programme in the field of evaluating material properties of timber and timber-based composite materials and may assist in finding a proper way to mount this device on timber when a high measuring accuracy is needed.

1.4 Outline of the thesis

The structure of the thesis is organized as follows: Chapter one is an introduction to the work completed and a brief description of the problems addressed. The methodology and research plan used in this study are presented in this chapter.

Chapter two presents review of available research investigations on torsion and compression tests using the optical methods to evaluate material properties of timber joists. The first part of this chapter reviews the literature on photogrammetry. Then a comprehensive review of available standard test procedures on the elastic and shear properties of timber is presented.

Chapter three presents the developed stereo camera system, including the image acquisition hardware and the image processing software. The chapter also presents the fundamentals of camera model and camera calibration theory that are used for finding the intrinsic and extrinsic parameters of the stereo cameras.

Chapter four investigates the validation of the binocular stereo system. In this chapter, we have studied several parameters affecting the accuracy of the stereo system, including the baseline length, the camera models, and the number of the calibration images. The targeting techniques, which were proposed as photogrammetric targets of the stereo camera system, are also reported with the conducted experimental tests.

Chapters five and six present the experimental work being carried out in this thesis to investigate the applicability of the stereo system on both the torsion and compression tests, respectively. The first part of Chapter five presents the experimental work conducted on timber beams during the torsion test to measure the rotations of the torsion samples, which are essential measurements to evaluate their shear modulus. The second part of this chapter reports the experimental work

with the proposed method to measure the rotation of the timber samples at a large number of points so that the values and variations of the shear modulus can be evaluated. Chapter six presents the experimental studies which were conducted during the compression test to evaluate the deformations of the glulam timber specimens under compressive loadings. The applicability of the proposed photogrammetric method for evaluating the performance of the LVDT displacement transducers on measuring the displacements in timber specimens is also illustrated and discussed in this chapter.

Finally, Chapter eight summarizes the thesis and presents concluding remarks. Future research directions based on this work are also suggested.

2. LITERATURE REIVEW

2.1 Timber and Glued-laminated Timber

Timber is a valuable structural material, not only because of its material properties, but also it is an environmentally friendly and a highly sustainable material that can be used for different construction purposes. This natural material with interesting features is widely available throughout the world. Although timber products can be obtained easily with a simple process, the cross-sectional dimensions and length of the timber are limited by the size of the trees to produce the particular type of wood. In addition to this, timber is also limited by the strength of the particular type of wood. The presence of natural defects, such as grain deviation and knots, as shown in Figure 2-1, results in the strength and stiffness properties of timber to be varied, making the behaviour of timber under loading more difficult to predict. To overcome the dimensional limitations of timber, engineered wood products (EWP) can be used to reduce or control the natural variations and defects.

Engineered timber products have highly predictable and reliable performance characteristics and provide high design flexibility (Cai, Z. and Ross, R.J., 2010). These products allow the use of smaller pieces as well as longer spans. Engineered timber products prove to be more environmentally friendly and, if used appropriately, are often less expensive than building materials such as steel or concrete (Thelandersson and Larsen, 2003). These products are extremely resource-efficient because they use more of the available resource with minimal waste.

As an engineered-wood product, glulam is a highly competitive material which has grown in popularity due to the ability to produce long lengths and large cross-sections whose dimensions are no longer restricted by the limited dimensions of the trees. Glued-laminated timber is a valuable structural material that optimizes the structural values of wood and can be manufactured in a variety of configurations. Glued-laminated timber members are manufactured by gluing, with the help of structural adhesives, suitably selected and prepared individual pieces of high strength lumber that are end-joined together to form large timber sections with long

lengths, which are known as laminations, under controlled conditions of temperature and pressure (Cai, Z. and Ross, R.J., 2010). Through the lamination process, a great variety of shapes can be created ranging from simple and straight cross-sectional shapes to complex arched or bent shapes with varying cross-sections. These types of materials have the advantage of providing lightweight, high strength, considerable stiffness and the ability to make long and complex shapes.

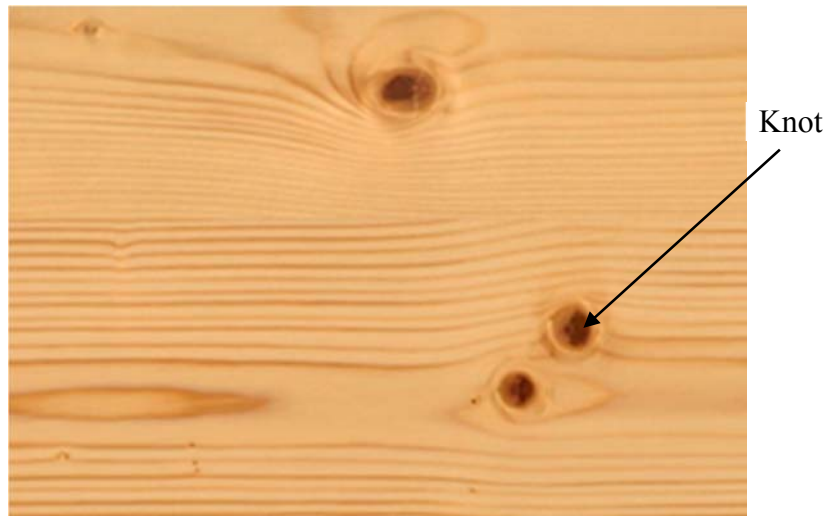


Figure 2-1: The prescene of some defects in wood.

2.2 Mechanical Properties of Timber and Timber-based Composite Materials

Any wood material glued with adhesives is defined as composite. Wood-based composites have been used for different structural applications. In order to use these products efficiently, it is important to have accurate knowledge of their mechanical properties.

The mechanical properties of wood composites rely on different parameters, including wood species, the type of adhesives used to glue the wood pieces, and the geometry of the wood pieces (Cai, Z. and Ross, R.J., 2010). The performances of

wood-based composites are characterized by a variety of engineering properties. Among these properties, mechanical properties are the most commonly used to evaluate the characteristics of wood-based composites. Mechanical properties include the elastic and strength properties which are of considerable importance when selecting materials or establishing design or product specifications (Cai, Z. and Ross, R.J., 2010). Strength properties describe the ability of a material to resist applied loads. These properties describe material behaviour related to compression, tension, shear, bending, and torsion. Strength properties rely on which direction the grains are stressed, but in general, these properties are distinguished in two directions, parallel and perpendicular to the grains (Cai, Z. and Ross, R.J., 2010).

Elastic properties relate the resistance of a material to deformation under an applied load and the ability of the material to recover its original dimensions when the load is removed (Cai, Z. and Ross, R.J., 2010). For an ideally elastic material with properties loaded below the proportional limit, all deformation is recoverable and the material returns to its original shape when the stress is removed.

2.2.1 Wood as an Orthotropic Material

Wood may be described as an orthotropic material with unique and independent mechanical properties in the directions of three mutually perpendicular axes: longitudinal, radial and tangential. The longitudinal (L) axis is the axis parallel to the grain (fibre) direction, the radial (R) axis is perpendicular to the grain and normal to the growth rings, and the tangential (T) axis is perpendicular to the grain direction and normal to the radial direction. These axes are illustrated in Figure 2–2. Properties of wood vary along these directions due to the orientation of the wood fibres, and due to the way in which a tree diameter increases as it grows (Cai, Z. and Ross, R.J., 2010). Although most wood properties differ in each of these three directions, differences between the same properties along the radial and tangential directions are relatively small compared to differences between the radial or tangential axis and the longitudinal axis (Miller, R.B., 1999). Because of that, most

wood properties for structural applications are usually given for two directions: parallel and perpendicular to the grain.

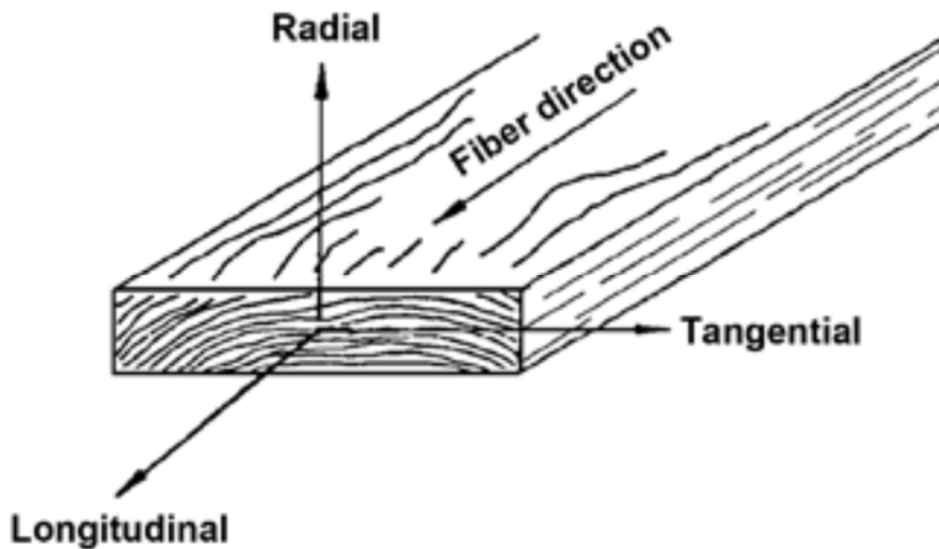


Figure 2-2: The three principal axes of wood with respect to grain direction and growth rings (Miller, R.B., 1999).

The elastic behaviour of wood can be characterized by three elastic parameters which are modulus of elasticity (E), modulus of rigidity (G), and Poisson's ratio (ν). These parameters are defined in each orthogonal direction, resulting in nine independent elastic parameters. Therefore, Hooke's three-dimensional law of elasticity for orthotropic materials such as wood can be expressed in a matrix form when the compliance coefficients are expressed in terms of the engineering parameters (Bodig and Jayne, 1982):

$$\begin{pmatrix} \varepsilon_{LL} \\ \varepsilon_{RR} \\ \varepsilon_{TT} \\ \varepsilon_{RT} \\ \varepsilon_{TL} \\ \varepsilon_{LR} \end{pmatrix} = \begin{pmatrix} \frac{1}{E_L} & -\frac{\nu_{TR}}{E_R} & -\frac{\nu_{TL}}{E_T} \\ -\frac{\nu_{RL}}{E_L} & \frac{1}{E_R} & -\frac{\nu_{TR}}{E_T} \\ -\frac{\nu_{LT}}{E_L} & -\frac{\nu_{RT}}{E_R} & \frac{1}{E_T} \\ & & & \frac{1}{G_{RT}} \\ & & & & \frac{1}{G_{LT}} \\ & & & & & \frac{1}{G_{LR}} \end{pmatrix} \begin{pmatrix} \sigma_{LL} \\ \sigma_{RR} \\ \sigma_{TT} \\ \sigma_{RT} \\ \sigma_{TL} \\ \sigma_{LR} \end{pmatrix} \quad (2.1)$$

The above matrix includes nine independent parameters which are three moduli of elasticity, three moduli of rigidity, and three Poisson's ratios. The characters E , G , and ν represent the elastic modulus, shear modulus, and Poisson's ratio, respectively. The indices, L,R, and T represent the longitudinal, radial, and tangential directions, respectively.

2.2.2 The Elastic Properties

Wood is not ideally elastic in that some deformations from loading are not immediately recovered when the load is removed; however, residual deformations are generally recoverable over a period of time (Thelandersson and Larsen, 2003). Although technically considered a viscoelastic material, wood is usually assumed to behave as an elastic material for most engineering applications. The main elastic properties include:

1- Modulus of Elasticity

Modulus of elasticity (MOE) or elastic modulus relates the applied stress to the strain within the elastic region. MOE can be determined from the slope of the linear portion of the stress-strain graph from zero to the proportional limit. As mentioned before, the elastic behaviour of wood can be characterized by three elastic constants denoted as E_L , E_R , and E_T , representing the elastic modulus in the longitudinal, radial, and tangential directions, respectively. For example, E_L relates the stress in the longitudinal direction to the strain in the longitudinal direction.

Elastic constants vary within and between species and with moisture content (MC) and specific gravity. Some elastic properties are of greater importance to the design community than others. For instance, the modulus of elasticity in the longitudinal direction, E_L is one of the principal elastic constants of timber.

2- Shear Modulus

Shear modulus (G), known as modulus of rigidity, is a material constant which relates shear stress to shear strain and indicates the resistance to deformation caused by shear stresses (Schwartz, M.M., 1984). It is a fundamental mechanical property of wood that is used in the design of timber and engineered wood products. Shear modulus of timber materials plays a very significant role in structural modelling, such as lateral torsional stability of the timber beams (EN 1995-1-1, 2004), and designing serviceability of wood-joists floor (Foschi, 1982). The shear modulus is also an important input for setting up analytical and finite element models (Chui, 2002, Jiang et al., 2004).

2.3 Current Methods for Measuring Displacement and Deformation in Structures

Evaluating mechanical properties of the materials under testing involves the measurement and analysis of their displacements and deformations. For example, measuring displacements and deformations in structural components under loading can be utilized to obtain material properties of timber such as MOE and G . Generally, there are two main approaches for monitoring the structural deformations and these are the contact and non-contact methods. The contact methods such as Linear Variable Differential Transformers (LVDTs), extensometers, and dial gauges are used to measure displacement or deformation of objects with very high accuracy. However, these methods have some limitations which may not be avoided. For instance, the contact instruments require a considerable amount of attention and can be damaged during destructive tests. In addition, they are limited to measuring point-wise and in one dimension only.

Moreover, the contact between the measuring devices and the surface of the object under testing may influence their reading values.

Non-contact methods offer a number of advantages over the contact methods for measuring deformation of structures. These techniques are useful because they can be used without direct contact with structural components. In addition, they provide the possibility of measuring the deformation at a large number of points and in three-dimensions. There are different techniques that have been proposed and applied for different applications including:

- Geodetic technique

This method is used to determine the 3D coordinates of specific points by making use of total stations. However, the measuring procedure of this technique is time consuming when they are used to measure dynamic deformations (Tsakiri et al., 2004).

- Terrestrial laser scanning

This technology is a new technique which produces dense three dimensional data without using targets. But, the cost of these devices is high and they produce poor accuracy of about 2mm (Maas and Hampel, 2006).

- Global positioning system (GPS)

These devices can be used to undertake deformation measurements. The limitations of this technology have restricted their use to specific applications. GPS-based measurements are low rate and have coverage problems. The total cost of the GPS system tends to be expensive. This sensor is restricted to measuring displacements at specific points on the object of interest (Maas and Hampel, 2006).

- Videometry

Videometry makes use of video sequences which produce 3D data in real time. This method is suitable for monitoring dynamic deformation. However, expensive camcorders are required in order to obtain accurate results from this technique.

➤ Close-range photogrammetric techniques:

These techniques can be utilized with a single camera to measure deformation in two dimensions or with two or multiple synchronized cameras to undertake measurements in three dimensions. They offer the possibility to capture 3D points with high accuracy and reduced time (Wolf et al., 2000).

2.4 Photogrammetry and Stereo Vision

In the most general terms, photogrammetry can be defined as a technique for obtaining reliable measurements of three-dimensional objects by measuring and analysing their two-dimensional photographs. Photogrammetry, as defined by the American Society of Photogrammetry and Remote Sensing (ASPRS), is “the art, science, and technology of obtaining reliable information about physical objects and the environment through processes of recording, measuring, and interpreting photographic images and patterns of recorded radiant electromagnetic energy and other phenomena” (McGlone et al., 2004). It is a non-destructive and non-contact remote sensing technology which can be used in different structures without the high costs. With rapid advancement in computer and software technology, photogrammetry has become a more extensive practise in different areas of engineering. The possibility of directly measuring 3D displacements and deformations of objects is a very attractive feature of photogrammetry.

2.4.1 Historical Background of Photogrammetry

Photogrammetry can be divided into aerial and terrestrial photogrammetry, depending on the distance between the camera and the object. In aerial photogrammetry, images are acquired overhead from an aircraft, satellite, or hot air balloon, providing topographic maps and land-use details. Terrestrial photogrammetry, known as non-topographic or ground-based photogrammetry, refers to the applications of photogrammetry in which images are acquired at locations on or near the earth’s surface. When the camera-to-object distance is less

than 100 m, terrestrial photogrammetry is further defined as close-range photogrammetry (Atkinson, 2001). Close-range photogrammetry has been applied in many different fields including architecture, industrial metrology, archaeological surveys, and engineering. The major application focus of close-range photogrammetry is the construction of detailed 3D models from a series of images. The images are usually taken from different viewpoints and produce measurements that can be used to create a 3D model. For civil engineering applications using photogrammetry, most activities fall in this category (Atkinson, 2001).

Although close-range photogrammetry has not been as popular in civil engineering structures as in other fields, it has been used as a possible approach in providing accurate consistent data and easy visualisation for different civil engineering tasks. In addition, the rapid development of digital imaging and computer technologies since the early 1990s has made close-range photogrammetry more feasible and affordable for civil engineering applications.

2.4.2 Review of Close-Range Photogrammetric Methods to Wood Properties

The close-range photogrammetric system is a non-contact technique for extracting reliable measurements of objects from images. The photogrammetric methods have been applied to evaluate material properties of wood and wood-based composites. Considerable amounts of research were undertaken in this area.

Recently, the capabilities of photogrammetry as a low-cost tool for stiffness analysis and finite-element (FE) validation under 4-point bending tests of structural timber have been presented by Guindos and Ortiz (2013). The developed photogrammetric technique utilized three Canon Eos 400D cameras with a resolution of 10 megapixels. The author proposes an approach to estimate three different modulus of elasticity (MOE): the *global MOE*, the *clear MOE*, and the *MOE in Knots*. The clear MOE is related to the defect-free areas where there are no knots. The MOE in Knots is related to the areas with knots. The global MOE is related to both areas with and without knots and represents the average stiffness of a specimen. The author concluded that the performance of the finite model was

improved considerably when using the clear MOE, instead of the traditional MOE which is usually used in the test standards which neglect shearing strain. The author also mentioned that photogrammetry assisted in reaching reliable conclusions with only a few tests, reducing the required number of tests considerably.

The application of a stereovision technique for evaluating the longitudinal modulus of elasticity of maritime pine (*Pinus pinaster Ait.*) during compression tests parallel to the grain was reported by Xavier et al. (2012). For comparison purposes, the axial compressive strain data at the centre of the specimen was evaluated by three different techniques. A stereo-camera system combined with digital image correlation (DIC) was employed to provide strain measurements. Additionally, two conventional techniques, a linear strain gauge and a linear variable differential transducer (LVDT) were also used to determine the strain state. The strain gauge was fixed at the centre of the specimen and the LVDT measured the relative displacement between the compression plates. The strain data measured over the entire target region by the optical system was averaged out and used to calculate the longitudinal modulus of elasticity. The strain data obtained from the strain gauge was also used to measure the longitudinal modulus of elasticity. The mean value of the longitudinal MOE determined from the measurements of the two techniques was compared and good agreements were found between the two measurement methods. The authors conclude that the optical system was found to be advantageous, leading to less scatter in the determination of MOE than strain gauge measurements.

Kang et al. (2011) reported the use of an optical measurement system with a digital image correlation (DIC) system, to investigate the changes in displacements of the surface of Willow tree disks and Oregon Oak planks during wood drying. The author concluded that with the help of the DIC system, strain changes of wood surface when drying can be better visualized and the DIC may provide more appropriate drying schedule preparation for unknown species or refractory wood species.

The DIC technique was applied by Shipsha and Berglund (2007) in transverse compression tests to measure displacement/strain distribution on samples having different annual ring patterns. The authors mentioned that his study would not have been possible with some traditional devices such as strain gauges.

Franke et al. (2006) proposed a photogrammetric approach, based on close-range photogrammetry and image processing, to investigate experimentally stress in timber engineering, enabling a more exact measurement of deformations, cracks and deteriorations during testing of specimens. The authors mentioned that it was possible to investigate the appearance and growth of cracks during loading of specimens and the strain progression can be determined easily.

The mechanical behaviour of European oak (*Quercus robur* L.) in transverse compression tests was studied by Ljungdahl et al. (2006) utilizing the DIC technique to evaluate the strain field in the region of interest. The full-field data obtained by the optical system permitted a good understanding of the stress-strain curve regarding the progressive deformation and failure of the structural elements of the material. In addition, the author mentioned that the full-field strain measurements gave evidence that the rays are the main microstructural factor controlling transverse anisotropy for this type of wood.

Serrano and Enquist (2005) applied an optical method based on the digital image correlation (DIC) principle to measure displacements and strains on adhesively bonded wood specimens. Testing wood-adhesive bonds is traditionally based on standard methods in which the load and displacements are measured for the evaluation of the strength of the bond line. The full-field measurements determined from the DIC method allowed comparing the strain distribution of three different adhesives at different loads.

Two geodetic techniques, specifically close-range photogrammetry and standard surveying, have been proposed by Tsakiri et al. (2004) to describe the behaviour of a timber beam under five-point bending testing. These techniques were proposed for the measurement of vertical deflections during the controlled loading applied to a timber beam. In addition to the two geodetic techniques, a dial gauge was also

used to measure the vertical deflection in the centre of the beam. The timber beam was loaded statically at its centre in order to determine its deflection response under testing. The bending mechanism of the timber beam was analytically modelled using finite element analysis implemented in the commercial software, ANSYS. During the bending test, the geodetic techniques as well as the dial gauge were used to take the deflection measurements at different load levels. The vertical displacements of the timber beam measured via photogrammetry were compared to those predicted by the finite element analysis and a good agreement was found between the two methods.

Jernkvist and Thuvander (2001) applied the DIC technique to determine the radial and tangential displacements in a single growth ring of Norway spruce wood under tension tests in the radial direction. A finite element model was developed to identify the orthotropic elastic properties of the material. The author mentioned that the identification of all in-plane engineering constants was possible.

Dumail et al. (2000) applied the DIC technique together with the Iosipescu shear test on Norway spruce wood (*Picea abies*) positioned in the radial-tangential plane. Instead of a local measurement at the centre of the specimen determined by a strain gauge, a mean value of the shear strain between the V-notches could be obtained. The author mentioned that there is no need of a correction factor for taking into account the inhomogeneity of the shear strain across the area of measurement. This approach has some advantages when compared to the traditional ones. In addition, because of the low stiffness properties of wood in the radial-tangential plane (perpendicular to the grain), the use of a non-contact technique is preferred to prevent local stiffening.

2.4.3 Application of the Photogrammetric Techniques to Materials Other than Timber

The photogrammetric and stereo vision techniques utilize targets which can be applied to a variety of materials, including wood, bricks, concrete, steel, and composite materials. These methods require the surface of the material to be prepared with a texture or targets which can be tracked and monitored before and after the deformation so that their 3D coordinates and deformations can be determined. Photogrammetry and image processing techniques have been used in timber to measure mechanical properties, 3D displacements, or deformations at various points of the same specimen, as proposed in various experiments (Choi et al., 1991, Dahl and Malo, 2009a, Dahl and Malo, 2009b, Franke et al., 2007, Garcia and Orteu, 2001, Maas and Hampel, 2006, Guindos and Ortiz).

The photogrammetric techniques could be applied to different materials other than timber. For example, these techniques have been utilized to provide a detailed description of the development of cracks in reinforced concrete beams under flexural load (Pease, 2006). They have also been used to detect and measure deflections in concrete beams (Detchev, 2011, Whiteman, 2002, Chounta & Ioannidis, 2012). Moreover, they have also employed to monitor the behaviour of concrete structures (Dias-da-Costa, et al, 2014).

The photogrammetric technique have also been applied to steel materials. The photogrammetric and image processing techniques have also been used to evaluate deformation monitoring of steel beams (Fraser and Brown, 1986, Jáuregui et al., 2002) and to study of vertical deflection measurement of bridges (Jáuregui et al., 2003). They have utilized to measure the rotation angles of steel beam-column connection experiments. (Koken, 2014). Furthermore, the use of photogrammetry in on-site monitoring of a pedestrian bridge, during load-tests (Valença, et al., 2008).

2.4.4 Application of the Photogrammetric Techniques to Industry

Industrial photogrammetry is the art of measuring objects from the photographs or imageries for industrial use. Over the past few years, optical 3-D measurement systems for industrial applications have gained increasing importance. The photogrammetric approaches have proven to be technically and economically successful with a high accurate 3D measurements (Fraser and Brown, 1986). The developments in digital photogrammetric systems have led to successful applications of photogrammetry in industrial applications, including automated manufacturing, fabrication, inspection, part identification assembly and construction, robot guidance and control. These techniques can be used to increase the efficiency of the system and reduce costs of the products. Industrial photogrammetry is applied in construction areas, engineering fields and also for research in these fields.

Photogrammetry and stereo vision approaches are very useful for precise measurement in industrial and engineering tasks. These techniques can be used to meet the requirements for a wide range of industrial applications and they are suitable to be used in a situation where more deformation measurements are to be determined. Some of many considered applications of photogrammetry tasks are motion capture, object tracking, damage detection, deformation monitoring, and measurement solutions for areas of high risk or limited accessibility. The use of photogrammetry enhances the operations of a wide range of industries. The following examples shows some of applications of photogrammetry and stereo vision to industry.

- Mining
- Traffic Engineering
- Environmental and Forestry
- Construction of Automobile
- Industrial measurement techniques
- Shipbuilding

2.5 Standard Test Methods for Elastic and Shear Properties

The testing standard agencies, as the European Committee for Standardization (known as CEN) and the American Standard of Testing Methods (ASTM) have recommended different test methods for determination of shear and elastic properties, including shear modulus and modulus of elasticity of timber in small clear wood and in structural sizes under flexural and torsion loadings. Based originally on ISO 8375, the European standard CEN (EN408:2010, 2010) details laboratory methods for the determination of some physical and mechanical properties of timber in structural sizes. This standard details testing procedures for structural timber and glued laminated timber. The following sections are detailing the test procedures recommended by this standard for the determination of shear modulus and modulus of elasticity.

2.5.1 Testing Methods for Shear Modulus

The CEN (EN408:2010, 2010) standard has proposed the torsion and shear field test methods to determine shear modulus of timber in structural sizes.

2.5.1.1 Torsion Test Method

The torsion test method has been included to obtain shear modulus (G) of timber in the recent proposed version of CEN (EN408:2010, 2010). In the procedure, the test specimen is clamped at the supports, which are spaced more than 16 times the cross-sectional depth and subjected to inducing torque along the longitudinal axis by a relative rotation of the supports. The relative rotational displacements in addition to the torque can be measured at two sections, 1 and 2 as shown in Figure 2-3. These sections are spaced within the free testing length, l_1 . The distance between the supports and these cross-sections, l_2 , should be two to three times the depth of the test specimen. The centres of the supports are in line such that clamping the test specimen will not cause any deformation that could influence the torsion results. The torque is applied by rotation of one or both supports. The loading is applied such that the relative rotation rate per time increment, $d\phi/dt$ is:

$$\frac{d\phi}{dt} = \frac{f_{v,k} \chi}{\eta G} \left(\frac{l_1}{h} \right) \quad (2.2)$$

where $f_{v,k}$ is the shear strength parallel to the grain, in newton per square millimetre, h is depth of the specimen, l_1 is the gauge length, G is the shear modulus, χ and η are the values that can be determined from Table 2-1

The shear modulus (G_{Tor}) is given by the following equation.

$$G_{Tor} = \frac{K_{Tor} l_1}{\eta h b^3} \quad (2.3)$$

K_{Tor} is the torque stiffness and can be determined using a linear regression equation as given in Figure 2-4. The linear regression analysis can be conducted on the linear elastic portion of the graph of applied torque within proportional limits and relative twist of the specimen.

l_1 = gauge length

h = depth of the specimen

b = width of the specimen

η = shape factor, depends on the depth to width ratio and can be determined from Table 2-1 given below.

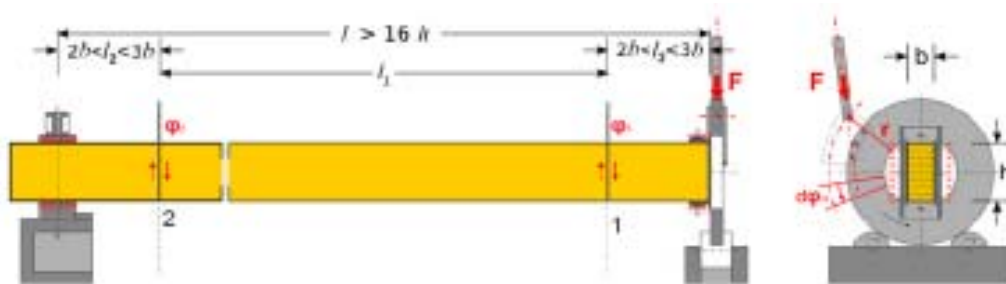


Figure 2-3: Example of test configuration with requirements of specific locations for the gauges (BS EN 408:2010).

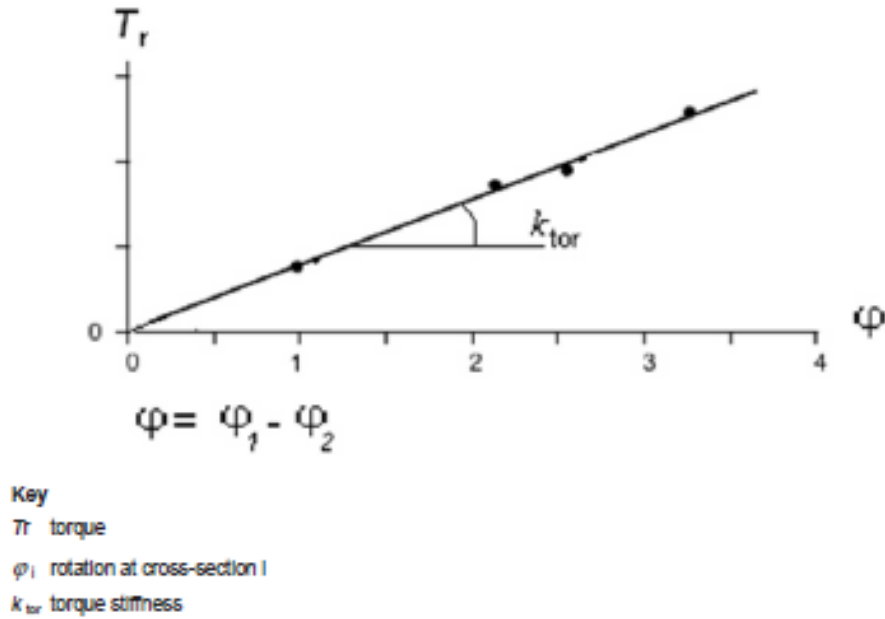


Figure 2-4: Torque versus relative rotation (BS EN 408:2010).

Table 2-1: Shape factor values for torsion test (BS EN 408:2010)

h/b	1	1.2	1.5	2	2.5	3	4	5	10
η	0.1406	0.166	0.196	0.229	0.249	0.263	0.281	0.291	0.312
χ	0.4158	0.4564	0.4618	0.4904	0.5162	0.5334	0.5634	0.5960	0.6270

2.5.1.2 Shear Field Test Method

Shear field test is recommended as the standard test method to determine shear modulus of structural-size timber beams. This method is based on measurement of the shear distortion during standardized four-point bending tests according to CEN (EN408:2010, 2010) standard. Shear distortion is required to be measured within the areas of constant transverse force. Precise measuring instruments are required to be placed on both sides of the constant transverse force and opposite each side of the beam (left-right, front-back) in order to perform accurate measurements of length displacements across the shear fields of the sample during testing.

The arrangements of the shear field test are shown in Figure 2-5. The test method recommends that the test specimen should be symmetrically loaded in bending at two points over a span of 18 times the depth of its cross-section. Providing that these requirements cannot be met exactly, the distance between the load points and the supports may be changed by an amount not greater than 1.5 times the specimen depth. The span and length of the test specimen may be changed by an amount not greater than three times its depth, taking into account that the symmetry of the test should be maintained. To minimize local indentation, the test method suggests using small steel plates which may be inserted between the specimen and the loading heads or supports. The length of these plates should not be greater than one-half of the depth of the specimen.

The test method also suggests that the applied load shall be applied at a constant rate. In the middle of the area under constant shear stress, a square is marked on both side faces, and placed symmetrically with respect to the height of the test piece. A device that measures the change of the square diagonals is fixed to the test specimen at the square corners as shown in Figure 2-6. The shear deformation can then be determined from these measurements as the mean value of the summation of the absolute readings of both diagonals at each side face of the cross-section as shown in Figure 2-7.

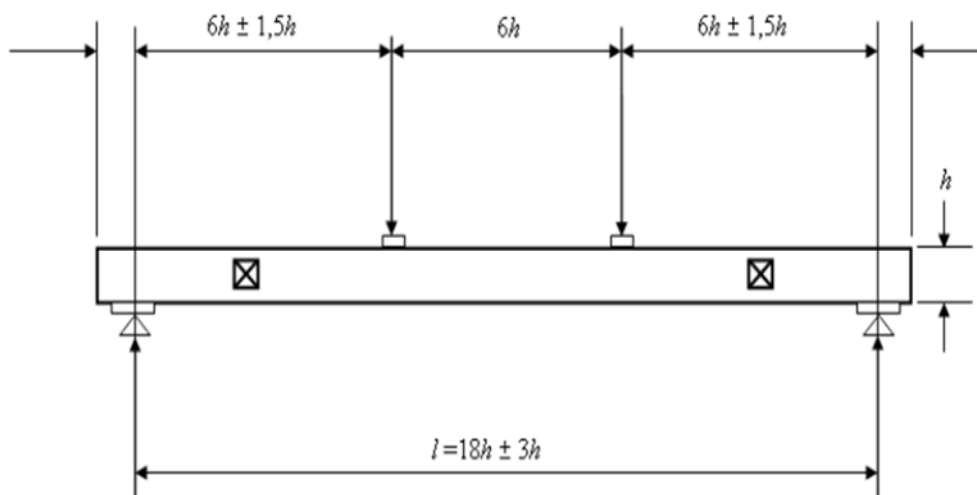


Figure 2-5: Test arrangement for shear field test (BS EN 408:2010).



Figure 2-6: Example of the shear field test apparatus fixed on one of both sides (BS EN 408:2010).

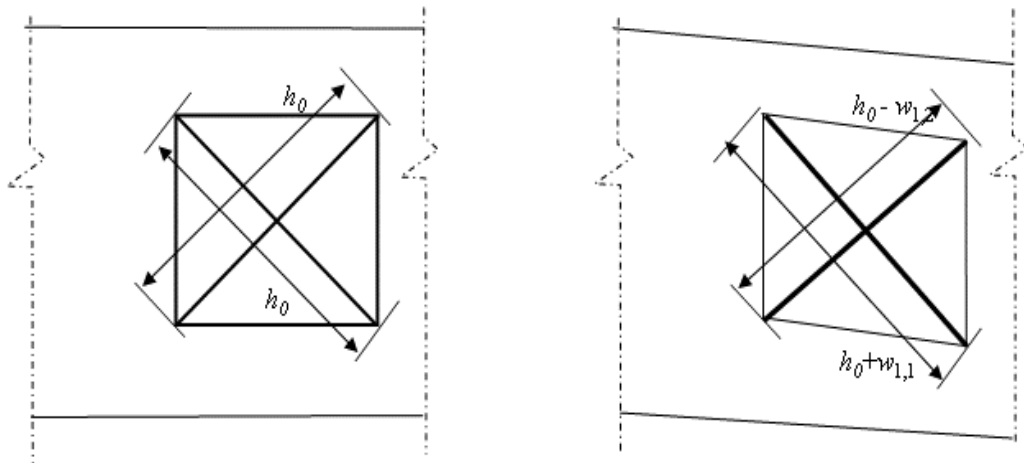


Figure 2-7: Deformation of the square with diagonals (BS EN 408:2010).

The shear modulus $G_{tor,s}$ is given by the equation:

$$G_{tor,s} = \alpha \frac{h_0 (V_{s,2} - V_{s,1})}{bh (w_2 - w_1)} \quad (2.4)$$

where

$$\alpha = \frac{3}{2} - \frac{h_0^2}{4h^2} \quad (2.5)$$

$$w_i = \frac{(|w_{i,1}| + |w_{i,2}|)}{2} \quad \text{with } i = 1,2 \quad (2.6)$$

w_i is the mean deformation of both diagonals on opposite side faces of the beam for a given shear load $V_{s,i}$, in millimetres;

$V_{s,2} - V_{s,1}$ is the shear load increment, in Newton.

2.5.2 Testing Methods for Modulus of Elasticity

The modulus of elasticity can be determined by static and dynamic test methods. The former is used more frequently and is based on the relationship between the deformation of a test specimen and the load, while the latter is based on relationship between the frequency of a vibrating sample of timber and its modulus of elasticity.

There are many standards and methods of obtaining static modulus of elasticity. The European standard CEN (EN408:2010, 2010) specifies different test methods for determining modulus of elasticity of structural timber and glued laminated timber: modulus of elasticity in bending; modulus of elasticity in tension parallel and perpendicular to the grain; modulus of elasticity in compression parallel and perpendicular to the grain. Some of the test methods are reviewed here in the following sections and the rest can be found in the previously mentioned standard.

2.5.2.1 Four-point Bending Test Method

The CEN (EN408:2003, 2003) standard added a global bending modulus of elasticity and the existing test has been renamed as the local modulus of elasticity. According to EN408 (2010), MOE can be determined locally and globally using the four-point bending test method. In this method, a full-size specimen is symmetrically loaded in bending at two points over a span of 18 times the depth of

the section as shown in Figure 2-8. If these requirements cannot be met exactly, the distance between the load points and the supports may be changed by an amount not greater than 1.5 times the specimen depth. The span and length of the test specimen may also be changed by an amount not greater than three times its depth, taking into account that the symmetry of the test should be maintained. The applied load is recommended by the standard to be at a constant rate. The EN 408:2010 test configuration for measuring the local MOE in bending is described in Figure 2-8.

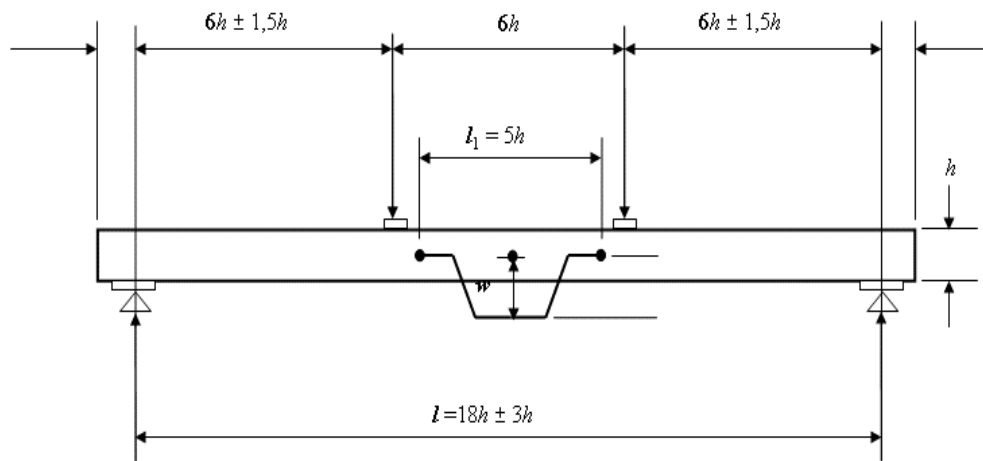


Figure 2-8: Test configuration for measuring local modulus of elasticity in bending (BS EN 408:2010).

The determination of the local MOE in bending is based on the deformation measured at the centre of a central gauge length of 5 times the depth of the section. The deformation and the load are observed at two different times during the test, i.e. (W_1, F_1) and (W_2, F_2) as described in Figure 2-9. This deformation is recommended to be taken as the average of measurements on both side faces at the neutral axis.

The local modulus of elasticity, $E_{m,l}$ of structural size specimen in the four-point bending test in bending can be calculated from following Equation:

$$E_{m,l} = \frac{al_1^2(F_2 - F_1)}{16I(w_2 - w_1)} \quad (2.7)$$

where,

$E_{m,l}$ is the local modulus of elasticity in the four-point bending test, in Newtons per square millimetre (N/mm^2).

$F_2 - F_1$ is an increment of load over the elastic part or the straight-line part of the load deformation curve, in Newton (N),

$W_2 - W_1$ is the deformation increment corresponding to the increment of load, in millimetres (mm),

I is the second moment of area of the section, in (mm^4),

l_1 is the gauge length for the determination of modulus of elasticity, in millimetres (mm),

a is the distance between a loading position and the nearest support, in millimetres (mm).

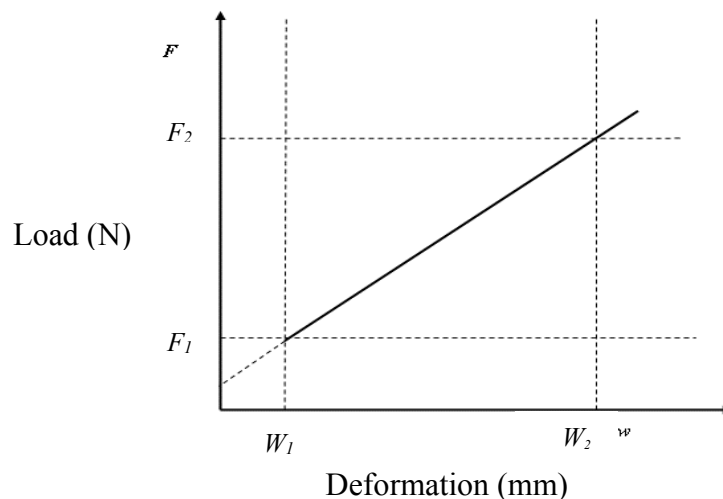


Figure 2-9: The graph of load-deformation within the elastic range of deformation (BS EN 408:2010).

The global modulus of elasticity in bending is assessed with the same test configuration for measuring local modulus of elasticity. The test arrangement for measuring the global MOE is illustrated in Figure 2-10. The determination of the global MOE is based on the deformation measured at the centre of the span and from the centre of the tension or compression edge. When this deformation is measured at the neutral axis, it is recommended to be taken as the average of measurements on both side faces of the test specimen.

The global modulus of elasticity $E_{m,g}$ in a four-point bending test can be calculated from the following expression:

$$E_{m,g} = \frac{3al^2 - 4a^3}{2bh^3 \left(2 \frac{w_2 - w_1}{F_2 - F_1} - \frac{6a}{5Gbh} \right)} \quad (2.8)$$

where

l is the span in bending, (mm),

b is the width or the smaller dimension of the cross section, (mm),

h is the depth or the larger dimension of the cross section, (mm),

G is the shear modulus which shall be taken as $G = 650 \text{ N/mm}^2$.

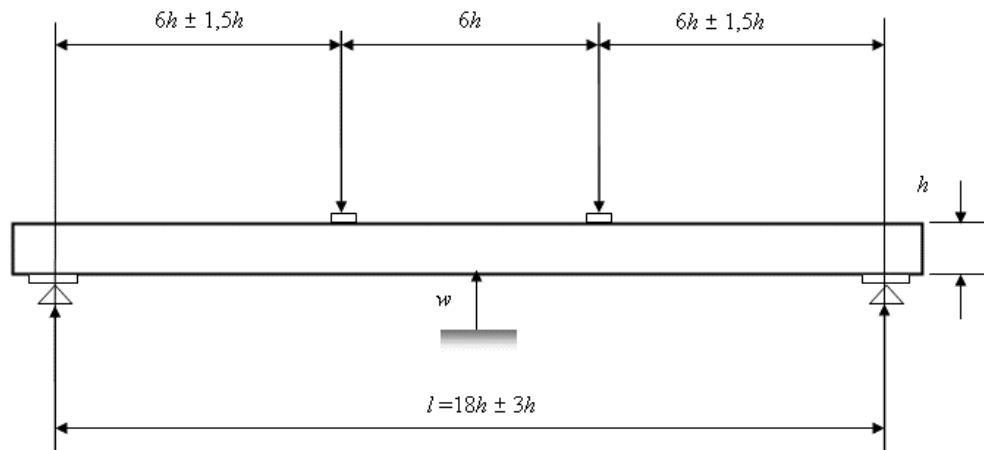


Figure 2-10: Test configuration for measuring global modulus of elasticity in bending (BS EN 408:2010).

2.5.2.2 Compression Test Methods

Among different test methods, the compression test is one of the most commonly used methods for determining modulus of elasticity and the other elastic and strength properties. The CEN (EN408:2010, 2010) standard for structural and glued-laminated timber includes two types of compression tests for measuring modulus of elasticity: one for measuring MOE parallel to grain and the other one for assessing MOE perpendicular to grain. The former is widely used and the deformation is measured over a central gauge length. In contrast, the perpendicular to grain test is reported for measuring MOE at a proportional limit.

➤ Test Specimen

As mentioned in the above-mentioned standard, the test specimen for the parallel to grain test should be of a full cross section having a length of six times the smaller cross-sectional dimension. Dimensions of the test specimen for structural as well as for glued laminated timber in compression perpendicular to grain are given in Table 2-2 and are shown in Figures 2-11 and 2-12. The two contact surfaces of the test specimen have to be accurately prepared to ensure that they are parallel to each other and aligned perpendicular to the longitudinal axis of the specimen.

Table 2-2: Dimension of structural timber or glued laminated timber test pieces (BS EN 408:2010).

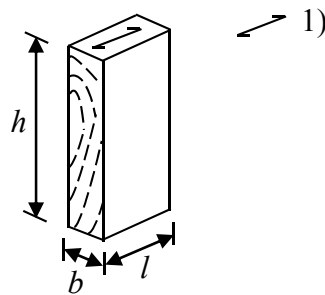
Specimen characteristics						
Structural timber				Glued laminated timber		
<i>b</i> (mm)	<i>h</i> (mm)	<i>l</i> (mm)	Volume (m^3)	<i>b x l</i> (mm^2)	<i>b</i> minimum (mm)	<i>h</i> (mm)
Tension						
45	180	70	0.01	25 000	100	400
Compression						
45	90	70	-	25 000	100	200

where:

b is the width of cross section, or the smaller dimension of the cross section, mm;

h is the height of the test specimen perpendicular to grain, in mm;

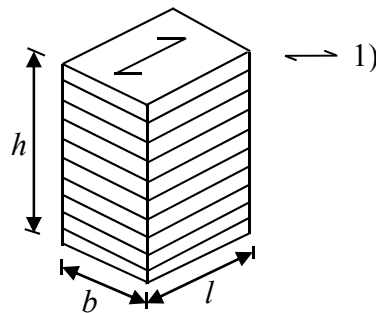
l is the length of test piece between the testing machine grips in compression and tension, mm.



Key

1) grain direction

Figure 2-11: Structural timber test specimen (BS EN 408:2010).



Key

1) grain direction

Figure 2-12: Glued laminated timber test specimen (BS EN 408:2010).

➤ Conditioning Test Specimen

All test specimens shall be conditioned in a controlled environment with a temperature of 20 ± 2 C° and relative humidity of $65 \pm 5\%$. The specimens should be conditioned to attain constant mass. This condition is considered to be achieved when the results of two successive weightings do not differ more than 0.1% of the mass of the test specimen.

➤ Loading Procedure

The CEN (EN408:2010, 2010) test configuration for measuring MOE in compression is described in Figure 2-13. The test specimen has to be mounted vertically between the platens of the testing machine and the compression loads applied. It is also required that the test specimen should be centrally loaded by means of spherically seated loading-heads which allow the application of compressive loads without bending. The spherical loading head shall be fastened after pre-loading to avoid slipping. The sample has to be loaded uniformly with a constant rate of loading throughout the test and the applied load shall be measured to an accuracy of 1%.

To minimize the effects of distortion, two displacement sensors such as extensometers are required to be placed symmetrically in the middle of the two opposite surface of the test sample so as to compute the average of the results. These sensors shall be at least at a distance from the contact surfaces of one third of the largest cross section size in order to negate the grip affect.

The deformation in compression parallel to the grain is measured in the load direction over a central gauge length of four times the smaller cross-sectional dimension of the test specimen. For compression perpendicular to the grain, the deformation is measured over a gauge length h_0 which is approximately 0.6 the height of the test specimen, h . This gauge length has to be located centrally in the height of the test specimen at a distance of at least $b/3$ to the loaded ends of the test specimen.

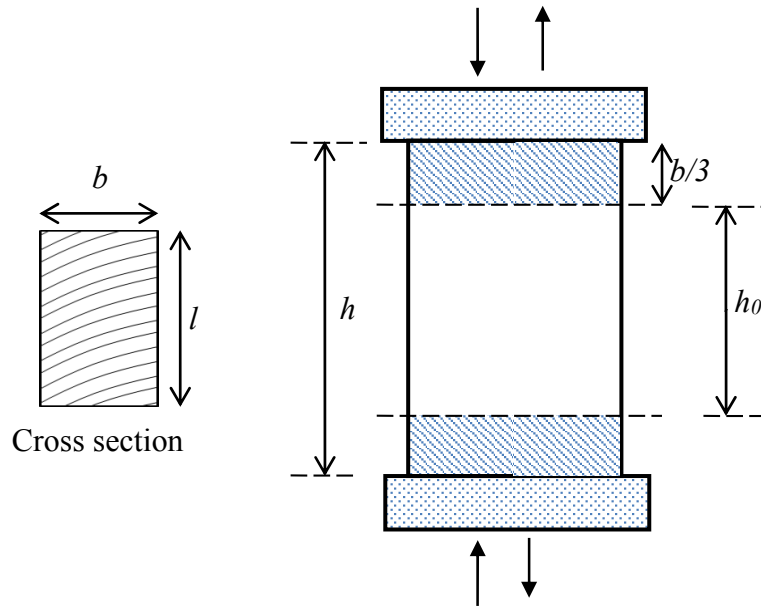


Figure 2-13: Typical compression test configuration in accordance with CEN (EN408:2010, 2010).

➤ **Calculation of MOE in Compression Parallel to the Grain**

The modulus of elasticity parallel to the grain in compression $E_{c,0}$ is given by the equation:

$$E_{c,0} = \frac{l_1(F_2 - F_1)}{A(W_2 - W_1)} \quad (2.9)$$

where

l_1 is the span in bending, (mm),

$F_2 - F_1$ is an increment of load on the straight line portion of the load deformation curve (N),

$W_2 - W_1$ is the increment of deformation corresponding to $F_2 - F_1$ (mm),

A is the initial cross section of the sample.

➤ Calculation of MOE in Compression Perpendicular to the Grain

The modulus of elasticity perpendicular to the grain in compression is assessed with the same test configuration for measuring MOE parallel to the grain. According to EN 408 standard, $E_{c,90}$ may be determined using the iterative process as follows:

- Estimate the maximum compression load $E_{c,90,max}$.
- Using the test results, plot the load-deformation curve.
- Calculate $0.1 E_{c,90,max}$ and $0.4 E_{c,90,max}$ and determine the intersection of these two points in the load-deformation curve.
- Through these two values draw a straight line 1 as shown in Figure 2-14.
- Parallel to line 1, draw line 2 having its origin at load $F = 0$ and at a distance from it equivalent to a deformation of $0.01 h_0$ as shown in Figure 2-14 where line 2 intersects the load-deformation curve is $E_{c,90,max}$.

According to EN 408:2010 standard, the modulus of elasticity perpendicular to the grain in compression $E_{c,90}$ is given by the following equation:

$$E_{c,90} = \frac{(F_{40} - F_{10}) h_0}{(w_{40} - w_{10}) bl} \quad (2.10)$$

where

F_{40}, F_{10} are the loads at 0.1 and 0.4 of $E_{c,90,max}$ (N),

w_{40}, w_{10} are the corresponding deformations at F2 and F1, respectively (mm),

h_0 is the gauge length (mm),

b, l are width and length of the specimens (mm).

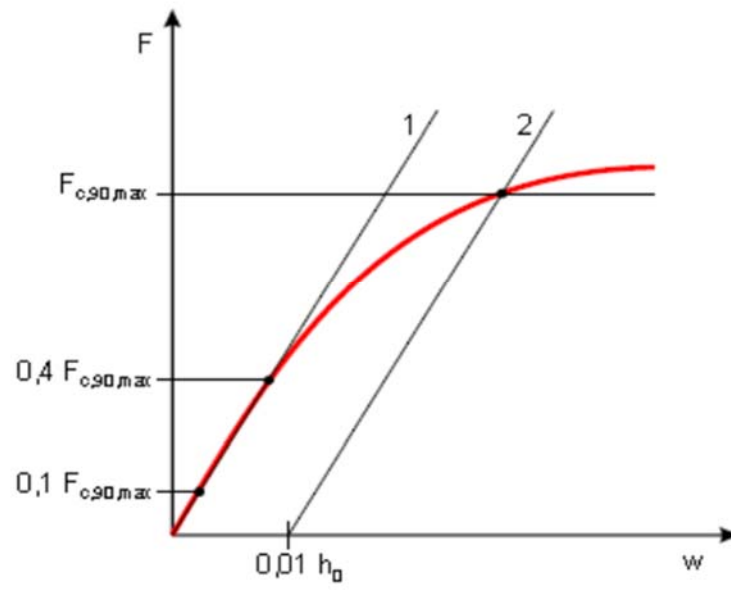


Figure 2-14: The graph of load-deformation of an EN 408(2010) perpendicular to the grain in compression.

3. STEREO VISION SYSTEM

3.1 Introduction

The main objective of this research is to evaluate the mechanical properties of timber and timber-based composite materials in a laboratory environment. This may be achieved by applying the principles of the photogrammetric and binocular stereo vision approaches. The goal of stereo vision is to obtain 3D information of an object of interest using two images of the 3D object, each acquired from different positions and orientations. The vision system consists of image acquisition hardware and image processing software.

In this chapter, the image acquisition hardware and the image processing software ,HALCON, are introduced. The camera model which is based on the perspective model is also introduced. The presented camera model will be extended to integrate the internal or intrinsic camera parameters and the external or extrinsic camera parameters corresponding to the position and orientation of the camera. In addition, camera distortion correction and how the mapping of objects in the 3D world corresponds to the 2D image coordinates are described. Furthermore, the camera calibration theory and the basic steps of doing the calibration have also been provided. Moreover, the principle of stereo vision, stereo camera calibration, the binocular stereo method, and stereo reconstruction are presented. Finally, the implementation of the proposed stereo vision system in prototype software is described.

3.2 Image Acquisition Hardware

In order to monitor the 3D deformations of glulam timber specimen during testing using the optical techniques, a stereo camera system is needed to obtain the 3D information using the stereo images. Such a system usually requires hardware components, including illumination, lenses, cameras, control PC and camera-computer interfaces.

3.2.1 Cameras and Lenses

The main components of the imaging system are the camera and the lens. In order to develop the stereo camera system, it is important to select a suitable camera for the application. The selection of the camera type and equipment is critical for the application and mainly depends on the required measurement accuracy. To select a suitable camera for an application, different criteria, including camera type, sensor type, image quality, frame rate, resolution, and the bus system of the camera are required to be considered. Based on the required object resolution, sensor type and resolution can be determined.

In order to select a camera for an application, sensor technology is the first important aspect that should be taken into account. There are two main types of sensor technology, CCD (charge-coupled device) and CMOS (complementary metal-oxide-semiconductor). CCD sensors are more sensitive to light and create high-quality images with low noise. CMOS sensors tend to have more noise and the light sensitivity of a CMOS chip is lower (Hornberg, 2007). CCD sensors are commonly used in applications where high image quality is required.

Once the camera has been selected, it is important to select an appropriate lens system to be used with the associated cameras. The characteristics of an imaging system are greatly affected by the choice of lens. There are different lens parameters that must be specified to adapt the camera to the specific application. These parameters include magnification, focal length, depth of field, and lens mount.

1. Magnification

Magnification (m) can be described as a measure of the relative size of the image of an object to the actual size of the object as given in the following equation (Galbiati Jr, 1990)

$$m = \frac{H_s}{H_o} = \frac{f}{WD} \quad (3.1)$$

where H_s is the size of the sensor, H_o is the field of view (FOV), f (focal length) is the distance between the lens and the image plane, WD , known as *working distance*,

is the distance between the front of the lens and the viewed object. Figure 3-1 shows the relationship between the parameters of the imaging system.

The magnification of the imaging system is based on the maximum field of view and the working distance. The magnification decreases as the objective working distance increases.

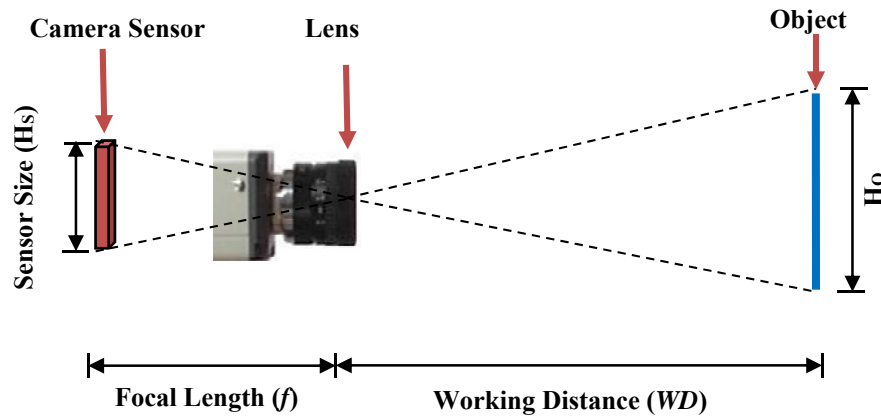


Figure 3-1: Relationship between the parameters of the lens.

2. Focal Length

The focal length, usually expressed in millimetres, is the distance between the lens and the focal point. Focal length is the most important factor for selecting the right lens for the camera system. The focal length is related to magnification and working distance by the expression (Galbiati Jr, 1990)

$$f = \frac{WD}{1 + \frac{1}{m}} \quad (3.2)$$

where WD is the working distance and m is the magnification. Based on the above equation, either the focal length or the working distance can be determined for a given magnification.

There are different types of lenses available, including fixed focal lengths and zoom lenses. The fixed focal length lens, also referred to as a "prime lens", has a focal

length that is not adjustable, resulting in a fixed working distance (Jain et al., 1995). Although these type of lenses offer limited magnification, they are stable and suitable for making accurate and repeatable measurements. The zoom lenses cover a range of focal lengths, making them flexible for many applications. However, they are unstable and not suitable for achieving accurate measurements from images.

3. Depth of Field

Depth of field (DOF) is the range of distances from the working surface in which the camera lens maintains the focus of the object within acceptable limits. DOF is important for applications when the point of interest is not located on the object of interest. The depth of field is affected by some parameters, including aperture size, magnification, and size of the sensor elements (Galbiati Jr, 1990).

4. Lens Mount and Lens Format

In order to combine a camera with a lens, the type of lens mounting system must be specified. C-mount and CS-mount are the most common types of lens mounting. The main difference between them is the *flange back distance* which is the distance from the back of the lens to the sensor of the camera. This distance is 17.5 mm for a C-mount, whereas it is only 12.5mm for a CS-mount (Hornberg, 2007). The C-mount is the most common type of lens mounting in use. In contrast to C-mount lenses, CS mount types suffer from more distortion.

In order to select the appropriate lens for optimal performance, the lens and camera must match, meaning that the image formed by the lens must cover the entire sensor of the camera. Therefore, it is essential to ensure that the lens is compatible with the optical size of the image sensor used in the camera. The format of the lens is required to be equal or greater than the format of the camera sensor. Using a smaller format of the lens than that of the sensor results in a poorly illuminated sensor, low light, and aberration will be an issue (Hornberg, 2007). For best performance, the lens format should be matched to the sensor format.

3.2.1.1 Camera and Lens Selections

The first step in developing the stereo system is to select a suitable camera for the experimental work of this research. The Basler Pilot piA2400-17gm cameras were selected and used in this research. The Basler cameras were selected in our stereo system for several reasons. They are CCD progressive scan cameras with a resolution of 2456 x 2058 pixels (5 Megapixel), which is sufficient not only for the required resolution of our applications, but also for further higher resolution if necessary. The image quality of these cameras allows the performance of precise measurements from images. A very important feature of these cameras is that they can be connected to a control computer through Ethernet cables, offering greater flexibility by allowing the camera to be located as far as 100 m from the control PC.

The next step in developing the stereo system is to select suitable lenses for the Basler cameras. The selection of the lens depends on the key factors which are mentioned before in this section. Based on the specification of the chosen camera and the feature size of the object, the necessary magnification can be determined using Equation 3-1, resulting in a magnification of 0.03 mm. Once the magnification of the system has been determined, either the working distance (WD) or the focal length of the camera lens (f) is required to be determined. Since the working distance is specified to be roughly 740 mm, the focal length of the lens was calculated from Equation 3.2, resulting in a focal length 21.55 mm. Therefore a 25mm length will suit our applications and the selection is now based on a number of choices such as lens shape, f-number, quality, cost and availability of the lens.

The Computar M2518-MPW lens was selected with the Basler cameras. The Computar lens is a high quality lens with low distortion. It was selected due to its accurate and fixed 25mm focal length, and therefore offers the best optimized image quality since they are designed for a fixed set-up. It is designed for application with a relatively close working range where the focus and aperture remains fixed. It is compatible with 2/3 type cameras (5 Megapixel) such as the Basler cameras. They feature a C-mount which is compatible with the chosen camera. The format of the lens is also suitable with that of the camera sensor.

3.2.1.2 Additional Cameras and Lenses

In addition to Basler cameras, four DMK 23GP031 cameras from the Imaging Source Company were also used for image acquisition during the torsion test. Figure 3-7 shows an image of these cameras. DMK 23GP031 is a high speed CMOS area scan camera with a resolution of 2592 x 1944 pixels. With up to 15 frames per second (fps), the DMK 23GP031 Gigabit Ethernet cameras are a very low cost, yet highly versatile imaging solution.

Azure- 3514M5M lens is a high quality lens with low distortion. It is a C-mount lens which is compatible with C- and CS-mount cameras. This lens has a resolution of 5 mega-pixels and a focal length of 35mm. Figure 3-8 shows an image of the said Azure- 3514M5M lens. The most important specification data for this lens is summarized in Table 3-5.

3.2.2 Frame-grabber Card

In order to deliver the images acquired by a camera to a computer, a special interface card, known as frame grabber, has to be used. There are different types of interfaces and the most common ones of direct transfer are USB, IEEE1394 (FireWire) and Gigabit Ethernet (GigE). Among these interfaces, Giga Ethernet offers many advantages. Gigabit Ethernet frame grabber supports direct connection to Gigabit Ethernet (GigE) cameras and enables a data transfer rate of up to 1000 MB/s (megabytes per second) (Hornberg, 2007). This ability offers greater flexibility by allowing the camera to be located as far as 100 metres from the control computer. In addition to its excellent support of many devices, Giga Ethernet is a good choice for stereo imaging applications. They offer better support for synchronizing multiple cameras so they can simultaneously capture an image of the same object. The Intel GigE frame grabber is compatible with the software library employed, and it is suitable to be used with the Ethernet stereo cameras.

3.2.3 Lighting Units

The success of an image analysis task, especially for highly accurate measuring purposes, depends on the visibility of objects of interest in the image. To obtain images with clearly visible objects, the lighting conditions during image acquisition have to be considered. Illumination makes the important features of an object visible and suppresses the undesired ones.

There are various different types of illumination commonly used in vision applications, including incandescent lamps, fluorescent illumination, structured light, and led illumination. Light-emitting diodes (LEDs) are the most widely used illumination in the industrial vision world (Hornberg, 2007). Provided with high-brightness, LEDs are presently the primary illumination technology and are becoming readily available at intensities that let them directly replace more traditional light sources. In addition, they use low power and generate low heat. Another attractive feature of LEDs is that they have a longer lifetime. Moreover, this type of illumination offers output stability and low maintenance. Because of the above-mentioned advantages, an LED illumination was preferred.

3.2.4 The Control Computer (PC)

To handle the high-quality image data during all tests, a powerful computer is required. A 19" Window 7 Workstation desktop computer was used as the hardware platform. The computer is provided with two processors of Intel (R) Xeon (R) CPU processor at a speed of 3.0 GHz, a ram of 16 GB, and a hard disc capacity of 1000 GB. Figure 3-11 shows an image of the computer which was used for all experiments conducted in this research.

3.3 Image Processing Software

When selecting a software library, it is essential that the software needs to be compatible with the operating system of the computer as well as with the hardware

used for the imaging system. It is also important to consider the functionality of the software and its level of development. The machine vision market offers software packages that are intended for specific applications without the need for programming. On the other hand, there are programmable software packages that offer the possibility to adapt the software to the application needs. Therefore, these types of software packages are preferred for our applications. HALCON provides a programming environment which is suitable for implementing image processing algorithms as well as for developing standalone applications.

HALCON is the comprehensive standard software library with an integrated development environment (IDE) for different machine vision tasks. It includes an extensive library of more than 1300 operators with outstanding performance for complex tasks, including pattern matching, measuring, camera calibration, and binocular stereo vision (MVTech Software GmbH., 2011c). This library provides efficient implementations of various image processing methods, which can be integrated easily into customised software development based on C, C++ or Visual Basic. Additionally, HALCON offers a full 3D camera calibration which determines the internal as well as the external camera parameters, allowing it to accurately describe the relationship between the camera and the measuring surface and to correct lens distortion.

3.3.1 HDevelop

HDevelop is a rapid prototyping tool that offers the possibility of developing and testing machine vision applications. Based on the HALCON library, HDevelop is a highly-interactive programming environment which is suitable for product development, research, and education (MVTec Software GmbH, 2011a). The image processing solutions can be developed faster and more efficiently even while acquiring images from a capture device.

3.3.2 The Development of Applications with HALCON

HALCON offers the possibility to develop image analysis applications. The development of an application using HALCON is a three-step approach as illustrated in Figure 3-2 (MVTec Software GmbH, 2011b). In the first step, the image processing program is written in HDevelop. This program is structured into procedures to represent different tasks. After testing the main program in the HDevelop environment, it can then be exported as C, C++, Visual Basic, and Visual Basic.NET, or C# source code. In the second step, the project application is developed in a standard development environment such as Microsoft Visual Studio. The exported source code can then be imported and the graphical user interface with the essential codes can be implemented in the selected programming environment. Finally, in the last step, the developed application can be compiled and linked with the HALCON library.

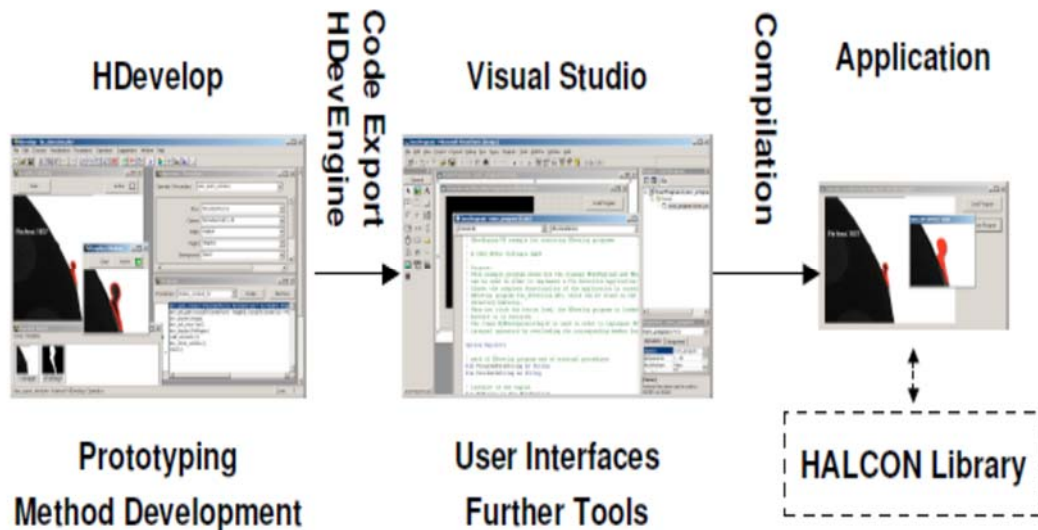


Figure 3-2: Development of application with HALCON (MVTec Software GmbH, 2011b).

3.4 Camera Calibration

Camera calibration can be described as the process of determining camera parameters which are essential to obtain accurate measurements of objects (Steger et al., 2008). These parameters can be classified into two sets, internal and external. Internal or intrinsic parameters describe the internal geometry and optical characteristics of the camera. External or extrinsic parameters describe the position and orientation, also known as pose, of the cameras relative to a world coordinate system. Camera calibration is essential to eliminate the lens distortions and obtain accurate measurements of objects. Calibrating the camera based on the image processing software, HALCON, can be performed easily and achieve extremely high accuracy of the camera position (pose) and the camera parameters and therefore accurate world coordinates from images can be derived (Steger et al., 2008).

3.4.1 Camera Models

In order to derive accurate world coordinates from images, the camera must be calibrated. To accomplish the calibration of a camera, it is necessary to have a model for the mapping of the three-dimensional (3D) points of the world in the two-dimensional (2D) image generated by the camera and lens. Generally there are two different types of lenses relevant to machine vision applications and these are the standard (regular) and telecentric lenses (Steger et al., 2008). The standard lens performs a perspective projection of the world coordinates into the image coordinates. With this type of lens objects become smaller in the image the further they are away from the camera. This combination of camera and lens is generally called a *pinhole camera model*. The telecentric lens performs a parallel projection of the world coordinates into the image plane. This means that objects have the same size in the image independent on their relative distance to the camera. The combination of camera and telecentric lens is called a *telecentric camera model*.

There are two types of cameras; line and area scan cameras, which are required to be considered. The main difference between these cameras is that area scan cameras

acquire the image in one step while line scan cameras generate the image line by line, requiring the camera to move relative to the object during the acquisition process. In the following section, only the camera model for area scan cameras is introduced since these cameras were employed in this research. More information about the camera model for line scan cameras can be found in (Steger et al., 2008).

3.4.2 Perspective Projection Model for Area Scan Cameras

The pinhole camera model, known as the perspective projection model, is the basis for all the camera models and most commonly used to approximate a real camera model (Steger et al., 2008). It describes a mathematical relationship between the coordinate of a three-dimensional (3D) point and its projection onto the image plane of an ideal pinhole camera. Figure 3-3 displays the perspective projection effected by a pinhole camera. The common coordinate systems, including image coordinates, camera coordinates, and world coordinates are shown in this figure. The three-dimensional world point P^w is projected through the projection centre of the lens to the two-dimensional point p generated by the camera in the image plane. In an ideal case where there is no lens distortion present, the object point p would lie on a straight line from the world point P^w through the projection centre, indicated by the dotted line (Steger et al., 2008). The lens distortions cause the ideal projected positions of point p to be modified.

The image plane is located at a distance f behind the optical (projection) centre. The principal distance, f , is the camera constant which describes the mapping of objects in 3D world coordinates to the 2D image plane. As shown in Figure 3-4, in order to simplify the computations, the image plane can be assumed to be laid at the distance f in front of the projection centre, although the image plane in reality lies behind the projection centre of the lens. This results in aligning the image coordinate system with the pixel coordinate system and simplifies many calculations.

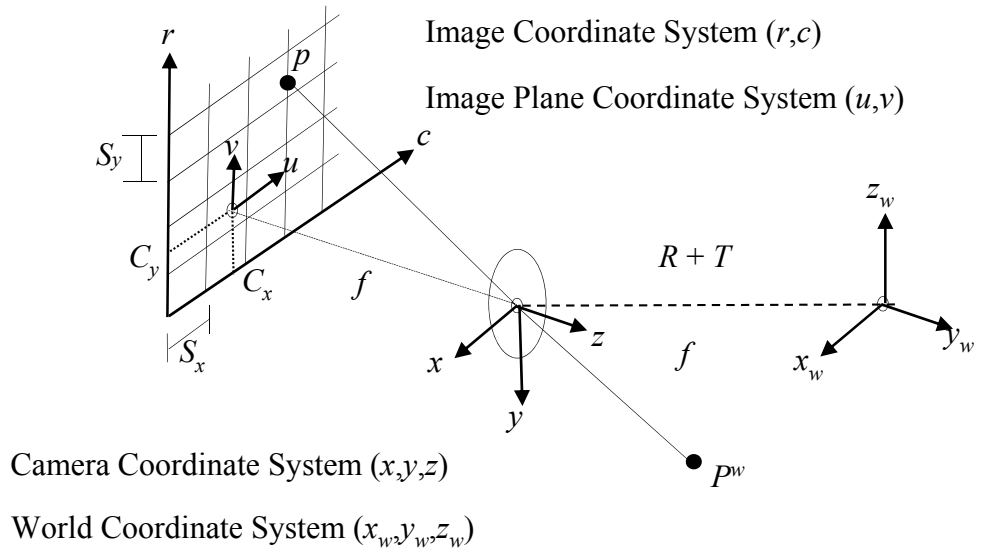


Figure 3-3: Perspective projections using a pinhole camera model (Steger et al., 2008).

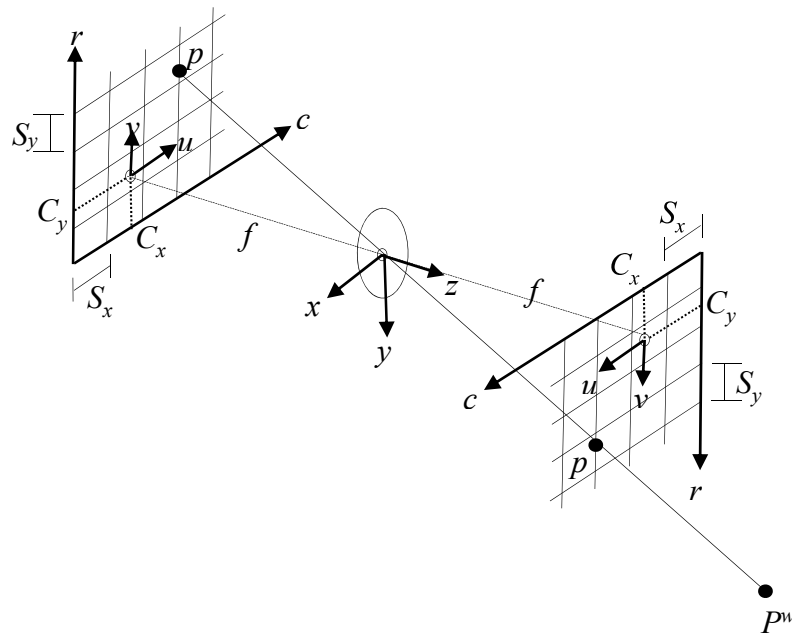


Figure 3-4: Image plane and virtual image plane (Steger et al., 2008).

The projections of the 3D world points into the 2D image points are based on the perspective projections. This transformation consists of the following three steps:

- ❖ Transformation from the world coordinates (WCS) into the camera coordinates (CCS).
- ❖ The projection of the 3D point coordinates in the camera coordinate system into the image plane coordinate system (IPCS).
- ❖ Transformation from the image plane coordinate system into the image coordinate system (ICS), known as the pixel coordinate system.

1. Transformation from World Coordinates to Camera Coordinates

The first step of the perspective projection is the mapping of objects in 3D world coordinates to the 2D image plane. In order to locate the 2D image points, the points in the world coordinate system (WCS) need to be transformed into the camera coordinate system (CCS). The camera coordinate system is defined as follows. The x and y axes are parallel to the column and row axes of the image, respectively. The z axis is perpendicular to the image plane and is oriented such that points in front of the camera have positive z coordinates. The transformation from the WCS to the CCS is a rigid transformation, which can be described by a rotation followed by a translation

$$P^c = RP^w + T \quad (3.5)$$

where $T = (t_x, t_y, t_z)^T$ is a translation vector defining the position of the camera centre and $R = R(\alpha, \beta, \gamma)$ is a rotation matrix, which describes the orientation of the camera. The rotation matrix is determined by the three rotation angles around the x , y , and z axes of the camera coordinate system respectively.

$R(\alpha, \beta, \gamma) =$

$$\begin{pmatrix} 1 & 0 & 0 \\ 0 & \cos \alpha & -\sin \alpha \\ 0 & \sin \alpha & \cos \alpha \end{pmatrix} \cdot \begin{pmatrix} \cos \beta & 0 & \sin \beta \\ 0 & 1 & 0 \\ -\sin \beta & 0 & \cos \beta \end{pmatrix} \cdot \begin{pmatrix} \cos \gamma & -\sin \gamma & 0 \\ \sin \gamma & \cos \gamma & 0 \\ 0 & 0 & 1 \end{pmatrix} \quad (3.6)$$

The six parameters of \mathbf{R} and \mathbf{T} are called the exterior camera parameters or camera pose, because they determine the position of the camera with respect to the world.

2. Projection into the 2D Image Plane Coordinates

The next step of mapping is the projection of the point $P^c = (x, y, z)$ given in the camera coordinate system (CCS) into the image plane coordinate system (IPCS). The projection of the pinhole camera model is a perspective projection, which is given by

$$\begin{pmatrix} u \\ v \end{pmatrix} = \frac{f}{z} \begin{pmatrix} x \\ y \end{pmatrix} \quad (3.7)$$

where the effective focal length, f , is the distance between the image plane and the optical centre, and u and v are the image plane coordinates. Equation (3.7) describes the perspective projection transformation by ignoring any lens distortions.

After the projection to the image plane, lens distortion causes the actual image point P to be laid at a different position. This is a transformation that can be modelled in the image plane alone without the need for 3D information (Steger et al., 2008). There are a number of different ways of modelling the lens distortions, but for most lenses, the distortion can be approximated sufficiently by a radial distortion given by (Steger et al., 2008). The corrected coordinates (\tilde{u}, \tilde{v}) can be expressed, according to the model, by:

$$\begin{pmatrix} \tilde{u} \\ \tilde{v} \end{pmatrix} = \frac{2}{1 + \sqrt{1 - 4k(u^2 + v^2)}} \begin{pmatrix} u \\ v \end{pmatrix} \quad (3.8)$$

where (u, v) are the coordinates of an image point in the image plane coordinate system. The parameter k is the radial distortion factor, which affects the acquired images. The distortion is barrel-shaped if k is negative and it is pincushion-shaped if k is positive. The effect of k for an image of the calibration plate is shown in Figure 3-5.

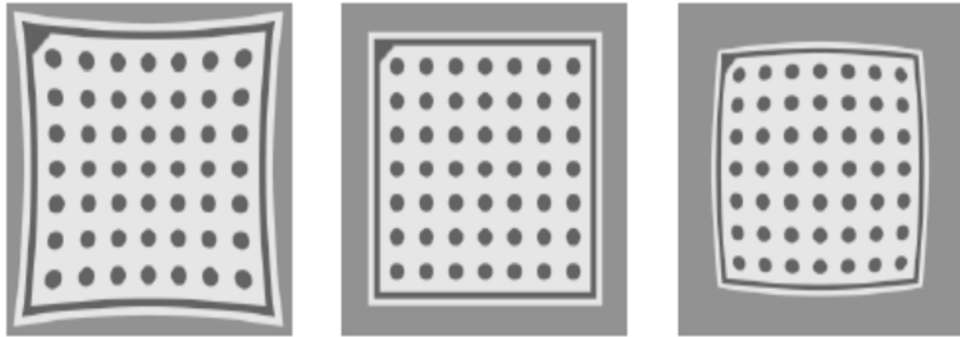


Figure 3-5: Effects of radial distortion with $k > 0$ (left), $k = 0$ (middle), and $k < 0$ (right) (Steger et al., 2008).

The advantage of using this radial distortion model is that it can be used to calculate the correction of the distortion analytically by the following expression (Steger et al., 2008). This is required when computing the world coordinates from the image coordinates.

$$\begin{pmatrix} u \\ v \end{pmatrix} = \frac{1}{1 + k(\tilde{u}^2 + \tilde{v}^2)} \begin{pmatrix} \tilde{u} \\ \tilde{v} \end{pmatrix} \quad (3.9)$$

3. Transformation into Pixel Coordinate

Finally, the last step of the perspective projection is the transformation of the point $(\tilde{u}, \tilde{v})^T$ from the image plane coordinate system into the image coordinate system (ICS) or the pixel coordinate system (r, c) . This is done by the use of the following equation:

$$\begin{pmatrix} r \\ c \end{pmatrix} = \begin{pmatrix} \frac{\tilde{v}}{S_y} + C_y \\ \frac{\tilde{u}}{S_x} + C_x \end{pmatrix} \quad (3.10)$$

where S_x and S_y are scale factors that represent the horizontal and vertical distances between pixels on the sensor. C_x and C_y represent the row and column coordinates of the principal point of the image, which also defines the coordinates of the image centre point.

The six parameters f , k , S_x , S_y , C_x , and C_y of the pinhole camera are needed to describe the complete projection from 3D world coordinates to 2D image coordinates. These parameters are independent of the exterior orientation of the camera, and hence constitute the internal or intrinsic parameters of the camera model. They can be determined by numerically solving the previous equations using known 3D points and their corresponding 2D image points (Steger et al., 2008).

3.4.3 The HALCON Calibration Plate

In order to calibrate a camera using HALCON, a specific planar calibration plate with known properties such as size, shape and colour is required to be used during the calibration process. For camera calibration, HALCON provides a special calibration plate and functions designed to be used with the calibration board. The HALCON plate consists of 49 circular marks inside a surrounding rectangle. The diameters of these marks as well as the distance between adjacent marks are known with high accuracy and saved in the calibration plate description file corresponding to the real ones on the calibration plate. An image of a typical calibration plate can

be seen in Figure 3-6. Planar calibration targets can be handled easily and in addition to that they can be manufactured very accurately. A rectangular border around the calibration target allows the inner part of the calibration target to be detected easily. A small orientation mark in one of the corners of the borders enables the camera calibration algorithm to uniquely determine the orientation of the calibration target. Circular marks are preferred because their centre point can be determined with high accuracy (Steger et al., 2008). Finally, the specific arrangement of the rows and columns of the circles allows the algorithm of camera calibration to determine the correspondence between the marks and their points easily.

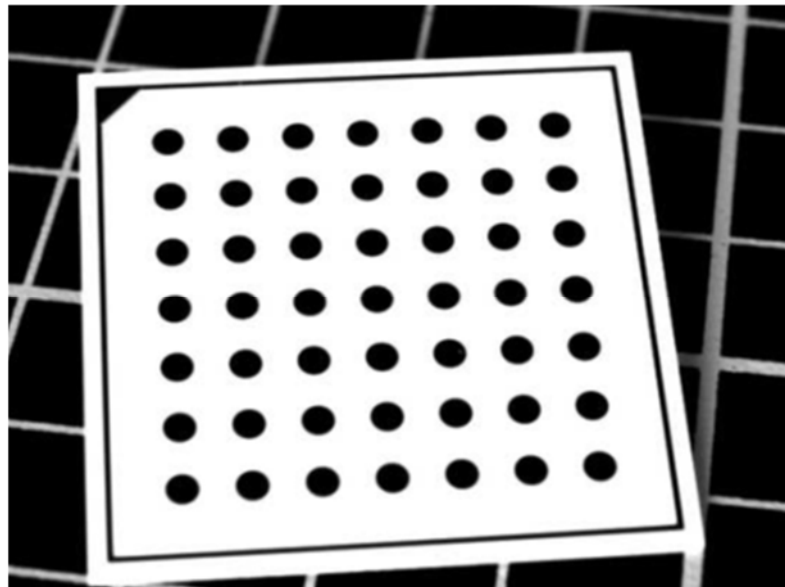


Figure 3-6: The HALCON calibration plate (Steger et al., 2008).

3.4.4 Camera Calibration Process

As mentioned before, camera calibration is the process of determining internal and external parameters of the camera. In order to accomplish the calibration, it is crucial that the locations of a sufficiently large number of 3D points in world coordinates are known and the correspondence between the world points and their

projection in the images are determined. The first requirement is usually accomplished by using a calibration plate with circular marks situated at different positions in the field of view (FOV). The second requirement is an extremely challenging problem in which for each point in the left image, the corresponding point in the right image has to be determined. Therefore, the calibration plate of HALCON, shown in Figure 3-6, is constructed in such a way that the correspondence between the calibration marks and their projections can be determined easily (Steger et al., 2008).

The camera parameters can be determined by minimizing the distances between the extracted 2D mark centres, m_i , and their projected 3D centres of the calibration marks M_i , and by using the following optimization function.

$$e(x) = \sum_{i=1}^k \|m_i - \pi(M_i, x)\|^2 \rightarrow \min \quad (3.11)$$

where k is the number of calibration marks, π is the projection from 3D world to 2D plane, and x consists of the interior and exterior orientation parameters of the respective camera model. For pinhole cameras, $x = (R, T, f, k, S_x, S_y, C_x, C_y)^T$.

Equation 3.11 is a difficult nonlinear optimization problem and hence good starting values for the camera parameters are required (Steger et al., 2008). The internal parameters can be determined from the specification of the image sensor and the lens, but the initial values of the external parameters are in general harder to obtain. For the planar calibration target described before, good initial values can be found based on the geometry and size of the projected circles (Steger et al., 2008).

The camera must be calibrated from multiple images taken from different positions and orientations. For pinhole cameras, the calibration target must not be parallel to each other in all images. In order to calibrate the camera, the following optimization problem has to be solved.

$$e(x) = \sum_{j=1}^l \sum_{i=1}^k \|m_{i,j} - \pi(M_i, x)\|^2 \rightarrow \min \quad (3.12)$$

where $m_{i,j}$ is the projection of the i -th calibration mark in the j -th image.

3.5 Stereo Vision

Stereo vision is a technique that uses two or more cameras to acquire slightly different views of any object to gain depth information, similar to depth perception with the human visual system. HALCON provides two stereo methods:

- **Binocular stereo** uses exactly two cameras and the surface of a specific view can be reconstructed using the corresponding surface points.
- **Multi-view stereo** can use more than two cameras. In this method, not only the surface of a specific view, but also the whole 3D object can be imaged. The 3D coordinates of selected points or the 3D surface can be reconstructed.

The method utilized in this research is based on the binocular stereo system. Therefore, the principles as well as the calibration of this system based on the setup of two cameras are introduced in the following sections. More information about the other approach is given in detail in (Steger et al., 2008).

3.5.1 Binocular Stereo Vision

Binocular stereo vision is a technique which uses two cameras to recover the 3D scene from a pair of stereo images taken from different positions and orientations. The stereo cameras must be calibrated and the calibration parameters are used to calculate the 3D real-world coordinates of any point from its stereo projections by triangulation (Hartley and Zisserman, 2003). Figure 3-7 shows the process of recovering 3D world points using the binocular stereo system. This process generally consists of different tasks, including camera calibration, rectification, correspondence search, and reconstruction.

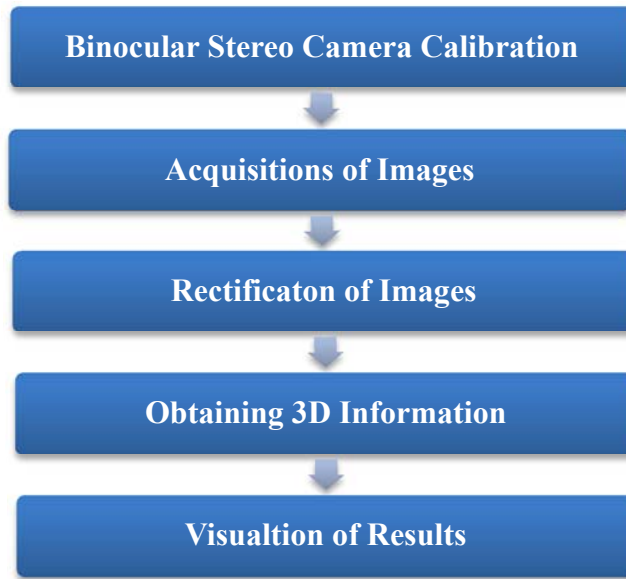


Figure 3-7: Flowchart of 3D reconstruction process.

3.5.2 Binocular Stereo Calibration

The first important step for the derivation of 3D information using a binocular stereo camera system is the calibration of the cameras. Stereo camera calibration involves the estimation of the intrinsic parameters of each camera as well as the relative position and orientation among the cameras (the translation and rotation of the second camera relative to the first one). The calibration of the stereo camera system is important to find the 3D coordinates of the object point under investigation.

3.5.2.1 Calibration Theory

In order to calibrate the stereo camera system, the method described in Section 3.4.1.3 is extended as follows: the centres of the calibration marks (M_i) are projected in both images as given before. The stereo system can be calibrated by solving the following optimization problem

$$e(x) = \sum_{j=1}^l \sum_{i=1}^k \|m_{i,j,1} - \pi_1(M_i, x)\|^2 + \|m_{i,j,2} - \pi_2(M_i, x)\|^2 \rightarrow \min \quad (3.13)$$

where M_i denotes the position of the calibration marks, $m_{i,j,1}$ and $m_{i,j,2}$ are the projections of the centres of the marks in the first and second set of calibration images, respectively. \mathbf{x} is the camera parameters which consists of the internal parameters of the first and second cameras as well as the relative orientation of the two cameras.

3.5.2.2 Stereo Camera Calibration Procedure

The procedure of stereo camera calibration in HALCON is very similar to the calibration of a single camera and is done in two steps. First, several images of a calibration plate should be acquired in different positions and orientations from each camera. The object coordinates of the calibration marks are given in the description file associated with the plate. In every image, the border of the calibration plate and the position of the circles can be determined. Then, the calibration parameters of the cameras used, the 3D points of the calibration plate and the relative position and orientation between the two cameras can be estimated. This is done in a least squares technique with suitable chosen start parameters.

3.5.3 Stereo Reconstruction

Very accurate measurements from a single image can be obtained by calibrating the camera and determining its parameters with respect to a plane in the world. The image measurements can be converted to world coordinates by intersecting optical rays with the plane. However, these measurements are 2D measurements within the world plane. In order to perform reconstruction of 3D points, at least two images of the same object of interest taken from different positions are required. This can be achieved by simultaneously taking images with two cameras. This process is known as *stereo reconstruction*.

The 3D reconstruction with the binocular stereo camera system is performed in such a way that for each point of the first rectified image the conjugate point in the second rectified image is determined (*stereo matching*). Either the disparity or the distance to the stereo camera system can then be computed for these conjugate points.

Additionally, 3D coordinates can be determined from the image coordinates of each pair of conjugate points directly.

3.5.3.1 Principles and Geometry of Binocular Stereo Vision

The concept of a binocular stereo system is illustrated in Figure 3-8. This figure represents a stereo camera system composed of two cameras, which observe the same objects from different positions. The optical centres of the first and second cameras are denoted by O_1 and O_2 , respectively. The principal points are denoted by the points C_1 and C_2 in the first and second image, respectively. The principal or focal distances are visualized by the dashed lines between the projection centres and principal points. The image is turned upside down because the image plane physically lies behind the optical centre. Therefore, the image coordinate system is defined such that its origin lies in the lower left corner, the row axis points upward, and the column axis points leftward.

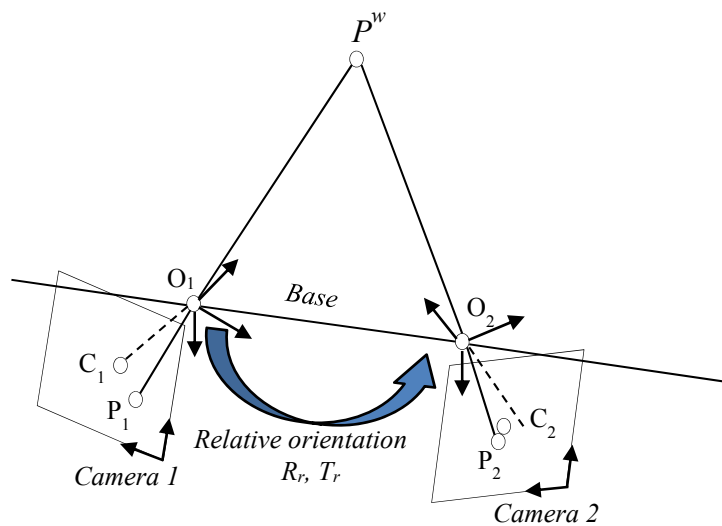


Figure 3-8: Geometry of a two-camera system.

The relationship between the two cameras can be described by the position and orientation of the two cameras with respect to each other, which can be expressed by a rigid-body transformation consisting of a rotation matrix, R_r , and a translation vector, T_r (Steger et al., 2008). This transformation given in the following equation transforms the coordinates of a point from the second camera coordinate system to the first camera coordinate system.

$$P_{C_1} = R_r P_{C_2} + T_r \quad (3.14)$$

This transformation consists of a rotation matrix, R_r , and a translation vector, T_r . The translation vector, known as the base, indicates the translation between the two camera centres.

To reconstruct 3D points, corresponding points in at least two images must be determined, meaning that the two points P_1 and P_2 in the images are the projections of the same world point P^w . Figure 3-9 represents schematically the epipolar geometry which describes the projection relation between points in images of two cameras. The lines of sight of the projection centres, O_1 and O_2 , intersect at the world point P^w and form a triangle plane which is called the *epipolar plane*. The intersection of the epipolar plane of point P^w with the two image planes are lines l_1 and l_2 , which are called the *epipolar lines*. The projections P_1 and P_2 of P^w can be found on these two lines. The line connecting the two projection centres intersects the image planes at two points, e_1 and e_2 , which are called *epipoles*. Once the epipolar geometry is known, the search for corresponding features can be reduced to one dimension (Steger et al., 2008). All possible positions of the world point P^w lie on the line O_1P^w for the left image and on the line O_2P^w for the right image. This is reflected in the left camera's image plane for O_2P^w by the line l_1 and in the right camera's image plane for O_1P^w by the line l_2 . Given a point P_1 in the first image, the corresponding point, P_2 , has to lie on the epipolar line in the second image.

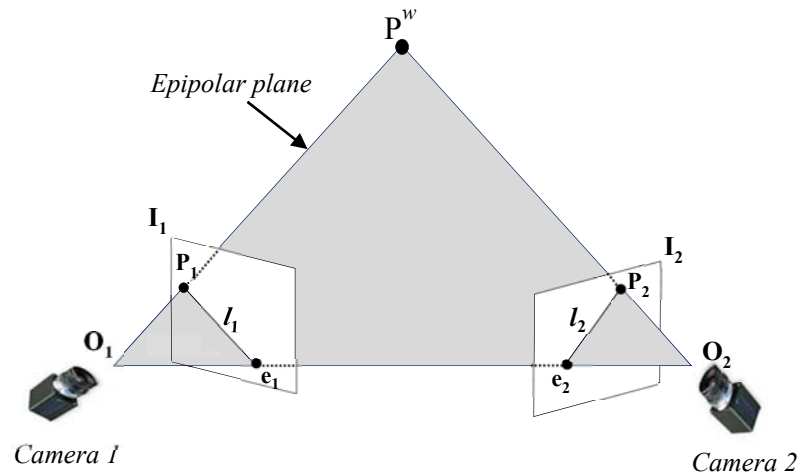


Figure 3-9: Epipolar geometry of a two-camera system.

Rectifying Stereo Images

Rectification is the process of transforming the left and right images to the epipolar standard geometry. In order to rectify stereo images, two image planes are required to be reconstructed such that they lie in the same plane. The camera coordinate systems are needed to be rotated in such a way that their x-axes become identical to the baseline. In addition, the rectification simplifies the configuration of epipolar lines as well as depth reconstruction (Steger et al., 2008). Figure 3-10 demonstrates the geometry of the stereo camera as viewed along the y-axis of the camera coordinate system. The lines joining the two projection centres of the two cameras are assumed to coincide with the x-axis of the first camera. Using the concept of similar triangles, the image plane coordinates of the projections of the point P into the two images can be expressed by

$$X_L = f \frac{X}{Z} \quad (3.15)$$

$$X_R = f \frac{X - b}{Z} \quad (3.16)$$

where f is the principal distance and b is the baseline of the system, which describes the distance between the optical centres of the cameras.

The depth (Z) can be calculated by combining the above two equations, resulting in

$$Z = \frac{bf}{(X_L - X_R)} = \frac{bf}{d} \quad (3.17)$$

where d , known as *disparity*, is the difference between the two image locations of the conjugate points.

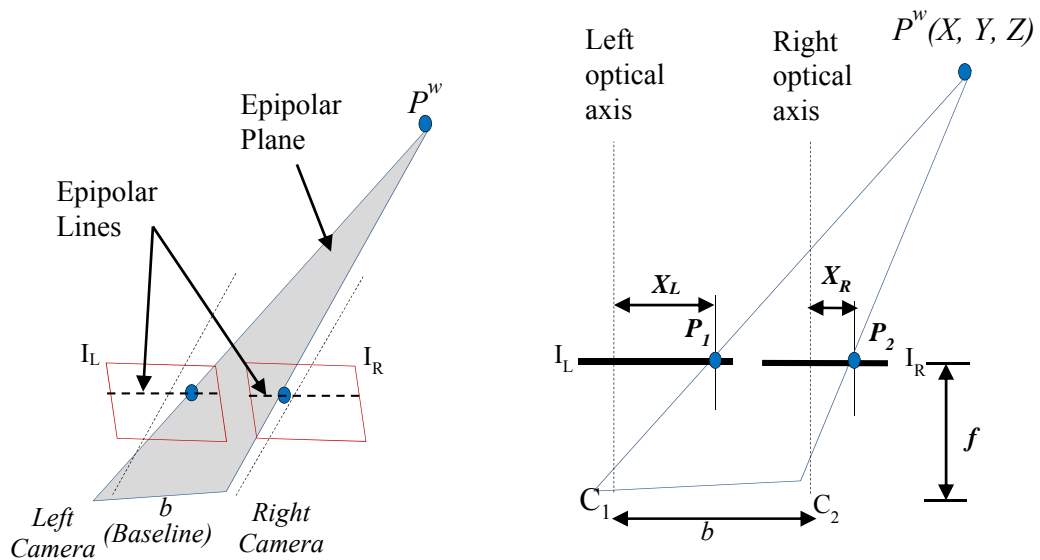


Figure 3-10: Geometry of Binocular Stereo (adapted from (Jain et al., 1995)).

3.6 Software Implementation

In order to use the proposed photogrammetric system to determine the deformation of timber specimens effectively and to record the image data in real time during testing, a software package is required to be developed. The integrated development tool of HALCON, HDevelop, can be used to implement the image acquisition and processing programs. HDevelop provides the user with the necessary functions and operators to write the image processing code to view, acquire, process, and save images of the object or area of interest. The code can then be converted into different programming languages such as C++ and Visual Basic in which the user's algorithm can be done easily.

3.6.1 The Microsoft Visual Studio

The Microsoft Visual Studio is an integrated development environment (IDE) which assists in developing graphical user interfaces to suit different applications. It has built-in languages, including C/C++, Visual Basic, and C#. Visual C++ supports the Component Object Model (COM) and Microsoft foundation classes (MFC), which is very convenient for creating GUIs with feasible features.

3.6.2 The Microsoft Foundation Classes (MFC)

MFC, or Microsoft foundation classes, is a library with a set of predefined classes in windows programming to assist in creating Windows applications. Written in the programming language C++, the MFC library provides the user with the ease of designing applications. MFC provides library classes and most codes necessary for managing and supporting all Windows controls, allowing easy creation of the Windows common objects and controls such as menus and dialog boxes. Additional feature of MFC is that it is very convenient for creating graphical user interfaces with a wide variety of buttons. Because of the above mentioned attractive features of MFC, the GUI of the software package was implemented with MFC.

3.6.3 The Implemented Graphical User Interfaces

In order to provide the user with the ease of using the stereo camera system, it is crucial to have a graphical user interface (GUI) which can represent the information and actions efficiently. A graphical user interface is a program interface item that allows the user to interact with the programs in more ways than just typing commands. It offers graphical icons and visual indicators to represent the information and action efficiently. A well-designed interface can help the user to use the program without the necessity to understand the theories and complicated algorithms.

Three major GUIs have been implemented during the study of this research. All of these interfaces were developed based on the approach of developing applications with HALCON as described in Section 3.3.2. The first interface was implemented in Visual basic as an initial interface for the torsion test. This GUI provides the user with the basic functions to calibrate the stereo camera system and save the image data during testing. The calibration can be performed by processing these calibration image data, extracting the calibration circular marks, and creating the calibration files and saving them to the hard disk of the computer. This was done with the help of functionalities provided by the HALCON software. Besides the functions of loading and saving images, the GUI also provides an interactive initial parameter setting which allows the user to set the appropriate parameters of the stereo camera system.

The second GUI was improved by being implemented in MFC, which includes a variety of controls. This GUI is developed in MFC dialog-based application using Visual C++ 2010. It was implemented to be used for the torsion test when using two stereo camera systems. Besides the ability to connect and view up to 4 cameras, the second GUI can also be used to calibrate the stereo camera system in real time or later after saving the calibration images. Figure 3-11 shows several controls employed in the system. The two top windows can view the stereo images of the first binocular stereo system while the two bottom windows can view the stereo images of the second binocular stereo system.

As shown in Figure 3-11, the GUI includes in general three control panels named as ‘*Image Acquisition Devices*’, ‘*Calibration Control*’, ‘ and *Recording*’. The first panel contains control buttons for performing different tasks. The browser button is used to select the folder where the acquired images are saved to. The other buttons can be used to carry out different tasks such as connecting or disconnecting the camera system. The cameras connected to the computer can be detected and then selected from the combo box to be used for the stereo imaging system. The second panel is used to perform the calibration of the stereo camera system. The number of images to be used for stereo camera calibration is required to be entered. The description file containing world measurements of the used HALCON calibration plate is also required to be selected. This panel also includes control for camera parameters. The combo box is designed to let the user select the camera model of the system. The focal length of the lenses can be entered in the associated box. Moreover, the width and height of the sensor cells can be adjusted in the associated box. Furthermore, the parameters used to extract the marks of the calibration plate can be specified in the given boxes. The third panel of this GUI is used to start saving the image data during testing based on a time interval that can be adjusted according to the desired time.

Finally, a third GUI was developed in MFC and used during the compression tests, as shown in Figure 3-12. The interface was used to calibrate the stereo camera system and to record the image data during testing. The calibration of the stereo camera system with this GUI was further improved by allowing the calibration to be performed in real time or later after saving the calibration images. Another helpful feature of the GUI is the capability of automatically determining the presence of the calibration plate of HALCON in the image sequences, allowing the user to locate the plate easily and enhance the speed of calibrating the stereo camera system. Additionally, the extracted calibration parameters of both cameras can be viewed in the interface as shown in the above-mentioned figure.

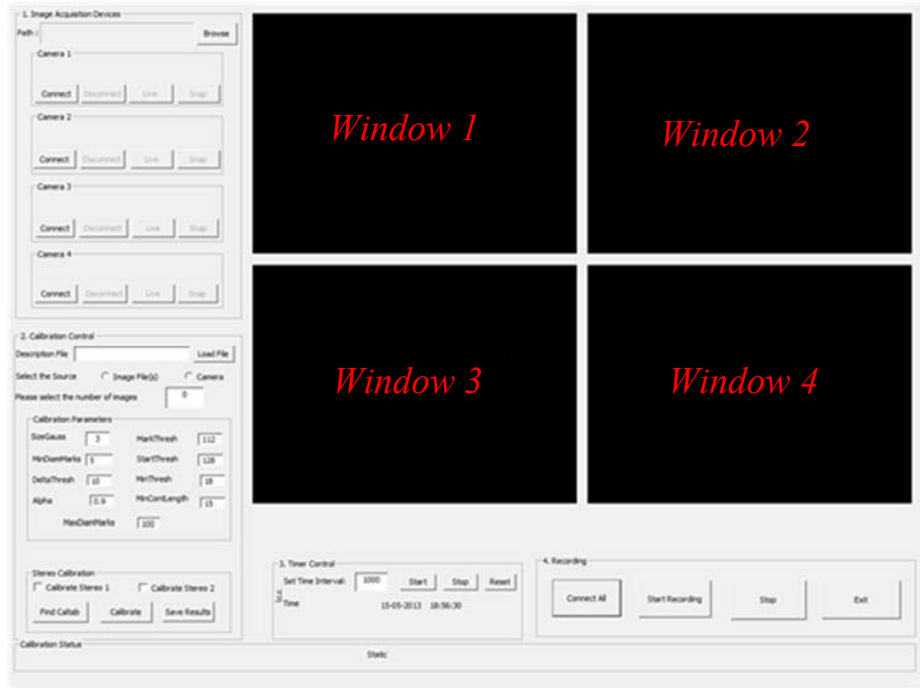


Figure 3-11: Developed graphical user interface used during the torsion tests.

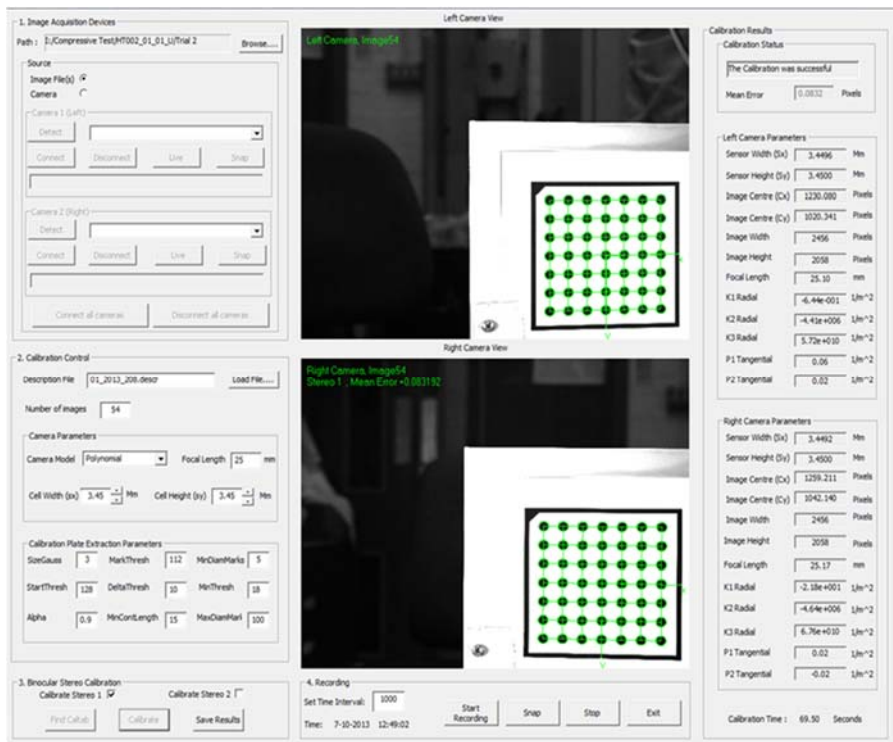
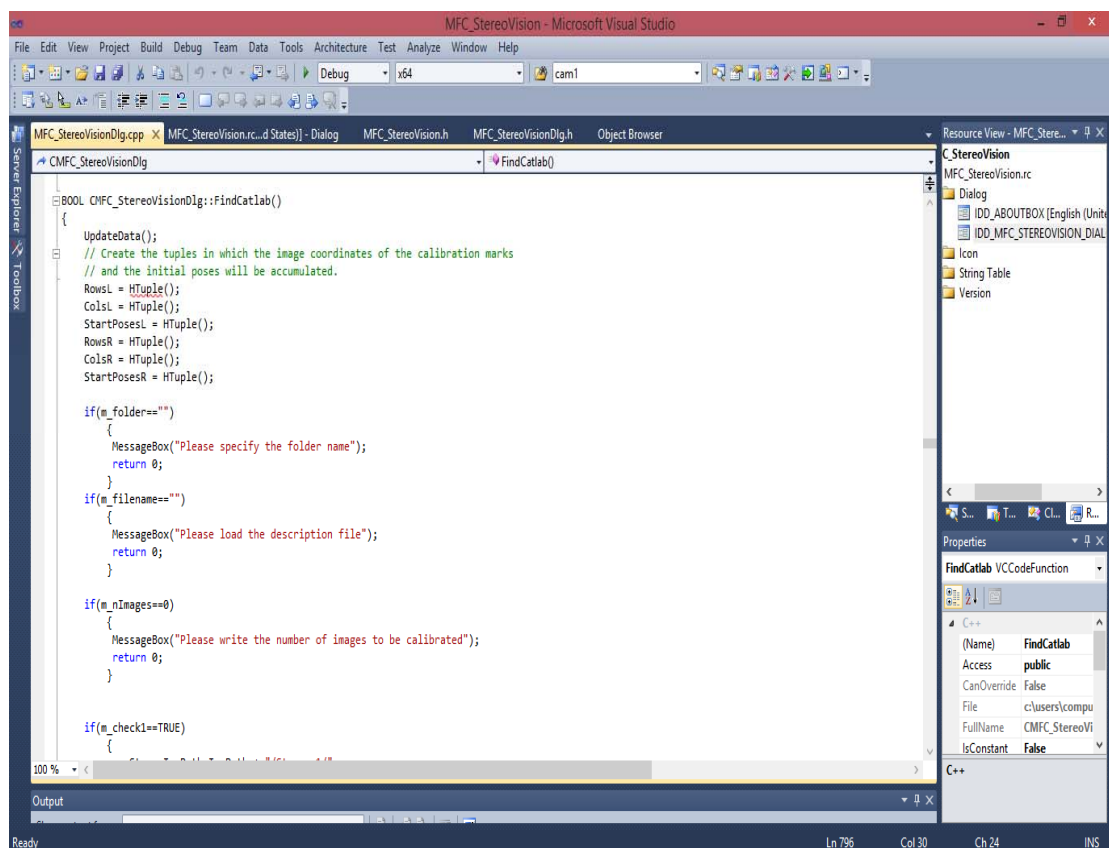


Figure 3-12: Developed graphical user interface used during the compression tests.

3.6.4 The Implemented Algorithms

3.6.4.1 Camera Calibration Algorithm

An algorithm was developed to calibrate the binocular stereo camera system based on the image processing software, HALCON. A part of the calibration code implemented in MFC is shown in Figure 3-13. The calibration algorithm consists of several steps. The basic steps of the calibration process are shown in Figure 3-14. First, the calibration images are acquired, saved and processed by HALCON operators in a loop. The *find-caltab* operator, for example, is used to find the region of the calibration plate in the processed image and *find-marks-and-pose* determines the 2D position of the calibration marks and estimates the pose of the plate. With this information, the operator *binocular-calibration* determines the camera parameters of the binocular camera system.



```
BOOL CMFC_StereoVisionDlg::FindCaltab()
{
    UpdateData();
    // Create the tuples in which the image coordinates of the calibration marks
    // and the initial poses will be accumulated.
    RowsL = HTuple();
    ColsL = HTuple();
    StartPosesL = HTuple();
    RowsR = HTuple();
    ColsR = HTuple();
    StartPosesR = HTuple();

    if(m_folder=="")
    {
        MessageBox("Please specify the folder name");
        return 0;
    }

    if(m_filename=="")
    {
        MessageBox("Please load the description file");
        return 0;
    }

    if(m_nImages==0)
    {
        MessageBox("Please write the number of images to be calibrated");
        return 0;
    }

    if(m_check1==TRUE)
    {
```

Figure 3-133: A part of the implemented C++ calibration code for calibrating the stereo camera system.

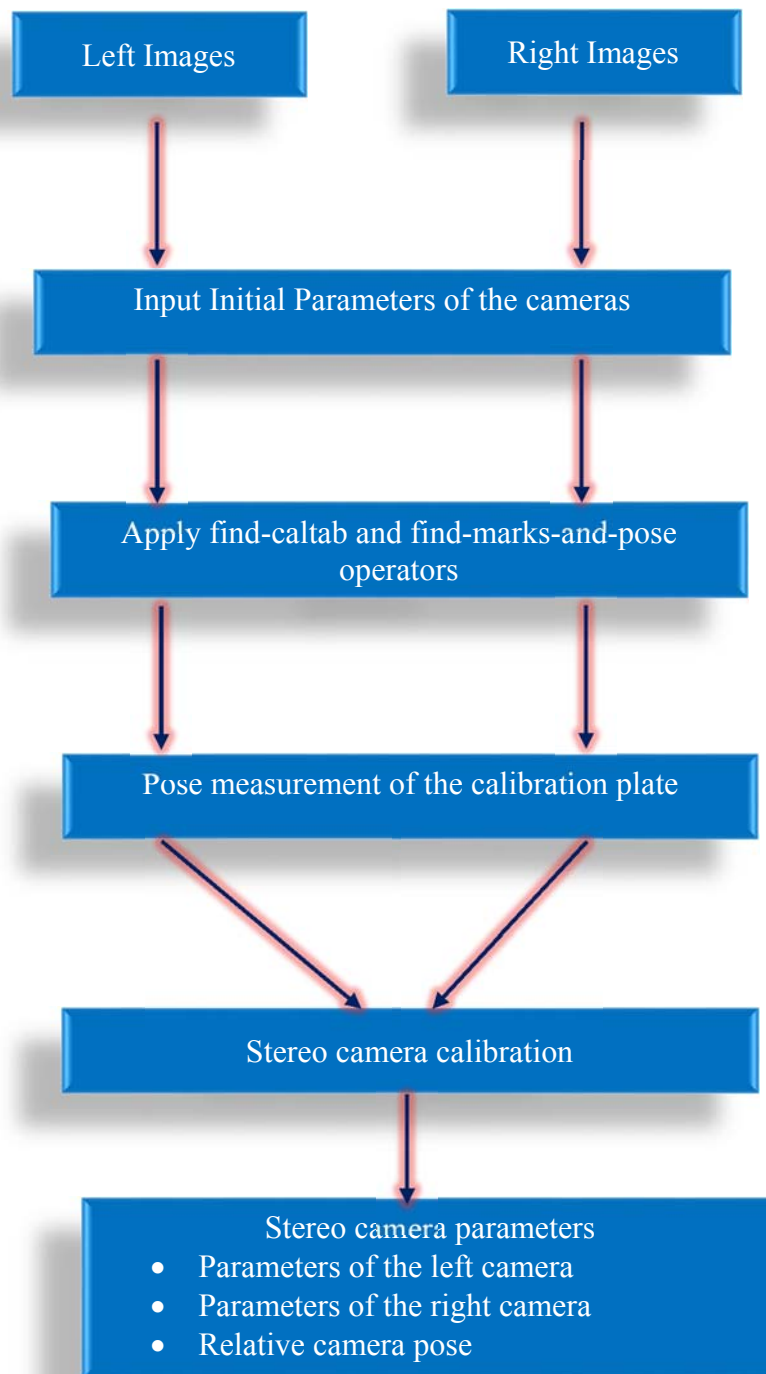


Figure 3-144: A diagram of the basic steps for stereo camera calibration.

3.6.4.2 Deformation Measurements Algorithm

Since the usage of cameras as measurement devices, different algorithms have been implemented for measuring the 3D coordinates of the photogrammetric targets. Circular-shaped targets are easy to detect and they have been used in different applications to achieve the highest accuracy (Clarke, 1994, Luhmann, 2010, Otepka and Fraser, 2004). All of the 3D deformation measurement algorithms were written in HALCON which provide a powerful library for processing the stereo images. The implemented algorithms process the stereo images, detect the target points, and determine the 3D coordinates of the points. The whole process was programmed in the software to be automated. Figure 3-15 summarizes the concepts and steps involved in the algorithms. The process starts with reading the calibration files, recorded during the calibration process, containing the internal and external parameters of the binocular stereo system. The stereo images of the targets recorded by the left and right cameras during testing were then displayed to be used in the image recognition process. The sub pixel-precise segmentation method provided by the software was used to reduce the area of interest of the stereo images by using the threshold values of the pixels corresponding to the targets. The potential targets that meet a specific shape and size were then extracted with sub-pixel accuracy. These targets were fitted to ellipse shapes and their image coordinates in both the left and right images were measured. The stereo-matching problem was then solved by sorting these targets in each of the left and right images according to their order in row and column coordinates from top to bottom. They were labelled and numbered to show how they match each other. The 3D coordinates of the target points were then determined from the intersection of two lines of sight within the binocular camera system using the theory of triangulation (Hartley and Zisserman, 2003). This was achieved by applying the operator '*intersect_lines_of_sight*' to the extracted target points. The 3D measurements were determined relative to the coordinate system of the left camera. To define a world coordinate system, three target points were employed. The first point defines the origin of the coordinate system, the second point lies on the x-axis and the third point lies on the y-axis. The transformation matrix was then determined from these points. Using the transformation matrix together with the calibration parameters of the stereo camera

system, the determined point coordinates were transformed from the coordinate system of the first camera into the world coordinate system. These 3D coordinates were then saved to the project computer and used in the calculation of the displacements and rotations of the targets during the period of tests.

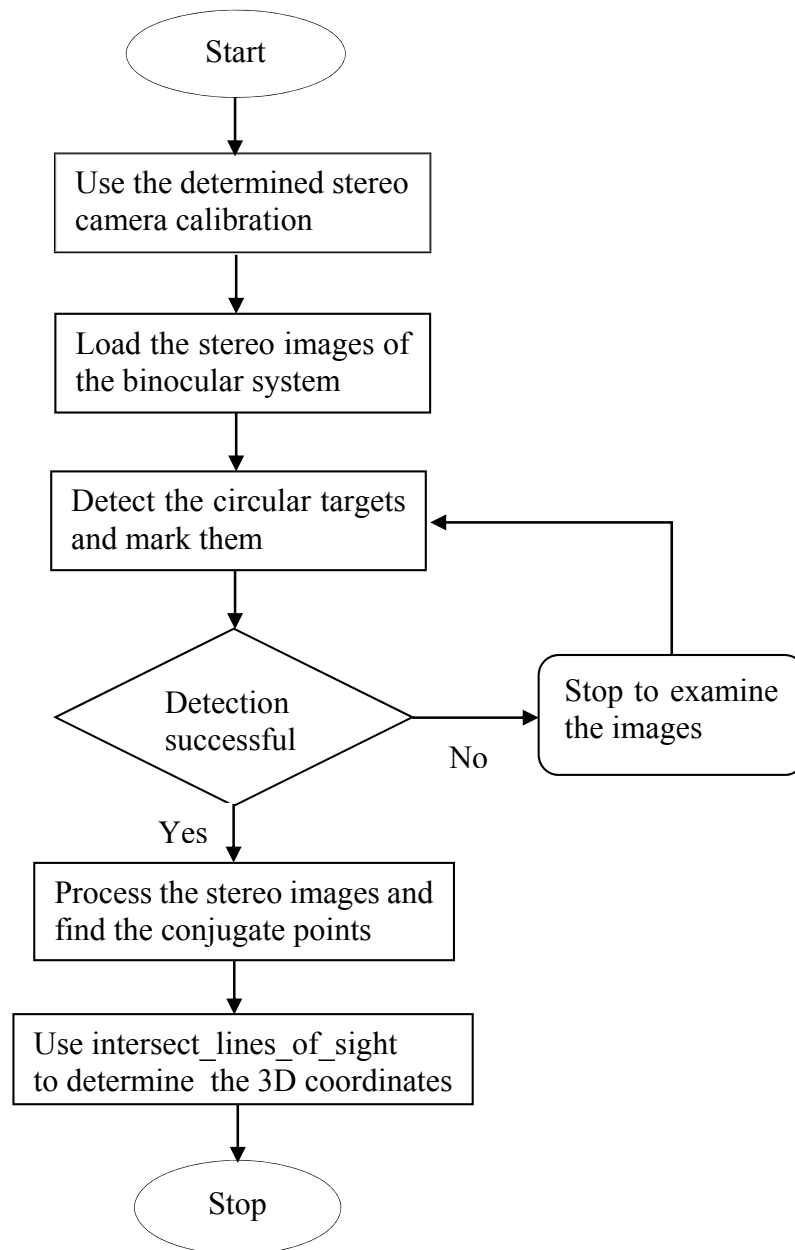


Figure 3-155: Flowchart of the stereo reconstruction algorithm based on HALCON.

4. VALIDATION AND EVALUATION OF THE PROPOSED STEREO CAMERA SYSTEM

4.1 Introduction

Three different experimental studies were considered in this chapter with different objectives. The first experimental study of our research was conducted using the developed photogrammetric approach with the objective to investigate the influence of several parameters, including the number of the calibration images, the camera model, and the baseline length, on the efficiency of the stereo camera system. The second experimental study was conducted to validate the optical system by conducting experimental tests and comparing the displacement values of specific points determined by the photogrammetric approach with those measured by the different traditional devices. Finally, the last experimental study was conducted on glulam timber specimens subjected to compressive loadings. The main objective of the study was to investigate and compare the effectiveness of different target techniques, which can be applied to the surface of the glulam timber specimens, on measuring the surface displacements in more detail. Three different marking techniques were proposed to generate the photogrammetric targets. These targets were applied to the surface of the glulam specimens prepared for the compression tests. For comparative purposes, experimental compression tests were carried out on these specimens to evaluate the efficiency of the proposed targets for measuring the displacements between two points on the surface of the samples. This was achieved by comparing the measurements results obtained by the LVDT with those obtained by the three different techniques using the binocular stereo camera system. The descriptions and the test results of all the experimental studies mentioned above are provided in the following sections.

4.2 Experimental Evaluation of the Parameters of the Stereo Camera System

The photogrammetric method was proposed in this research to monitor the deformations of the glulam timber specimens under loadings. Before using this method with the combined photogrammetric targets in this research, it was essential that several parameters affecting the accuracy of photogrammetric approach, including the camera models, the numbers of the calibration images, and the baseline length, were investigated. It was also necessary that the photogrammetric technique needed to be validated.

Experimental studies were proposed to evaluate the accuracy of the stereo camera system. The first experimental study was carried out to investigate how the camera model and the number of the calibration images affect the accuracy of the stereo system. These images are required to calibrate the stereo camera and determine the internal and external parameters of the stereo cameras. In the second experimental study, a calibration plate of HALCON, which consists of circular targets whose 3D coordinates are known precisely, was proposed to validate the accuracy of the stereo system by comparing the real 3D coordinates of the targets with those calculated by the stereo cameras based on different baseline lengths.

4.2.1 Materials and Testing Equipment

As shown in Figure 4-1a, the target used in the first investigation consisted of black circular marks on a white background. A square calibration plate of HALCON was employed as a target for the second investigation. The image of this plate is shown in Figure 4-1b. This target consists of 49 marks whose 3D coordinates are known with a high accuracy. The coordinates of these targets are given in the calibration description file which is available according to the dimension of the calibration plate as mentioned in (MVTec Software GmbH, 2011c).

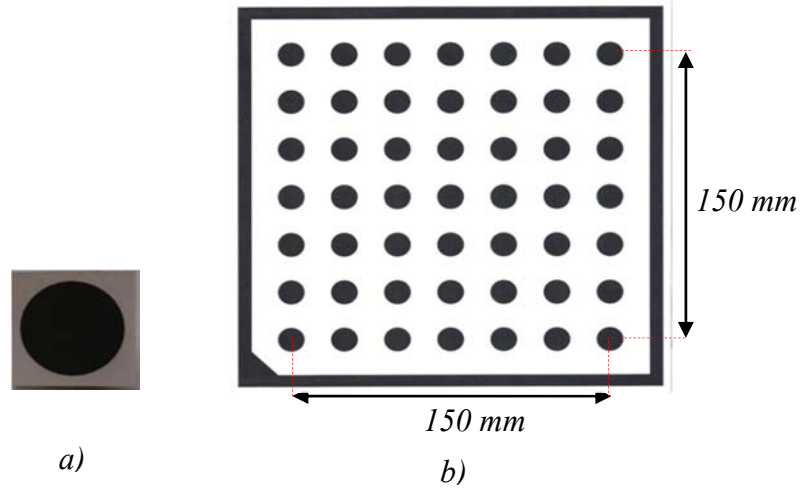


Figure 4-1: Images of the employed targets for a) the first investigation, and b) the second investigation.

The photogrammetric camera system used in this study consists of two Basler Pilot piA2400-17gm cameras, two lenses with a fixed focus of 25mm, two LED light units, a tripod, a frame for adjusting the distance between the cameras, pan tilt units, and a desktop computer. The image of the stereo camera system is shown in Figure 4-2. More details about these cameras are provided in Chapter 3. The two motorized pan tilt units with remote controls were used to assist in adjusting the camera positions. The LED lights were used for illumination.

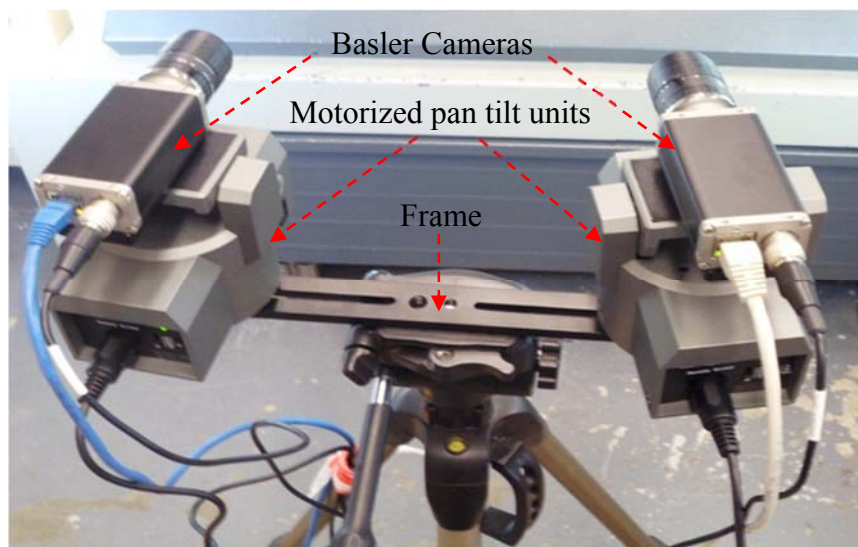


Figure 4-2: Stereo camera system mounted on a tripod.

4.2.2 Experimental Setup and Procedure

The flow diagram of the experimental tests conducted in the first study is summarized in Figure 4-3. Two investigations were considered in this study. In the first investigation, two circular targets were placed on the loading plates of the Zwick machine connected to a desktop computer (the machine computer), PC1. The machine computer controls the movements of the loading plates. The experimental setup of the tests conducted in this investigation is shown in Figure 4-4. The cameras were mounted on an adjustable frame setup on a stable tripod. The stereo cameras were connected, through Ethernet cables, to PC2 where the image processing software is installed. The focus of the cameras was set to make the targets in complete focus. Two LED light illuminations were employed to provide a homogenous illumination of the targets.

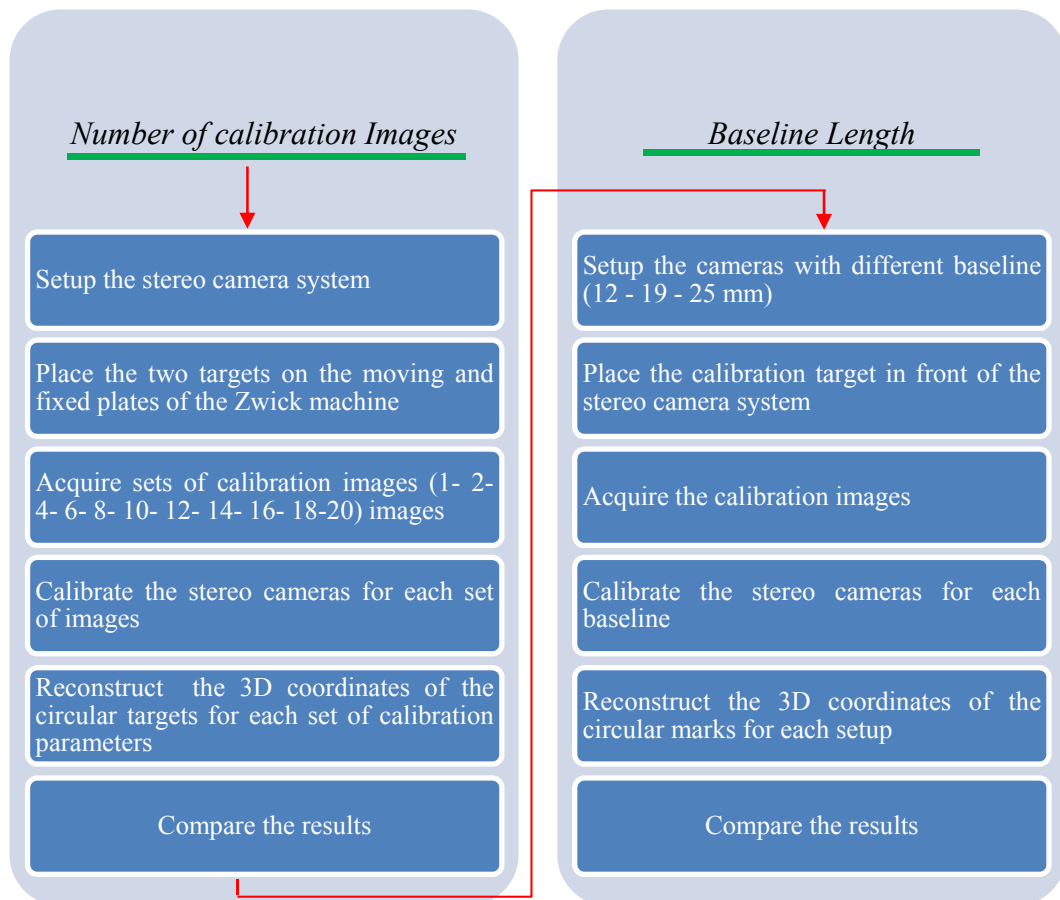


Figure 4-3: Flowchart of the experimental tests conducted in this investigation.

Before being used in this study for 3D measurements, the stereo cameras were calibrated according to the calibration procedure of HALCON previously described in Chapter 3. A 100x100 mm calibration plate of HALCON was used to perform the stereo camera calibration. The calibration target was placed on the plane, where the measurements need to be done. The calibration plate was moved along the entire FOV of the cameras and stereo images of the plate were captured by the stereo camera system at different positions and orientations. Eleven sets of calibration images (1, 2, 4, 6, 8, 10, 12, 14, 16, 18, and 20) were taken and the calibration was performed for each of these images. In every calibration set, the border of the calibration plate and the image coordinates of the circular marks were extracted from the calibration images. Using the stereo calibration parameters of the used cameras, the 3D points of the calibration plate and the relative position and orientation between the two cameras were then estimated by means of the calibration functions provided by HALCON. This is done in a least squares techniques with suitable chosen start parameters. The stereo calibration results were stored in the hard drive of the PC2 as a *.cal* file which can be read by the image processing software. The calibration results were then saved to the PC2.

Initial images representing the zero-displacement case of the targets were captured by the stereo cameras to allow comparison with the rest of the data. The Zwick machine was set to move down the loading plate by an appropriate magnitude and the developed GUI was used to control the cameras to acquire and record simultaneous images of the targets with a time interval of about 1 second. The captured images as well as the corresponding time were stored to the hard disk of PC2 for processing on later occasions. At the end of loading the sample, the machine was set to let the crosshead displacement control stay in the same position to allow capturing the final state of the sample.

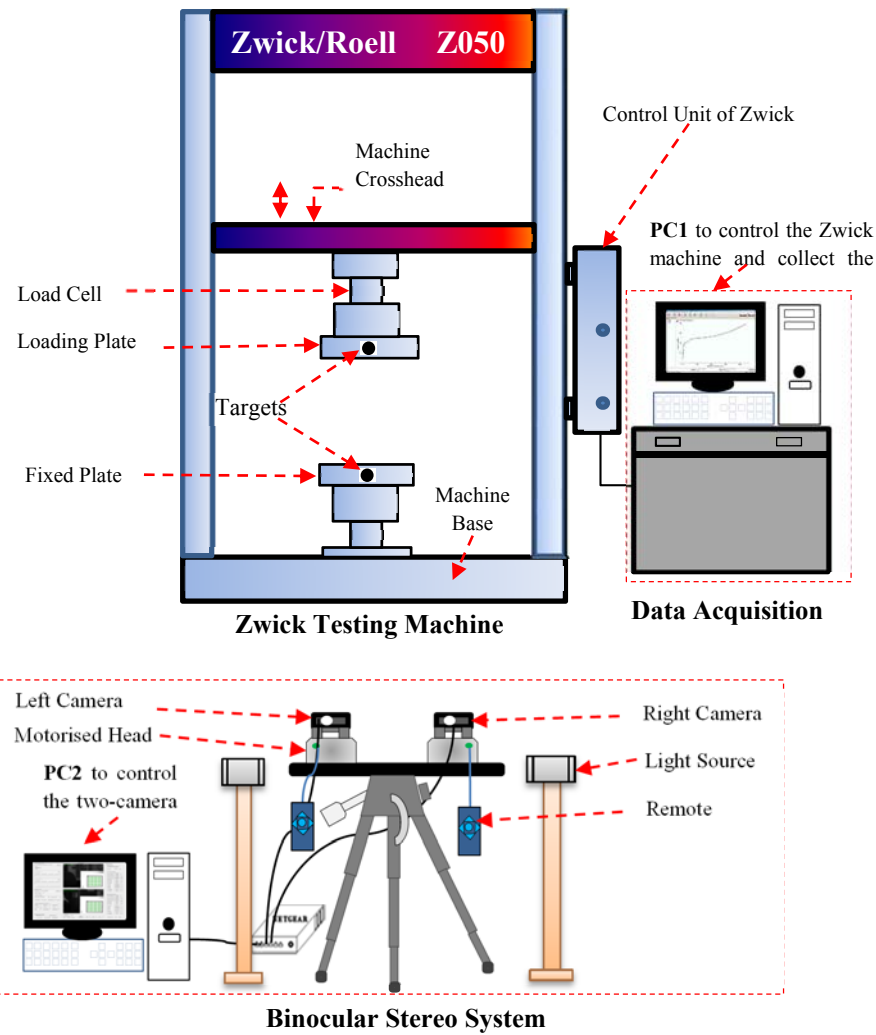


Figure 4-4: Schematic plot of the test set-up with instrumentation of the first study

In the second investigation, three experimental tests conducted with different baseline lengths of 12,19, and 25cm, respectively. The stereo cameras were mounted on a tripod and the baseline distance was first set at about 12cm. The image of the test setup is shown in Figure 4-5. The photogrammetric plate consisting of the circular targets was placed in front of the stereo camera system at a working distance which allows the cameras to cover the entire photogrammetric target. The cameras were connected to PC2 and made to focus on the target plate.

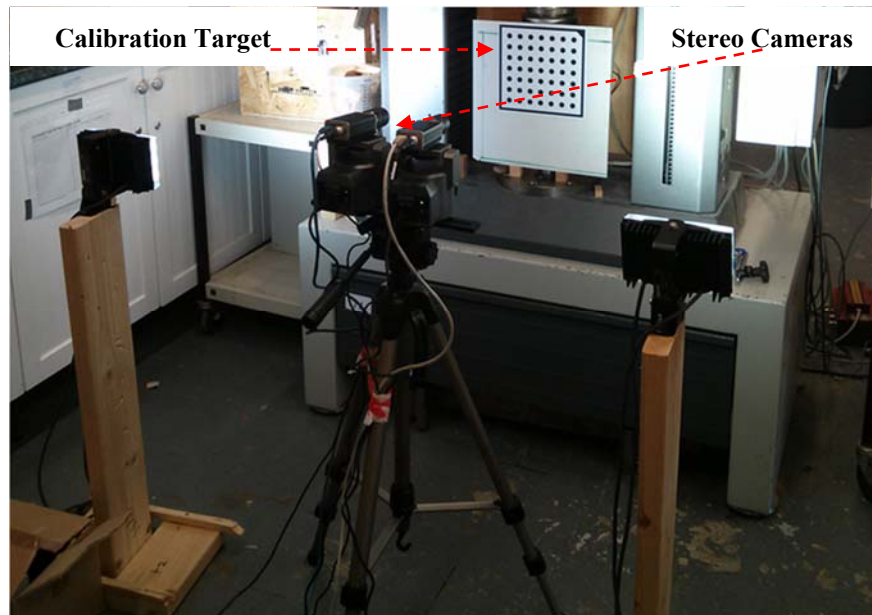


Figure 4-5: Test set-up and instrumentation of the second investigation.

Before being used in this study for 3D measurements, the stereo cameras were calibrated according to the previously described calibration procedure. The calibration plate was moved along the entire FOV of the cameras and 20 images of the plate were captured by the stereo camera system at different positions and orientations. Figure 4-6 shows five pairs of the calibration images acquired during the calibration process. The whole process of finding the calibration plate, extracting the circular marks, and determining the correspondences between the extracted marks and the corresponding 3D world coordinates were carried out automatically. The calibration parameters are used to calculate the 3D position of any point from its stereo projections by triangulation.

The same test setup and procedure was repeated for the second and third experimental tests but with baseline lengths of 19cm and 25 cm, respectively. In each of these tests, the stereo cameras were calibrated based on the same calibration procedure and the calibration files were saved to the PC. After performing the calibration, stereo images of the target plate were then captured by the two calibrated cameras and saved to the PC to be processed later.

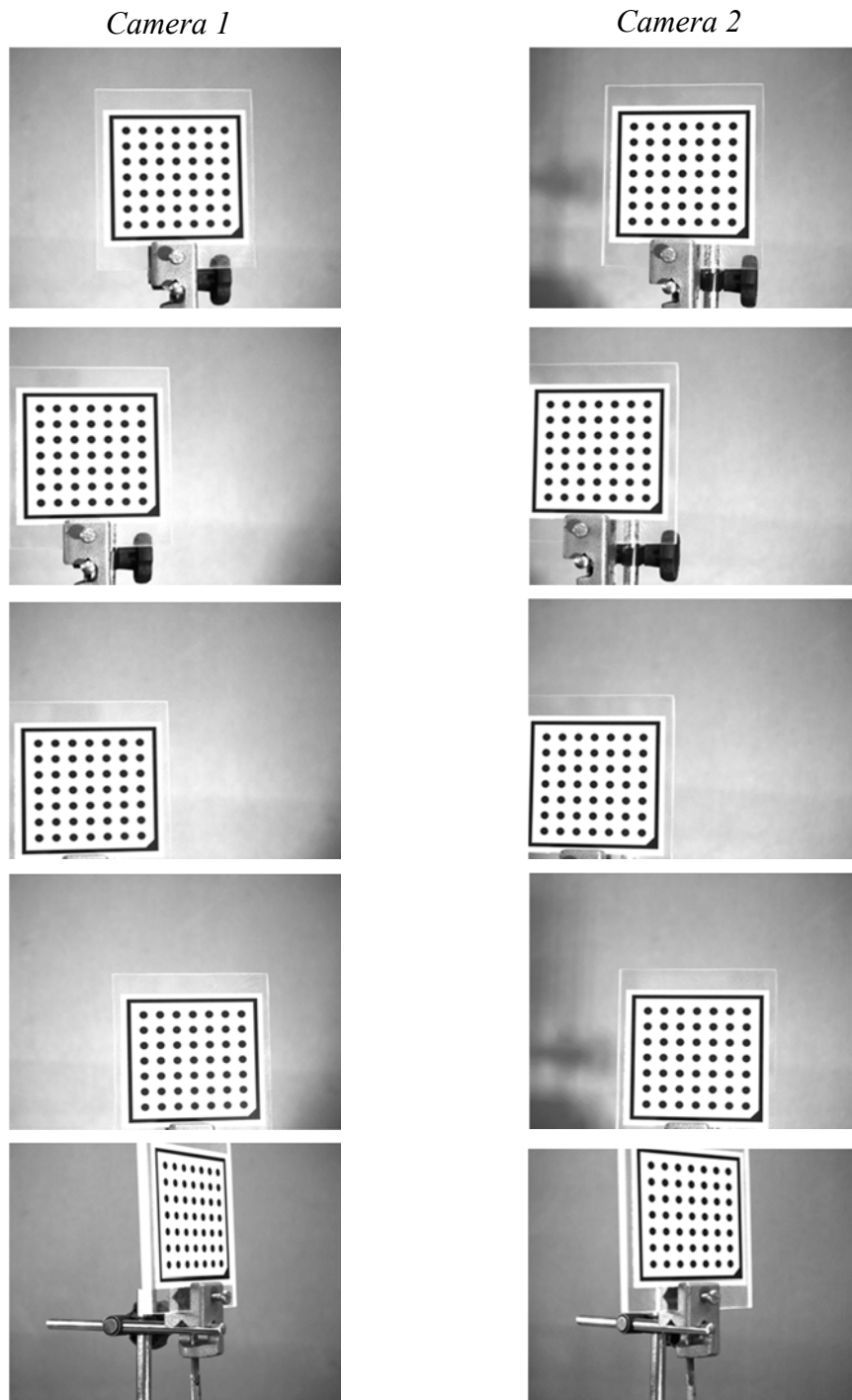


Figure 4-6: Five image pairs of the calibration plate acquired at different positions and orientations.

4.2.3 Calculation Methods

4.2.3.1 Determination of the 3D Coordinates of the Targets

In order to determine the 3D coordinates of the circular black targets from the stereo camera system, both the internal and external camera parameters of the stereo cameras have to be determined. It is also important that the conjugate points for each object point of interest in the stereo image pair have to be determined. These requirements can be accomplished in two steps given below:

In the first step, the parameters of the two cameras can be determined by the calibration of the stereo camera system. To perform the calibration, it is essential that the 3D coordinates of a large number of points in world coordinates are known. This can be accomplished, for example, by using the calibration plate of HALCON with circular marks acquired at different positions in the field of views (FOV) of the stereo cameras. The HALCON calibration plate of HALCON is constructed in such a way that the correspondence between the calibration marks and their projections can be determined easily (Steger et al., 2008). After finding the coordinates of the image points, the stereo camera parameters can be obtained using the operator, termed "*Binocular_Calibration*", of the Imaging Processing Library of HALCON.

The second step involves an extremely challenging problem known in image processing as "stereo matching process", which requires that for each point in the left image, the corresponding point in the right image has to be determined. First, the image coordinates of two image points captured from the same object point of interest are computed. These points are referred to as conjugate points. The 3D world coordinates of any target point of interest can be directly reconstructed via the operator termed as '*Intersect_Lines_of_Sight*' utilizing the image coordinates of the conjugate points, together with the stereo camera parameters.

4.2.3.2 *The Implemented Calibration and 3D Reconstruction Algorithms*

The author of this research developed a customized software package which can be employed to calibrate the stereo camera system, capture the stereo images, and record the images during testing. The tailor-made software was developed in Visual Basic 6.0 which was easier to learn and to design the GUI. The communication between the PC and the stereo cameras was accomplished using the functions provided by HALCON. Two main algorithms were implemented in HDevelop to calibrate the stereo cameras and to process the images acquired by the calibrated cameras. The first algorithm was implemented to perform the calibration of the stereo camera system. The second implemented algorithm assists not only in finding the photogrammetric targets on the stereo images but also in determining the corresponding points between the images and calculating the 3D coordinates of the target points. Figure 4-7 summarizes the concepts and steps involved in the 3D reconstruction algorithm and more details can be found in Chapter 3. The steps of the algorithm are as follows:

Step 1: Calibrate the stereo camera system and save the calibration files.

Step 2: Read the calibration files, recorded during the calibration process and including the internal as well as the external parameters of the stereo cameras.

Step 3: Display the stereo images of the targets recorded by the calibrated cameras during testing.

Step 4: Apply the sub pixel-precise segmentation method to extract potential targets that meet a specific shape and size.

Step 5: Fit the extracted targets to ellipse shapes and measure their centroids in the image coordinates in both stereo images.

Step 6: Sort the targets in each of the left and right images according to their order in row and column coordinates from left to right and from top to bottom.

Step 7: Determine the 3D coordinates of the target points by triangulation (Hartley and Zisserman, 2003).

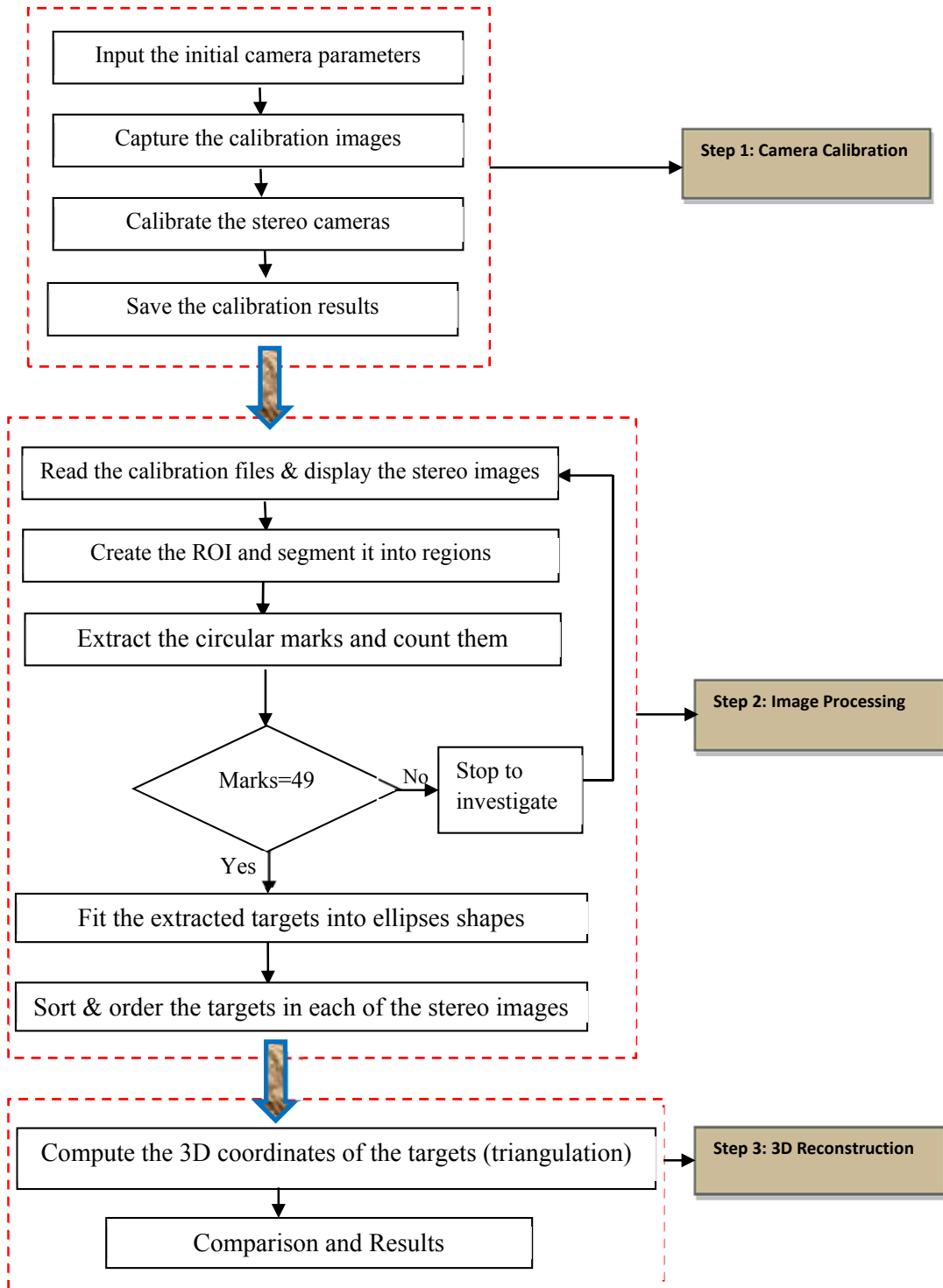


Figure 4-7: Flow diagram of the 3D reconstruction Algorithm.

Figures 4-8a and 4-8b provide parts of the implemented algorithm in HDevelop, showing the operators used to read the calibration images and reconstruct the 3D coordinates of the detected targets.

```

HDevelop - E:/Accuracy 8/T1/Accura
File Edit Execute Visualization Procedures Operators Suggestions Assistants Window Help
*main (:)
5
6 * I setup a stereo cameras ('camera1 is left of camera2').
7 * Both cameras will be calibrated by some images of a 100mm calibration plate.
8 * will be identified their 3D position will be determined.
9 -----
10
11 * Set the image path
12 ImgPath := 'C:/Accuracy 8/T1/'
13
14 * Read an image to get its size and open a window with an appropriate size
15 read_image (Image, ImgPath+'Camera 1/'+'Image1_01')
16 get_image_size (Image, Width, Height)
17 dev_close_window ()
18 dev_open_window (0, 0, Width/4, Height/4, 'light gray', WindowID)
19 dev_set_part (0, 0, Height - 1, Width - 1)
20 dev_set_line_width (3)
21 dev_set_color ('red')
22 dev_set_draw ('margin')
23 dev_display (Image)
24 set_display_font (WindowID, 14, 'mono', 'true', 'false')
25 disp_continue_message (WindowID, 'black', 'true')
26 stop ()
27
28
29 * Read the stereo camera parameters
30 read_cam_par (ImgPath+'Stereo 1/CamParamL.dat', CamParamL)
31 read_cam_par (ImgPath+'Stereo 1/CamParamR.dat', CamParamR)
32 read_pose (ImgPath+'Stereo 1/cLPcR.dat', cLPcR)

```

a)

```

HDevelop - E:/Accuracy 8/T1/Accuracy 8 Ellipse.hdev * - (
File Edit Execute Visualization Procedures Operators Suggestions Assistants Window Help
*main (:)
192 * Get a 3D point from the intersection of two lines of sight within a binocular camera system
193 intersect_lines_of_sight (CamParamL, CamParamR, cLPcR, R1, C1, R2, C2, X1, Y1, Z1, Dist1)
194
195 * Determine the transformation matrix from three given points:
196 * Select three points, which define a given world coordinate system,
197 * where the first points defines the origin of the CS,
198 * the second lies on the x-axis and the third in the x-y-plane, e.g., on the y-axis
199
200 RL_DefiningTheCS := [R1[24], R1[27], R1[3]]
201 CL_DefiningTheCS := [C1[24], C1[27], C1[3]]
202 RR_DefiningTheCS := [R2[24], R2[27], R2[3]]
203 CR_DefiningTheCS := [C2[24], C2[27], C2[3]]
204
205 dev_set_window (WindowID)
206 dev_clear_window ()
207 dev_display (ImageL)
208 * Determine the coordinates of these points wrt the rectified camera coordinate system
209 intersect_lines_of_sight (CamParamL, CamParamR, cLPcR, RL_DefiningTheCS, CL_DefiningTheCS, RR
210 Origin := [XCP[0], YCP[0], ZCP[0]]
211 PointOnXAxis := [XCP[1], YCP[1], ZCP[1]]
212 PointInXYPlane := [XCP[2], YCP[2], ZCP[2]]
...

```

b)

Figure 4-8: a) The initial part of the algorithm showing the HALCON operators used to open windows and read the calibration parameters, and b) the last part of the algorithm showing the operators used to reconstruct the 3D coordinates of the targets.

4.2.4 Results and Discussions

4.2.4.1 Results of the calibration

To reconstruct the 3D coordinates of the photogrammetric targets captured by the stereo cameras, both the internal and the external parameters of the stereo camera system were calculated by calibrating the binocular stereo camera system using the calibration procedure previously described in Chapter 3. This was achieved via a least square solution with suitable chosen parameters of the cameras that can be determined from the specification of the camera sensor and lens. Table 4-1 shows a selected example of the internal as well as the external parameters, including the rotation angles and the translation vector determined for the stereo cameras.

Table 4-1: The calibration results for the stereo camera system.

Parameter	Camera 1	Camera 2	3D pose parameters (Translation and Rotation)	
Focus (m)	0.025	0.025	T _X (m)	0.22
Kappa (m ⁻²)	74.51	94.82	T _Y (m)	0.00
S _x (m)	3.45	3.45	T _Z (m)	0.04
S _y (m)	3.45	3.45		
C _x (Pixels)	1245.63	1268.0	R _X (degree)	359.83
C _y (Pixels)	1029.50	1020.35	R _Y (degree)	343.74
ImageWidth	2456	2456	R _Z (degree)	359.17
ImageHeight	2058	2058		

4.2.4.2 The effect of the Camera Model and the Number of Calibration Images

In order to obtain accurate measurements from the stereo images, the calibration is an important aspect for the system. The documentation of the HALCON (MVTech Software GmbH., 2011c) recommends using at least 10 images for calibrating the stereo camera system. According to the above-mentioned documentation, two well-known distortion models, the division and polynomial models can be used for the area scan cameras. The division model only takes into consideration the radial

distortion while the polynomial model considers only the global distortion. In order to investigate how the number of the calibration images and the camera model affect the accuracy of the system, the stereo camera system was calibrated using different camera models and different numbers of the calibration images. Using the different calibration results, the positions of the calibration marks have been determined based on the algorithms described before. The calibration parameters of the stereo cameras were used to reconstruct the 3D coordinates of the circular target using the corresponding images of the points acquired by the calibrated cameras.

The effect of the two models and the number of the calibration images on the test results are indicated in Figure 4-9. In this figure, the standard errors versus the number of the calibration images were plotted. It can be seen that the HALCON calibration results, based on the camera model and the number of the calibration images, exhibit significant standard error values, meaning that the number of calibration images highly influence the calibration results. It is obvious that the two models give stable measurements when the numbers of the calibration images are higher than two. It can be easily seen that 4 images or more are required to gain accurate measurements of the stereo camera parameters and hence accurate measurement of the calculated points.

Figure 4-10 shows the relationships between the number of the calibration images and the maximum relative displacement between the two circular targets attached to the loading plates of the compression testing machine. In the case of the division model, the calibration parameters provide precise measurement of the maximum relative displacement between the two marks when the number of images is two or more. On the other hand, in the case of the polynomial model, four or more images are required to get the same stability of the results.

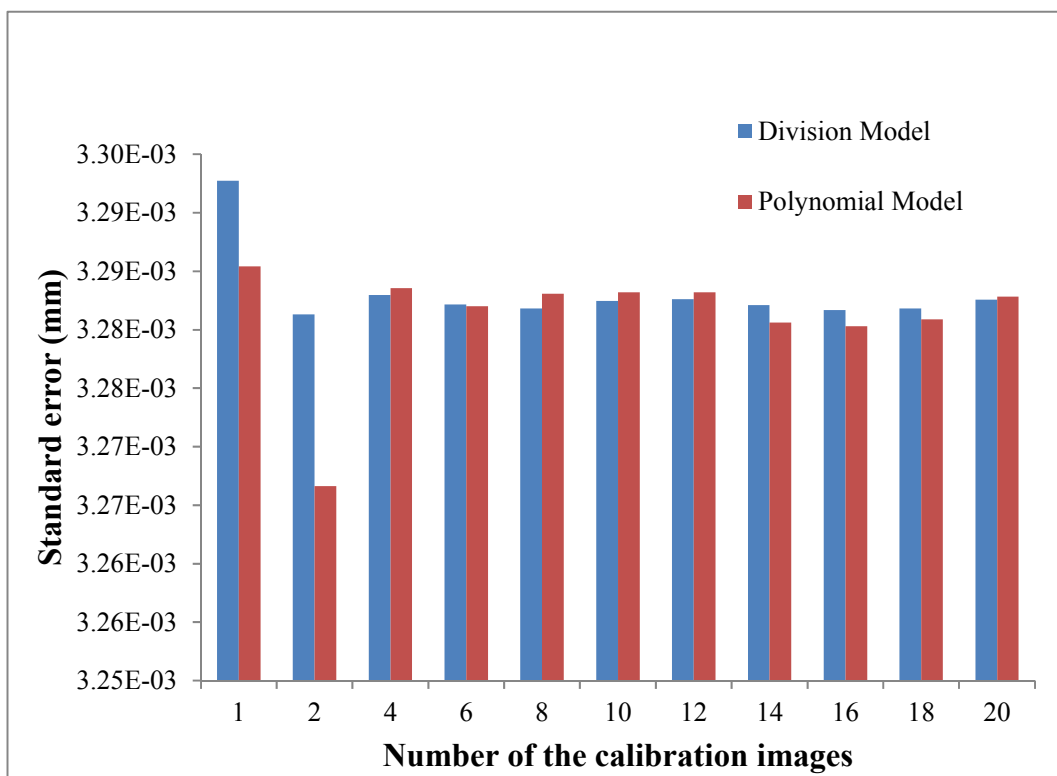
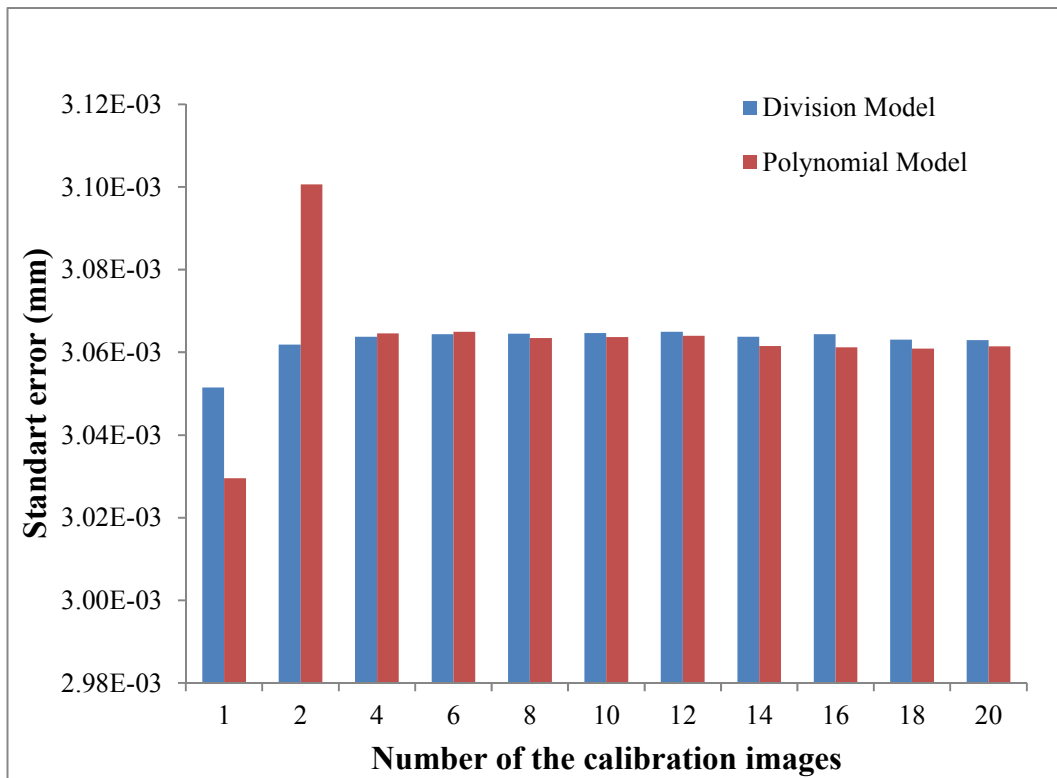


Figure 4-9: The influence of the number of the calibration images on the results of test 1 (top), and test 2 (bottom).

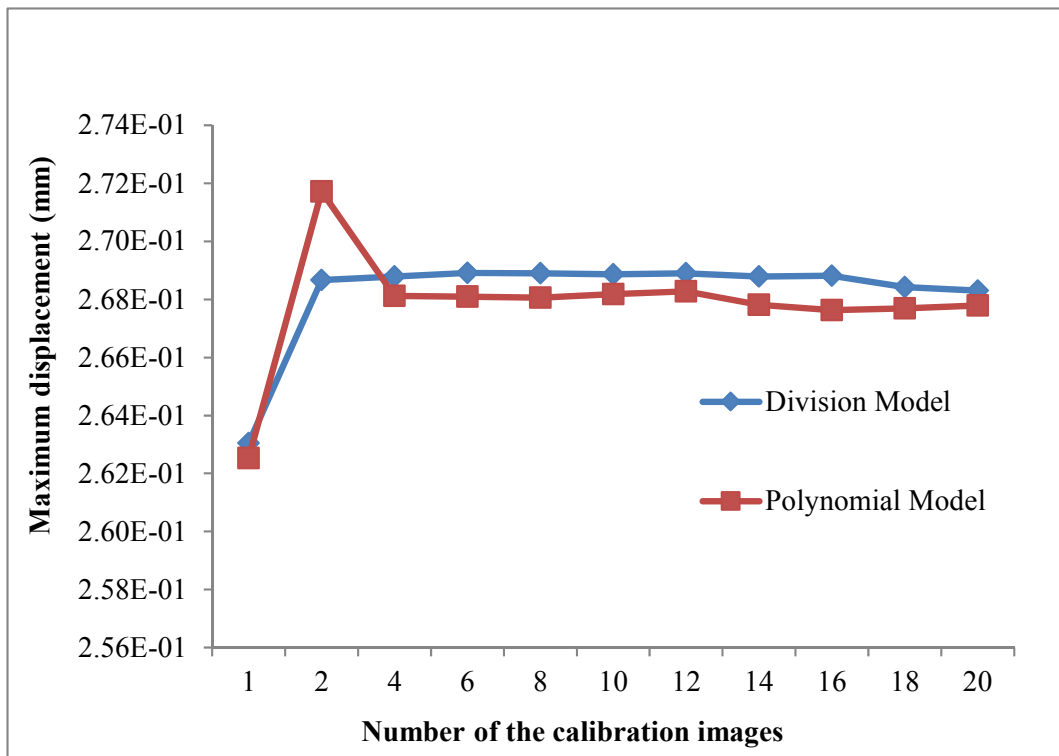
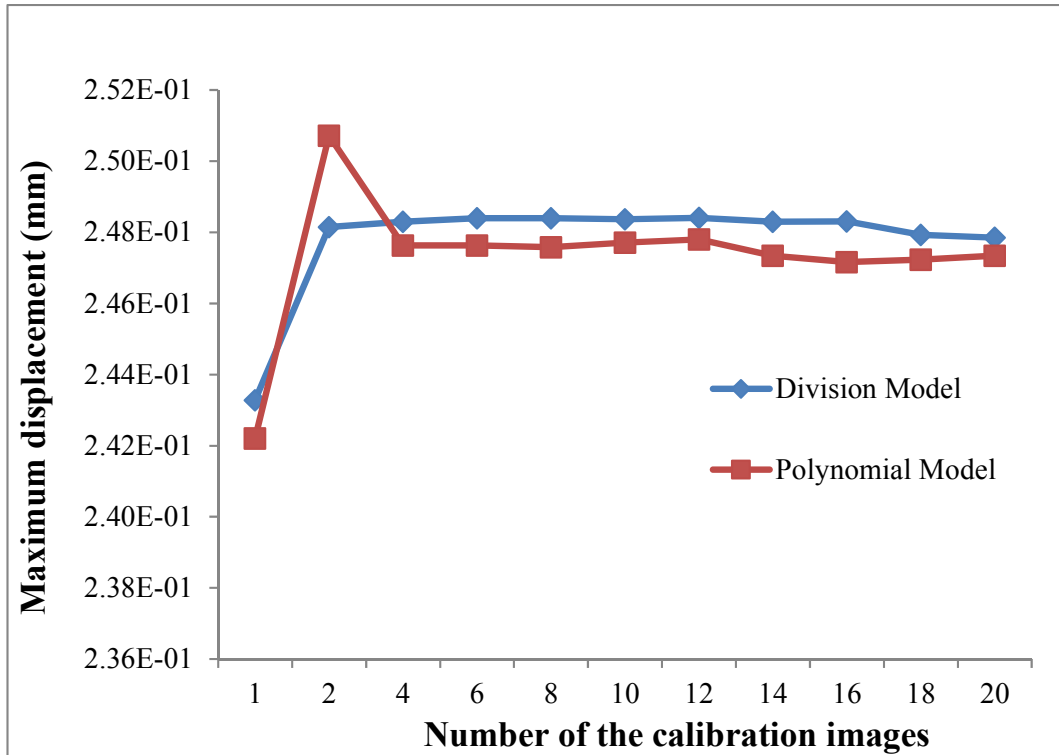


Figure 4-10: The influence of the number of the calibration images in the stability of the results of test 1 (top), and test 2 (bottom).

4.2.4.3 The effect of the Baseline Length

The stereo image pairs of the circular marks were acquired by the calibrated stereo camera system using three different configurations with baseline lengths of 12mm, 19mm, and 25 mm, respectively. Using the calibration results, the 3D coordinates of the 49 targets for each setup of the stereo cameras were calculated using the algorithm previously described. The screen shot of the HALCON interface showing the detection of the circular marks in one of the experimental test is shown in Figure 4-11. The centroids of three target points of the calibration plate were selected to define this coordinate system. Figure 4-12 shows the defined coordinate system which was used for the analysis of the test results. The central target point of the plate was set to be the origin (0, 0). The z-axis of the coordinate system is pointing into the plate, the positive x-axis is pointing to the right, and the positive y-axis is pointing upwards.

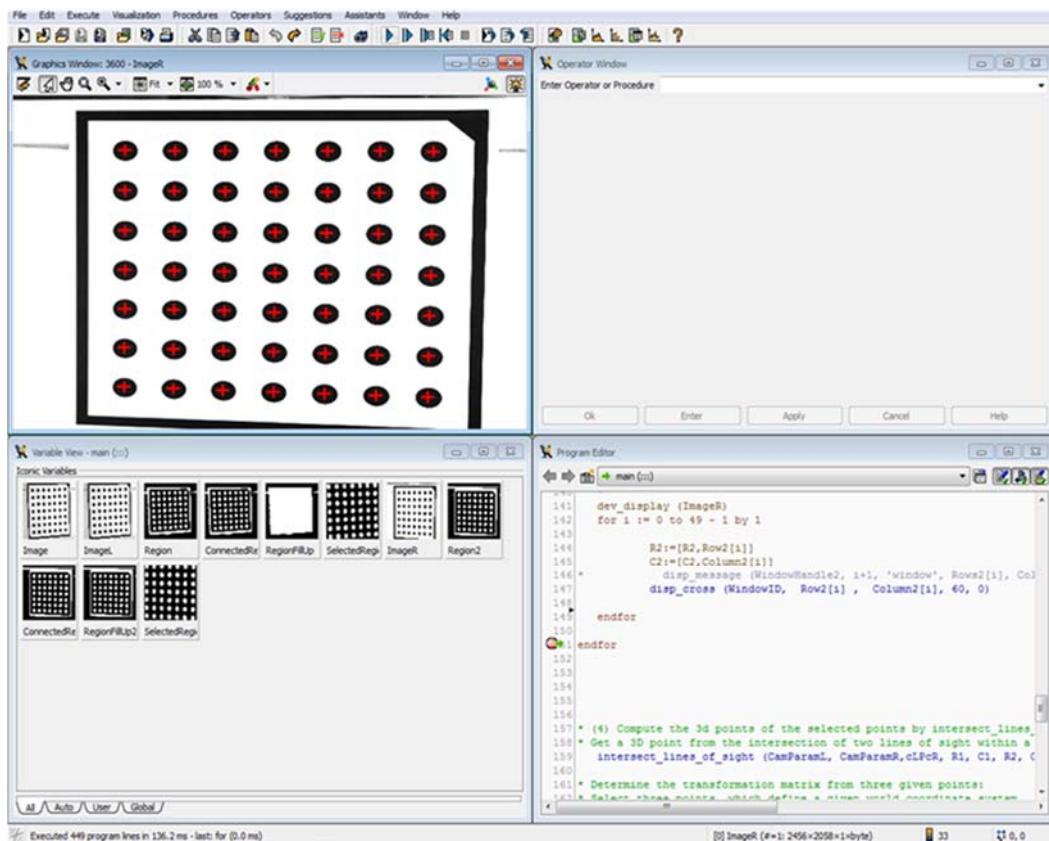


Figure 4-11: Snapshot of the HALCON interface showing the detection of the circular marks.

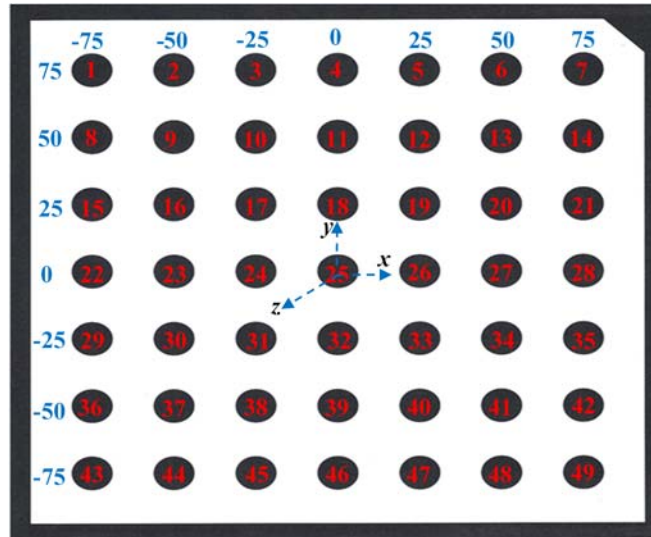


Figure 4-12: The calibration target with the defined coordinate system.

As an example, Table 4-2 listed the 3D coordinates of the targets calculated using the camera setup with a 12mm distance between the two cameras. The exact coordinates of the monitored targets are also included in this table. For comparative purposes, the minimum, maximum, average, and standard deviation of the difference between the measured and the exact coordinates of the targets are reported in Table 4-3. By comparing the results presented in the table, it can be seen that the accuracy of the third configuration, in which the distance between the optical centres of the stereo cameras were 25mm, is higher than the other two configurations. This means that the smaller baseline length has the largest errors. The reduction in the errors when the baseline length was longer can be attributed the fact that the disparity will be bigger and the influence of the matching error is less. Increasing the distance between the cameras reduces the distortion of the captured images. Although the wider baseline length generates a lower error, the valid range of working distance (along the z direction) may become shorter when the baseline is large. Therefore, with wider focal distance the geometric distortion between the left and right views increases which results in a shorter working range (overlapping of depth of fields).

Table 4-2: The measured 3D coordinates of the targets using 12mm baseline.

Point No.	Measured (mm)			Exact (mm)		
	X	Y	Z	X	Y	Z
1	-75.12	76.10	2.17	-75	75	0
2	-49.89	75.93	1.82	-50	75	0
3	-24.70	75.78	1.14	-25	75	0
4	0.38	75.64	0.47	0	75	0
5	25.46	75.53	-0.11	25	75	0
6	50.45	75.40	-0.62	50	75	0
7	75.39	75.31	-0.83	75	75	0
8	-75.38	50.81	1.54	-75	50	0
9	-50.15	50.69	1.17	-50	50	0
10	-24.83	50.59	0.74	-25	50	0
11	0.23	50.47	0.22	0	50	0
12	25.32	50.38	-0.17	25	50	0
13	50.35	50.30	-0.41	50	50	0
14	75.29	50.20	-0.68	75	50	0
15	-75.54	25.38	1.16	-75	25	0
16	-50.32	25.32	0.77	-50	25	0
17	-25.00	25.26	0.45	-25	25	0
18	0.08	25.19	0.00	0	25	0
19	25.24	25.09	-0.32	25	25	0
20	50.24	25.05	-0.66	50	25	0
21	75.22	25.02	-0.50	75	25	0
22	-75.76	0.08	0.80	-75	0	0
23	-50.48	0.06	0.75	-50	0	0
24	-25.15	0.06	0.49	-25	0	0
25	0.00	0.00	0.00	0	0	0
26	25.00	0.00	0.00	25	0	0
27	49.94	0.02	0.04	50	0	0
28	74.85	0.02	0.11	75	-25	0
29	-74.99	-25.06	0.51	-75	-25	0
30	-50.05	-25.10	0.29	-50	-25	0
31	-25.05	-25.11	0.13	-25	-25	0
32	-0.03	-25.12	0.06	0	-25	0
33	24.96	-25.11	0.04	25	-25	0
34	49.90	-25.08	0.09	50	-25	0
35	74.82	-25.06	0.15	75	-25	0
36	-75.01	-50.17	0.60	-75	-50	0
37	-50.07	-50.21	0.38	-50	-50	0

Point No.	Measured (mm)			Exact (mm)		
	X	Y	Z	X	Y	Z
38	-25.07	-50.22	0.23	-25	-50	0
39	-0.07	-50.23	0.16	0	-50	0
40	24.93	-50.21	0.14	25	-50	0
41	49.86	-50.17	0.18	50	-50	0
42	74.77	-50.14	0.24	75	-50	0
43	-75.01	-75.23	0.74	-75	-75	0
44	-50.08	-75.27	0.53	-50	-75	0
45	-25.09	-75.28	0.39	-25	-75	0
46	-0.10	-75.29	0.31	0	-75	0
47	24.89	-75.26	0.29	25	-75	0
48	49.82	-75.20	0.32	50	-75	0
49	74.73	-75.15	0.36	75	-75	0

Table 4-3: Example of the measured 3D of the targets using 12mm baseline

Point No.	Baseline (12 mm)			Baseline (19 mm)			Baseline (25 mm)		
	X	Y	Z	X	Y	Z	X	Y	Z
Minimum	0.00	0.00	0.00	0.00	0.00	0.00	0.00	0.00	0.00
Maximum	0.76	0.66	2.17	0.41	0.49	1.33	0.32	0.22	1.05
Average	0.19	0.16	0.50	0.09	0.14	0.57	0.10	0.07	0.37
Stdev	0.17	0.14	0.47	0.09	0.12	0.39	0.08	0.06	0.28

The relative marks positions have been compared to the theoretical position in order to show the evolution of the difference between the results. Figure 4-13 displays the maximum difference between the real and estimated measurements in the x, y, and z direction calculated for the three baseline distances. Along the z direction, there is an evolution higher than two millimetres between the different camera configurations while along the x and y direction, there is a difference higher than 0.5 mm.

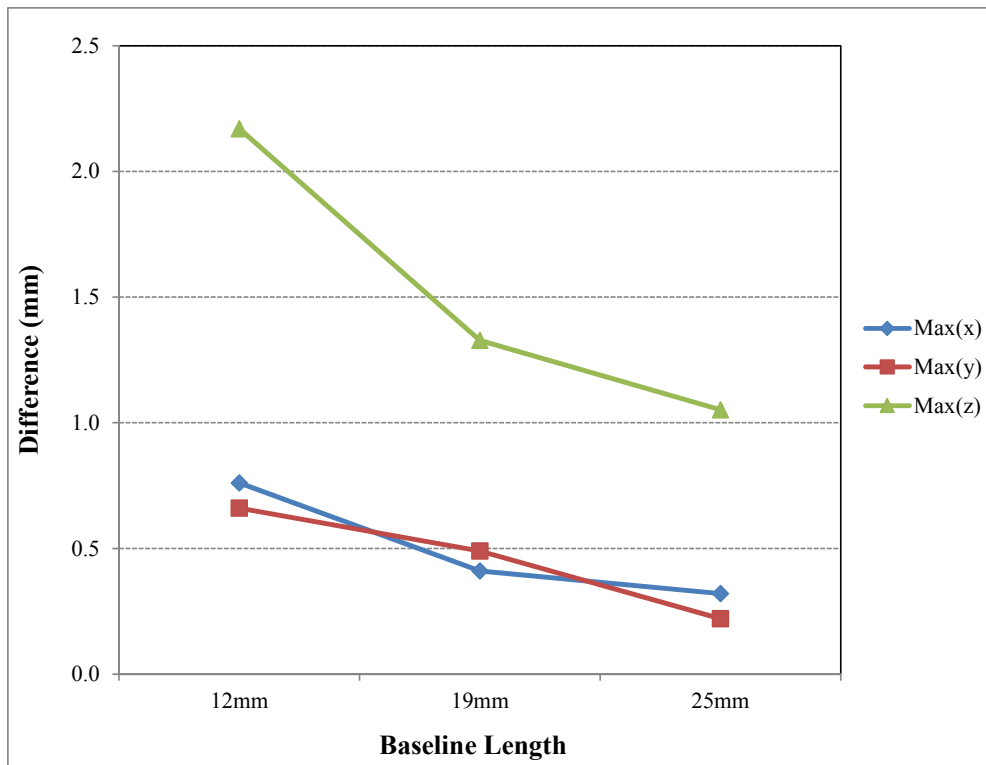


Figure 4-13: The maximum differences between the exact and measured 3D coordinates of the targets.

4.3 Experimental Validation of the Stereo Camera System

The proposed photogrammetric approach needs to be validated before being used for any displacement, deformation or rotation measurements. Therefore, an experimental study was proposed to evaluate the accuracy of the stereo camera system and validate it by comparing the vertical displacements of the targets monitored by the stereo cameras with those measured by another two different devices.

4.3.1 Materials and Methods

4.3.1.1 Materials and Testing Equipment

The targets used in this study were two circular marks which were printed on a high quality paper. As shown in Figure 4-14, this target was printed on a high quality paper with a white background so that it can be easily distinguished during the image processing. A Zwick/Roell Z050 (Zwick GmbH & Co, Germany) universal testing machine with a maximum load capacity of 50 kN was only used to move the loading plate of the machine vertically so that the movement of the target attached to this plate can be tracked by the stereo camera and the relative displacements between the two targets can be calculated.

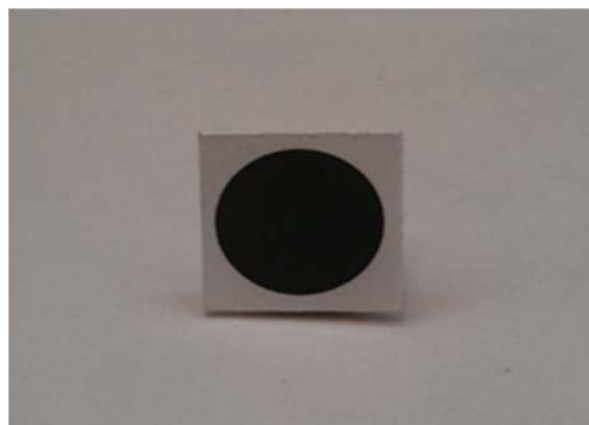


Figure 4-14: The image of the target monitored by the stereo cameras.

4.3.1.2 Displacement measurement sensors

In the validation tests, the displacements of the loading plate of the Zwick machine were measured by three means:

1. Linear variable differential transformer (LVDT)

LVDT is an accurate and reliable method for measuring the deformation in applications where linear displacement measurements are required. LVDTs are available in wide varieties of measurement range, generally ranging from 100 microns to 25cm. The LVDT selected was D5-200AGRA type, manufactured by R.D.P. Design Electronics Ltd. (I RDP. Electronics Ltd), with a linear measurement range of ± 2.54 mm and an accuracy of 1 microns. It consists of a transformer and a movable magnetic core. An image of this sensor is shown in Figure 4-15.



Figure 4-15: Image of the LVDT transducer.

2. *Digital micrometre*

A digital micrometre (MDC-75M; Mitutoyo, Kawasaki, Japan, 0.001 mm) was also used in this study as a displacement measurement device. An image of this device is given in Figure 4-16.



Figure 4-16: The image of the digital micrometre.

3. *The Stereo Camera System*

The same stereo camera system employed in the previous study was also used in this study. The camera system is composed of two Basler Pilot piA2400-17gm cameras, equipped with a fixed focus of 25mm, a frame mounted on a tripod, pan-tilt units with remote control for adjusting the cameras, and a desktop PC. Two LED light illuminations were also employed to provide a homogenous illumination of the used targets. An image of the stereo cameras is shown in Figure 4-17.



Figure 4-17: The Basler stereo cameras.

4.3.2 Experimental Setup and Procedure

The experiment set-up, shown in Figure 4-18, was used in this study to evaluate the accuracy of the optical measurement system. In this set-up, two photogrammetric targets consisting of black circular marks printed on a white background were glued to the loading plates of the Zwick testing machine. One of these targets was glued to the moving plate and the second one was glued to the fixed plate. The stereo cameras were placed in front of the targets and connected, through Ethernet cables, to a PC where the image processing software is installed. To measure the relative displacements between the loading plates, three different methods were employed: a digital micrometre, a Linear Vertical Displacement Transducer (LVDT) and the photogrammetric approach based on a two-camera setup. The digital micrometre and the transducer were inserted between the two plates to measure the relative vertical displacements between them. A magnetic base was used to hold these sensors at one end and the other end of the sensors was in contact with the fixed

plate. At the beginning of the experiment and before moving the loading plate, the zero-displacement case of the circular targets was captured by the two cameras to allow comparison with the subsequent data. The crosshead displacement control is then moved down by an appropriate magnitude and the implemented software was used to automate recording the field of target images with a time interval of about 1 second. The images are stored in an allocated file on the computer hard disk for processing on later occasions.

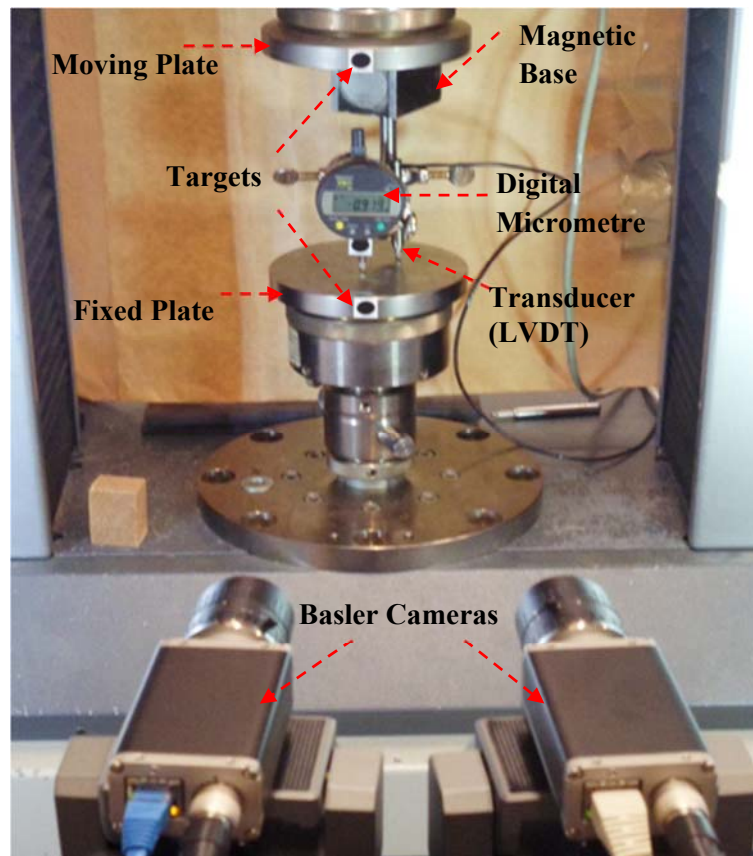


Figure 4-18: The photogrammetric set-up and instruments used during the accuracy evaluation test.

In order to perform the accuracy evaluation tests, the system of the two Basler cameras was calibrated based on the calibration procedure of HALCON described before. The implemented graphical user interface (GUI) for the binocular stereo system showing the extracted circular marks during the calibration process is shown in Figure 4-19. The calibration parameters are determined to be used in the calculation of the 3D position of any point of interest from its stereo projections by triangulation. The outputs of the calibration were saved to the desktop computer, PC2.

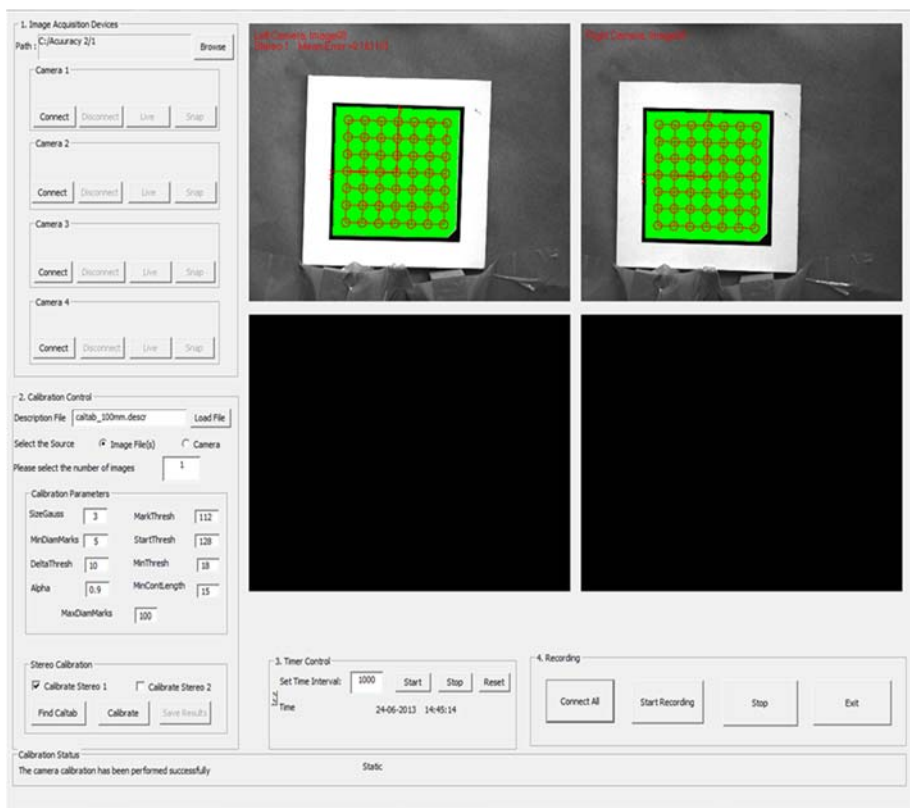


Figure 4-19: Screen shot of the implemented GUI showing the stereo camera calibration process.

4.3.3 Calculation Methods

The image processing algorithms written in HALCON were employed to process all the recorded stereo images and determine the 3D coordinates of the targets. The 3D coordinates of each target point of interest are derived by intersecting the line of sight of the respective conjugate image points determined by a matching process. Using the image coordinates of the conjugate points and the camera parameters, the x, y, and z coordinates of the selected targets can be calculated by the operator '*intersect_line_of_sight*'. This operator can handle reconstructing the 3D coordinates without rectifying images. The distance between the two targets was then calculated using the following Equation:

$$\text{Distance} = \sqrt{(X_1 - X_2)^2 + (Y_1 - Y_2)^2 + (Z_1 - Z_2)^2} \quad (4.1)$$

The relative displacements between the targets can then be calculated from the difference between the distances calculated at each time step.

The following Equation was used to calculate the percent errors of the displacement measurements.

$$\text{Percent error} = \left(\frac{P_{data} - D_{data}}{D_{data}} \times 100 \right) \quad (4.2)$$

where

P_{data} is the displacement measured by the photogrammetric system, and

D_{data} is the displacement measured by the traditional device.

4.3.4 Validation of Test Results

In this study, the effectiveness of the proposed photogrammetric approach in measuring the relative displacements of the targets was taken into consideration. The relative vertical displacements of the compression loading plates were measured by the three different measuring systems, the LVDT, the digital micrometer, and the photogrammetric approach. The measurement data provided by LVDT instrumentation were saved with the corresponding time to the desktop computer. The stereo images of the circular targets were acquired by the stereo cameras and the relative displacements of the targets were calculated based on the image processing procedure described before. The readings of the digital micrometer were taken from the stereo images captured during the experiments. The vertical displacements obtained using photogrammetry measurements were compared with those measured by the two traditional devices, the LVDT reading and the digital micrometre. These comparisons are shown in Figure 4-20. It can be seen that the photogrammetric results describe very well the measured vertical displacement using the other two methods.

The maximum errors between the vertical relative displacements measured by the photogrammetric technique and the displacements measured from the digital micrometre are found to be about 0.01 mm. It was also found that maximum errors between the vertical relative displacements measured by the photogrammetric technique and the relative displacements measured from the LVDT sensor are found to be about 0.02 mm. These results are also confirmed from Figure 4-21 which shows the correlation between all the three measurement techniques. Figure 4-21a) shows the vertical displacements determined by the digital micrometre plotted against those determined by the photogrammetric approach. Figure 4-21b) shows the vertical displacements determined by the LVDT plotted against those determined by the photogrammetric approach. These figures indicate a high correlation between all techniques with R-square value of 0.99.

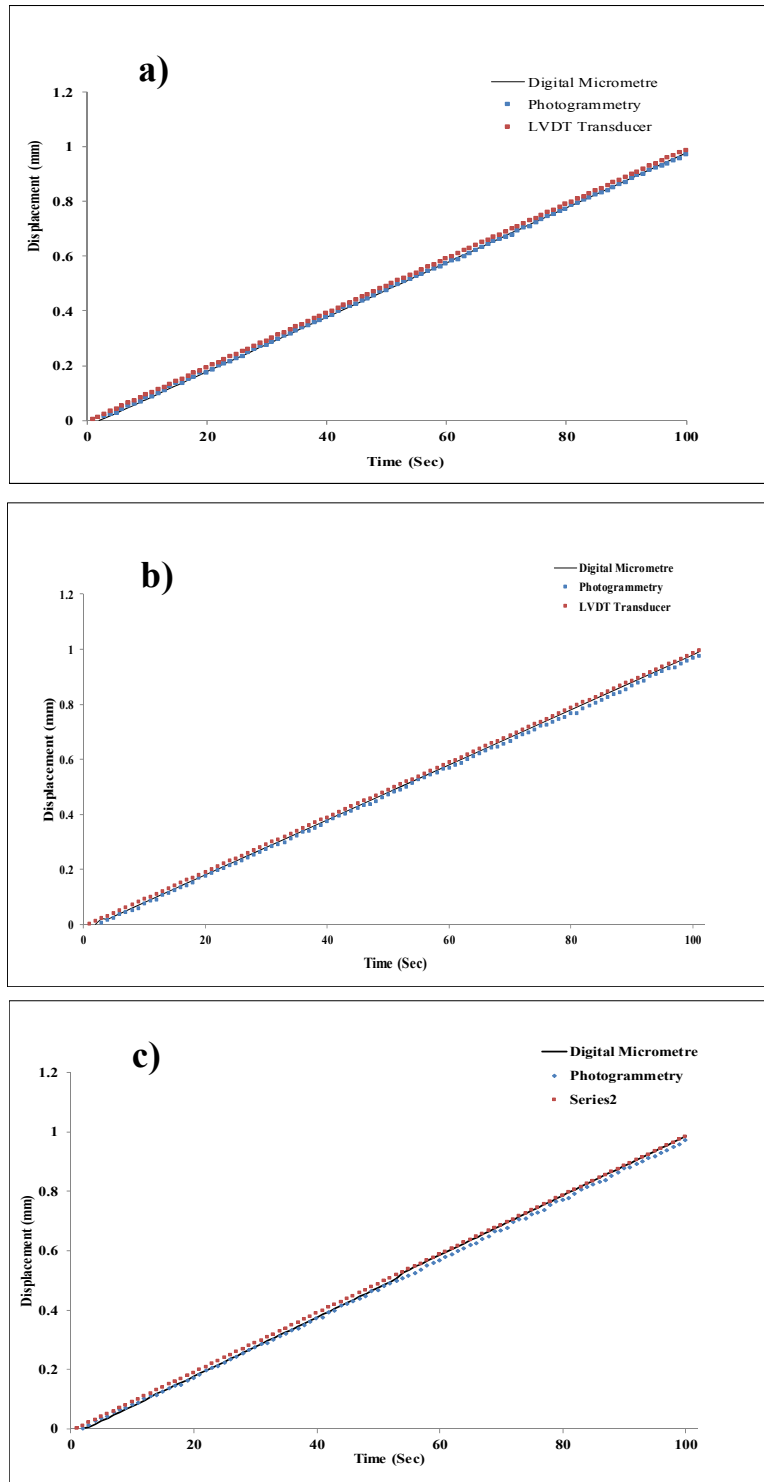
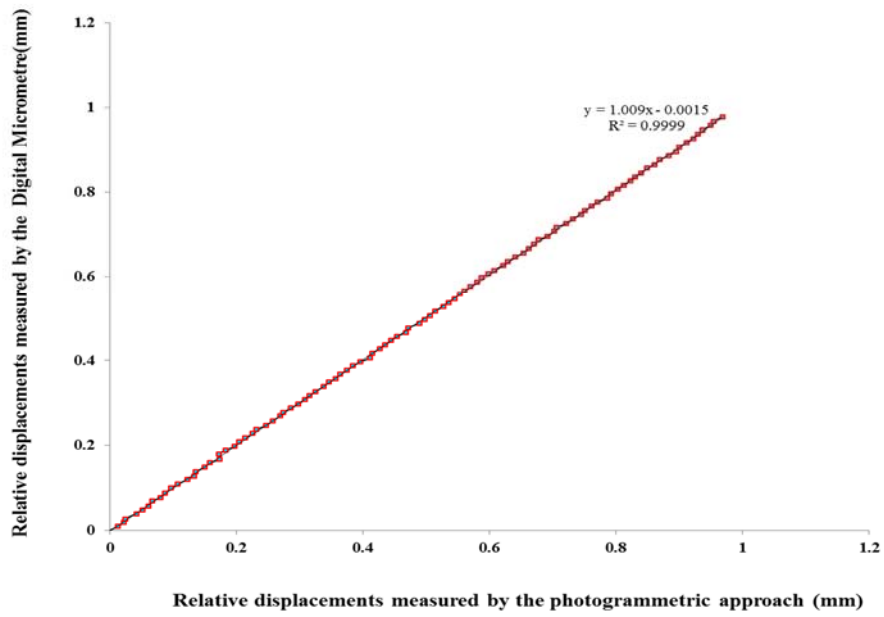
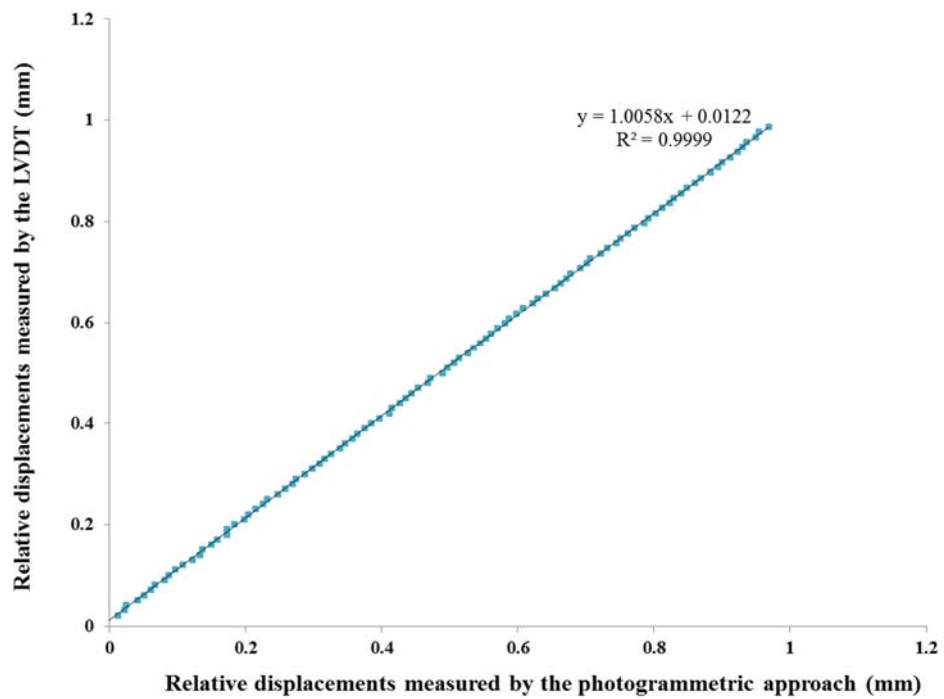


Figure 4-20: Comparison of the relative displacement results measured by the three sensors (a) Test 1, (b) Test 2 and (c) Test 3.



a)



b)

Figure 4-21: The correlation between the vertical displacements measured by a) the photogrammetric approach and the digital micrometre, b) the photogrammetric approach and the LVDT sensor.

Table 4-4 lists the minimum, maximum, average, and standard deviation of the percent error results of the vertical relative displacements calculated for the three experimental tests. For each test, two comparisons were performed for the three measuring techniques. The first comparison was made between the photogrammetric approach (indicated as Ph) and the digital micrometer (indicated as Dm) and the second comparison was made between the photogrammetric approach and the transducer (indicated as LVDT). From the table, it can be seen that the largest differences in the percentage error between the photogrammetric system and the digital micrometer calculated from the first test, second, and third test data are 3.11, 3.37, and 3.76%. A similar trend was found in the percentage error differences between the photogrammetric system and the LVDT and the percentage error calculated from the first test, second, and third test data are 3.59, 3.77, and 3.51%. The test results show that the measurements obtained by photogrammetric system are in good agreement with both readings of the digital micrometer and the LVDT. The small values of the standard deviations shown in the table validate the accuracy of the optical system. The similar results indicate high stability of the camera system.

Table 4-4: The statistical analysis of the photogrammetric approach and the traditional devices.

Test No.	1		2		3	
Measuring Techniques	Ph/Dm	Ph/LVDT	Ph/Dm	Ph/LVDT	Ph/Dm	Ph/LVDT
Min. (%)	0.00	0.01	0.57	0.01	0.03	0.02
Max. (%)	3.11	3.59	3.37	3.77	3.76	3.51
Average (%)	0.73	1.06	1.76	0.59	1.62	0.78
Std	0.54	0.85	0.61	0.65	0.82	0.66

4.4 Experimental Investigation of Different Target Techniques

The efficiency of the photogrammetric approach can be affected by the target type used to be monitored by the camera system during testing. Therefore, it is necessary to investigate and compare different target techniques which can be applied to the surface of the glulam timber specimens. In this study, three different target techniques were applied to the surface of the specimens which were investigated under compressive loadings. The first target is the painted mark which was painted on the sample surface. The second target is the glued mark which was printed on a piece of paper and then glued to the sample surface. The last target is the pinned mark which was a printed mark attached to a pin that was pinned to the sample surface as shown in Figure 4-22. All of these marks represent black circular targets on a white background to be easily distinguished during the stereo matching and processing of the images. Unlike the pinned mark, the other two marks require preparing the sample to ensure that the wood surface is flat and free of grease. Because of the difficulty to apply the paint on the wood surface, the edge of the painted mark is not quite clear. The edge of the glued marks, however, shows a good quality.

In order to evaluate the efficiency of the proposed targets for measuring the displacements at specific points, experimental compression tests were carried out on the test specimens. The relative displacements between two points were obtained by the LVDT to evaluate the efficiency of the proposed targets for measuring the displacements between two points on the surface of the samples. This was achieved by comparing the measurement results obtained by the LVDT with those obtained by the three different techniques using the binocular stereo camera system. The different type of target setup was evaluated and checked if they deform in the same manner as the wood during the compression tests. In addition, the target displacements were checked to see if they are the same for all the tests.

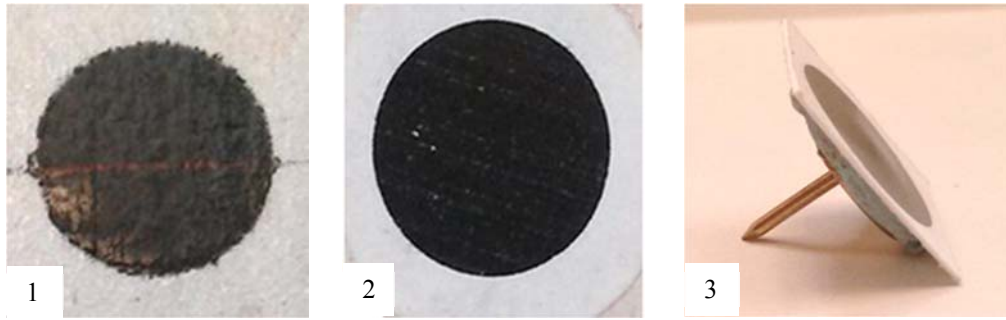


Figure 4-22: Different type of targets used in the tests

- 1) the painted mark.
- 2) the glued mark.
- 3) the pinned mark.

4.4.1 Materials and Testing Equipment

The material used in this study are glulam timber beams which were cut into cubic glulam blocks to provide samples to be used in the present study. A sample of a glulam specimen with its dimensions are shown in Figure 4-23. A Zwick/Roell Z050 (Zwick GmbH & Co, Germany) universal testing machine with maximum load capacity of 50 kN was used to test the specimens. This machine was equipped with a load cell connected, via a data acquisition system, to a desktop computer (PC1) that has its own software to be used for controlling and monitoring the experiments and collecting the data (time, load, deformations).

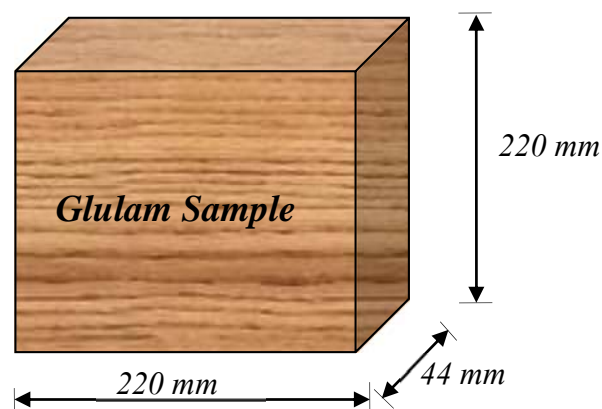
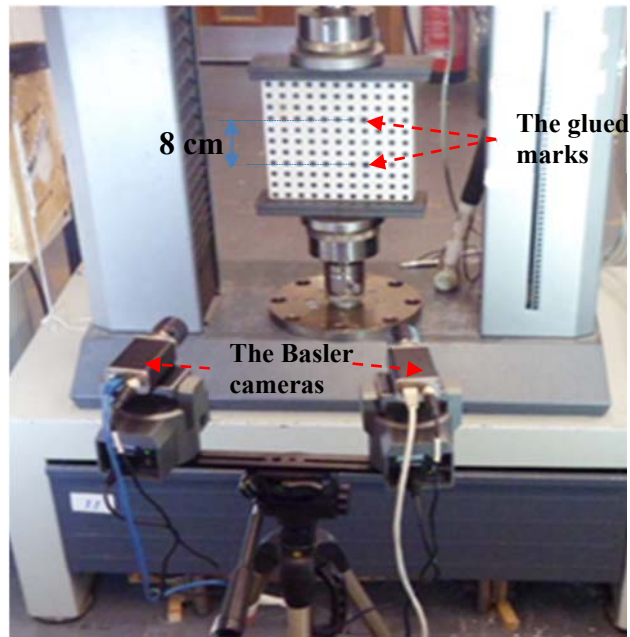


Figure 4-23: A Schematic diagram of the test specimen with its dimensions.

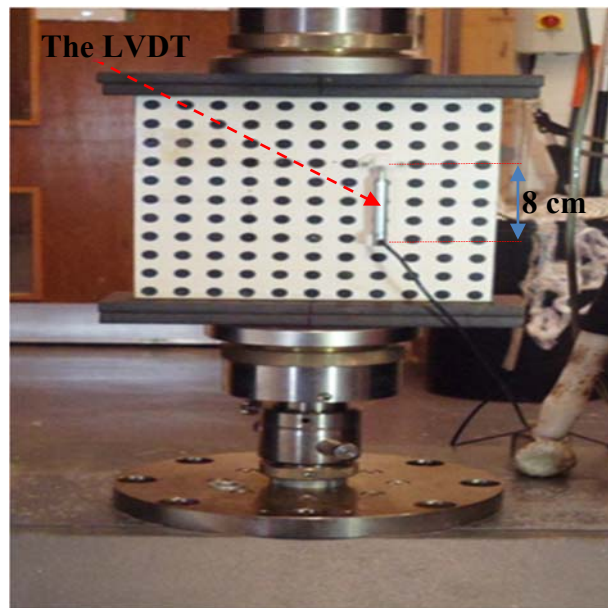
4.4.2 Experimental Setup and Procedure

Figure 4-24a) shows the first experimental setup which was used in this study for evaluating the efficiency of the proposed target techniques. In this setup, The stereo cameras were set-up on a stable tripod and calibrated according to the calibration procedure of HALCON. The glulam timber sample was placed in the Zwick testing machine in front of the optical system. The glued marks were applied to the surface of the sample and placed to monitor the position between two points over the gauge length (8cm). For comparative purposes and after calibrating the stereo camera system, the timber sample was tested three times in the perpendicular to the grain direction for each different target setups (the painted mark, the glued mark, and the pinned marks). Figure 4-25 shows the different set-ups of the targets and the LVDT on the glulam specimen. The pinned targets were applied deeply and less deeply to the surface of the specimen. The compression tests were conducted in displacement control, with a 0.02 mm/second cross-head displacement rate of the testing machine. A maximum force of 7kN and a pre-load of 1kN were used during all tests. After pre-loading the sample, an initial pair of stereo images was captured by the two cameras before applying loads to the timber sample to allow comparison with the subsequent data. During the load application, the implemented software was used to automate recording stereo images of the surface of the sample with a time interval of about 1 second. At the end of loading the sample, the machine was set to let the crosshead displacement control stay in the same position to allow capturing the final state of the sample.

The setup of the last experimental test is shown in Figure 4-25b). In this setup, the same glulam specimen was inserted into the Zwick machine and the LVDT sensor was mounted directly on the surface of the specimen to monitor the displacements over the gauge length (8cm) on the sample during the compressive loading. The LVDT was placed in the same position where the photogrammetric targets were placed in order to compare the displacements occurring in that position and measured by the LVDT with those obtained from processing the stereo images. During the load application, the load and relative deformation measured from the LVDT were recorded through the data acquisition system.



a)



b)

Figure 4-24: Examples of different experimental setups a) the photogrammetric system monitoring the targets glued to the specimen, and b) the LVDT transducer monitoring the relative displacements over the gauge length.

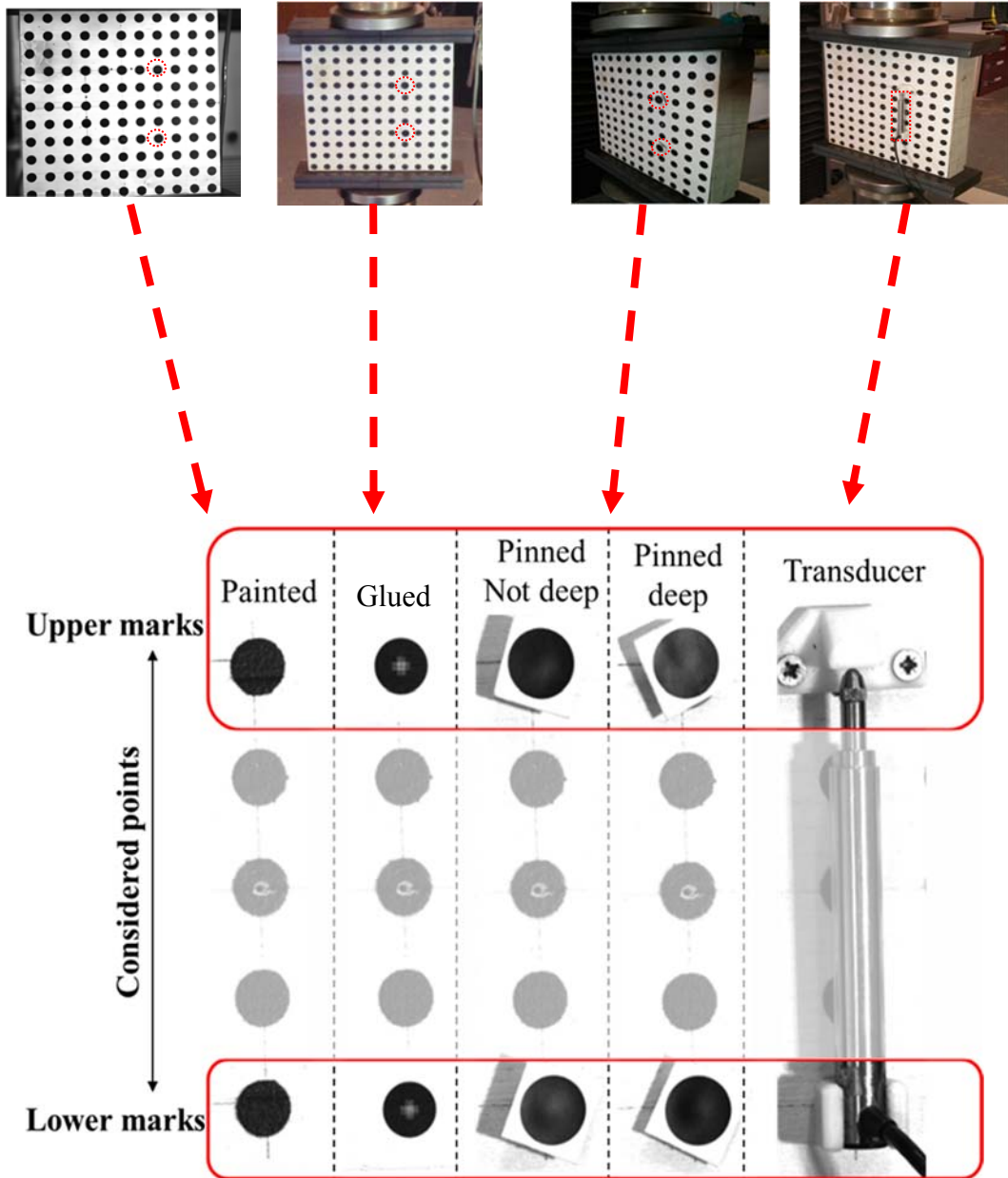


Figure 4-25: The setup and location of the photogrammetric marks and the LVDT on the surface of the glulam specimen.

4.4.3 Results and Discussions

With the reliability of the results confirmed through the validation experiments, the proposed photogrammetric method was applied to investigate and compare the performance of different target techniques which can be applied to the surface of the glulam timber specimens to measure the displacements at specific locations. Figure 4-26 shows the displacement measurements for each type of marking as well as for a transducer. The first part of the curves (from 0 to 25s) shows an unstable measurement of the displacements according to the different marking techniques and these measurements are fluctuating more than the second part in which the curves are steadier. According to the test results of the different marking type, the tendency of the first trial is always different to the next trials.

Comparing the results of the relative displacements computed using both the painted and glued marks indicates that the diagrams of these types of marks are almost the same with a maximum displacement of about 0.23mm. The maximum displacement of the transducer was 0.33mm which was close to that measured by the deep pinned mark. This result could be because these targets were installed directly to the surface of the laminated timber specimen. When compared to the results of the LVDT transducer, the maximum error in relative displacements computed using the deep pinned, pinned, painted and glued marks were 9%, 21%, 30% and 30% respectively. Figure 4-27 shows the average of the standard error with respect to the different marking techniques and the LVDT. The painted marks and the glued marks have a similar value with $3.31\text{E-}3$ mm and $3.35\text{E-}3$ mm, respectively. The deep and less deep pinned marks have a value of $2.54\text{E-}3$ mm and $2.3\text{E-}3$ mm, respectively. These values are close to that of the LVDT transducer which has a standard error value of $3.83\text{E-}4$ mm. These results clearly indicate that the deep pinned marks have the same trend of the LVDT transducer. This is mainly due to the setup of these marks since they were installed in a contact with the surface of the glulam test specimen.

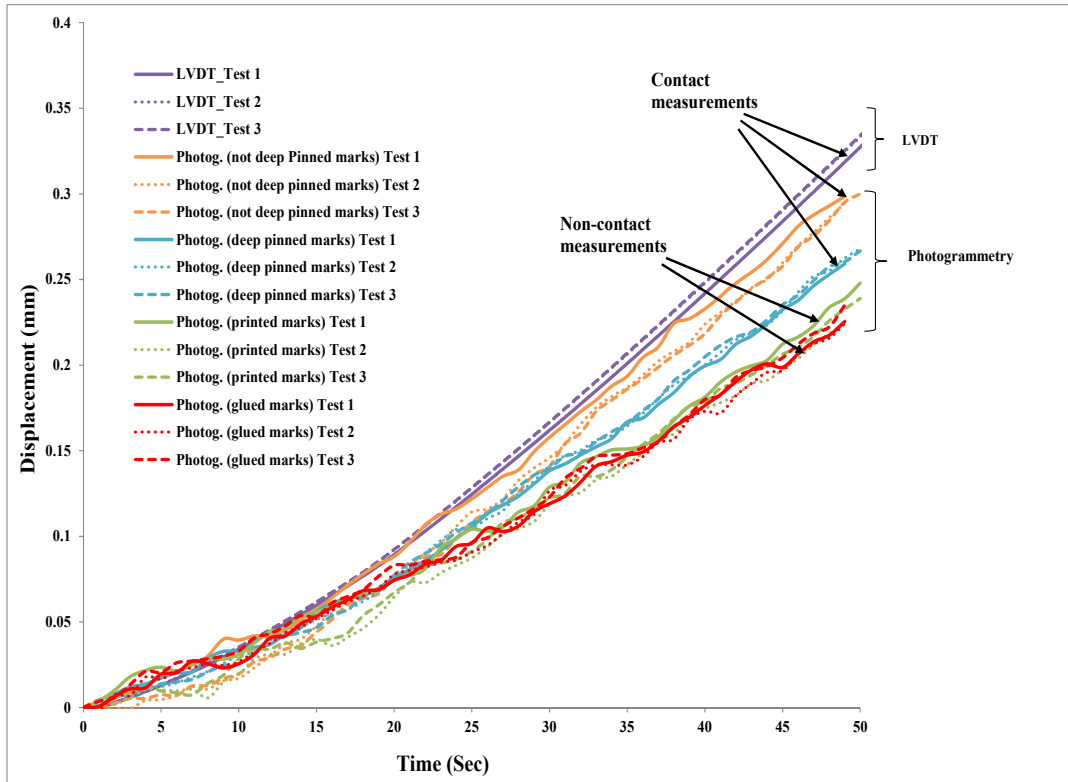


Figure 4-26: Displacement measurements according to the marking type and the used LVDT.

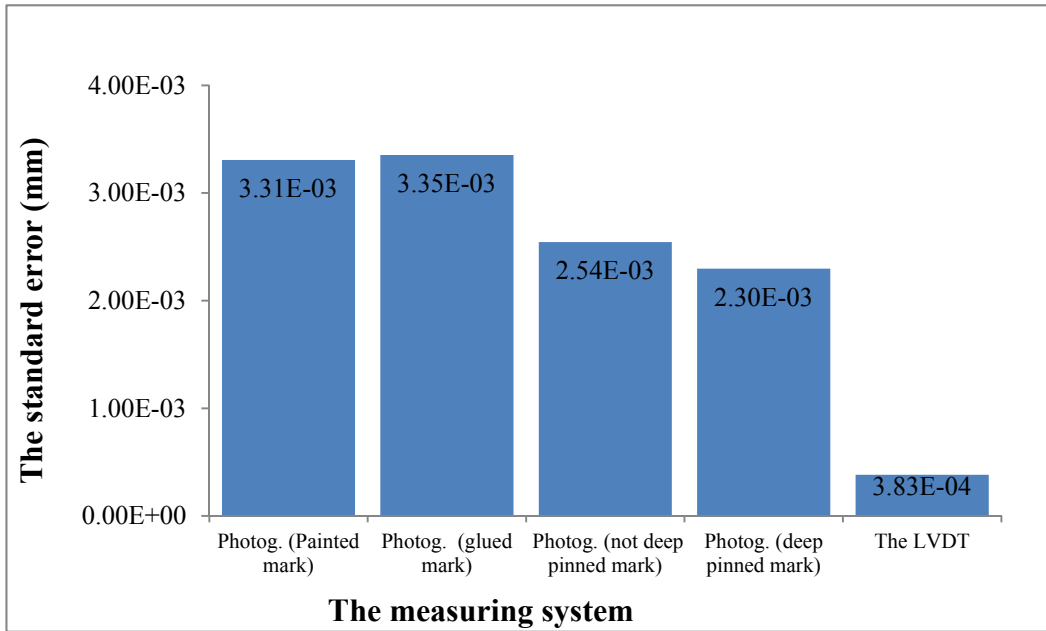


Figure 4-27: Standard error according to marking type.

4.5 Summary

In this study, the non-contact binocular stereo system developed in this project was improved by investigating several parameters of the stereo camera system such as the camera model, the number of calibration images, and the baseline length. Experimental studies were carried out and the optical system was validated by comparing displacement values measured by the photogrammetric approach with those obtained from different traditional devices. The good agreement of the test results between the photogrammetric approach and the other two methods reveals that the proposed optical approach is very efficient to determine the deformation of the photogrammetric targets tracked by the stereo camera system.

Finally, different targeting techniques were proposed and applied to the surface of the tested timber samples as photogrammetric targets for the stereo camera system. These techniques were evaluated and compared experimentally during the compression tests. The painted and glued targets which were installed directly to the surface of the laminated timber specimen had approximately the same displacement measurements. On the other hand, the relative displacements determined by both the pinned marks were very close to those measured by the LVDT transducer. This may be attributed to the similar setup of these techniques since they were installed in contact with the surface of the glulam test specimen. The significant difference between the displacement measurements of the contact and non-contact measuring techniques require developing a technique which can assist in finding a proper way to evaluate the performance of these sensors.

5. EVALUATION OF TORSIONAL BEHAVIOUR AND SHEAR MODULUS OF GLULAM TIMBER BEAMS

5.1 Introduction

The shear modulus, G , is a fundamental mechanical property of wood that is used in the design of timber and engineered wood products. The timber material has relatively low shear stiffness. The shear modulus is critical when designing for lateral-torsional stability of joists (EN 1995-1-1, 2004). G is also significant in designing serviceability of wood-joist floors (Foschi, 1982), and is an important input for setting up analytical and finite element models (Chui, 2002).

According to European Committee for Standardization 'CEN' (EN 408:2003, 2003) and American Standard of Testing Materials 'ASTM' (ASTM-D198-94, 1996), bending tests is the most common approach to evaluate the shear modulus of timber and glulam materials. However, this method has been found difficult to evaluate the shear stiffness of structural-size specimens. The bending test creates a combination flexural and shear stresses leads to difficulties in obtaining the true value of shear stiffness (Vafai, 1973, Riyanto, 1998).

The torsion test is recommended by the most recently updated British Standard, BS EN 408:2010+A1:2012, as a standard test method to characterize properties of structural-size timber-composite materials. One objective of the torsion test is the determination of shear modulus of the material. This test is the only method that imposes a state of pure shear stress on a specimen and it has been proved to have more advantages for measuring the shear modulus value of timber and glulam beams (Hindman et al., 2005). Recently, the torsion test has been adopted by more and more researchers (Gupta et al., 2002, Gupta, 2005, Hindman et al., 2005, Khokhar et al., 2009, Khokhar et al., 2010, Zhang et al., 2011) to evaluate the shear modulus of structural-size timber and glulam beams.

In the torsion test, the exact measurement of the relative angle of twist over a gauge length is essential to determine the shear strain and hence enable the calculation of shear modulus. The rotations measured by the torsion tester machine may include

small slippage between the board and the clamps of the torsion testing machine. Therefore, angle measurement devices are used to measure the rotations of the torsion specimens. Traditionally, the inclinometer is one of the most commonly used instruments for measuring the rotation of the glulam samples during the torsion test. However, the size of the device and the nature of the surface contact measuring have prevented inclinometers to be used in measuring more details of the shear deformation of glulam beams. To overcome this difficulty the photogrammetric approach was proposed in this research to measure the surface rotations of the samples.

This chapter presents the experimental studies performed to investigate the feasibility of the developed photogrammetric system on the torsion test. Two main studies were considered for torsional experiments and two angular measurement instrumentations, inclinometers and stereo camera systems, were used in these studies. The first experimental study was conducted on five timber glulam beams subjected to torsional loading. The main purpose of this study was to validate the developed optical system and then to employ it for proper use of the torsion test. Another objective of this study was to investigate the difference between the rotations of the long and short sides of the cross-section of the torsion specimens. Using photogrammetric method, the displacements along the long side of the cross-section of the specimens were also considered in this study.

In the second experimental study, the developed non-contact photogrammetric approach was enhanced to measure more details of angles of twist of glulam timber beams subjected to torsional loading. Torsion tests was conducted on twelve glulam timber beams according to (EN 408:2010, 2010) procedure of the standard torsion tests. The main purpose of this study was to evaluate the values and the variation of the shear modulus of glulam beams. Another objective of this study was to evaluate torsional behaviour of glulam timber beams and to investigate more details of the angular deformation of the torsion specimens. This may assist in understanding the torsional behaviour of the specimens and give a basis for further studies. The materials, experimental setup, test procedures and results of the first and second studies are described in Sections 5.2 and 5.3, respectively.

5.2 The Applicability of the Photogrammetric Approach on the Torsion Test

The photogrammetric approach was proposed to evaluate torsional behaviour and shear modulus of glulam timber beams. Based on this method, the first experimental study was conducted on glulam timber beams using the torsion test. The main purpose of this study was to validate the developed photogrammetric technique and then to employ it for proper use of the torsion test in order to evaluate the shear modulus and the torsional behaviour of timber glulam beams. The angular measurements of inclinometers and binocular stereo cameras were compared to examine agreement between these two sensors. After validating the proposed method, the photogrammetric method was employed to measure the displacements along the long side of the cross-section. The difference between the rotations of the long and short sides of the cross-section was also considered in this investigation.

5.2.1 Materials and Methods

5.2.1.1 Materials

Glulam timber beams with nominal cross-sectional dimensions of 95×45 mm were used in this study as torsion test specimens. The timber glulam beam are graded to GL24 class strength. Each beam was cut into 2.0m length to produce test specimens for the torsion test method. Figure 5-1 shows an image of these glulam beams.

Before testing and in order to investigate more details of the rotation of their cross-sections, the glulam beams were prepared for stereo camera measurements by painting 5 elliptical target points on the surface of the testing samples and these targets were marked 15 mm centre to centre to give traceable marks on the sample surfaces. Figure 5-2 shows an image of a sample after being prepared with photogrammetric targets. The rectangular cross-section beams were stored in a conditioning room with a constant temperature of about 20 degrees and relative humidity of about 65% to ensure uniform and constant moisture content (MC) of about 12%.



Figure 5-1: Glulam timber specimens for torsion tests.

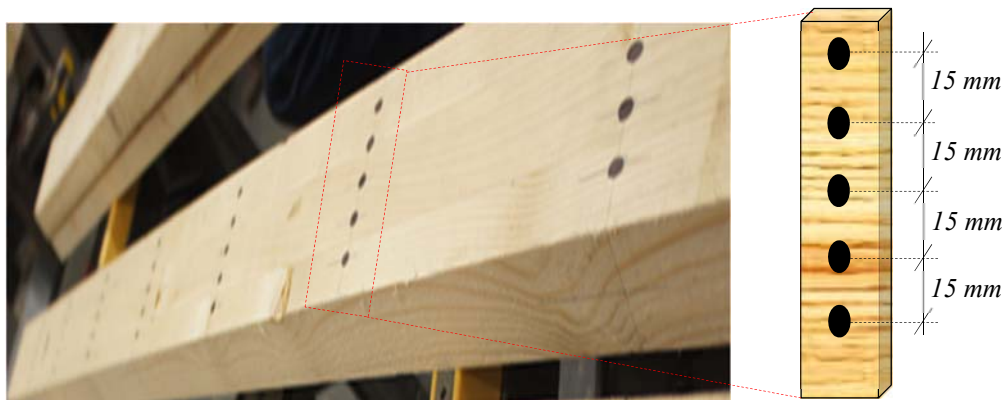


Figure 5-2: Torsion specimens after applying targets to their surfaces (left) and details of the applied targets (right).

5.2.1.2 Torsion Testing Machine and Equipment

A Tinius-Olsen (Tinius Olsen, Pennsylvania USA) torsion testing machine capable of applying up to 1 kilo newton-metre (kN-m) torque was used to test the specimens. Figure 5-3 shows a photograph of the testing machine. The torsional driving machine is a bench based unit designed to perform torsion tests on specimens to find their modulus of rigidity.



Figure 5-3: Torsion testing machine.

The torsional driving machine consists of two units, a driving unit with a rotating loading chuck at one end of the machine and a movable unit with a stationary weighing chuck at the other end. The driving unit is used to apply torque which can be measured using a torque sensor mounted on the movable unit. The movable unit is adjustable and can change its position to accommodate specimens of varying lengths.

The torsional driving machine is a computer controlled torsion testing machine and it is supplied with Test Navigator software which can be used to measure torque and rotation with a measurement accuracy of $\pm 0.5\%$ of the applied torque and $\pm 0.05^\circ$ of the rotation.

➤ *Chucks of the Testing Machine*

The torsional testing equipment of the machine has two chucks, the loading and weighing chucks. The loading chuck is mounted on the drive unit and can rotate the

specimen during testing. The rotation of this chuck during testing can be read from the angular deflection scale taped on the loading chuck. The loading chuck is shown in detail in Figure 5-4. The weighing chuck is mounted on the movable unit and will remain in a stationary position during the testing process. An image of a weighing chuck is shown in Figure 5-5.

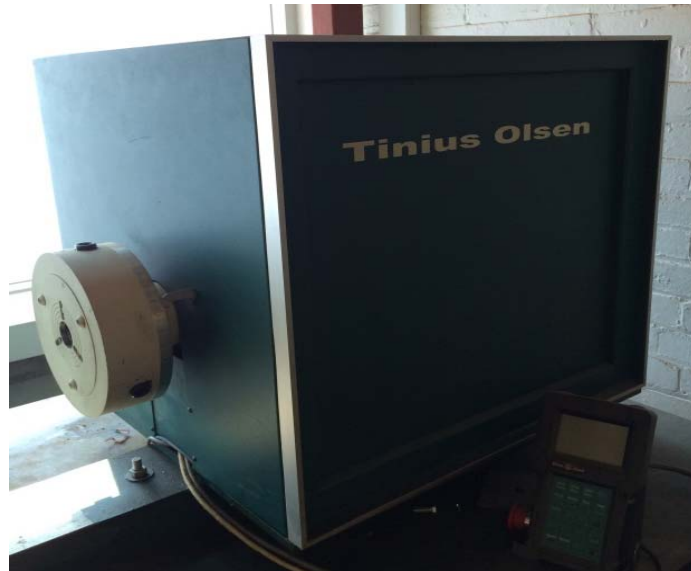


Figure 5-4: The drive unit with the rotating loading chuck.



Figure 5-5: The fixed weighing chuck of the machine.

➤ *Testing Clamps*

The chucks of the torsion testing machine were limited to testing small rectangular cross section specimens. To overcome this limitation and to allow testing structural size glulam beams, a pair of testing clamps, which were fabricated by (Khokhar, 2011), were employed in this study. The steel clamps have been specially fabricated to allow easy installation of rectangular specimens with different lengths and to hold specimen ends with a large contact area so as to avoid excessive embedding. They are also used to grip the specimen without any risk of slippage or damage to the section of the specimen during the torsion test. These clamps also allow the specimen to move longitudinally when twisting by the applied torque. Figure 5-6 shows images of both clamps at the fixed and rotating end of the tested specimen.



Figure 5-6: Clamps of the torsion tester at the fixed end (left) and at the rotating end (right).

5.2.1.3 Angular Measurement Sensors

When using the torsion test, the angular deformation of the specimen should be measured in the central part to avoid the effects of load concentrations at the end. Measurement of torsion angles using the testing machine is not feasible. Therefore,

two angular measurement instruments, inclinometers and a stereo camera system were used in this study. The inclinometer is a contact device that can only measure the angle of twist at the location where the device is installed. On the other hand, the stereo camera system is a non-contact method which can be used not only to measure the angle at specific locations but also to provide more details of the sample rotations at different positions.

➤ *Inclinometer*

Inclinometers (Model IS-2-30, Level Developments, UK), as shown in Figure 5-7, were used to measure the angles of twist at the attached points. The IS-2-30 is a dual axis sensor capable of measuring angles with a measurement range of $\pm 30^\circ$ in two directions with an accuracy of $\pm 0.05^\circ$. The inclinometer is capable of measuring the relative twist angle in both X and Y directions and can be used to acquire the angular position using the RS232 serial port. Because of its small size and light weight, this sensor is suitable to work in a variety of applications.



Figure 5-7: Dual-axis inclinometer.

Because it was difficult to install the clamps vertically since the high torsion force causes a spillage between the test clamp and tester machine, wooden wedges as shown in Figure 5-8 were fabricated to attach inclinometers horizontally onto the specimen. The clamps are made of wood with the angle between the top surface of the sample and horizontal planes of about 30°. These configurations allow inclinometers to be in a horizontal plane initially before performing the tests.

In order to collect data during testing from inclinometers and to record and synchronise their outputs with the camera system, a data log interface was developed by the author of this study and it was implemented based on Visual Basic programming language. This package allows inclinometers to capture readings simultaneously and all data received from these sensors are then transferred directly to a desktop computer, depending on the time interval specified by the user of the software. Figure 5-9 shows an image shot of the graphical user interface of this package.

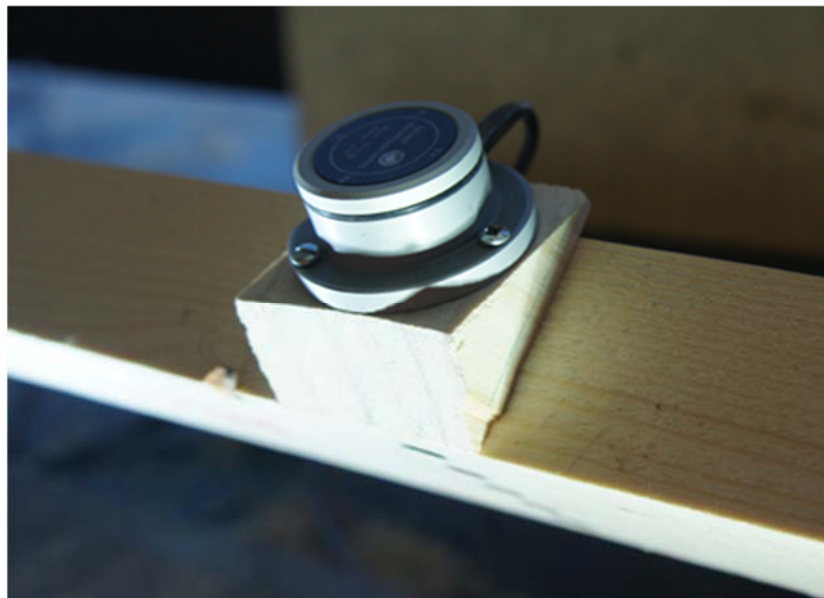


Figure 5-8: Dual-axis inclinometer attached to a wooden mount.

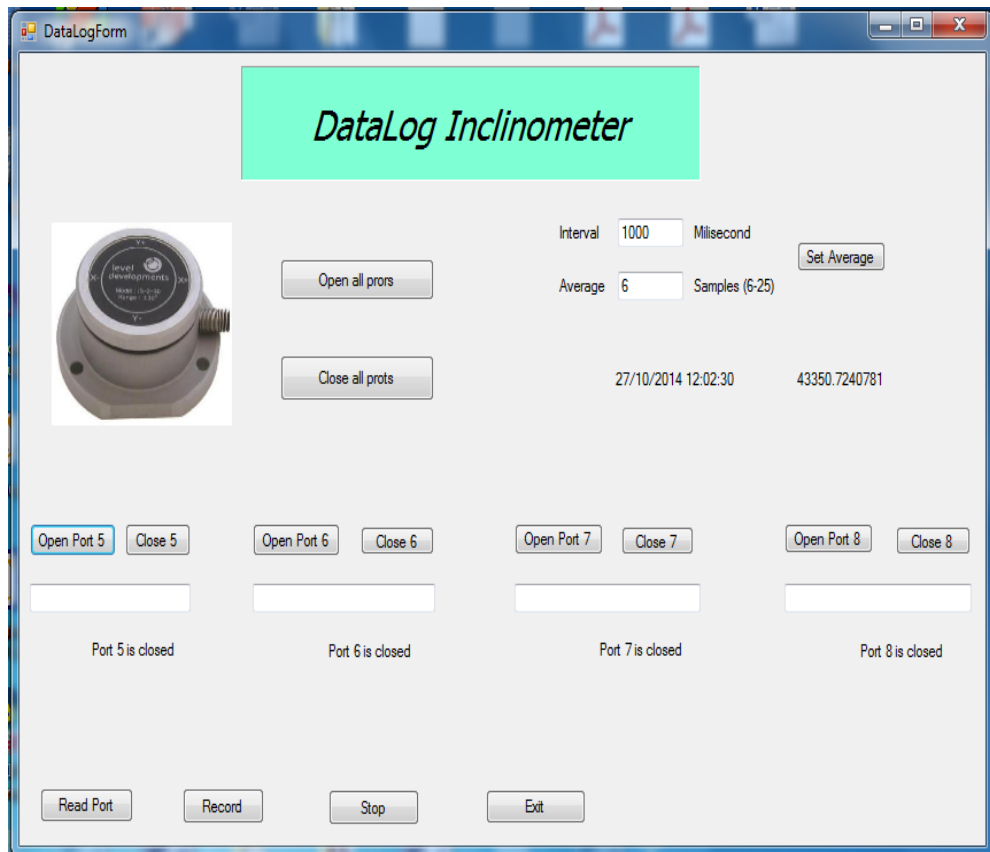


Figure 5-9: Data log system for inclinometers.

➤ Stereo Camera System

The stereo camera system in this study consists of two Basler Pilot piA2400-17gm cameras which are able to acquire images at a resolution of 5 million pixels. The two cameras were equipped with 25mm *Computar* lenses and were mounted on tripods and placed in front of the torsion samples. The Basler cameras were connected, through Ethernet cables, to a desktop computer where the image processing software, HALCON, is installed.

The image processing of the proposed photogrammetric approach is intensive computational work. It requires an automated software package to process the massive acquired image data in each test. A tailor-made toolbox was developed for tracking the rotations and displacements of photogrammetric targets painted on the

surface of the torsion samples. In this study a software package was developed based on Visual Basic and the image processing software, HALCON. Figure 5-10 shows a screen shot of the software during the process of calibrating the stereo camera system. The initial data acquisition and recording subroutines were programmed in Visual Basic with the use of libraries from HALCON Application Programming Interface (API). The subroutines were used to record the data in real time.

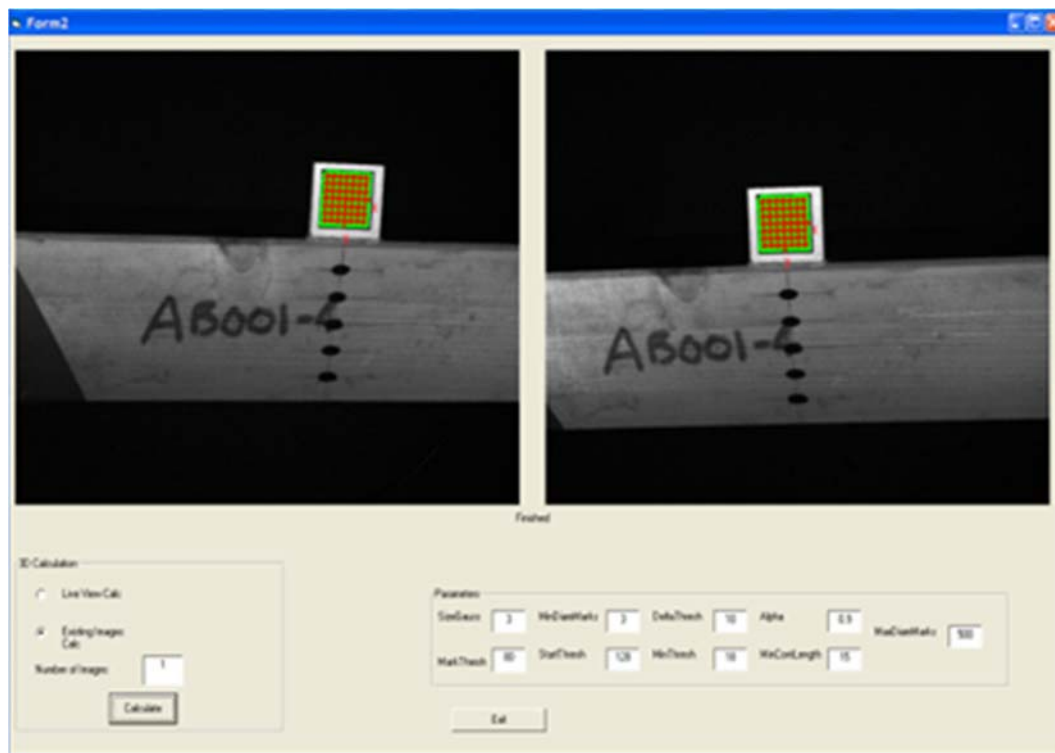


Figure 5-10: The implemented photogrammetric software for torsional tests.

5.2.1.4 Test Setup

Figure 5-11 illustrates the schematic diagram for the test setup and an image of this setup is shown in Figure 5-12. The rotating chuck of the torsional testing machine was connected to the drive unit. The fixed weighing chuck of the machine was mounted on the base beam to allow motion along the axis of the specimen. The steel clamps were secured in the testing machine by mounting them between the rotating and non-rotating chucks of the machine. The clamps were positioned symmetrically about the central point of the cross-section of the specimen, allowing the specimen to rotate about its neutral axis. In order to mount the torsion sample between the steel testing clamps, the left hand weighing chuck was moved along the bed of the machine and the jaws of the chucks were opened to permit insertion of the specimen. The specimen was inserted into the machine by attaching its right end to a clamp mounted on the weighing chuck and its left end with a clamp attached to the loading chuck.

To measure the actual rotation of the glulam beam during testing, inclinometers were employed to allow recording angles of twist at the attached points. As shown in Figure 5-11, four inclinometers were attached to the upper surface of each sample. This was achieved by means of screws placed on the three mounting holes of each sensor. The two end inclinometers were mounted at a distance of 200 mm from the clamps to avoid possible end effects arising from the attaching clamps. This distance met the requirement recommended by the standard which suggests the distance to be about twice the depth of the torsion specimen. All inclinometers were placed at 500 mm apart from each other and were connected via cables to a data acquisition system (DAS). All data received from the inclinometers was transformed through the DAS directly to a desktop computer, PC1 where the data log interface developed to record their readings was installed.

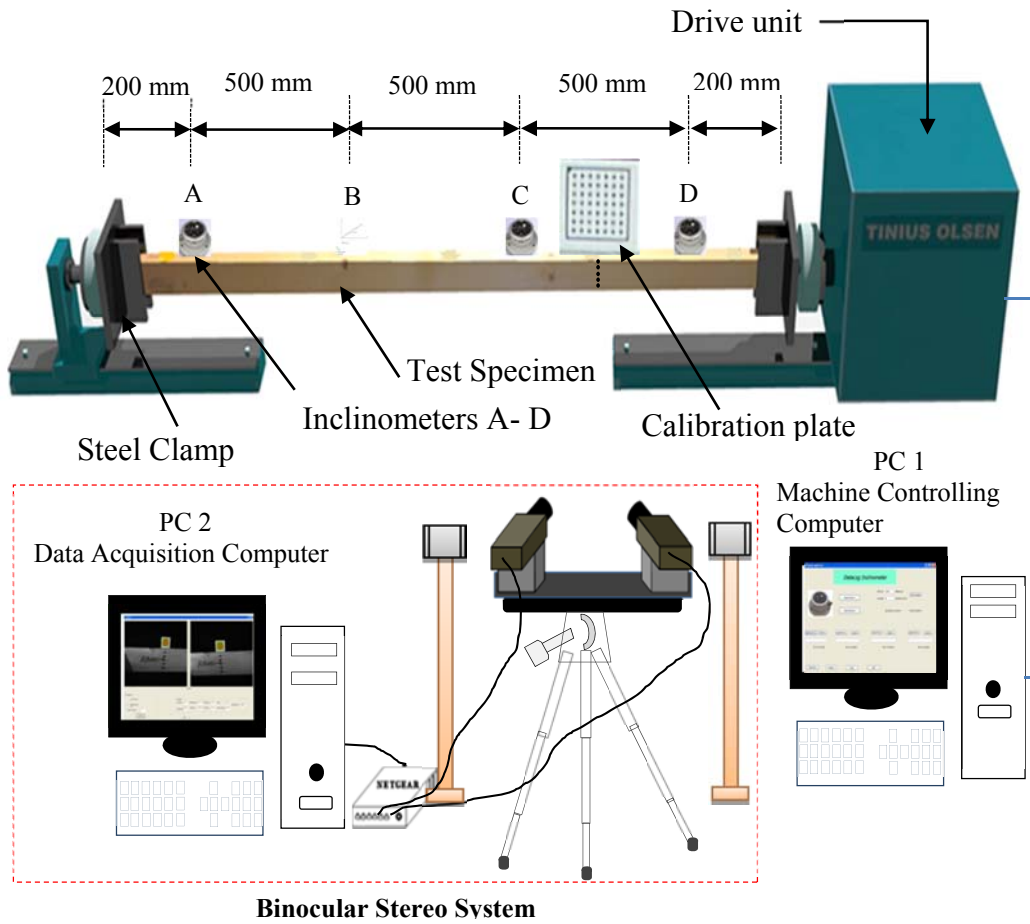


Figure 5-11: Schematic torsional experimental setup with instrumentation.



Figure 5-12: Image of the test setup of the specimen on the torsion machine with instrumentation.

In addition to inclinometers, a stereo camera system was employed to measure the rotations of the long side of the cross section. The two camera system was used to monitor the right most section which is connected to the rotating end. The stereo cameras were placed around 1.5m away from this section. In the middle of the selected section, as shown in Figure 5-13, a calibration plate was glued to the top surface of the specimen. The calibration plate with a predefined geometric shape can not only calibrate the stereo camera system, but can also be used to measure the sample rotation at the attached location on the surface. In order to measure the rotation of the long side of the cross-section of the sample in more detail, the target points, which were placed under the calibration plate, were employed as shown in the following figure. To avoid over-exposure and reduction of quality, the lenses of the cameras were set to small apertures with an increased field of depth so that more details in a wider area could be captured. Two LED illuminators were used to negate the influence of the natural and indoor lighting and to provide a homogenous illumination of the torsion sample.

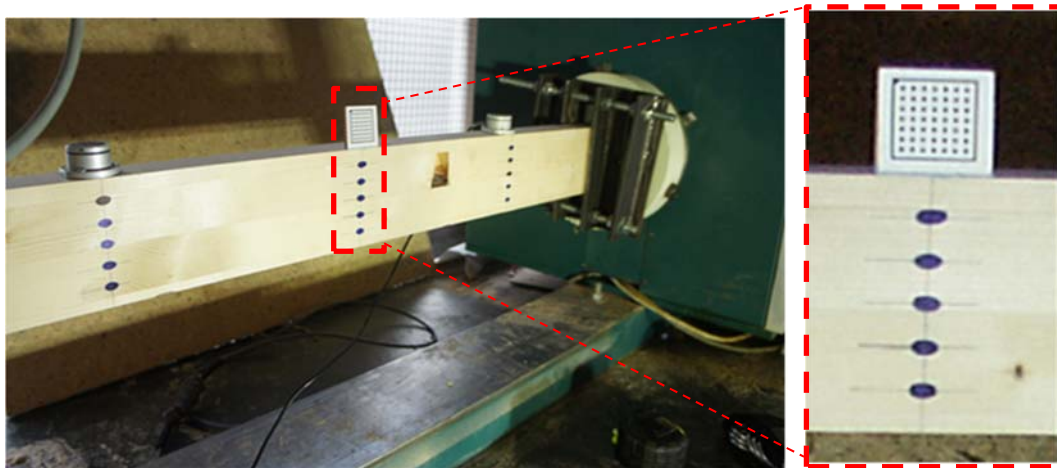


Figure 5-13: The selected section of the beam to be monitored (left) and details of the calibration plate and target points (right).

5.2.1.5 Testing Procedure

Before being used in this investigation, the two-camera system was calibrated using a calibration plate and based on the stereo camera calibration of HALCON. The plate was used as a reference object during the calibration. Images of the plate from each camera were taken simultaneously. The calibration parameters of the stereo camera system were computed and the calibration files were saved to the desktop computer, PC2.

After calibrating the optical system, the torsion tests were carried out according to (EN 408:2010, 2010) procedure of the standard torsion tests. The same configurations of the photogrammetric systems which were used during the calibration process were also used during the torsion tests. Five glulam timber beams were used in this study. The torsion tests were conducted on these beams in the elastic range using the Tinius Olsen torsion machine. Each sample was tested similarly by applying a torque using a constant rate of twist of about 8 degrees per minute prior to yielding. The torsion torque was applied to the specimen within the elastic range by a motor which was attached to the rotating chuck. The chuck on the opposite end of the specimen remained fixed and transferred the torque to the load cell to be recorded by the machine controlling computer. Once the test has started, the Tinius-Olsen software monitors the test in real time and records the applied torque and time according to the settings of the machine control being used for the test. The implemented software packages developed for inclinometers and stereo camera system were also employed to record their data during the period of the test. After the test was complete, the results were saved, the machine was stopped, and the loading chuck was then returned to its initial test position to allow the test specimen to be cleared or removed from the machine.

5.2.2 Results and Discussions

5.2.2.1 Calibration Results of the stereo camera system

In order to reconstruct the 3D coordinates of the photogrammetric targets captured by the optical system and hence determine the rotational deformations of these targets, the internal and the external parameters of the stereo camera system have to be determined. The calibration parameters of the stereo camera, including the rotation angles and the translation vector were determined by calibrating the stereo cameras using the image processing software, HALCON. This was performed by using a least square solution with suitable chosen parameters of the cameras which were determined from the specification of the camera sensor and lens. Selected examples of the calculated parameters are listed in Table 5-1 and Table 5-2.

Table 5-1: The camera parameters of the stereo camera system.

Camera : Parameter	Description	Unit	Left Camera	Right Camera
Focus	Focal length of the lens	m	0.025	0.025
Kappa	Radial distortion coefficient	m ⁻²	-33.26	115.91
Sx	Width of a cell on the CCD-chip	m	8.31e-006	8.34e-006
Sy	Height of a cell on the CCD-chip	m	8.31e-006	8.31e-006
Cx	X-coordinate of the image centre	Pixels	1893.5	515..2
Cy	Y-coordinate of the image centre	Pixels	587.95	688.4
ImageWidth	Width of the images	Pixels	2456	2456
ImageHeight	Height of the images	Pixels	2058	2058

Table 5-2: 3D pose parameters (rotation and translation).

Translation vector (X Y Z [m])	X	-0.231
	Y	0.038
	Z	0.045
Rotation angles [degree]	Rot(X)	0.404
	Rot(Y)	3.304
	Rot(Z)	356.46

5.2.2.2 Target Tracking and 3D Reconstruction Results

The concept and steps involved in the 3D reconstruction are described in Chapter 2 and will be described briefly in this section. The photogrammetric method is based on the comparison between two images of the target points acquired before and after deformation of the torsion specimens. An algorithm was developed using the interface of the image processing software, HALCON. The algorithm reads the calibration files and displays the stereo images of the timber sample recorded before and after deformation. The photogrammetric targets were detected and fitted to ellipse shapes and their image coordinates in both the left and right images were determined using the sub pixel-precise segmentation method provided by the software. The 3D coordinates of the targets expressed in the camera coordinates of the left camera were determined using a triangulation technique (Hartley and Zisserman, 2003). Using this 3D data, the displacements and rotations of the photogrammetric targets can be calculated at different time intervals.

5.2.2.3 Comparison of the Inclinometers and Photogrammetric Measurements

The accuracy of the photogrammetric method is greatly influenced by cameras, lighting, algorithms of the calibration, and algorithms of the 3D reconstruction. To validate the accuracy of the stereo system, the rotation of the calibration plate is captured by two cameras and compared with the average readings from the two inclinometers next to the plate. The comparison of the results from the inclinometers and the photogrammetric approach is shown in Figure 5-14 from which a good agreement between these two methods can be observed.

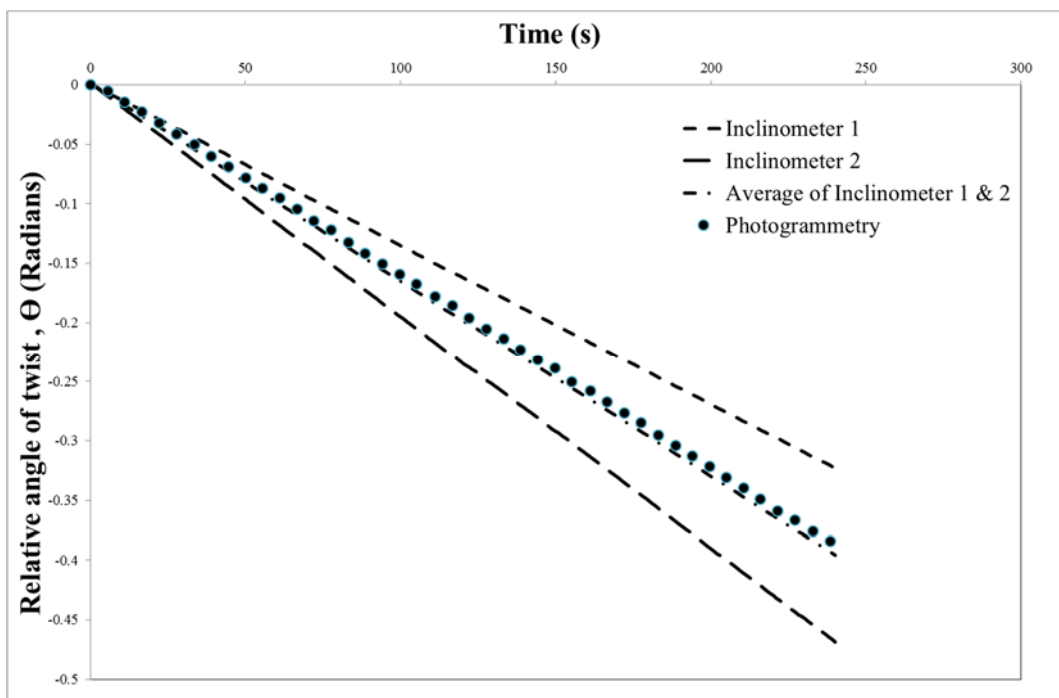
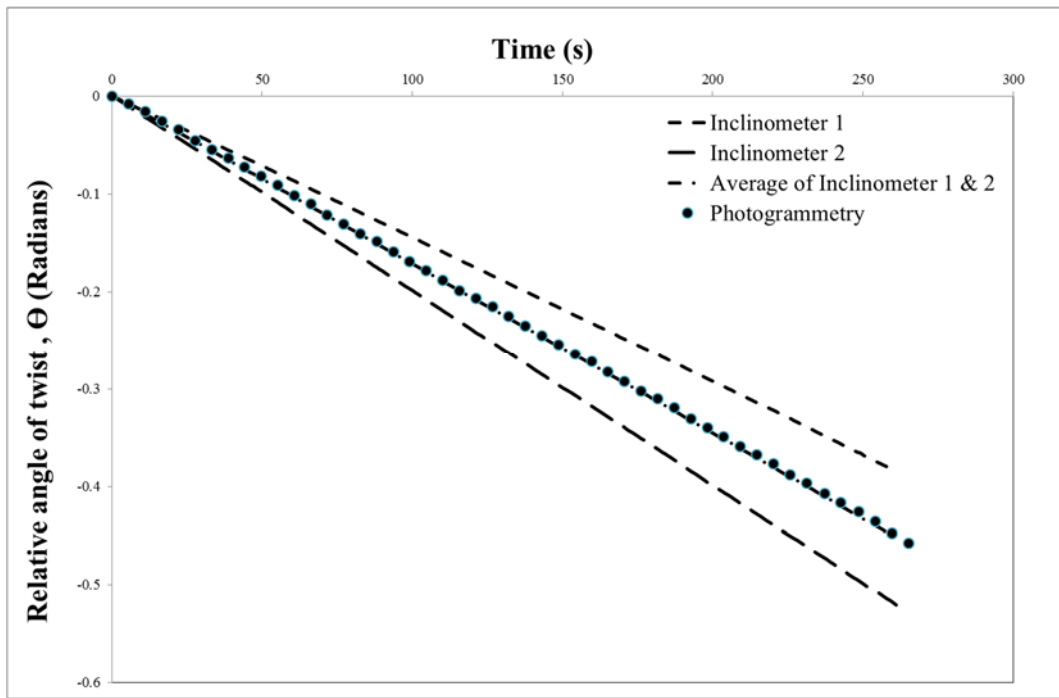


Figure 5-14: Comparison between the measurements of inclinometers and the photogrammetric system for sample 1 (top) and sample 2 (bottom).

5.2.2.4 Shear Deformation along the Long Side of the Cross-section

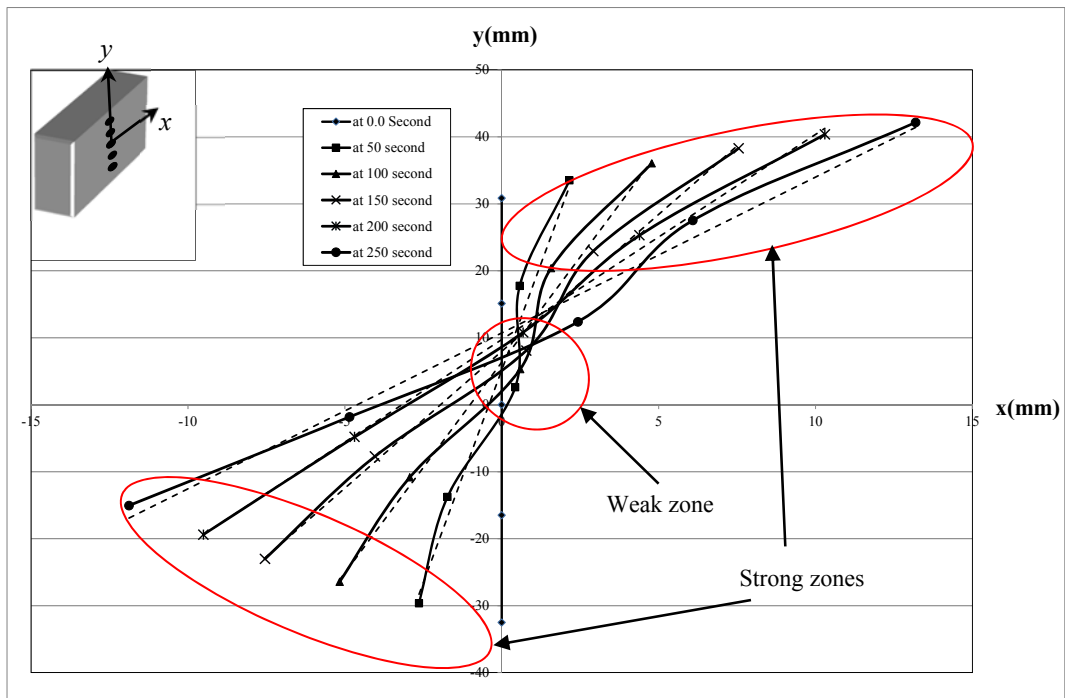
The ability of monitoring and measuring any target points inside of the field of view (FOV) has become the most attractive feature for researchers to apply the photogrammetric method in their experimental research, especially when it is not feasible to use conventional sensors. In this research, the photogrammetric method is also employed to calculate the displacements of the photogrammetric targets along the long side of the cross-section for the region of interest which is exactly below the calibration plate, as shown in Figure 5-13. This was achieved by first calibrating the stereo camera system and finding the internal as well as the external parameters of this system. Using these calibration parameters of the stereo camera system and triangulation, the 3D coordinates of the target points were determined based on the procedure described in Section 5.3.4.7. The 3D coordinates of the central target calculated from the initial images taken before applying torque to the specimens was used to define a point (P1) which was used to be an origin of the coordinate system. The 3D coordinates of each target at the initial images and the deformed images were used to define two points, P2 and P3. The 3D coordinates of the three points were used to define vector 1 (V1) and vector 2 (V2). Using the two vectors, the rotations of the photogrammetric targets for each time interval were calculated according to the following equation.

$$\cos \theta = \frac{V_1 \cdot V_2}{|V_1| \cdot |V_2|} \quad (5.2)$$

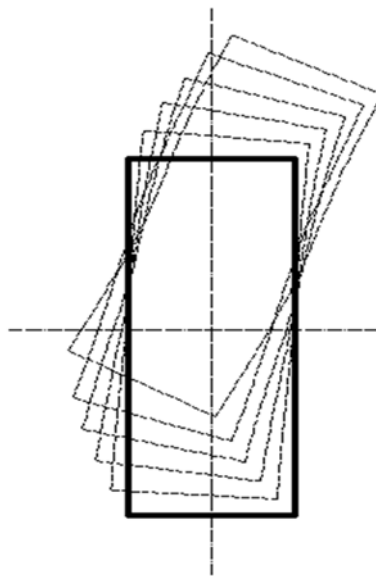
The photogrammetric system was also employed to investigate the displacements of the longer side of the cross section of the torsion specimens. The displacements of the targets exactly below the calibration plate occurring when subjected to a torsional loading were calculated. This was achieved by using the 3D coordinates of the photogrammetric targets and calculating the displacements in the X and Y directions via Equation 5-1. The central target was employed to be an origin of the coordinate system.

Figure 5-15a) shows an example of the displacement of the longest edge of the cross-section measured in the X and Y directions. These displacements correspond to approximately 50 seconds of torsional deformation. The applied torque caused the longer side of the cross section of the beams to deform in the axial direction. This indicated that the plane cross section no longer remains plane after twisting. This deformation might affect the torsional stiffness and hence the shear modulus of the glulam specimens. Although under the Saint-Venant's torsion theory, there should not be a cross-sectional distortion within the x-y plane, it can be seen that significant deformations in the x-y plane has been observed, even under a relatively low torque at the 50th second. So, it has non-negligible effects on the shear strain and shear stress for timber materials in torsion.

It can be seen from Figure 5-15a) that the applied torque causes the longer side of the sections, which were plane prior to twisting, to deform in the axial direction, meaning that the plane cross sections no longer remain plane after twisting. The deformations of the cross section will affect the torsional stiffness of the glulam specimens. From the displacement shown in Figure 5-15a), two different zones can be easily recognized with different gradients of increase in displacement, i.e. a weak zone with a larger increase than the strong one.



(a)



(b)

Figure 5-15: a) Displacements of the longer side of the cross-section b) original and deformed cross-section.

In a torsion test, the inclinometers are normally mounted on the short side of the cross-section. Considering the non-linear displacements observed along the long side of the cross-section, it is important to understand the difference between the rotation of the long and short side of the cross-section. The average rotation of the long side was calculated as indicated by the dash line in Figure 5-15 (a). From the average displacements, the rotations of the long side were calculated. Figure 5-16 shows the comparison of the average rotations of the long (from the photogrammetric method) and short sides (from the inclinometers). The maximum difference between the two methods was approximately 5%. Although a small difference can be observed between the two measurements, it is clear that there is a noticeable agreement between them, indicating that the inclinometers' rotational measurements of the short side are acceptable in structural member level. This is also supported by a scaled sketch of the original and deformed shape of cross-section shown in Figure 5-15b. However, it may not be a good approach to investigate the shear strain/stress distribution of the glulam beams. A more sophisticated technique such as a photogrammetric method should be considered.

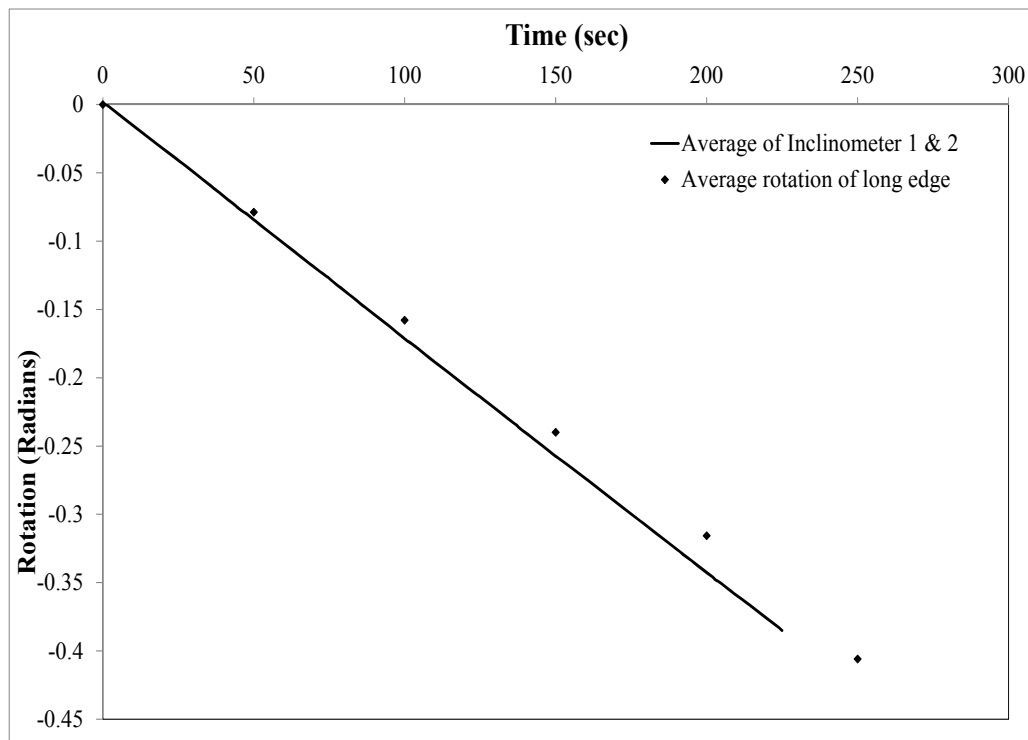


Figure 5-16: Comparison of rotation of the short side and long side.

5.3 The Validation of the Photogrammetric Approach

Since measuring the rotation of timber and glulam specimens during the torsion test is important for evaluating their shear modulus, the photogrammetric approach was proposed and implemented for this type of measurement. In order to validate the stereo camera system, two rotational measurement sensors, an optical and an inclinometer sensors were used in this study and they were intended to measure the rotational deformation on both the short and long sides of the cross section, respectively. Further details have been provided in the following sections.

5.3.1 Materials and Methods

5.3.1.1 Materials and Testing Equipment

Two timber beams with nominal cross sectional dimensions of 216×45 mm were used in this study. These beams have a length of approximately 3.5 m were and had been graded to the C16 strength class. To ensure uniform and constant moisture content of about 12%, the timber beams were stored in a controlled-environment room with a constant temperature of 20°C and relative humidity of 65%.

Before testing and in order to employ the stereo camera system for angular measurements, the timber beams were prepared by applying photogrammetric targets to their surfaces in accordance with the inclinometer location. 11 targets were glued exactly to the middle of the sample and were intended to measure the rotations along the depth of the test specimen. To be easily distinguished during image processing, these targets were printed on a white background and glued to the surface of the beams.

The torsion testing equipment which was used in the previous torsion test was also used in this study. Figure 5-17 shows an image of the stereo camera system and the inclinometer used in this study. The photogrammetric system consists of a pair of Basler Pilot piA2400-17gm cameras, Computar (M2518-MPW F1.8) Megapixel lenses, two LED light units, and a tripod with a frame for adjusting the cameras. The Computar lenses with a constant focal length of 25mm and pixel size of 3.45 microns.



Figure 5-17: Image of the stereo camera system (left) and inclinometer (right).

5.3.1.2 Test Set-up and Testing Procedure

Image of test configuration is shown in Figure 5-18. The timber specimen was placed in the torsion testing machine (Tinius Olsen, Pennsylvania USA) in front of the photogrammetric camera system to allow the rotation angles of the long side of the test sample to be investigated. To monitor the rotations of the targets, the Basler cameras were mounted on a frame with a stereo baseline of approximately 30 cm. These cameras were connected via a Gigabit Netgear switch to a desktop computer with the image processing software, HALCON, installed. For comparison purposes, an inclinometer was mounted on the upper edge (45 mm dimension) of the test sample. This sensor was located exactly at the middle of the sample and above the photogrammetric targets.

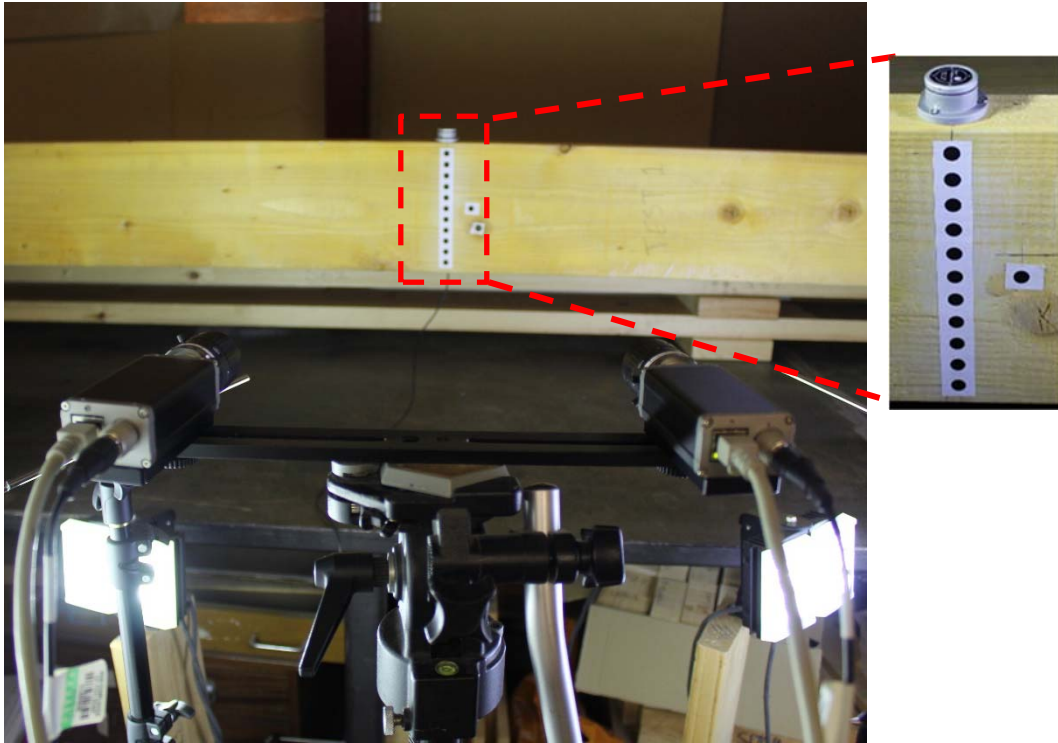


Figure 5-18: Image of test arrangement for torsion test.

Before testing, the stereo camera system was calibrated using a standard calibration plate of HALCON with a dimension of 100mm x 100mm. The calibration plate was placed on the plane, where the measurements need to be done. As mentioned on the documentation of HALCON (MVTech Software HALCON GmbH.), the plate was acquired from the left and right cameras in 20 different positions and orientations relative to the camera system. The graphical user interface (GUI) implemented in the Microsoft Foundation Classes (MFC) by the author of this research was employed for stereo camera calibration to extract the calibration parameters of the camera system during the calibration process. This was done by taken images of the plate from each camera of each stereo system simultaneously. A screen-shot of the developed GUI during the process of calibrating the stereo camera system is shown in Figure 5-19. This GUI shows the extracted calibration marks from the two calibration images of the calibration plate acquired by the stereo cameras in the process of calibrating the stereo camera system.

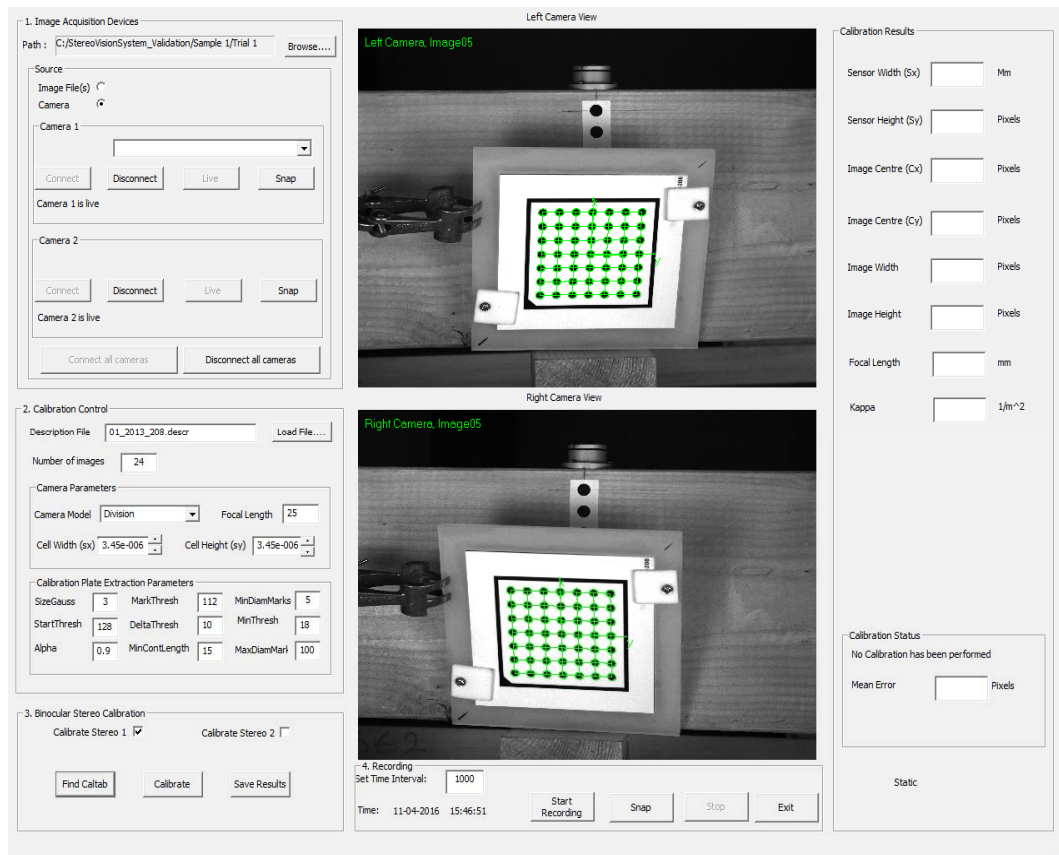


Figure 5-19: Image of the developed GUI during stereo camera calibration.

Once the two camera systems were calibrated and their internal and external parameters were saved, the torsion machine was then set to apply torque to the specimen. Using displacement control approach, torque was applied to all the test specimens and the rotation angles of twist measured from the torsion tester were only used to control the application of the torque. All the test specimens were tested three times at three different speed rate of $2^\circ/\text{minute}$, $4^\circ/\text{minute}$, and $6^\circ/\text{minute}$. For each of these rate of twists, each sample was tested similarly by applying a torque within the elastic range to the specimen until the torsion angle of the tester reached 30° . The same configuration of the optical system which was used during the calibration process was also used during conducting the torsion tests. The load, time, and angular deformation measured from the inclinometers were then recorded through the data acquisition system. During the torque application, the implemented software was automated to record stereo images of the surface of the sample at a time interval of 5 second.

5.3.2 Results and Discussion

5.3.2.1 Calibration Results of the Optical System

The calibration parameters of the stereo camera system were determined by performing the binocular stereo camera calibration of the system using the recorded images of the calibration plate and the calibration functions provided by the image processing software. This was achieved via a least square solution with suitable chosen parameters of the cameras that can be determined from the specification of the camera sensor and lens. Table 5-3 and 5-4 show the internal as well as the external parameters, including the rotation angles and the translation vector determined. These parameters are essential to reconstruct the 3D coordinates and hence their rotational deformations of the photogrammetric targets captured by the stereo cameras.

Table 5-3: Internal camera parameters of the stereo camera system.

Camera : Parameter	Description	Unit	Left Camera	Right Camera
Focus	Focal length of the lens	m	0.025	0.025
Kappa	Radial distortion coefficient	m ⁻²	157.21	84.05
Sx	Width of a cell on the CCD-chip	m	3.45e-006	3.45e-006
Sy	Height of a cell on the CCD-chip	m	3.45e-006	3.45e-006
Cx	X-coordinate of the image centre	Pixels	1495.44	1250.13
Cy	Y-coordinate of the image centre	Pixels	1019.40	1000.14
ImageWidth	Width of the images	Pixels	2456	2456
ImageHeight	Height of the images	Pixels	2058	2058

Table 5-4: 3D pose parameters (rotation and translation).

Translation vector (X Y Z [m])	X	0.25
	Y	-0.021
	Z	0.25
Rotation angles [degree]	Rot(X)	359.33
	Rot(Y)	344.87
	Rot(Z)	359.38

5.3.2.2 3D Reconstruction of the Photogrammetric Targets

The utilized photogrammetric approach is based on the comparison between two images acquired during the test, one before and after deformation. An algorithm was implemented in the HALCON software to process the stereo images and find the rotations of the targets acquired during the period of the test. The whole process was programmed in the software to be automated. A screen shot of the first part of this algorithm is shown in Figure 5-20 (top). The steps involved in the algorithm starts with reading the calibration files and displaying the stereo images of the timber sample recorded during testing. Based on their shape and size, the photogrammetric targets were determined and tracked from the two sequences of stereo images using the sub pixel-precise segmentation method. As can be seen in Figure 5-20 (bottom), the detected targets were displayed on the graphic window of the interactive programming environment of HALCON, HDevelop. These targets were fitted to ellipse shapes and their image coordinates in both the left and right images were determined and ordered by a matching process. Using the image coordinates of the conjugate points and the camera parameters, the 3D coordinates (x,y, and z) of the targets expressed in the camera coordinates of the left camera were derived by intersecting the line of sight of the respective conjugate image points using the operator *'intersect_line_of_sight'* based on the theory of triangulation (Hartley and Zisserman, 2003). These 3D data were then transformed into the object coordinate system, as defined in Figure 5-20 (bottom). These coordinates were then used in the calculation of the rotations of the targets during the period of the tests.


```

HDevelop - C:/Users/Computer/Desktop/2016 Validation of Torsion/HT001_T1_V1.hdev * - [Program Editor]
File Edit Execute Visualization Procedures Operators Suggestions Assistants Window Help
main (:)
1 * My program to demonstrate the extraction of 3D coordinates of photogrammetric targets applied to timber specimens and acquired by calibrated binocular stereo
2
3 * Set the image path
4
5 ImgPath := 'C:/StereoVisionSystem_Validation/Sample 1/Trial 1/'
6 read_cam_par (ImgPath+'Stereo 1/CamParamL.dat', CamParamL)
7 read_cam_par (ImgPath+'Stereo 1/CamParamR.dat', CamParamR)
8 read_pose (ImgPath+'Stereo 1/cLPCR.dat', cLPCR)
9 * Reopen the windows with an appropriate size
10 dev_close_window ()
11 dev_close_window ()
12 dev_set_draw ('margin')
13 dev_set_color ('green')
14 dev_set_line_width (2)
15 dev_update_off ()
16 dev_update_window ('off')
17 dev_open_window (0, 0, 600, 400, 'black', WindowHandle1)
18 dev_open_window (0, 610, 600, 400, 'black', WindowHandle2)
19 set_display_font (WindowHandle1, 14, 'mono', 'true', 'false')
20 set_display_font (WindowHandle2, 14, 'mono', 'true', 'false')
21
22 * Create the tuples in which the image coordinates of the
23 * circles will be accumulated
24 R1:=[]
25 C1:=[]
26 R2:=[]
27 C2:=[]
28 Angles_Deg:=[]
29 * step 1: extract the black circles
30 for index := 1 to 180 by 1
31 * Read and display the images
32 dev_set_window (WindowHandle1)
33 dev_clear_window ()
34 disp_message (WindowHandle1, 'First Camera', 'window', 6, 6, 'red', 'false')
35 read_image (ImageL, ImgPath+'Camera 1/'+ImageL'+(index$'02d')+'.tif')
36 dev_clear_window ()
37 dev_display (ImageL)
38 fast_threshold (ImageL, Region, 0, 50, 1)
39 * The obtained region is separated into connected components
40 connection (Region, ConnectedRegion)

```

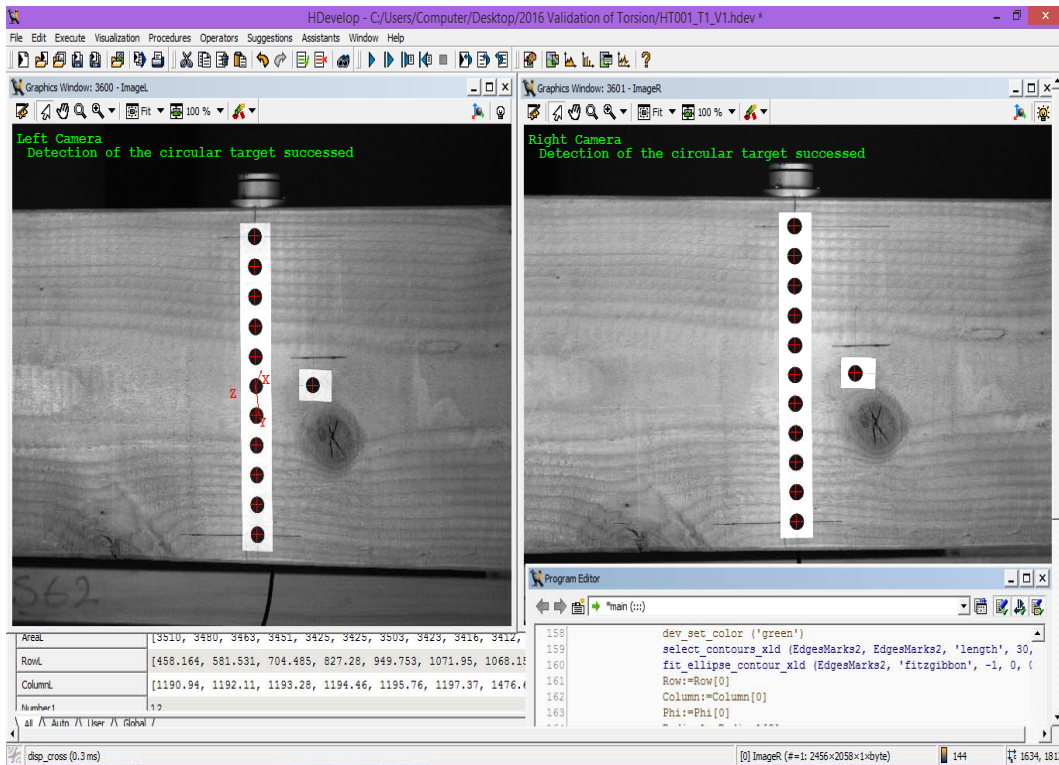


Figure 5-20: The implemented HALCON algorithm for extracting the targets.

5.3.2.3 Comparison of rotation angles between the Inclinator and the Photogrammetric Approach

In this study, the torsion tests were conducted with the purpose to validate the stereo camera system as well as to investigate the influence of the rate of loading on the rotation measurements on both the short and long sides of the cross section of the test samples. Therefore, the photogrammetric system and the inclinometer were used for these measurements. Each test specimen was tested in torsion three times with three different speed rate of 2, 4, and 6 degrees per minute.

For each of the above mentioned tests, the average rotations of the photogrammetric targets and the rotations of the inclinometer were plotted in the same figure. The test results for the slow speed rate ($2^{\circ}/\text{minute}$) is shown in Figure 5-21. Figures 5-21a) and 5-21b) show comparisons of the rotational data between the inclinometer and the stereo camera system for sample 1 and sample 2, respectively. Time is represented on the horizontal axis and values of rotation angles are represented on the vertical axis. The slow rate of loading test results in a good agreement between the rotation data measured by the two methods and indicate remarkable results. It is evident that that the measurements of the rotations of the short side with inclinometers are acceptable. This result was confirmed by investigating the correlation between the measurements of both the optical and inclinometer sensors. The rotation results of inclinometers and stereo camera systems were plotted against each other. Figures 5-22a) and 5-22b) show the comparison of these data for the first and second beams, respectively. Using the linear regression analysis, the test results shown in the above mentioned figures indicate a high degree of correlation with a value of R square equal to 0.99.

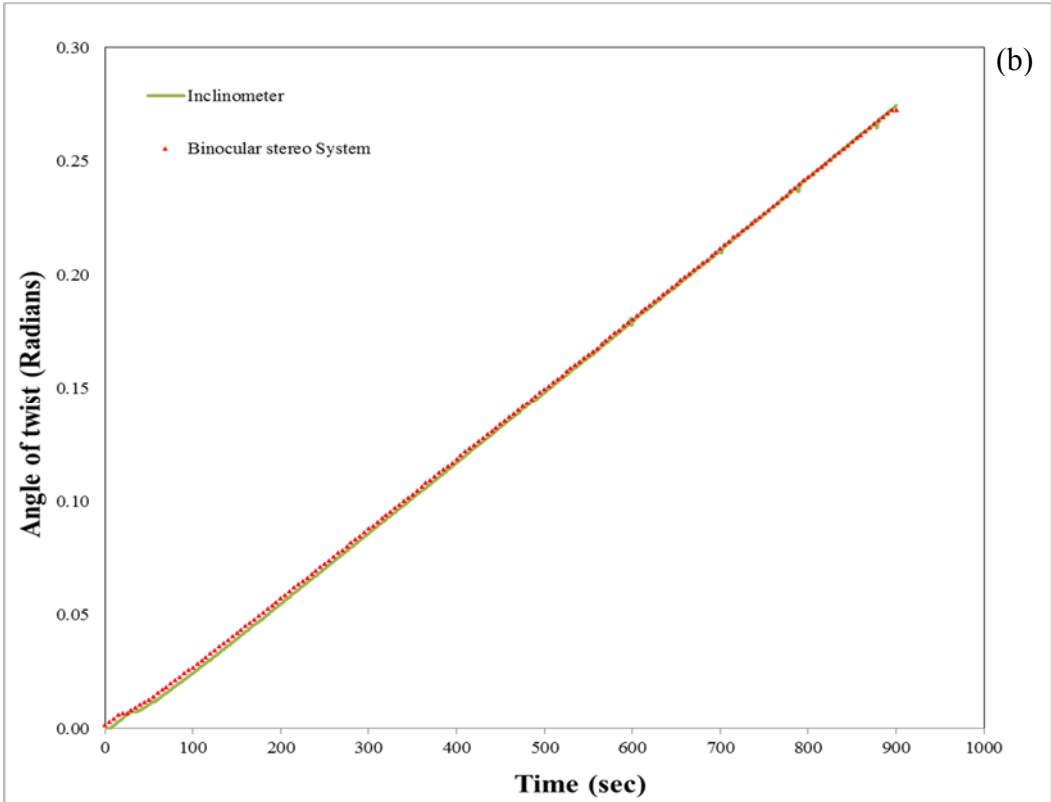
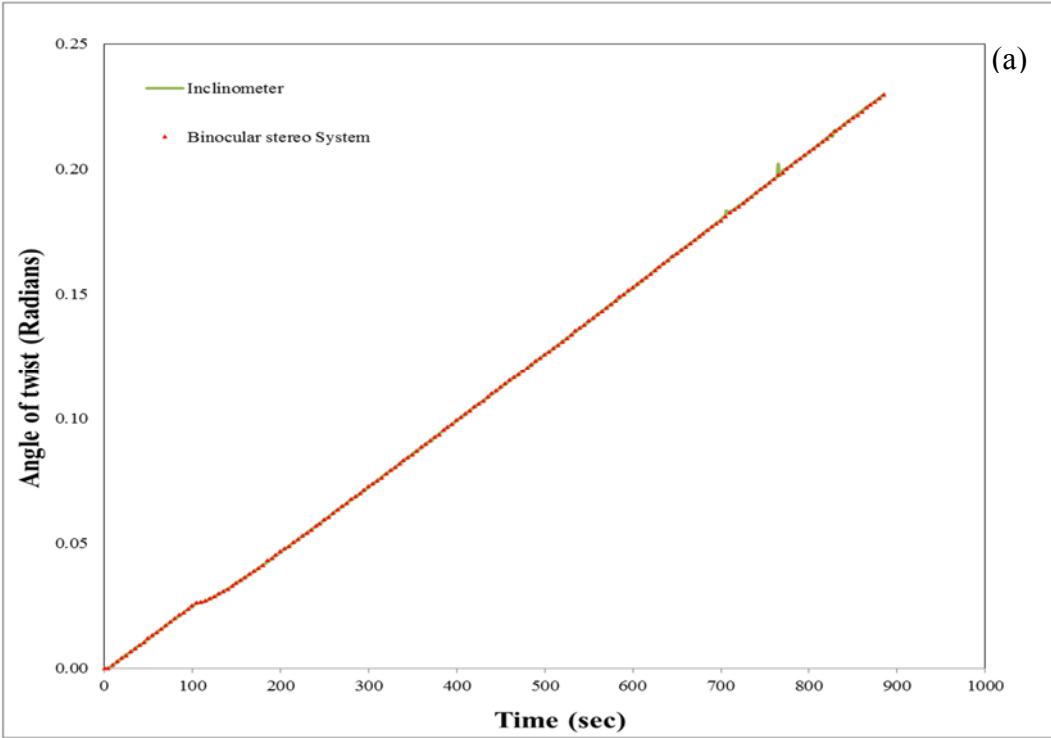


Figure 5-21: Comparison between the inclinometer and optical measurements for a) sample 1, and b) sample 2 under a speed rate of 2 degrees per minute.

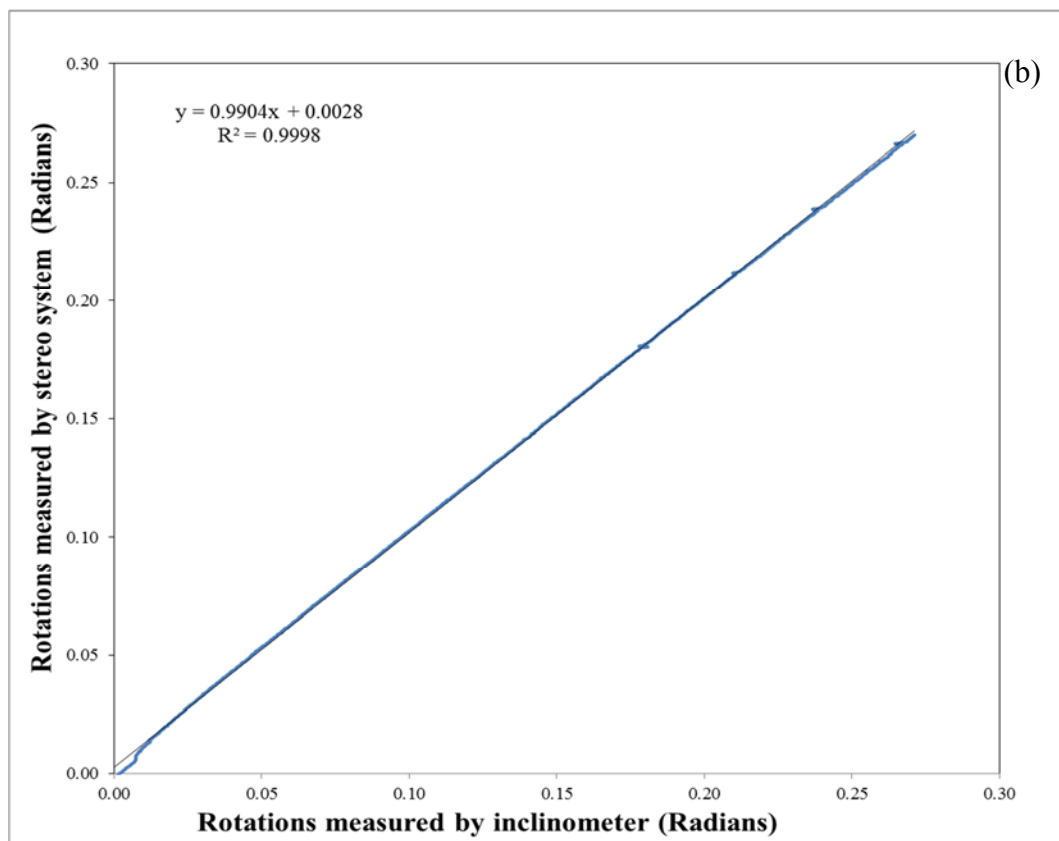
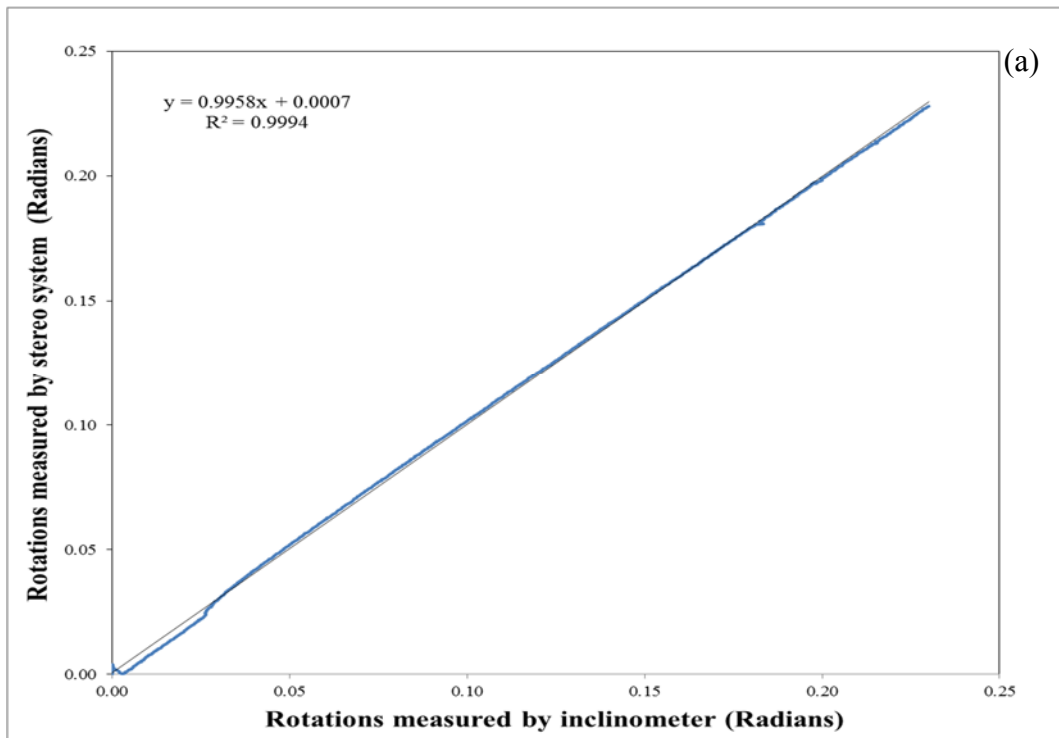


Figure 5-22: Relationship between measurements of the inclinometer and the optical system (R^2 Values) measured in a) sample 1 and b) sample 2.

For the torsion test with the speed rate of $4^{\circ}/\text{minute}$, the comparison between the rotations measured by the inclinometer and those determined by the camera system show a similar results of the speed rate of $2^{\circ}/\text{min}$ test. There is no significant difference between the rotation angles recorded by the inclinometer and those measured by the photogrammetric system. Figure 5-23a) shows an example of these comparisons for the first specimen and indicates a remarkable correspondence. In this figure, the rotations obtained from the two-camera system describe very well the measured rotations using the inclinometer sensor which highlights the efficiency of the proposed approach. The correlation figures between the rotation measurements of both the optical and inclinometer sensors indicate a high degree of correlation between the two method used for angular measurements.

On the other hand, the test results for the highest rate of loading ($6^{\circ}/\text{minute}$) are of considerable importance. As shown in Figure 5-23b), the rotation measurements obtained from the photogrammetric system and the inclinometer reading were plotted on the same figure. Although the rotations measured by both techniques followed a similar trend, there is a significant difference between their measurements. At the beginning of the applied loading and within the first 100 seconds, the rotation measurements for both the inclinometer and the photogrammetric targets were almost the same, but the magnitudes of those measured by the inclinometer decreased dramatically, especially after the first 100 seconds of conducting the torsion test. This may be attributed to the fact the inclinometer readings under a higher rate of loading might be influenced by the setup of this device on the wood specimen and the pins used to attach this sensor might move during loading. Further research needs to be conducted to investigate this result. By comparing the results of the three rate of loading tests, the maximum difference between the measurements of the inclinometer sensor and the photogrammetric method was about 7%. This result could be related to the setup of the inclinometer sensor since this device is installed in a contact with the surface of the timber specimen and this sensor might move significantly at the highest speed rate of 6 degrees per minute.

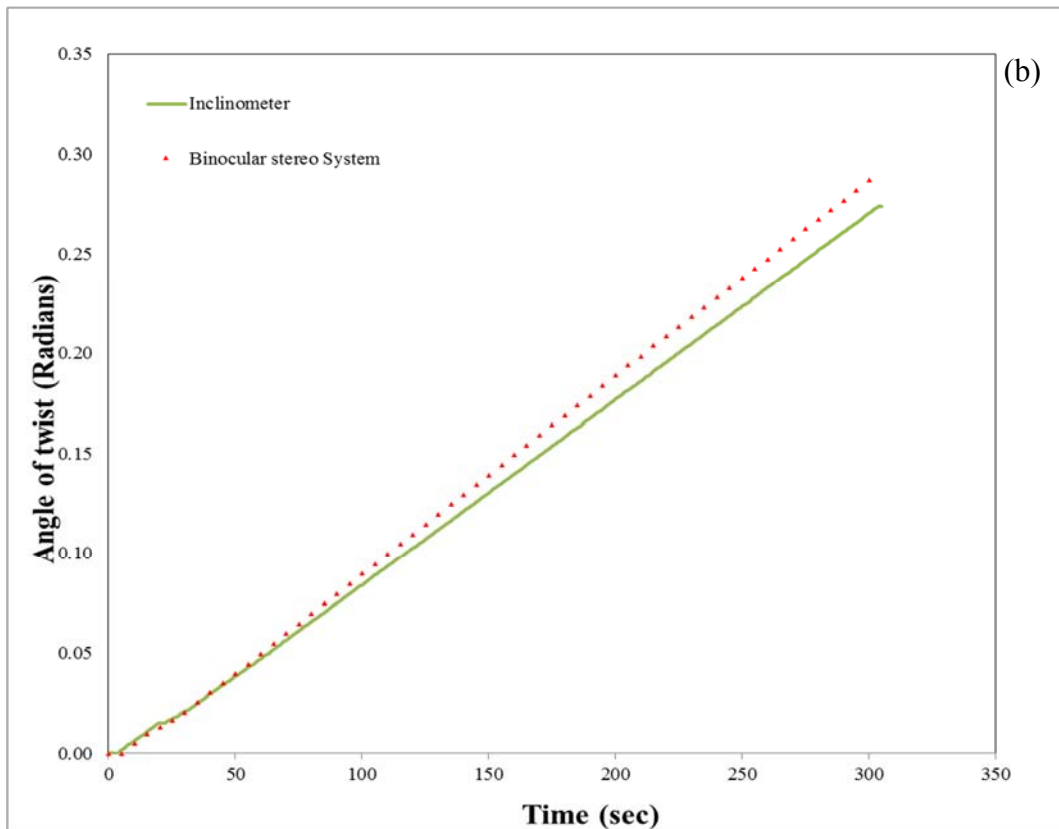
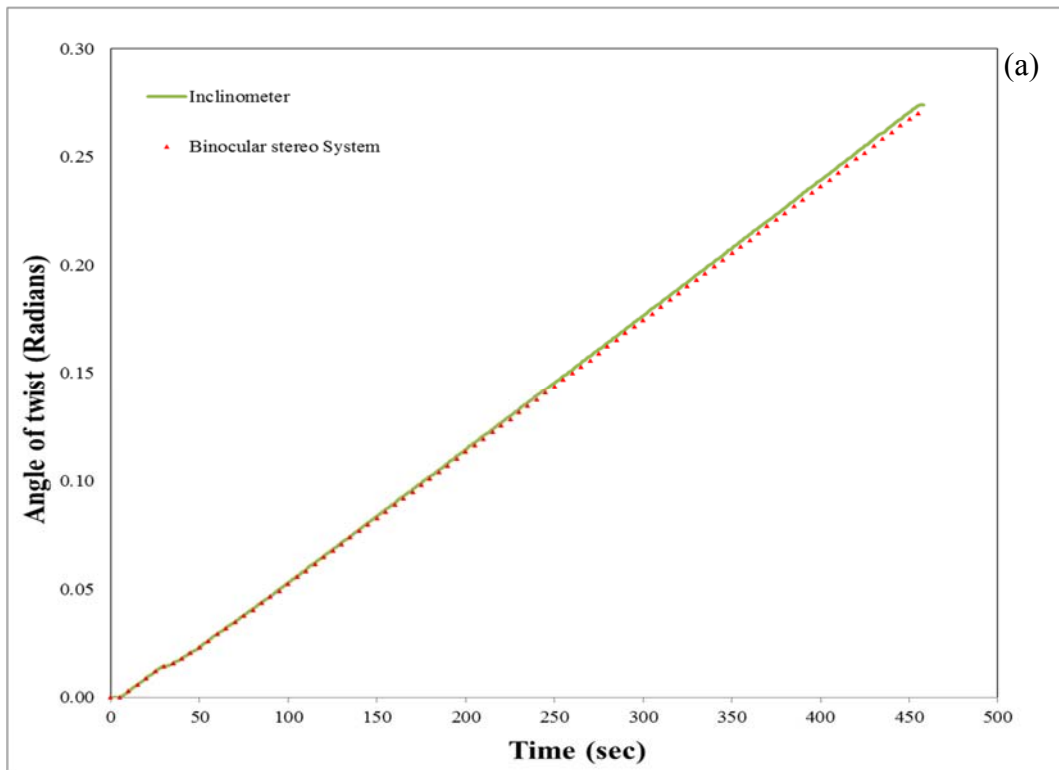


Figure 5-23: Comparison between inclinometers and optical measurements for sample 2 under a speed rate of a) 4°/min, and b) 6°/min.

5.4 Evaluation of Torsional Behaviour and the Variations of Shear Modulus of Glulam Timber Beams

After performing the first experimental study (presented in Section 5.2) and gaining encouraging results by comparing the angular measurements obtained by both the optical and inclinometer sensors, another study was considered to enhance the proposed method and to expand its applications on the torsion test. The main purpose of this study was to investigate more details of the angular deformation and to evaluate the variations of the shear modulus of glulam specimens under the torsion test. To achieve this, patterns of photogrammetric targets was proposed to perform this investigation. These targets were painted on the surface of the test samples to be tracked by the stereo cameras. The performance of inclinometers for measuring angles of twist was also considered in this study. The methodology and measurement process performed in this study can be summarized in the following workflow diagram shown in Figure 5-24.

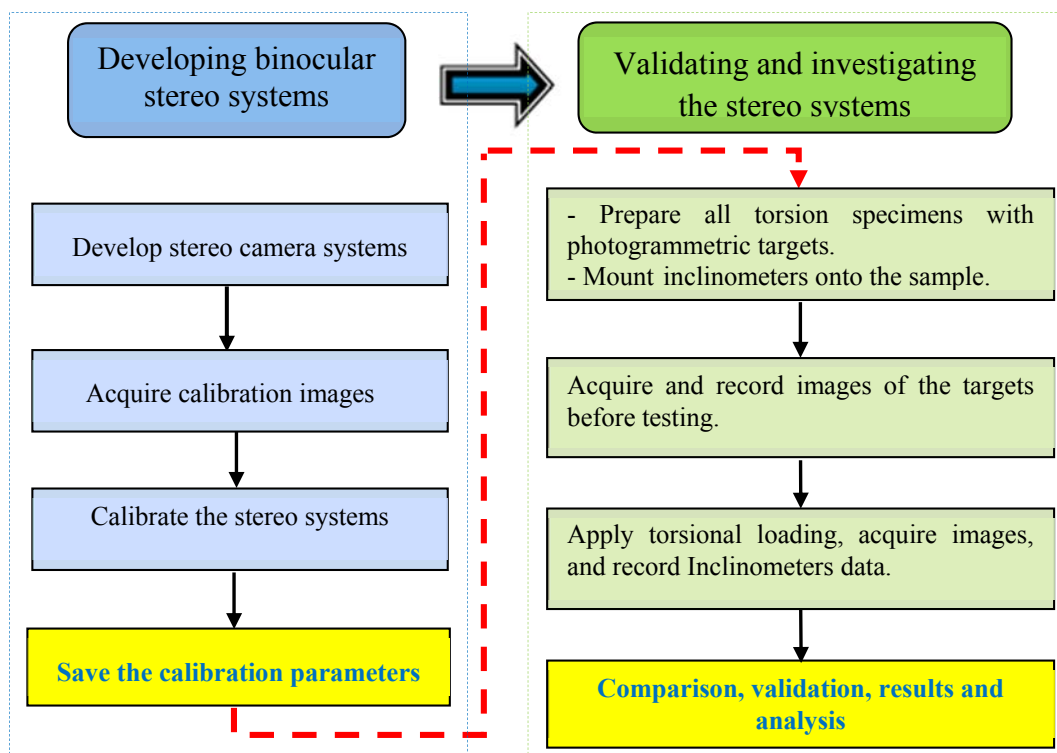


Figure 5-24: Workflow diagram of the experimental torsion test.

5.4.1 Materials and Methods

5.4.1.1 Test Specimen Materials

Twelve rectangular cross-section glulam timber beams were used in this study as samples for the torsion tests. The timber glulam beam are graded to GL24 class strength. Figure 5-25 shows an image of these glulam beams. In order to ensure that the test results would be reliable, the glulam samples were kept in the same condition to have the same moisture content. As described in EN 408 (2010) standards, in order to ensure uniform and constant moisture content (MC) of about 12%, the glulam samples were stored in a conditioning room with a constant temperature of 20°C and a relative humidity of 65%. Before starting to test the samples, the width and depth of each specimen were measured at three places (at the two ends and at the middle). In order to avoid retesting of the same sample, a mark was made on each specimen. All these twelve samples were assigned a letter with a sequence of numbers (HT001 to HT012). The specific dimensions of the glulam samples are provided in Table 5-5. The total length of each beam was about 4 meters (m). This length met the requirement of EN408:2010 standard, which requires the length of the test specimen to be at least 19 times the depth of the section.



Figure 5-25: Glulam samples for torsion test.

Table 5-5: Dimensions of the timber samples.

Sample ID	Length (mm)	Average width (mm)	Average depth (mm)
HT-001	3998	44.22	220.33
HT-002	3998	44.54	220.67
HT-003	3995	44.29	220.33
HT-004	3997	44.41	220.00
HT-005	3999	44.46	220.67
HT-006	3999	44.71	220.67
HT-007	3997	44.40	220.67
HT-008	3998	43.90	220.33
HT-009	3998	44.50	220.67
HT-010	3998	44.57	220.33
HT-011	3994	44.47	220.67
HT-012	3998	44.37	220.33

In order to employ the stereo camera systems for proper use of the torsion test, these glulam beams were prepared for stereo camera measurements by applying black photogrammetric targets to their surfaces. This was achieved by using the following steps: First, the circular marks were drawn in AutoCAD software. The drawn pattern was then copied to a desktop computer connected to a laser cutter machine. A good quality paper was inserted into the machine and the paper was cut precisely to the drawn pattern of the marks. The surface of each sample was prepared by painting the area of interest with a white paint to serve as a background which can assist in distinguishing the targets during image processing. The photogrammetric pattern was then placed on the white paint of each sample and a black paint was applied to produce the circular marks on the background. Figure 5-26 shows the process of preparing a sample with photogrammetric targets. All the glulam samples after being prepared with the photogrammetric targets are shown in Figure 5-27.

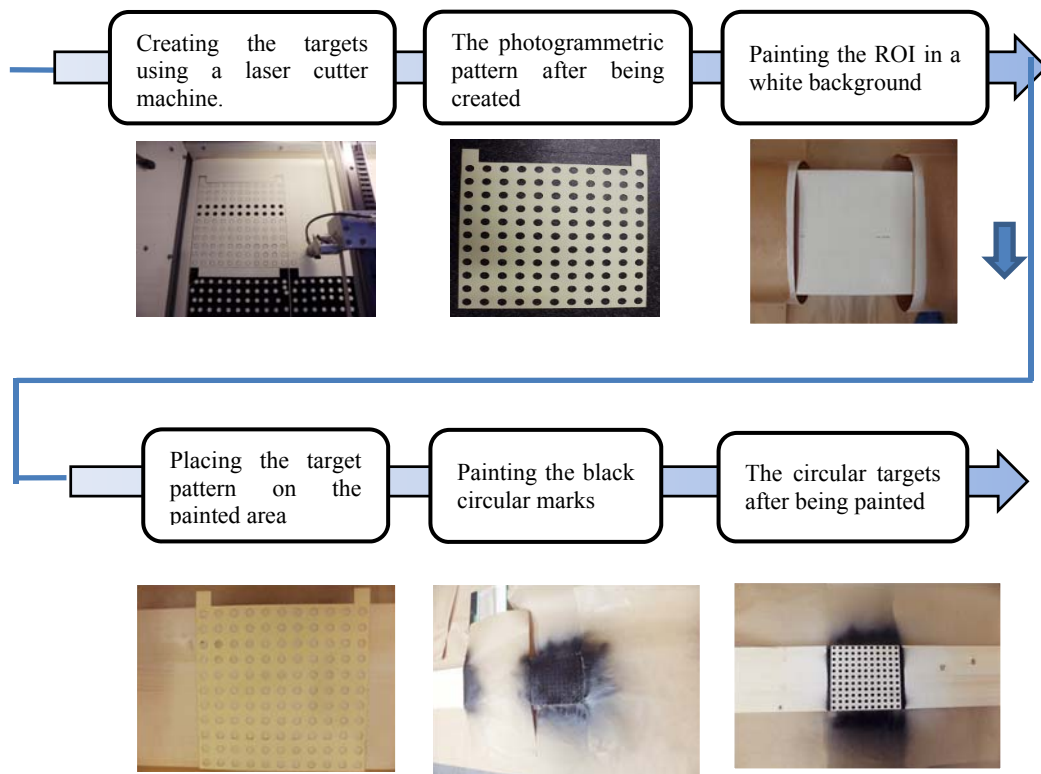


Figure 5-26: The process of creating the photogrammetric pattern on the torsion specimens.



Figure 5-27: The glulam samples after being painted with the photogrammetric patterns.

5.4.1.2 *Torsion Testing Apparatus*

The torsion testing machine which was described in Section 5.2.1.2 was used to perform the torsion tests on the timber beams. Two angular measurement instrumentations, inclinometers and binocular stereo camera systems, were used to monitor the rotational deformations of the samples during testing. The inclinometers considered in this study (Model IS-2-30) were utilized to measure the twist deformation response of the specimen at the location where the device is mounted. A data log interface was developed by the author of this study to display, record and transfer data received from inclinometers simultaneously to a desktop computer (PC1), depending on the time interval specified by the user of the system. This interface allow inclinometers to capture readings simultaneously and then transfer these data directly to a desktop computer. Figure 5-28 shows an image shot of the graphical user interface of this package.

In addition to inclinometers, two binocular stereo camera systems were used in this investigation for image acquisition to monitor the torsion angles of the specimens. Each of the binocular systems, which are shown in Figure 5-29, consists of two DMK 23GP031 cameras (described in Section 3.2.1.2) with a total resolution of 2592 x 1944 pixels and high speed CMOS area scan sensor. The two stereo cameras were fitted with an Azure- 3514M5M lens having a constant focal length of 35mm and pixel size of 2.2 microns. The stereo cameras, mounted on adjustable tripods, were focused onto the region of interest. The DMK 23GP031 cameras were connected via Gigabit Netgear switch to a desktop computer (PC2) where the image processing software was installed. Additionally two LED light sources were employed to assist in providing a homogenous illumination of the calibration plate during the calibration process.

In order to acquire and process the stereo images of the proposed photogrammetric approach, a software package was developed based on visual C++ 2010 and the graphical user interface (GUI) of the package was implemented in the Microsoft Foundation Classes (MFC), providing the functions necessary to calibrate the binocular system and to record the image data during testing. The developed software makes use of libraries included in the image processing software,

HALCON version 11, including functions not only for calibrating the binocular stereo system easily and accurately but also for 3 dimensional image photogrammetry. Figure 5-29 shows a screen-shot of this GUI which has four windows (windows 1 and 2 to display images taken by the first stereo system, and windows 3 and 4 to display images taken by the second stereo system).

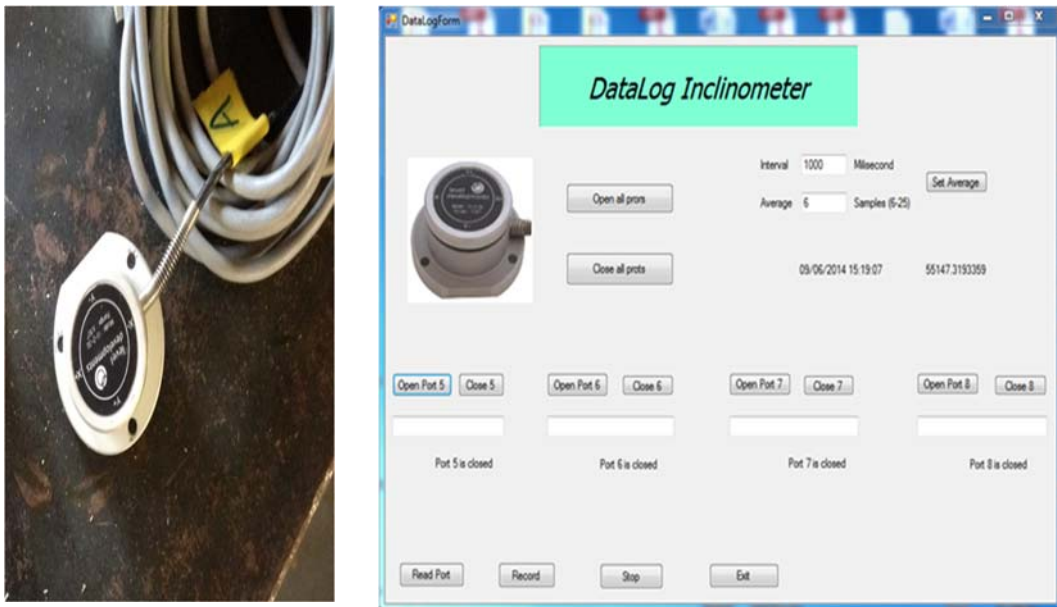


Figure 5-28: Dual-axis inclinometer (left) and the developed data log interface for recording the readings of inclinometers (right).

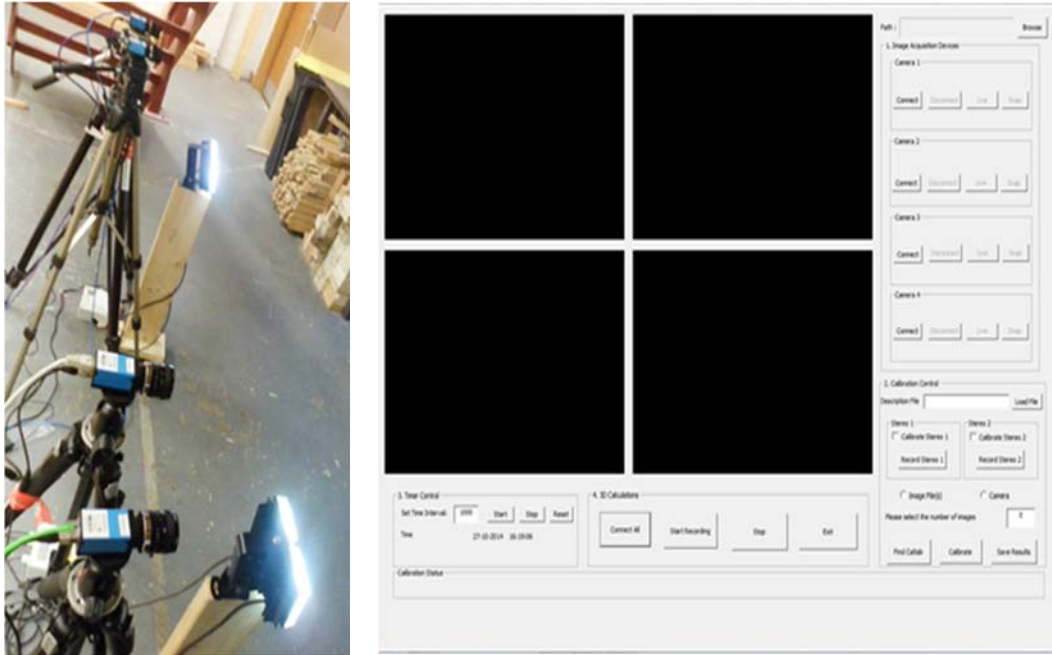


Figure 5-29: The binocular stereo camera systems (left) and the implemented photogrammetric software for image acquisition and camera calibration (right).

5.3.2 Experimental Setup and Procedure

Figure 5-30 shows schematically the components of the torsion test setup and an image of this experimental setup is shown in Figure 5-31. The torsion test setup is similar to that described in Section 5.2.1.4. For a correct evaluation of the shear modulus and to increase the accuracy of angle of twist measurements, two methods, inclinometers and stereo camera systems, were employed to measure the rotational deformations of the timber surface during the test. As illustrated in Figure 5-23, a total of four inclinometers, denoted by the letters A, B, C and D, were attached to the upper surface of the torsion sample. The two end inclinometers (A and D) were mounted at a distance of 130 mm from the clamps to avoid possible end effects arising from the attaching clamps. The other two inclinometers (B and C) were placed at the middle of the torsion specimen sufficiently away from the grips according to the standard EN 408. The inclinometers were connected to a data acquisition system which transforms all data received from the inclinometers directly to a desktop computer, PC2.

In addition to inclinometers, two stereo camera systems (left and right) were used to monitor the angle of twist between the photogrammetric targets utilizing their computed 3D coordinates at each time interval. The first stereo camera system consisting of camera 1 and camera 2 was placed in front of the left photogrammetric pattern. The second camera system consisting of camera 3 and camera 4 was placed in front of the right photogrammetric pattern. For validation purposes, inclinometers B and C were placed exactly above the photogrammetric patterns. Prior to all torsional tests, the two camera systems were calibrated using a calibration plate and based on the stereo camera calibration of HALCON. In the calibration process, a 100mm x 100mm calibration plate was placed in front of the two cameras near the location of the proposed photogrammetric pattern as can be seen in Figure 5-32. The cameras and lens were locked to prevent them from moving during testing. The calibration plate was acquired from the left and right cameras in different positions and orientations relative to the stereo camera system. The outputs of the calibration were saved to the desktop computer, PC1.

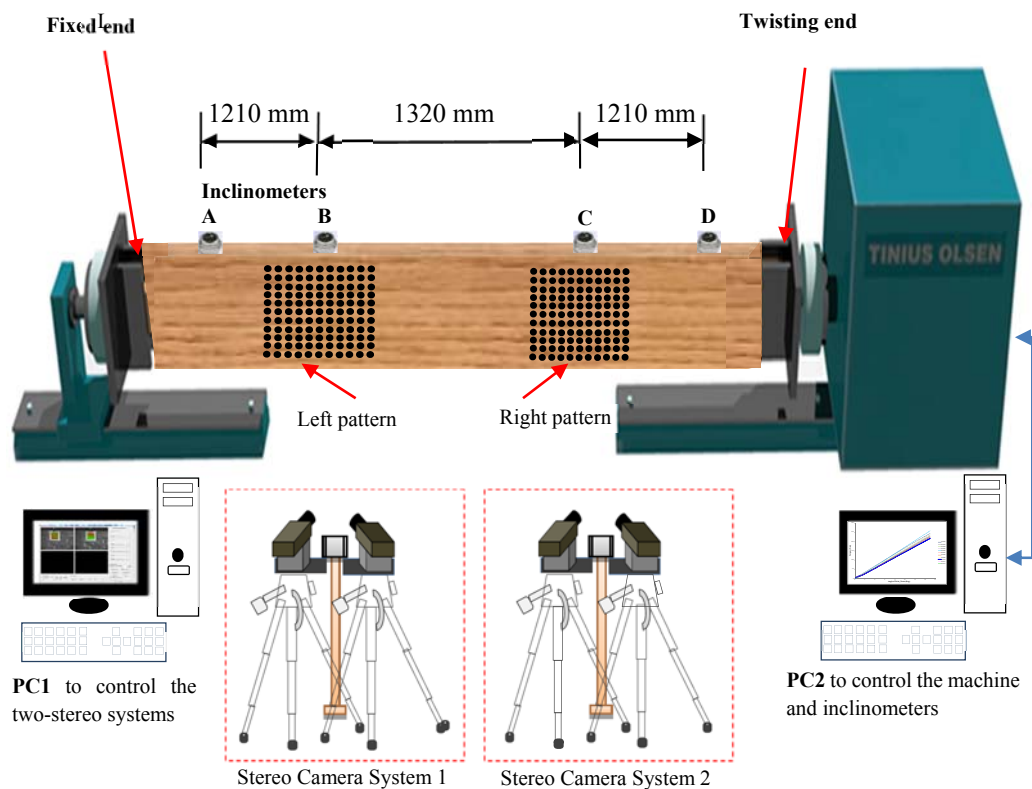


Figure 5-30: Torsion test arrangement and equipment.



Figure 5-31: Image of experimental setup of the torsion test (left) and a detail of the photogrammetric pattern (right).

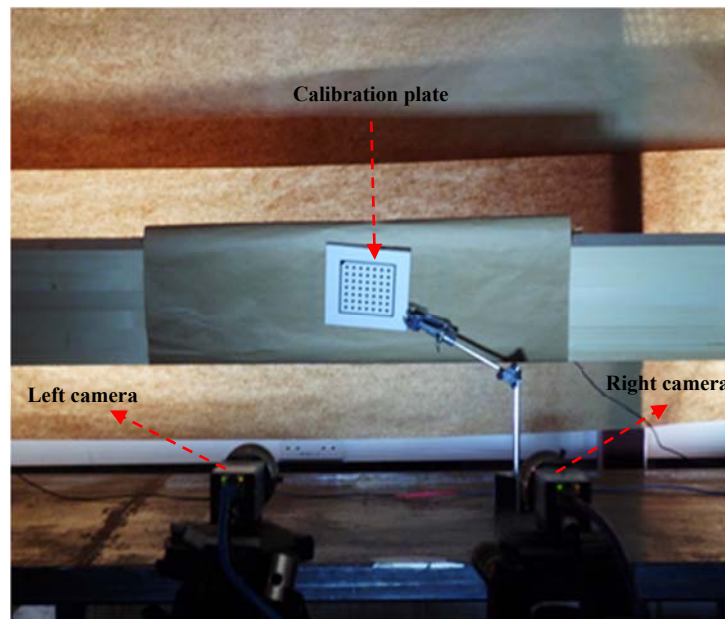


Figure 5-32 : Image of the stereo camera system 1 during the calibration process.

Once the binocular stereo systems have been calibrated, the torsion tests were carried out four times for each torsion specimen according to the (EN 408:2010, 2010) procedure of the standard torsion tests. Twelve glulam timber beams were used in this study. Preliminary torsion tests were carried out on the first sample (HT-001) to determine the rate of loading and to estimate the elastic range of the sample in order to ensure that no permanent deformation occurred during testing under torsional loading. Each sample was tested similarly by applying a torque in the clockwise direction within the elastic range to the specimen at a constant rate of twist equal to five degrees per minute both in loading and unloading until the torsion angle of the tester reached 15° . The direction of the torsion torque was then reversed to an anticlockwise direction with the same loading rate until the torsion angle of the tester reached 15° . Finally, the loading chuck was then returned to its initial test position to allow the test specimen to be removed from the machine. During testing, the implemented GUI was used to automate capturing and recording stereo images of the two regions of interest with a time interval of about 5 seconds. The implemented GUI developed for inclinometers was also employed to record their reading every one second during the period of the test.

5.4.3 Calculation Methods

5.4.3.1 Calculation of Torsional Stiffness

Torsion stiffness, K_{Tor} , is an important characteristic in determining the values of shear modulus. Determining torsional stiffness is based on torque and angle of twist data. The torsional stiffness of the samples can be obtained from a linear regression analysis conducted on the linear elastic range of the graph of the applied torque and the relative angle of twist (EN 408:2010, 2010). In order to obtain comparable values of the torsional stiffness, it is important to determine the range for which torque data are used for obtaining the shear modulus. In order to account for hysteresis effects, the measurements at the initial small increment of torque and at the end of the elastic range were not included. Therefore, for each loading phase, the torque data was examined at the zero load level and at the end of the elastic

limit. The range for which torque data are used for obtaining the shear modulus was determined by considering the deviation from the straight line plotted in the torque versus relative angle of twist curves. Consequently, the linear regression analysis based on the least square fit was established within this range of the applied load for the determination of the torque stiffness.

5.4.3.2 Calculation of Shear Modulus

Based on the Saint-Venant torsion theory of rectangular cross-section, the value of the shear modulus for each torsion specimen (G_{Tor}) can be calculated using the equation given in the standard (EN 408:2010, 2010):

$$G_{Tor} = \frac{K_{Tor} l_1}{\eta h b^3} \quad (5.1)$$

where K_{Tor} is the torque stiffness, l_1 is the gauge length, h is the depth of the timber specimen (the major cross-sectional dimension), b is the width of the specimen (the minor cross-sectional dimension), and η is a constant value, depends on the depth to width ratio and can be determined from a table given in the above-mentioned standard.

5.4.3.3 Calculation of Angular deformation of the Photogrammetric Targets

It is not feasible to employ the torsion testing machine for the direct measurement of the angular deformations. Therefore, as seen schematically in Figure 5-33, inclinometers as well as the binocular stereo camera systems were employed for this type of measurement. In order to compare the results of inclinometers and photogrammetric systems, the averages rotations of the photogrammetric patterns were determined. This was achieved by finding the pixel coordinates of the targets of each pattern and averaging these values to define a point (P_1) with the average pixel coordinates of the pattern. The pixel coordinates of the other two points, P_2

and P_3 , as shown in Figure 5-33, were determined for each pair of the stereo images by processing the initial images before applying torque to the specimens. Utilizing the calibration parameters of the stereo camera system and triangulation, the 3D coordinates of the three points were determined to define vector 1 (V_1) and vector 2 (V_2), Using the two vectors, the rotations of the photogrammetric patterns for each time interval were calculated according to the following equations.

$$\cos \varnothing = \frac{V_1 \cdot V_2}{|V_1| \cdot |V_2|} \quad (5.2)$$

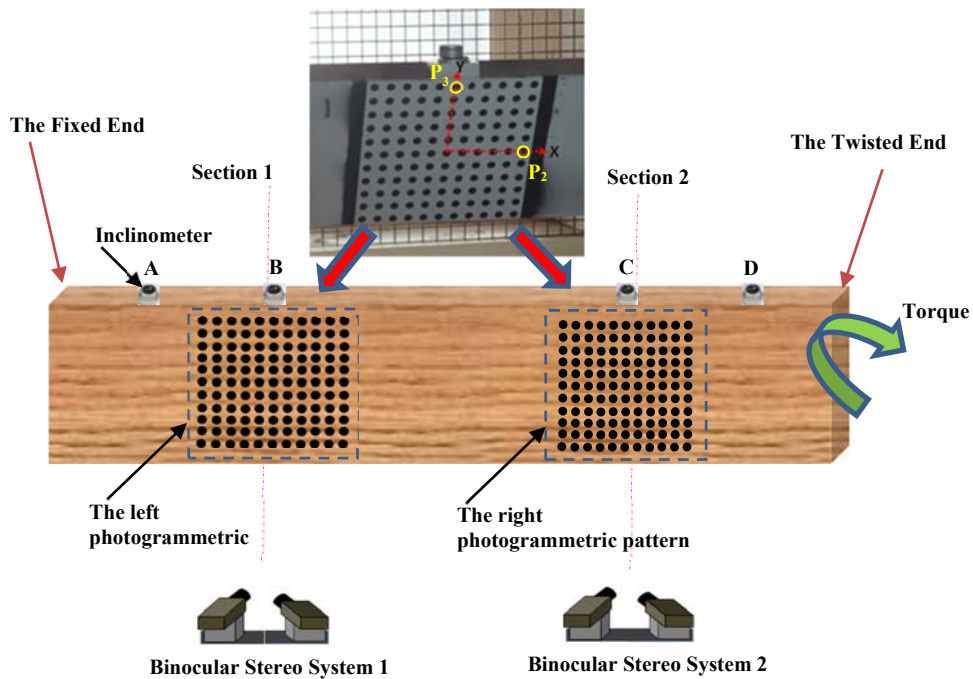


Figure 5-33: Schematic of the angular deformation sensors.

5.4.4 Experimental Results and Discussion

Before performing torsion tests in each torsion specimen, preliminary tests were carried out on the first trial specimen (HT001) to locate the upper limit of the elastic range for the tested specimen under torsional loadings. From the results of these tests, it was found that the torsion specimen could be twisted by up to 15° before it began to behave non-linearly. The maximum torque applied to the specimen to be within the linear-elastic range was about 250 N.m. Based on this finding, torsion tests were conducted on the remaining eleven specimens (HT002 - HT012) under cyclic loading in the clockwise and anticlockwise directions. Each specimen was tested four times and the results of these tests are presented and discussed in the following sections.

5.4.4.1 Torsional Behaviour of the glulam Timber Beams

To evaluate the torsional behaviour of the glulam specimens, the recorded torques measured from the torque cell of the torsion machine, were analyzed and displayed graphically. As an example, the torque versus time graph obtained from the first torsion test conducted on glulam specimen HT002 under loading and unloading phases is shown in Figure 5-34. Time is represented on the horizontal axis and values of torque are represented on the vertical axis. This plot indicates that the relationship between the values of torque and the corresponding time is approximately linear during the different phases of loadings.

In addition, the relationship between the applied torque and the relative angle of twist over a specific gauge length, which is the distance between inclinometers B and C, was also examined to investigate the linear behaviour of the torsion specimens. Figures 5-35 and 5-36 show the plot of torque versus relative angle of rotation measured, respectively, by inclinometers and stereo camera systems for specimen HT002 during all loading-unloading cycles in both the clockwise and anti-clockwise directions. It can also be seen from the above mentioned figures that applying torsional torque in both the clockwise and anticlockwise directions yields an approximately linear behaviour, confirming that the torsion specimen was within

the elastic range. It is also obvious that the response of the specimens to torque was not significant for both the loading and unloading phases.

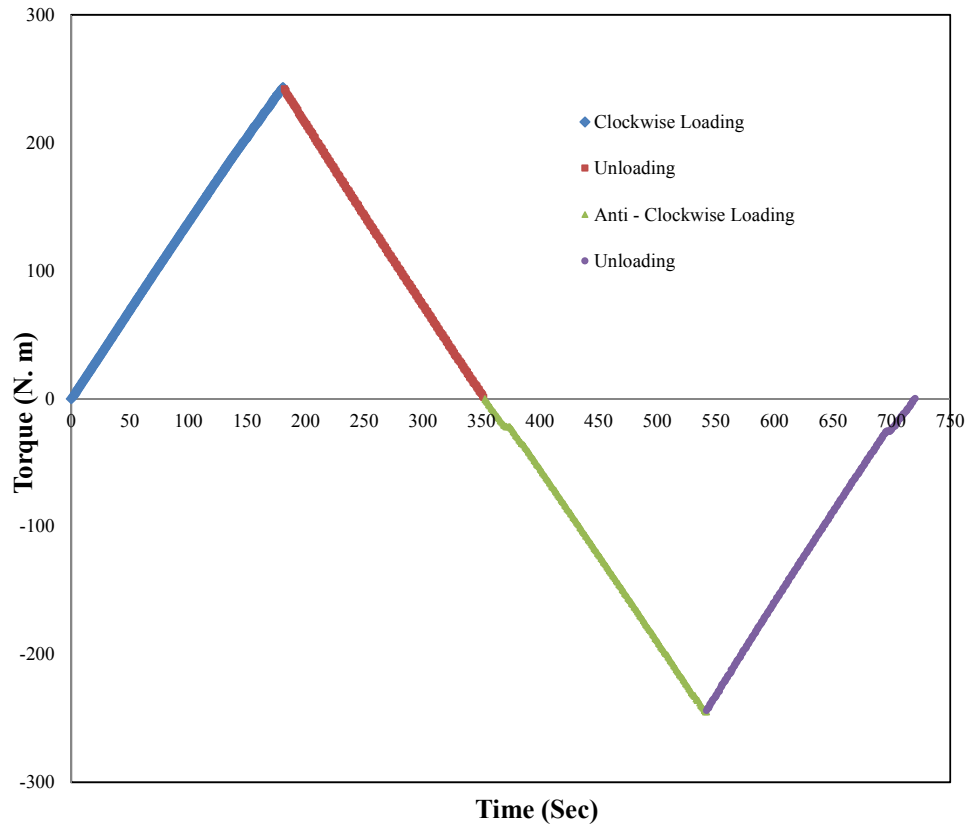


Figure 5-34: Responses of the sample HT002 to torques during the four phases of loading in trail test 1.

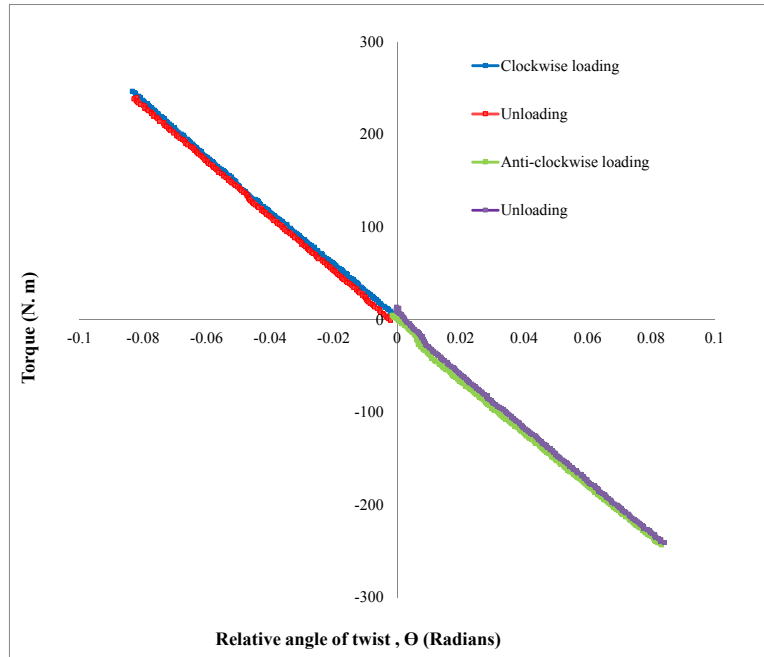


Figure 5-35: Torque versus relative angle of twist recorded by inclinometers for specimen HT002.

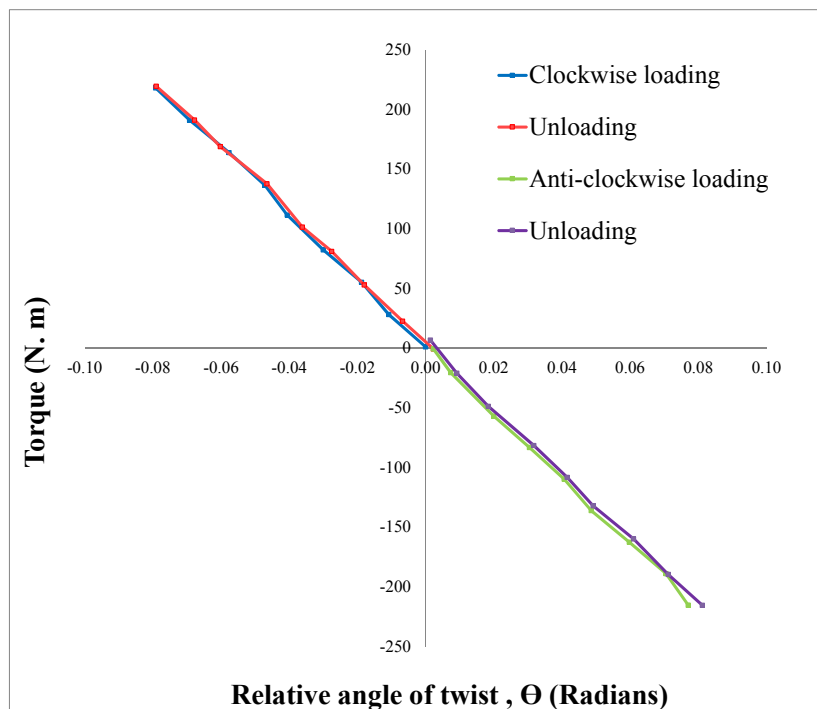


Figure 5-36: Torque versus relative angle of twist recorded by stereo camera systems for specimen HT002.

From the test results of the torsion tests, all tested glulam specimens exhibit the same linear behaviour, although there is a large degree of variability in the maximum values of torque applied to twist the torsion specimens up to 15°. Graphs of torque versus angle of twist measured by the torsion tester for all glulam specimens (HT002 to HT012) are shown in Figure 5-37. By comparing these graphs, the relationship between the applied torque and the corresponding twist is linear with different gradients. It is clear that specimen HT002, indicated by the blue line, has the highest maximum torque and slope and hence the highest stiffness. It can be seen from the figure that specimens HT007 and HT010 have the lowest values of the highest maximum torque and slope and hence the smallest stiffness. These results give only a primary indication of the stiffness of the torsion specimens and how they differ from each other, but a stronger evidence of this finding will be provided in the following sections when calculating the shear modulus for all the tested glulam beams.

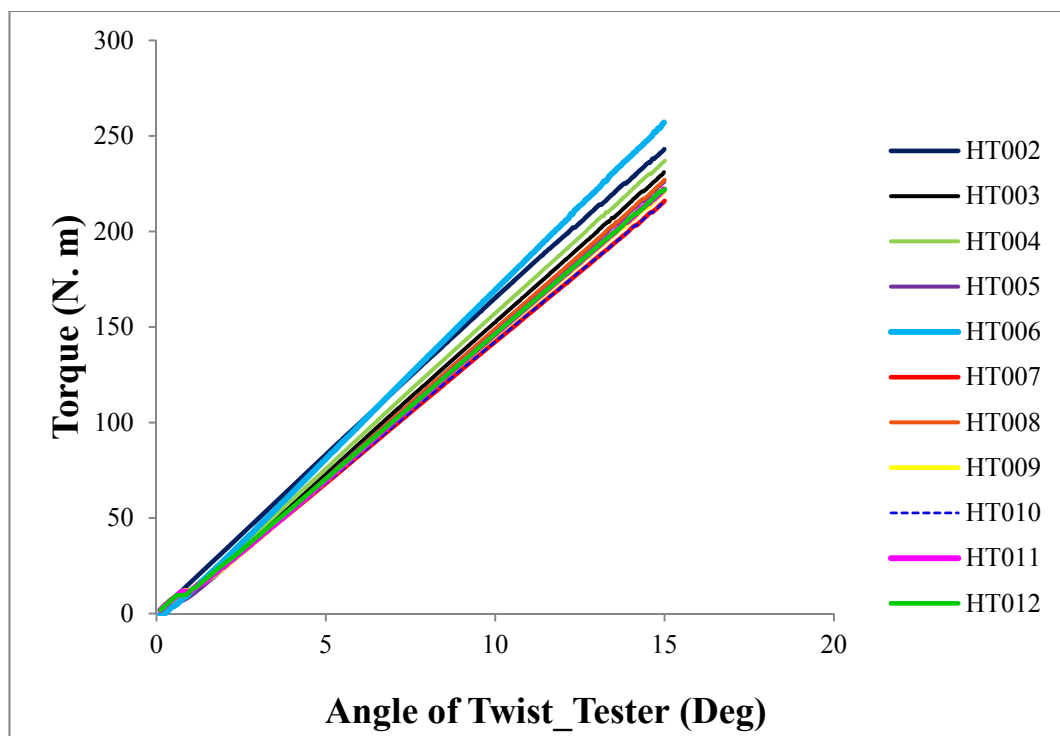


Figure 5-37: Torque versus angle of twist for all torsion specimens.

5.4.4.2 *Relationship between Torque and Relative Angle of Twist*

The glulam beams were tested in torsion under torque loading and unloading applied in both clockwise and anticlockwise directions. The torque values in addition to the angles of twist were measured simultaneously at two sections over a gauge length of about 1320mm, which is the distance between inclinometers B and C. The relative twist was obtained from the difference between the readings in radians of the two inclinometers. Typical examples of establishing the relationship between the applied torque and the relative angle of twist are shown in Figure 5-38 in the top and bottom graphs for samples HT002 and HT003, respectively. The coefficient of variation (R^2) shown in these figures was about 0.999, indicating that the relationship between the relative twisting angles and torque is linear and confirming that the torsion specimen deformed within the elastic range. As can be seen from the figures, the slope of torque-twist graph yields the torsional stiffness which is an essential characteristic to calculate the shear modulus of the tested specimens. By comparing the torsional stiffness calculated during all loading-unloading phases, it is clear that the torsional stiffness calculated at each loading-unloading phase is very closely related to each other. For both clockwise and anti-clockwise directions, the torsional stiffness in loading is relatively higher than in unloading with a small difference of about 1.3%. The difference between the loading and unloading phases was small and about 1.3%. However, torsional stiffness obtained at the loading phase in the clockwise direction was relatively higher than that obtained at the loading phase in the counter-clockwise direction with a difference of about 2.2%. These findings may indicate that twisting timber specimens in either clockwise or anti-clockwise direction do not have substantial influence on the torque stiffness and, hence, the values of shear modulus. However, in order to evaluate these results, it is essential that the shear modulus should be calculated from the loading and unloading data in either of the two directions. Therefore, the values of shear modulus for each loading-unloading phase were obtained and compared and the results are presented in the following section.

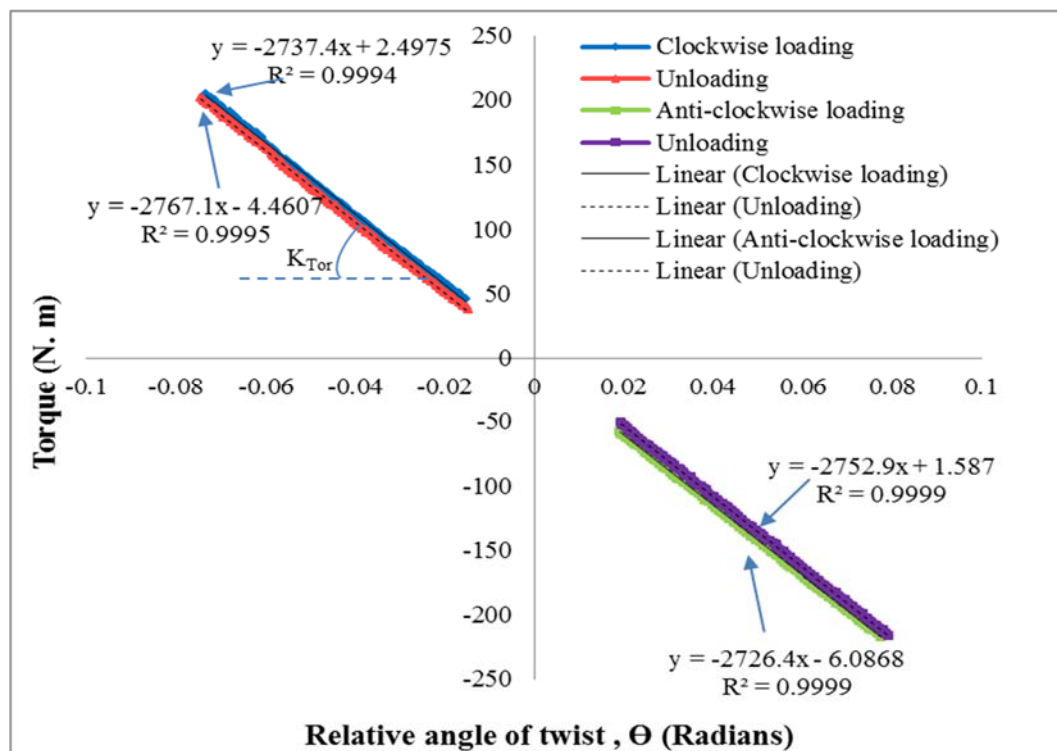
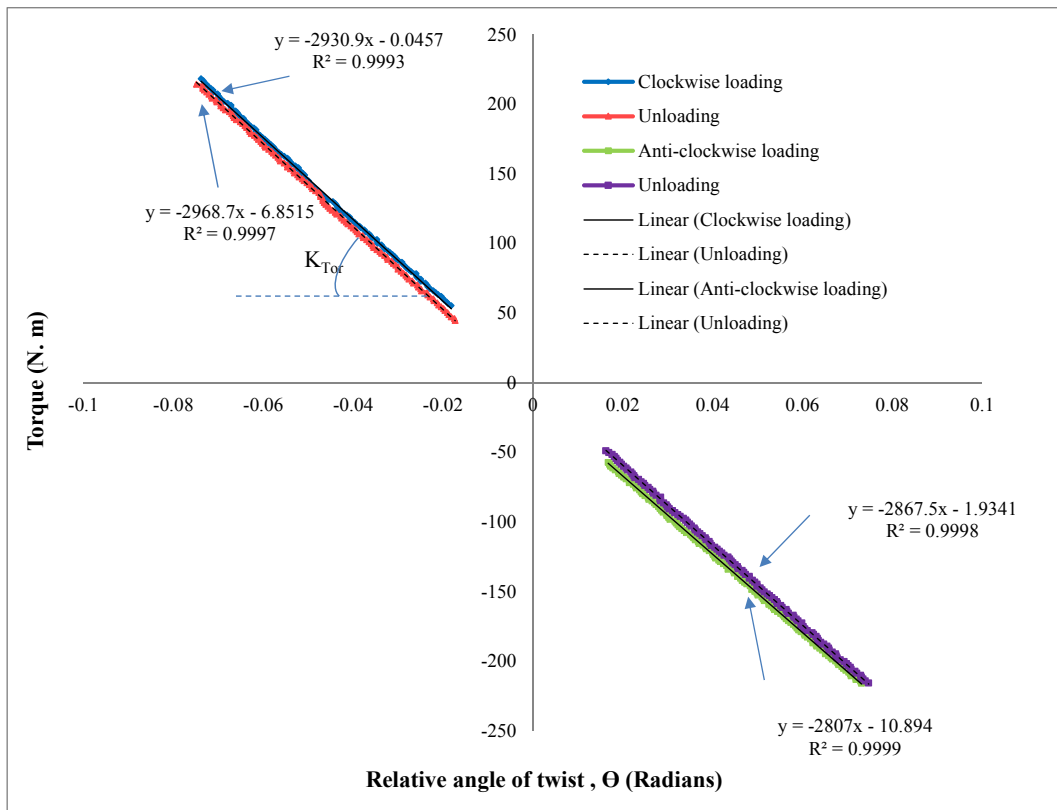


Figure 5-38: Determination of torsional stiffness of specimen HT002 (top) and specimen HT003 (bottom).

5.4.4.3 *Torsional Shear Modulus of the Beams based on the data of inclinometers*

After determining the torsional stiffness of the test specimens for each loading and unloading phase, the shear modulus was calculated using these data and other torsional data as given in Equation 5-1. From this, four values of shear modulus were computed from each load-unload cycle.

Table 5-6 summarizes the values of the shear modulus of the glulam specimens calculated from each loading-unloading phase in both clockwise and anticlockwise directions. The average values of the shear modulus of each timber specimen, which was determined by averaging the four measured values of shear modulus from all loading and unloading phases, are also listed in the table. The calculated shear modulus ranges from 593 to 757 MPa with a mean value of 649 MPa. The difference can be explained by the fact that inhomogeneity and the variability of the wood specimens as well as the presence of defects such as knots affect the overall stiffness of the wood specimens.

In addition, it can be seen that the average values of shear modulus calculated for each trial test are very close to each other, although there is a small difference between these values measured in the first two trials and those measured in the last two trials. These results are proven in Figure 5-39 which represents graphically the average the shear modulus of test specimens calculated in each trial test. For all torsion specimens, the average values of the shear modulus calculated in the first and second trials are approximately equal to each other and this is true for those measured from the third and fourth trials. All of these values are in good agreement and relatively close to each other with a difference ranges from 1% to 5%. Furthermore, from column 7 in the above-mentioned table, it is obvious that the shear modulus' values obtained from the first two torsion tests are relatively higher than those obtained from the last two torsion tests.

Table 5-6: Shear modulus of the torsion samples in clockwise and anti-clockwise directions.

Average shear modulus (MPa)							
Specimen ID	Trial No.	Clockwise direction		Anti-clockwise direction		Average	COV%
		Loading	Unloading	Loading	Unloading		
HT002	1	670	671	667	654	666	1.20
	2	669	671	670	674	671	0.32
	3	644	653	655	652	651	0.76
	4	642	653	648	651	649	0.74
HT003	1	627	625	623	627	625	0.29
	2	643	641	639	640	641	0.23
	3	643	647	641	647	644	0.46
	4	642	648	641	646	644	0.52
HT004	1	700	699	680	681	690	1.54
	2	697	702	687	684	692	1.26
	3	675	673	670	670	672	0.36
	4	672	673	675	670	673	0.30
HT005	1	672	673	662	669	669	0.72
	2	669	673	662	668	668	0.65
	3	644	650	647	644	646	0.44
	4	641	649	647	645	645	0.52
HT006	1	753	755	751	744	751	0.62
	2	750	756	757	744	752	0.76
	3	729	737	735	731	733	0.49
	4	726	737	728	732	731	0.64
HT007	1	627	626	627	623	626	0.28
	2	623	625	627	622	624	0.37
	3	606	610	605	604	606	0.45
	4	605	610	606	605	607	0.40
HT008	1	671	674	666	669	670	0.51
	2	670	672	664	668	669	0.50
	3	668	671	657	654	663	1.21
	4	666	671	658	657	663	1.06
HT009	1	626	626	622	633	627	0.72
	2	627	627	624	632	627	0.54
	3	598	605	595	602	600	0.73
	4	598	606	593	602	599	0.94
HT010	1	628	630	610	613	620	1.64
	2	626	629	611	612	619	1.52
	3	613	617	614	613	615	0.30
	4	613	618	614	613	614	0.37

Specimen ID	Trial No.	Loading	Unloading	Loading	Unloading	Average	COV%
HT011	1	638	638	626	627	633	1.06
	2	636	641	627	625	632	1.16
	3	608	613	602	611	608	0.78
	4	604	609	601	608	605	0.66
HT012	1	670	673	662	667	668	0.71
	2	669	671	664	667	668	0.45
	3	638	638	633	639	637	0.40
	4	635	641	636	639	638	0.38

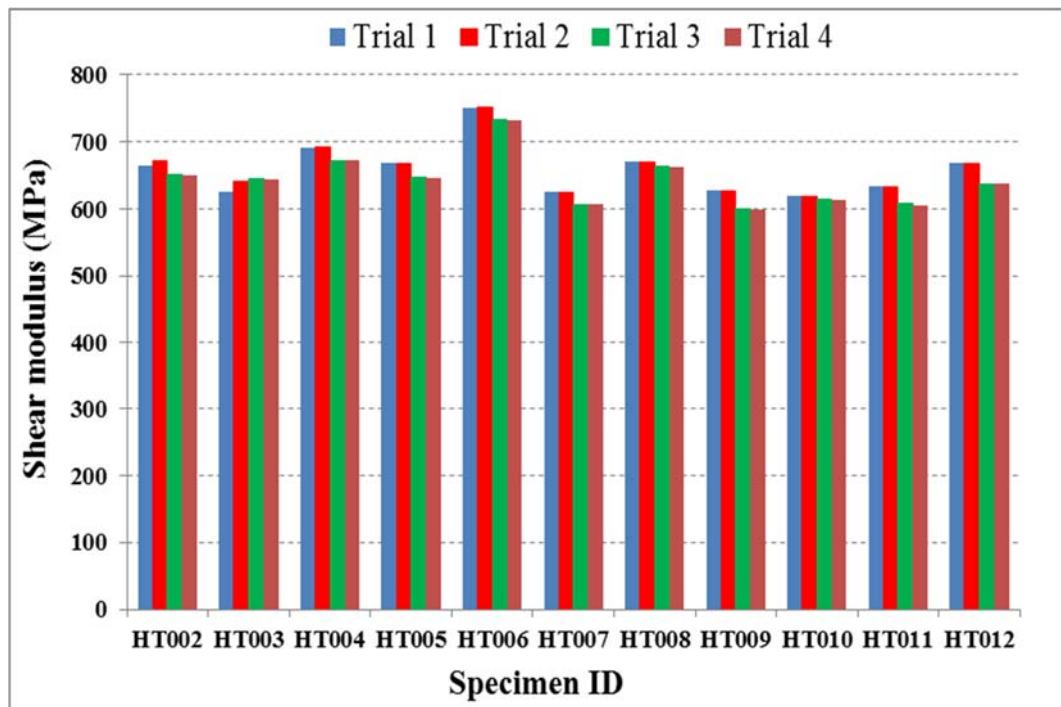


Figure 5-39: The average shear modulus of the torsion specimens calculated from each trial torsion test.

Table 5-7 presents the experimental average values of the shear modulus of each specimen calculated from all trial tests for each loading and unloading in both the clockwise and counter clockwise directions. The G_{Avg} indicated in this Table represents the average shear modulus of all loading cycles of a test specimen,

whereas $G_{\text{Avg-dir}}$ represents the average shear modulus of each loading cycle of all tested specimens. Coefficients of variation COV as well as the standard deviation are also listed. From the loading and unloading cycles, the average values of shear modulus range from 648 to 655 MPa with a consistent standard deviation of (37-39) and COV of (5.7-6.1%). The small and consistent values of COV may indicate that the torsion test is suitable for determining the shear modulus since the torsion specimen will be under pure torsion. From Table 5-7, the highest average values of shear modulus was found in specimen 06 and was about 742 MPa. The lowest values of the shear modulus of about 620 MPa was found in specimens HT007, HT009, HT010 and HT011. Figure 5-40 demonstrates a graphical representation of the average shear modulus obtained for all glulam beams. In this figure, the average G results for each of the 11 glulam beams (HT002- HT012) listed in Table 5-7 are compared relative to the average shear modulus of all beams.

Table 5-7: Average shear modulus of each of the torsion samples in all trial tests.

Specimen	Average Shear modulus (MPa)				G_{Avg}
	Clockwise direction		Anti-clockwise Direction		
	Loading	Unloading	Loading	Unloading	
HT002	656	661	659	659	659
HT003	639	640	636	640	639
HT004	686	687	678	676	682
HT005	656	661	655	656	657
HT006	740	746	743	738	742
HT007	615	618	616	614	616
HT008	669	672	661	662	666
HT009	612	616	608	617	613
HT010	619	623	612	613	617
HT011	621	625	614	618	620
HT012	653	656	649	653	653
$G_{\text{Avg-dir}}$	651	655	648	650	649
Std	38	38	39	37	
COV	5.8	5.9	6.1	5.7	

The overall average G of all of the fabricated glulam beams tested in torsion is 649 MPa. This value agrees well with the published value of the same board of glulam beam GL24 and conforms to the requirements of BS EN 14080 (2009) as shown in Table 5-8 which gives characteristic material properties for homogenous and combined glulam members.

Table 5-8: Relative characteristics properties for homogenous and combined glulam(BS EN 14080 (2009)).

GluLam strength classes	GL24	GL28	GL32	GL36
Bending Strength (N/mm ²)	24	28	32	36
Bending MoE (N/mm ²)	11500	12500	13500	14500
Shear Modulus (N/mm ²)	650	650	650	650
Density (kg/m ³) *	380 (350)	410 (380)	430 (410)	450 (430)

* The density values are indicative properties with the combined GluLam values in (brackets)_

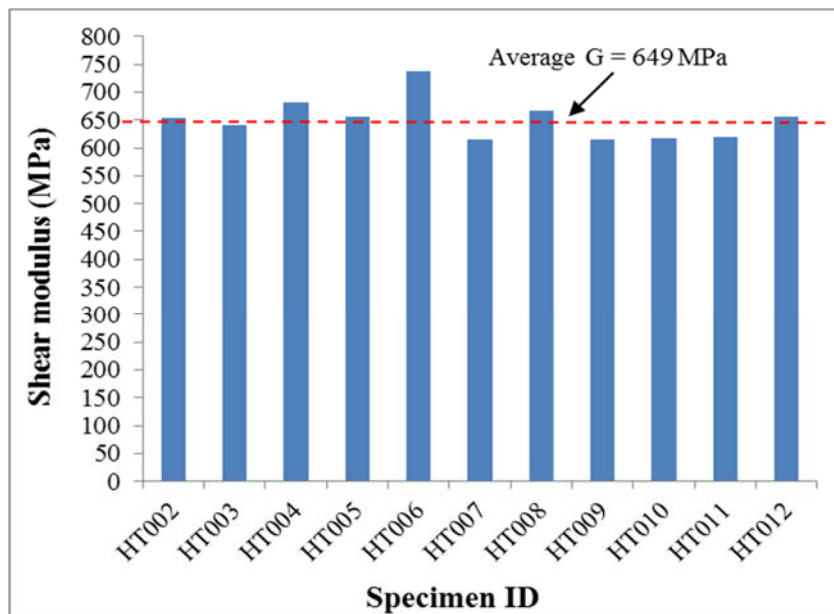


Figure 5-40: The average shear modulus of the torsion specimens.

5.4.4.4 Effects of the Direction of the Applied Torque and Loading Phases on the Values of Shear Modulus

To assess possible misalignment of the test specimens and to observe whether inducing torque in a clockwise or anticlockwise direction influences the torsional behaviour and hence the shear modulus of the specimens, the torsion tests were conducted on each torsion specimen under cyclic loading. Each torsion test consists of phases of torque loading and unloading in a clockwise direction, followed by loading and unloading phases in an anticlockwise direction. From the results of shear modulus contained in Table 5-6, it can be observed that the experimental values of shear modulus measured for all trial tests conducted on each torsion samples are consistent regardless of the direction of the torque or the loading phases. However, there is a small deviation which is expected for engineered wood products such as glulam beams. As mentioned before, the experimental values of shear modulus are in good agreement and relatively close to each other with a difference range from 1% to 5%. This may indicate that shear modulus is less sensitive to torque direction as there was no significant influence of the torque direction on the measured shear modulus.

To assess the correlation between these measurements, the correlation between the values of shear modulus measured in clockwise and anticlockwise directions under torque loading and unloading phases was determined by plotting their values against each other. As shown in Figure 5-41, the values of the G measured during loading in the clockwise direction correlate well with those measured during loading in the anticlockwise direction. This is also true for the G measured during unloading in the clockwise and anticlockwise directions. As can be seen from the figure, a very strong correlation was obtained with an R square value of about 0.98 and 0.98, respectively. It is clear that there is a low variability in the test results and this is expected for engineered wood products such as glulam beams. No significant amount of difference was found during all loading phases.

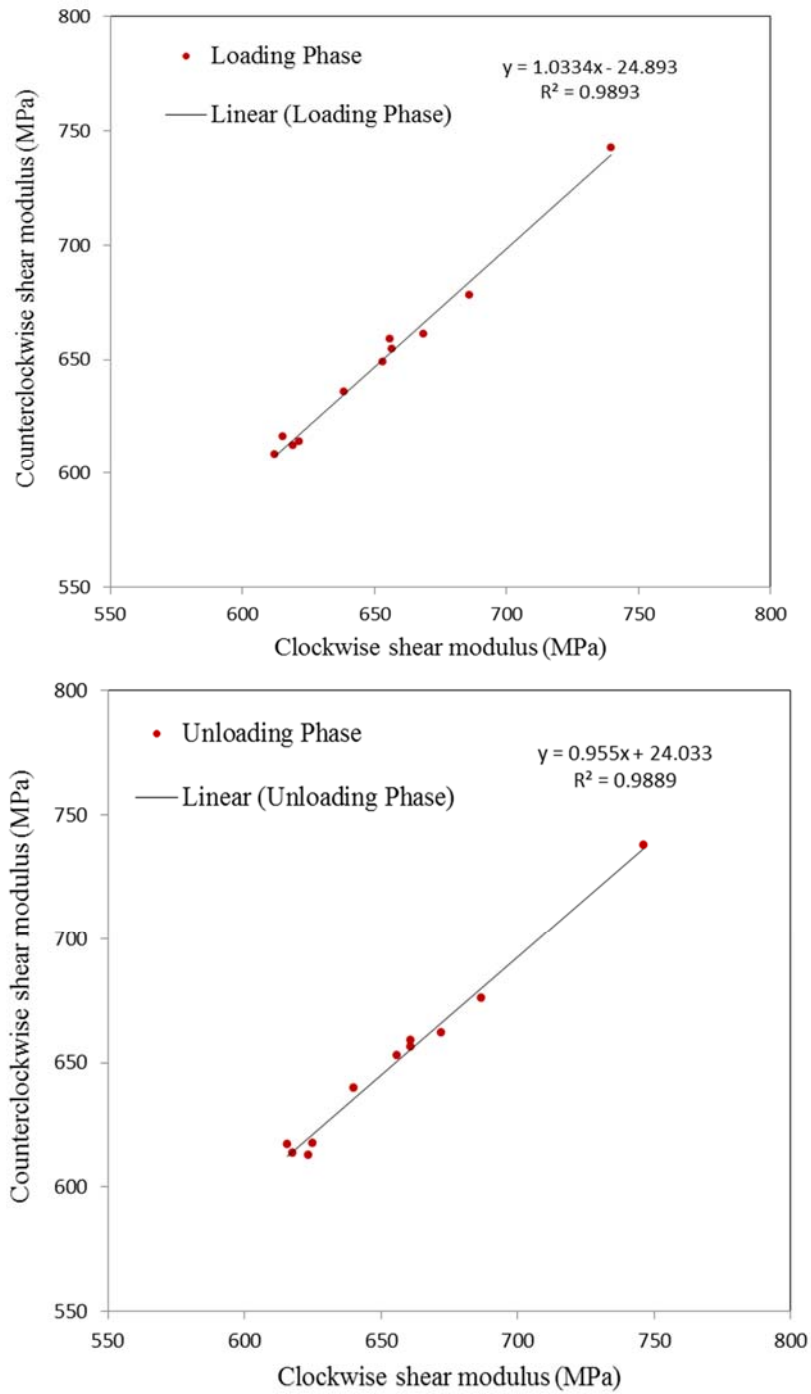


Figure 5-41: The correlation between the values of shear modulus measured in clockwise and anticlockwise directions under torque loading (top) and unloading (bottom) phases.

5.4.4.5 Influence of Inverting the Glulam Samples

To investigate the effects of inverting the torsion samples on the torsional behaviour, sample HT010 was tested under torsional loads in two ways: the right way up and upside down. Therefore, two names, HT010A and HT010B, were defined for this specimen to define the right way up and upside down respectively. Table 5-9 reports the average shear modulus of this specimen calculated in both directions. When installing torsion specimens the right-side up, it can be seen that the average values of shear modulus calculated from the first and second trials are relatively higher than those measured from the third and fourth trials. On the other hand, when inverting specimen HT010, the average values of the shear modulus calculated from the first and second trials are relatively smaller than those calculated from the third and fourth trials. It can be concluded that mounting the torsion specimens the right way up during the torsion test yields higher values of shear modulus than those obtained when inverting the specimen, although this finding was based on only a single piece of glulam beam, specimen HT010.

Table 5-9: The average shear modulus of specimen HT010 calculated in different ways.

		Average shear modulus (MPa)				Average	COV%
		Clockwise direction		Anti-clockwise direction			
Specimen ID	Trial No.	Loading	Unloading	Loading	Unloading		
HT010A	1	628	630	610	613	620	1.64
	2	626	629	611	612	619	1.52
	3	613	617	614	613	615	0.30
	4	613	618	614	613	614	0.37
HT010B	1	608	612	609	618	612	0.71
	2	607	613	608	619	612	0.86
	3	629	634	624	629	629	0.69
	4	628	633	623	629	628	0.68

5.4.4.6 Calibration Results of the Stereo Camera Systems

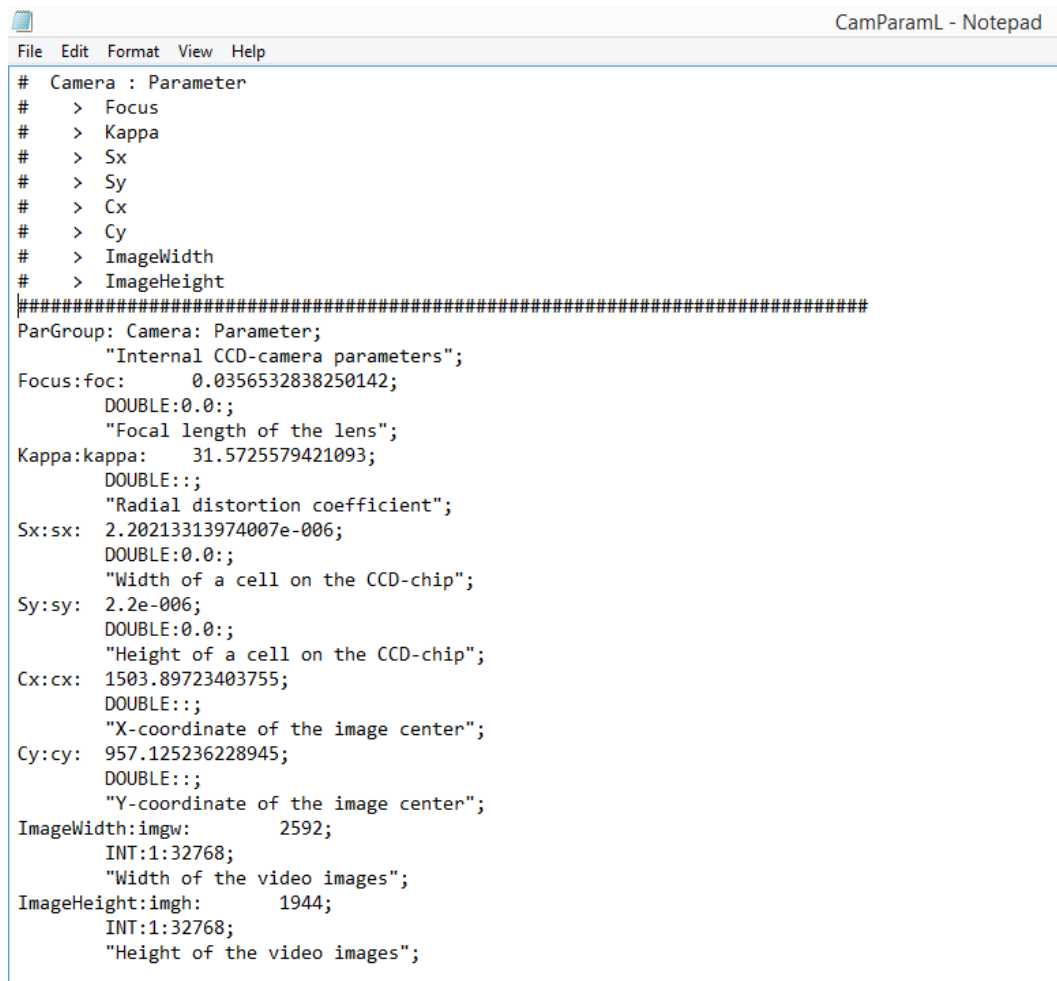
In order to reconstruct the 3D coordinates and hence their rotational deformations of the photogrammetric targets captured by the stereo cameras, the internal as well as the external parameters of the stereo camera systems were determined by performing the binocular stereo camera calibration of each system using the image processing software. This was achieved via a least square solution with suitable chosen parameters of the cameras that can be determined from the specification of the camera sensor and lens. Table 5-10 and 5-11 show selected examples of the internal as well as the external parameters, including the rotation angles and the translation vector determined from the first stereo system (camera 1 and 2). The file containing the calibration parameters of the left camera, generated by the calibration procedure of HALCON, is shown in Figure 5-42. A screen-shot of the developed GUI during the process of calibrating the stereo camera system is shown in Figure 5-43.

Table 5-10: Internal camera parameters of the first stereo camera system.

Camera : Parameter	Description	Unit	Left Camera	Right Camera
Focus	Focal length of the lens	m	0.035	0.035
Kappa	Radial distortion coefficient	m ⁻²	31.57	-14.16
Sx	Width of a cell on the CCD-chip	m	2.2e-006	2.2e-006
Sy	Height of a cell on the CCD-chip	m	2.2e-006	2.2e-006
Cx	X-coordinate of the image centre	Pixels	1503.89	1424.04
Cy	Y-coordinate of the image centre	Pixels	957.12	992.70
ImageWidth	Width of the images	Pixels	2592	2592
ImageHeight	Height of the images	Pixels	1944	1944

Table 5-11: 3D pose parameters (rotation and translation).

Translation vector (X Y Z [m])	X	0.175
	Y	-0.008
	Z	0.000
Rotation angles [degree]	Rot(X)	359.68
	Rot(Y)	355.53
	Rot(Z)	359.16



```

# Camera : Parameter
# > Focus
# > Kappa
# > Sx
# > Sy
# > Cx
# > Cy
# > ImageWidth
# > ImageHeight
#####
ParGroup: Camera: Parameter;
  "Internal CCD-camera parameters";
Focus:foc: 0.0356532838250142;
  DOUBLE:0.0;
  "Focal length of the lens";
Kappa:kappa: 31.5725579421093;
  DOUBLE:;;
  "Radial distortion coefficient";
Sx:sx: 2.20213313974007e-006;
  DOUBLE:0.0;
  "Width of a cell on the CCD-chip";
Sy:sy: 2.2e-006;
  DOUBLE:0.0;
  "Height of a cell on the CCD-chip";
Cx:cx: 1503.89723403755;
  DOUBLE:;;
  "X-coordinate of the image center";
Cy:cy: 957.125236228945;
  DOUBLE:;;
  "Y-coordinate of the image center";
ImageWidth:imgw: 2592;
  INT:1:32768;
  "Width of the video images";
ImageHeight:imgh: 1944;
  INT:1:32768;
  "Height of the video images";
  
```

Figure 5-42: A screen shot of the calibration parameters of the left camera generated by the calibration procedure of HALCON.

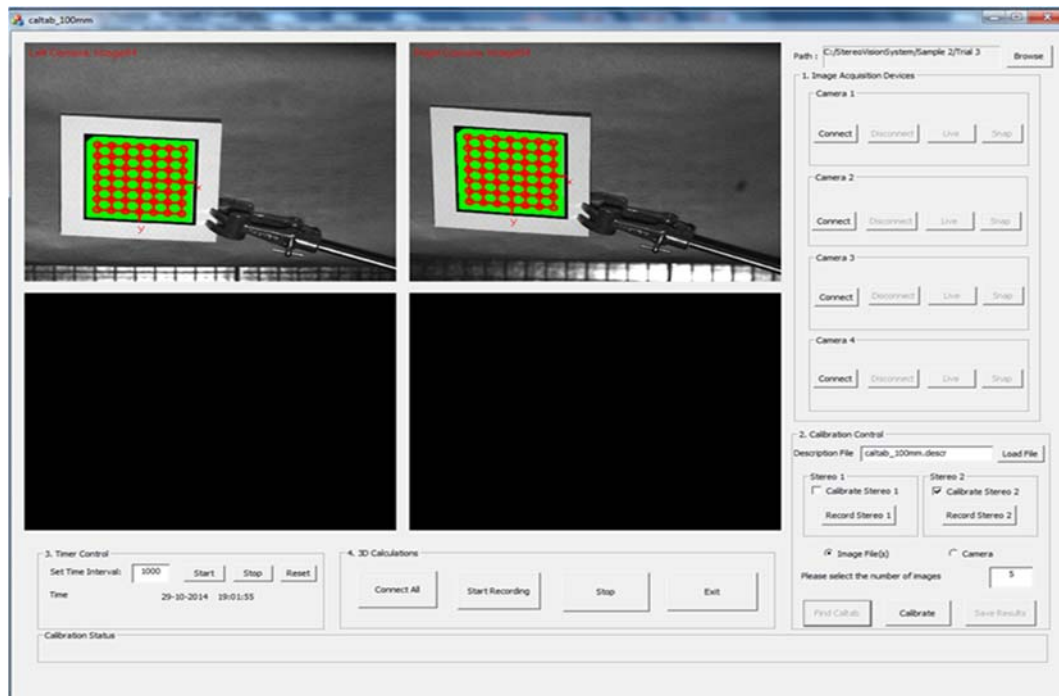


Figure 5-43: A screen shot of the developed GUI during stereo camera calibration.

5.4.4.7 Target Tracking and 3D Reconstruction

The image processing algorithm, which was developed and described in Chapter 2, is described briefly in this section. This utilized the photogrammetric approach which is based on the comparison between two images acquired during the test, one before and after deformation. Figure 5-44 demonstrates the concept and steps involved in the algorithm. The process starts with reading the calibration files and displaying the stereo images of the timber sample recorded from the left and right cameras during testing. Based on their shape and size, the potential targets were determined and tracked from the two sequences of stereo images using the sub pixel-precise segmentation method. These targets were fitted to ellipse shapes and their image coordinates in both the left and right images were measured. The 3D coordinates of the targets expressed in the camera coordinates of the left camera were determined using the theory of triangulation (Hartley and Zisserman, 2003). These coordinates were then used in the calculation of the displacements and rotations of the targets during the period of tests.

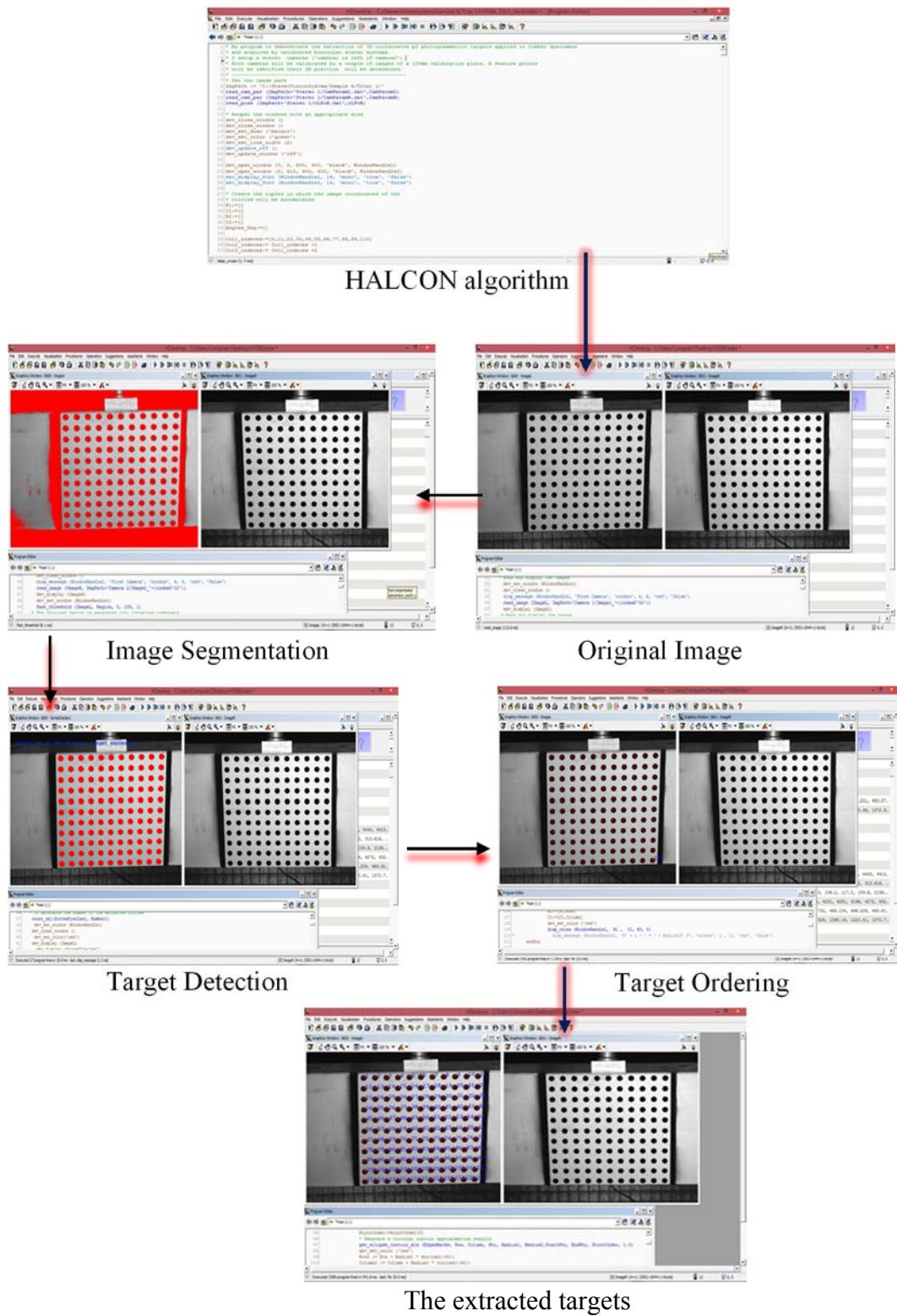
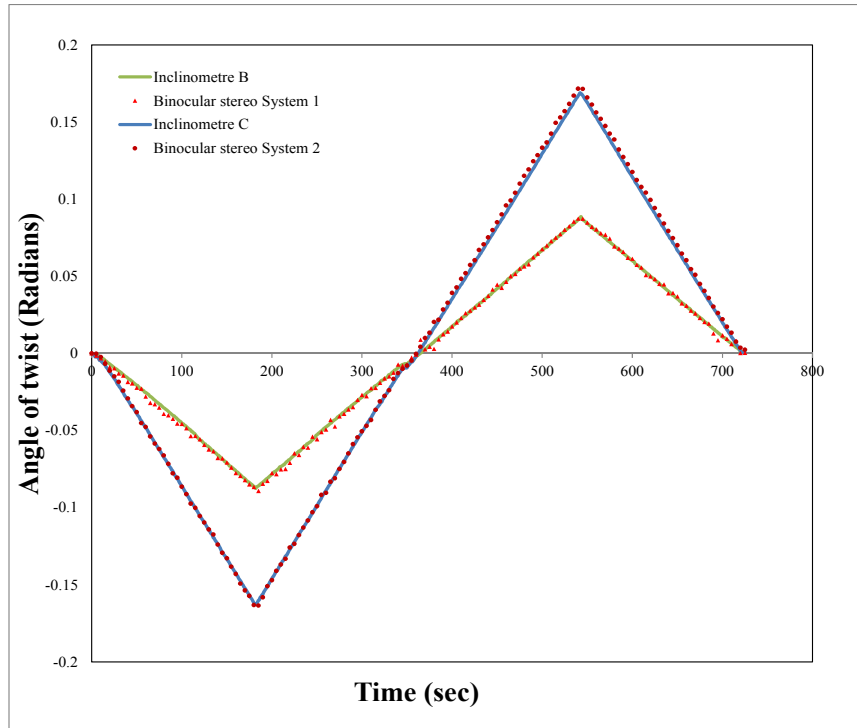


Figure 5-44: The image processing steps for extracting the targets.

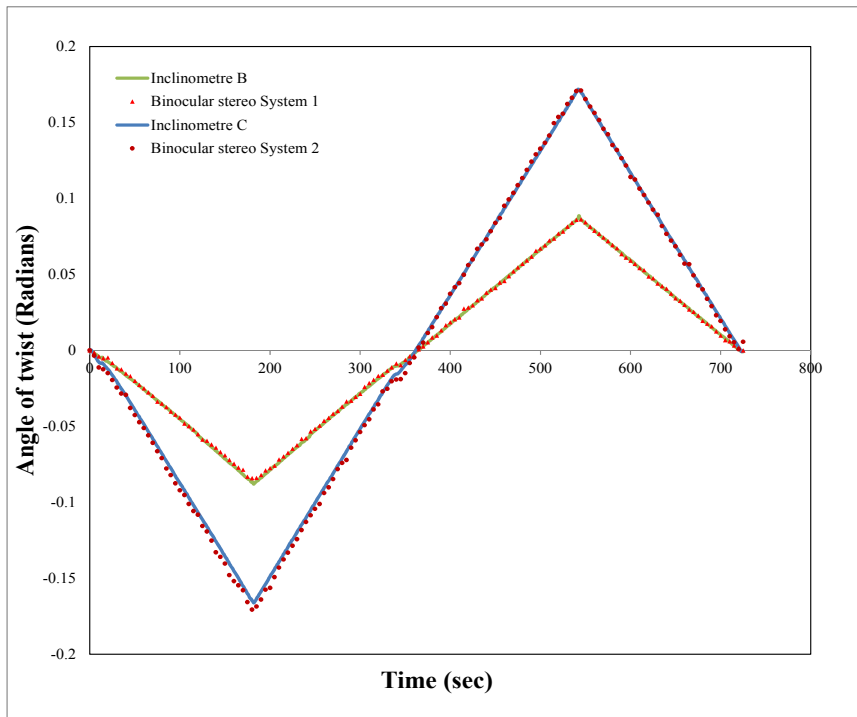
5.4.4.8 Comparison of Angular Deformations Measured by Inclinometers and the Non-contact Measurement Systems

To understand the differences between the rotations of the long and short sides of the cross section, the rotations of the photogrammetric patterns 1 and 2 and the rotations of the inclinometers B and C, were plotted in the same figure. These data were measured in both clockwise and anticlockwise directions under torque loading and unloading phases. Figures 5-45a) and 5-45b) show some selected examples of these comparisons and indicate remarkable results. It is evident that a good agreement between the two methods has been observed and this indicates that the measurements of the rotations of the short side with inclinometers are acceptable.

To investigate the correlation between the measurements, the rotation results of inclinometers and stereo camera systems were plotted against each other and a very strong correlation was observed for each glulam timber specimen. Selected examples of this comparison are shown in Figures 5-46a) and 5-46b) in which the rotations of specimen HT004 measured in the torsional direction by the inclinometers B and C which are measured by the first and second binocular stereo systems, were plotted against each other. These figures provide further evidence of this when considering the correlation of determination (R^2) of the angular measurements of inclinometers vs. stereo camera systems. From the results shown in these figures a high degree of correlation with a value of R square equal to 0.999 was observed.

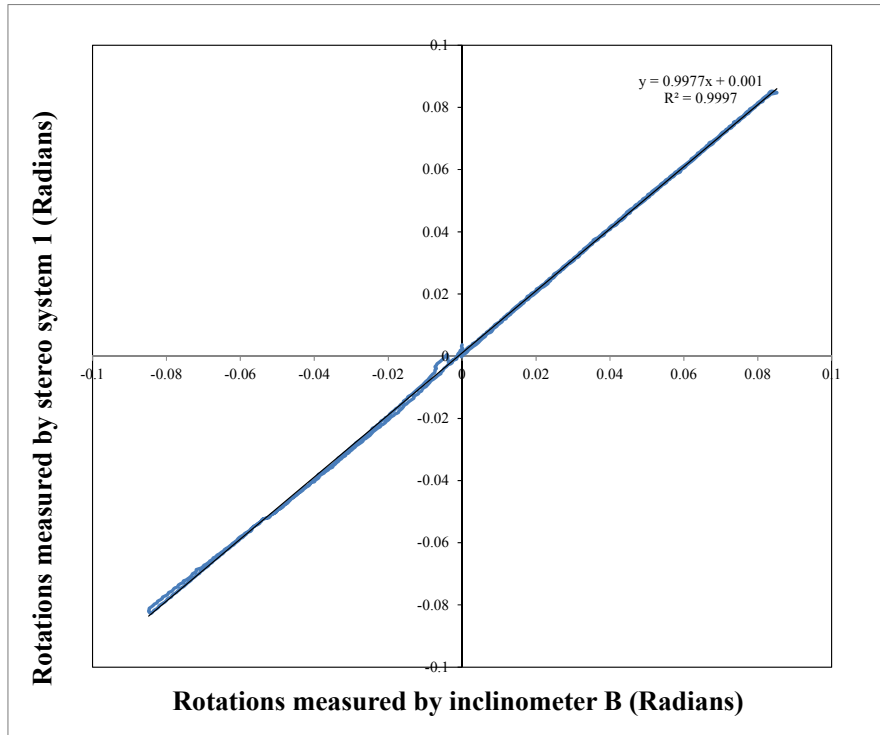


(a)

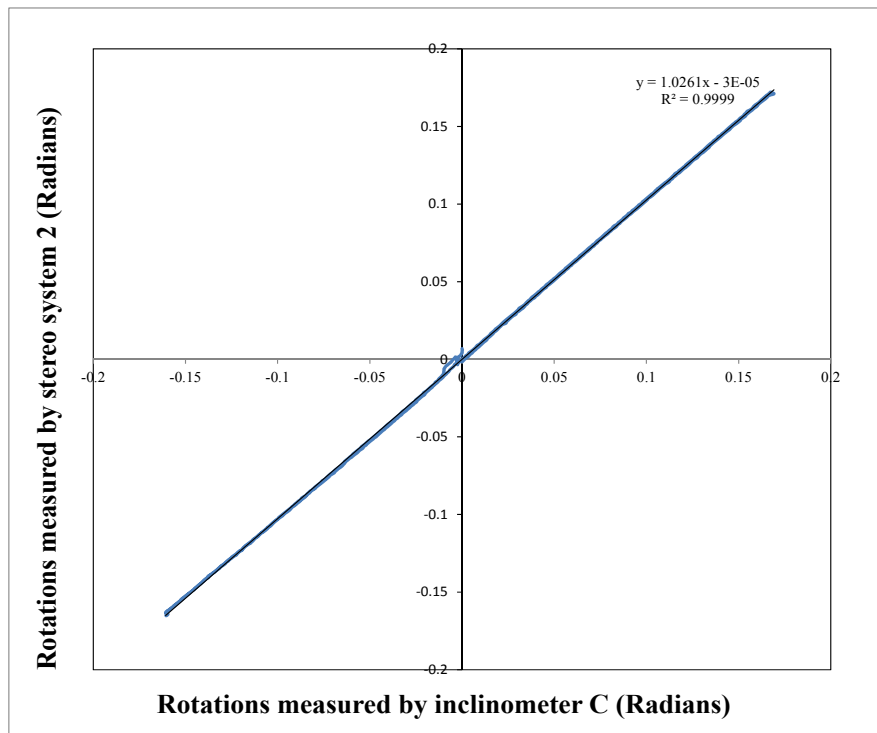


(b)

Figure 5-45: Comparison between inclinometers and optical measurements for a) sample HT005 in the first trial torsion test, and b) sample HT009 in the first trial torsion test.



(a)



(b)

Figure 5-46: Comparison of the rotations measured in specimen HT004 between a) between inclinometer B and the stereo camera systems 1 and b) inclinometer C and the stereo camera systems 2.

5.4.4.9 Torsional Deformation along the Long Side of the Cross-section

It is essential to investigate the torsional deformation along the long side of the cross section to check if it face distortion during the torsional loadings. The traditional devices such as inclinometers can only monitor the torsional deformations at the points where the devices are installed. The non-contact binocular stereo systems were employed to measure the displacements along the long side of the cross section for each region of interest. As illustrated in Figure 5-47 the beam fixed at one end is subjected to torsion at the other end. In this study, two regions of interest, the left and right regions, were selected to be monitored by the non-contact binocular stereo systems. The first one is the left area which is very close to the fixed end. The second one is the right area which is close to the rotating end. These regions were placed under the inclinometers, as shown schematically in Figure 5-47. The photogrammetric patterns consist of 121 circular targets arranged in 11 columns and 11 rows. The columns are labelled L1 to L11 and each column contains 11 target points from P1 to P11. The central target was set to be an origin of the X-Y coordinate system.

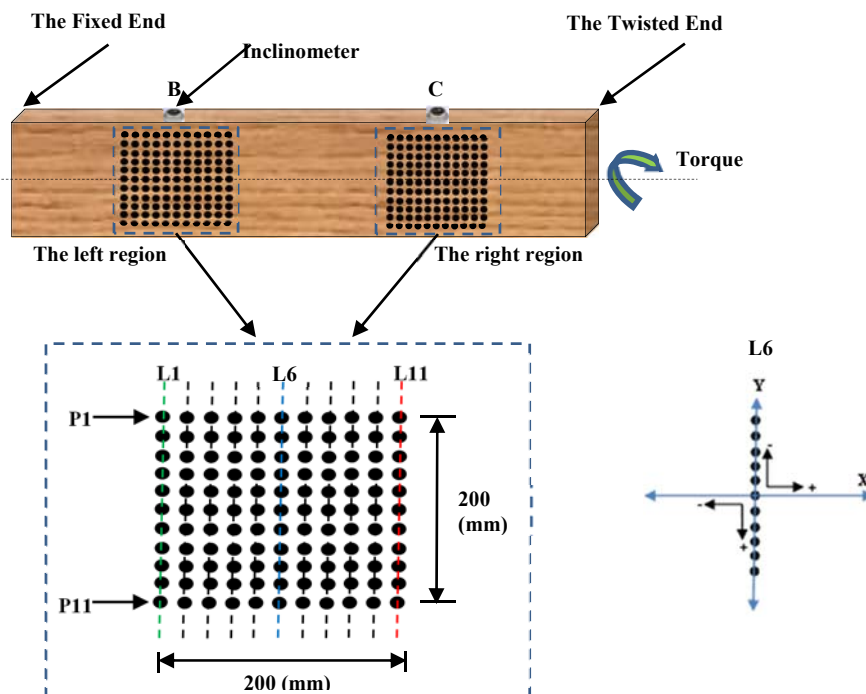


Figure 5-47: Illustration of targets arrangement in the torsion specimen.

After calibrating the stereo camera systems and finding the internal as well as the external parameters of these systems, the 3D coordinates of the photogrammetric targets were determined based on the procedure described in Section 5.3.4.7. These 3D measurements were then employed to measure the displacements along the long side of the cross section for each region of interest.

To investigate the displacements of the longer edge of the cross section occurring when subjected to a torsional loading, the warping displacements of the vertical targets exactly below the two inclinometers, B and C, were calculated for all loading and unloading phases. Figures 5-48 and 5-49 show some examples of the displacement measurements in the X and Y directions measured in column 6 of the left and right pattern, respectively. These displacements correspond to approximately one degree of torsional deformation. The deformations were plotted during loading and unloading in both the clockwise and anticlockwise directions. It can be seen from the above mentioned figures that the applied torque causes the longer side of the sections, which were plane prior to twisting, to deform in the axial direction, meaning that the plane cross sections no longer remain plane after twisting. The deformations of the cross section will affect the torsional stiffness of the glulam specimens.

As illustrated in the previously-mentioned figures, the displacements of the targets painted close to the fixed end deform differently from those close to the rotating end of the torsion specimen. Compared to the sections close to the fixed end, the sections close to the rotating end have larger horizontal displacements. It can also be seen that the photogrammetric target points along the tangential direction in each pattern follow similar deformations during loading and unloading cycles in both clockwise and anticlockwise directions. The torsional rotations are greater at the top and bottom of a section than in the middle of the section

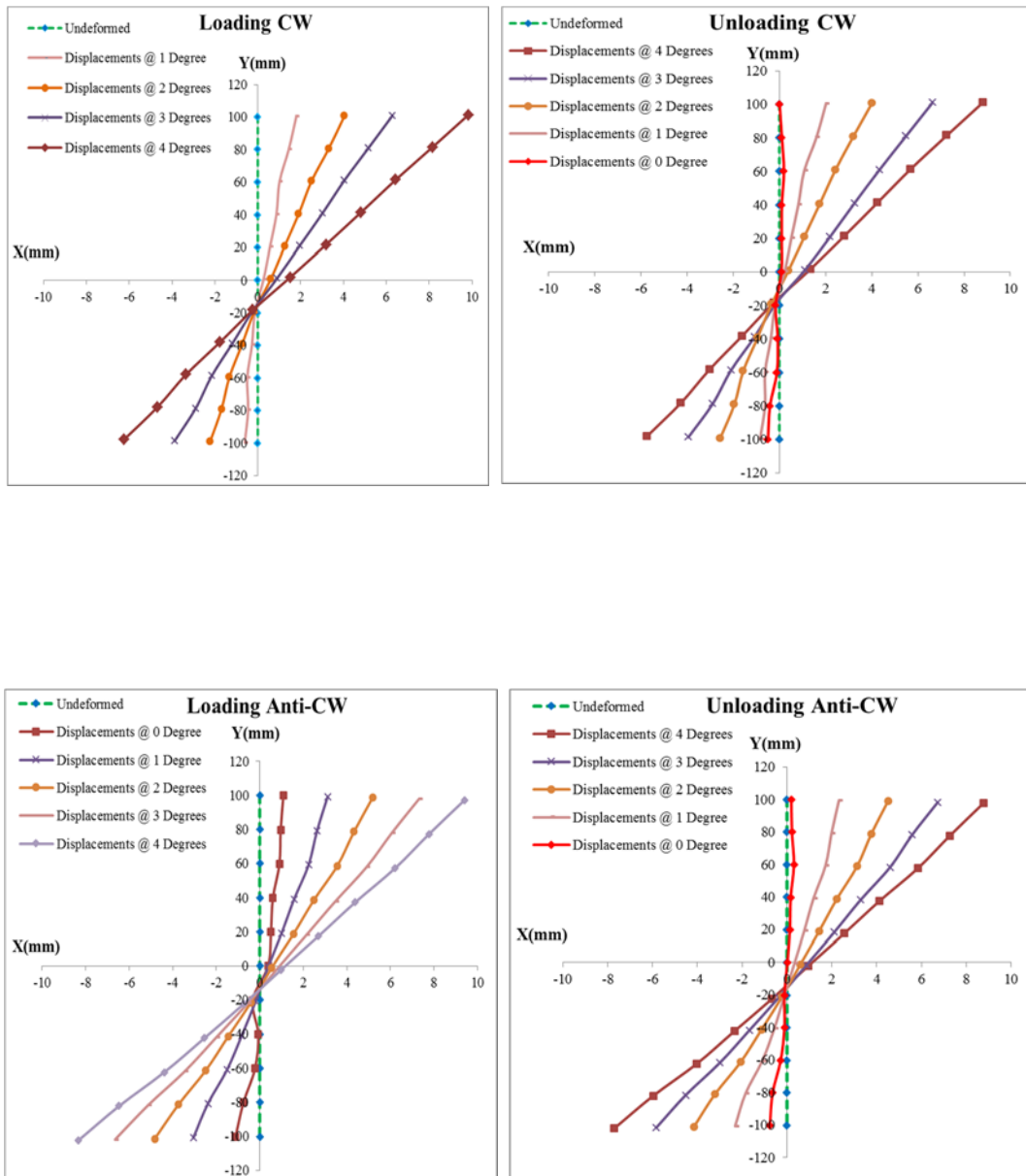


Figure 5-48: Deformations of points located on line L6 of the left pattern at different loading and unloading phases.

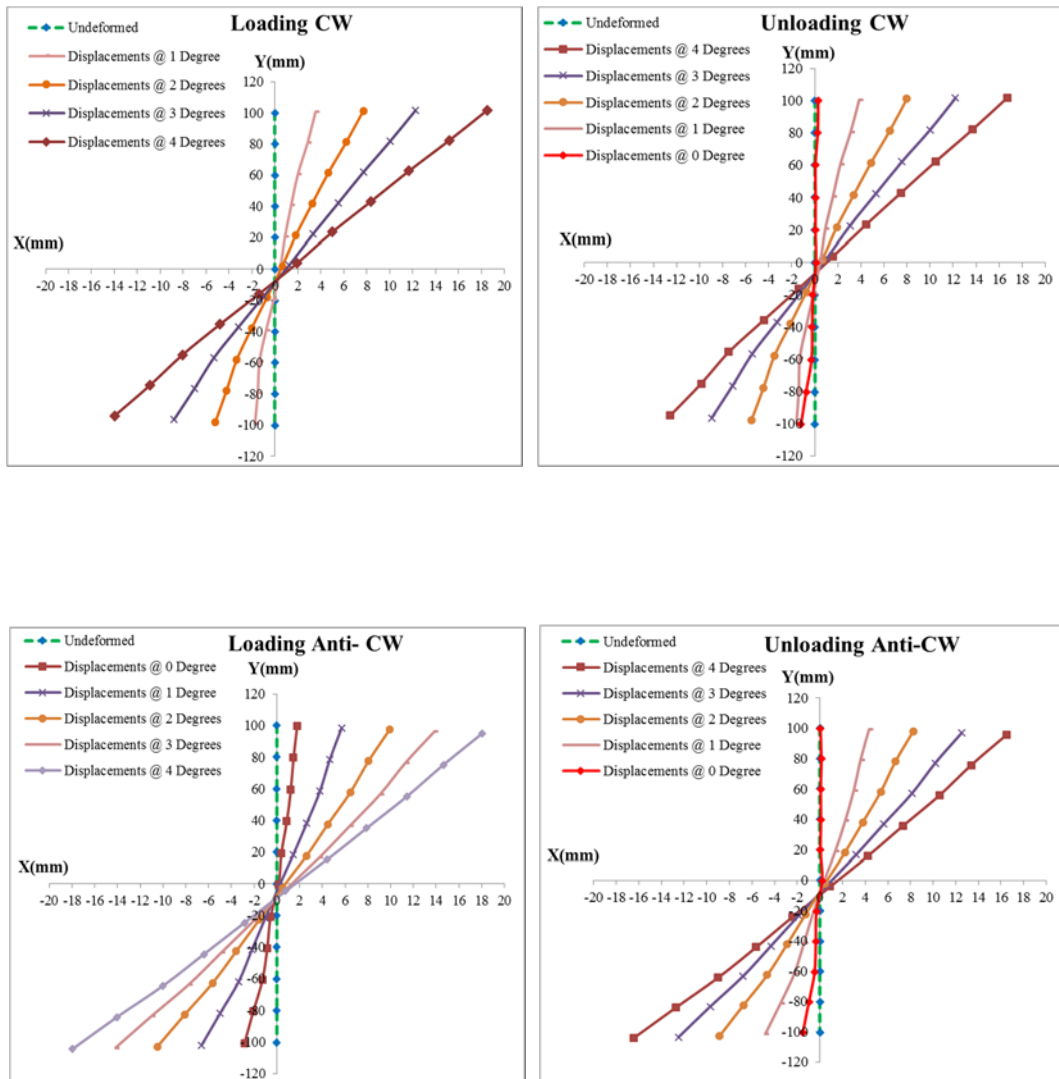


Figure 5-49: Deformations of points located on line L6 of the right pattern at different loading and unloading phases.

5.4.4.10 Effect of Shear Span on the Variation of Shear Modulus

The torsion specimens were non-destructively evaluated under torsional loading applied within the elastic range. It becomes essential to examine the effect of span variations on the shear modulus at different cross-sections. Therefore, based on the shape of the photogrammetric patterns, shown in Figure 5-50, three shear spans S1, S2, and S3 at the middle section of the torsion specimens were considered. The shear span, S1, is the distance between sections 1 and 6, representing a gauge length of 1420mm. The second shear span, S2, is the distance between section 2 and section 5 (the distance between inclinometers B and C), representing a gauge length of 1320mm and the third shear span, S3, is the distance between section 3 and section 4, representing a gauge length of 1220mm.

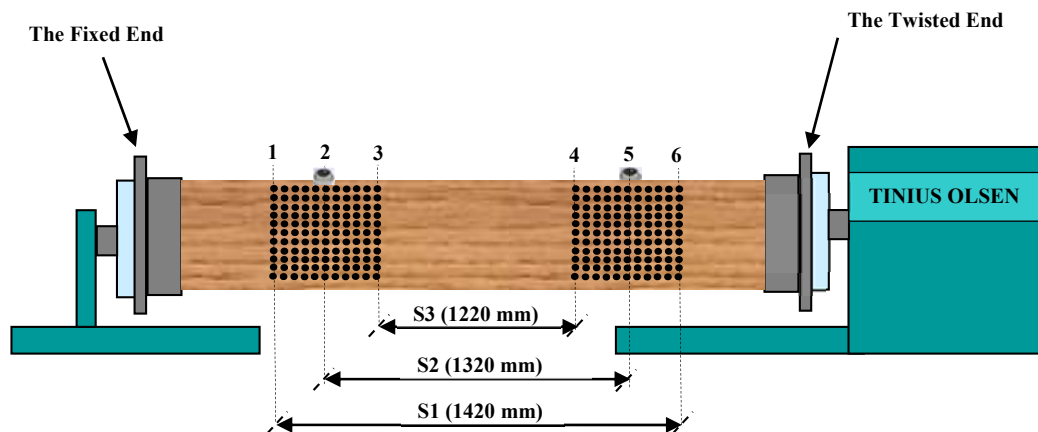


Figure 5-50: Diagram of different shear spans used to determine the shear modulus of various segments.

The values of torque in addition to the stereo images of the photogrammetric patterns were recorded continuously during testing. The relative rotation of each two cross-sections over their gauge length (shear span) was measured utilizing the 3D coordinates of the targets distributed on the longer side of the cross section. Using these data in addition to the geometry of the torsion specimens, the shear modulus values for each shear span were calculated using Equation (5.1) (Chapter 5).

Four trial torsion tests were conducted on each torsion specimen and the results were averaged. From these results, values of G were obtained for the three shear spans. Table 5-12 presents the calculated average values of the shear modulus of the three regions of each specimen. The G_{Avg} indicated in this Table represents the average shear modulus of all shear spans of a test specimen, whereas $G_{Avg-span}$ represents the average shear modulus of each shear span of all tested specimens. From Table 5-12, it can be observed that the average shear modulus varies significantly when considering the three different shear spans of each timber joist. By examining the values of shear modulus listed in the table for each test specimen, it is apparent that the shear modulus varies substantially with the different shear span. These results are provided graphically in Figure 5-51.

The largest shear modulus appears to occur at the lowest shear span which is far away from the gripping. On the other hand, the largest span which is very close to the gripping attained the smallest shear modulus. The same trend of variation was also observed in all test specimens. This result can be clearly observed from the charts plotted in Figure 5-51. The values of the shear modulus calculated in the shear span S2 are (10-16%) higher than those calculated in the larger span S1 and about (12-17%) lower than those calculated in the smaller span S3. For instance, the shear modulus of 613 MPa was attained for shear span S2 of specimen HT002 and was 11% higher than the average shear modulus of S1 and was 15% lower than the average shear modulus of S3. The main reason for this effect might be because the larger span considered in this study is between two sections and one of them is close to the rotating end of the test specimen. The rotation angles affect the shear stiffness and hence the values of shear modulus. The angle of twist in a given length is inversely proportional to the shear modulus.

From these results and within the selected shear spans, it can be concluded that the larger the shear span the smaller the value of shear modulus. The comparison suggests that testing joists in different shear spans are essential to evaluate the variations of the shear modulus values at these different gauge lengths.

Table 5-12: The shear modulus values of three spans of torsion specimens.

Average Shear Modulus (MPa)				
Specimen ID	Shear Span			G_{Avg}
	S1	S2	S3	
HT002	547	613	718	626
HT003	568	667	745	660
HT004	562	667	745	658
HT005	568	633	745	649
HT006	630	720	803	718
HT007	544	624	730	633
HT008	571	667	799	679
HT009	521	578	659	586
HT010A	495	561	651	569
HT010B	535	608	717	620
HT011	541	624	740	635
HT012	515	569	656	580
$G_{avg-span}$	550	628	726	634

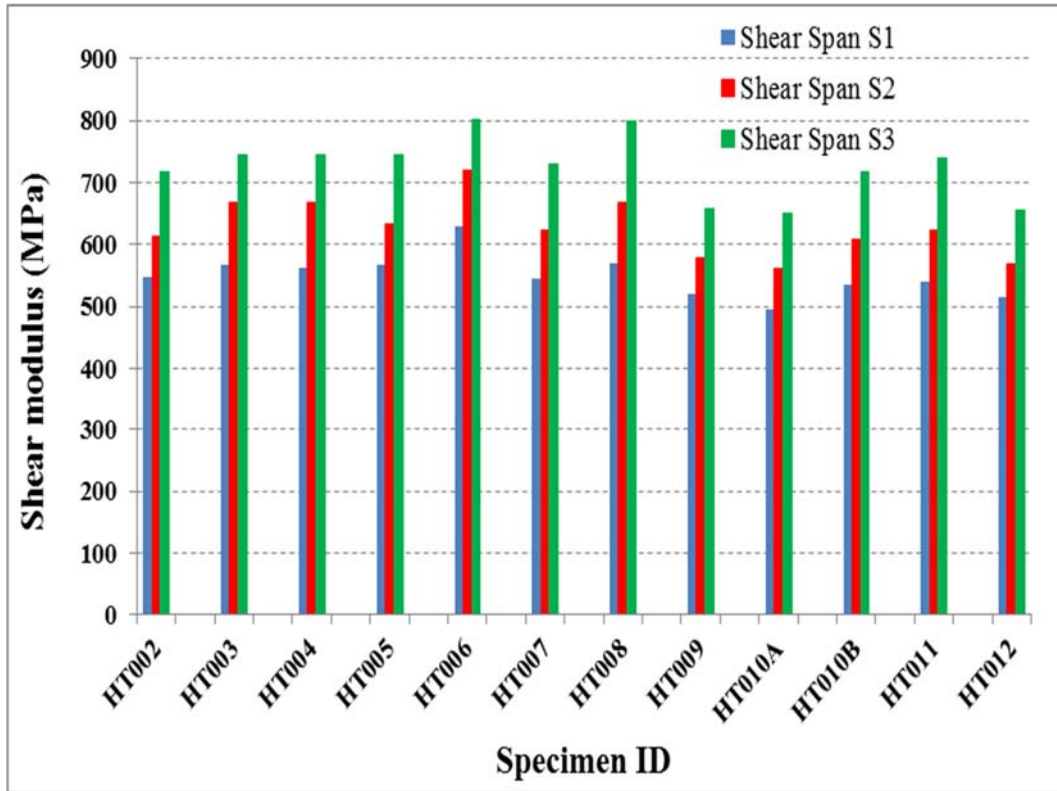


Figure 5-51: Variations of shear modulus at different shear spans.

5.4.4.11 Shear Modulus along the Long Side of the Cross-Section

To examine if the shear modulus is constant or varies along the depth of the torsion specimens, the central line (column) of the pattern was divided into four line segments, A, B, C, and D, as shown in Figure 5-52. The rotations of these segments of the patterns under torsion were calculated and compared. Figure 5-53 shows an example of the comparisons between the rotations of the different segments. From the figure, it is clear that the top segment, A, of the depth rotated more than the one at the bottom, B. The other two central segments, B and C, rotated in a range between the rotation measurements of A and D. All torsion specimens under all torsion tests followed the same trend of the rotations of the depth portions.

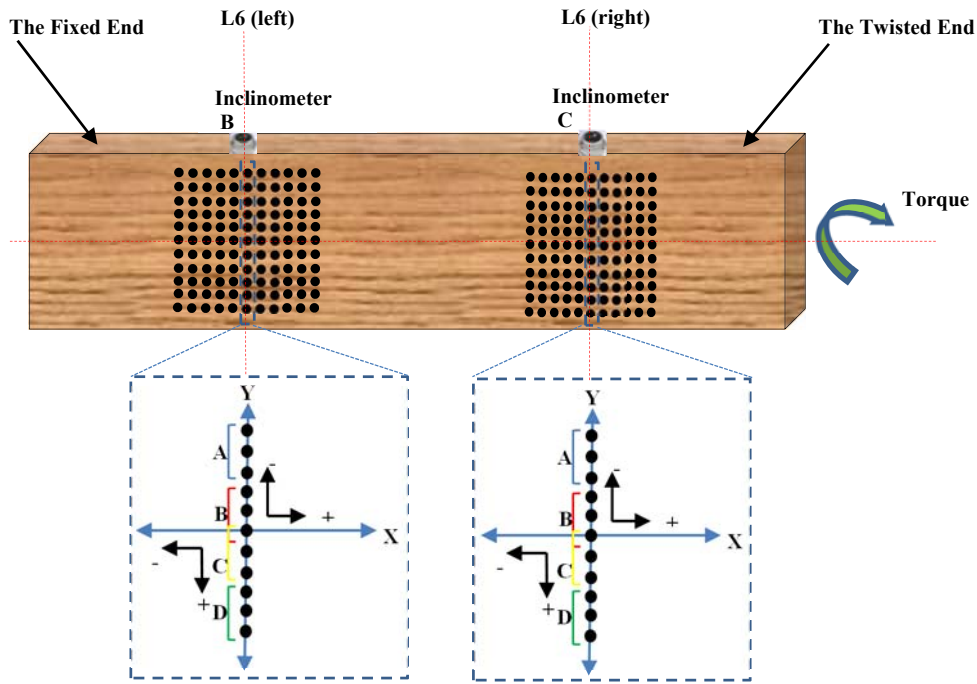
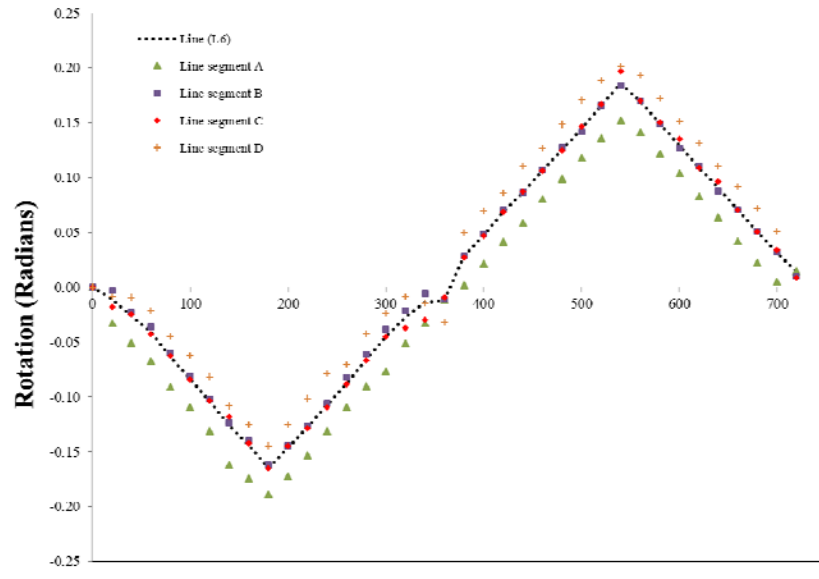


Figure 5-52: Illustration of the regions selected to evaluate their shear modulus.

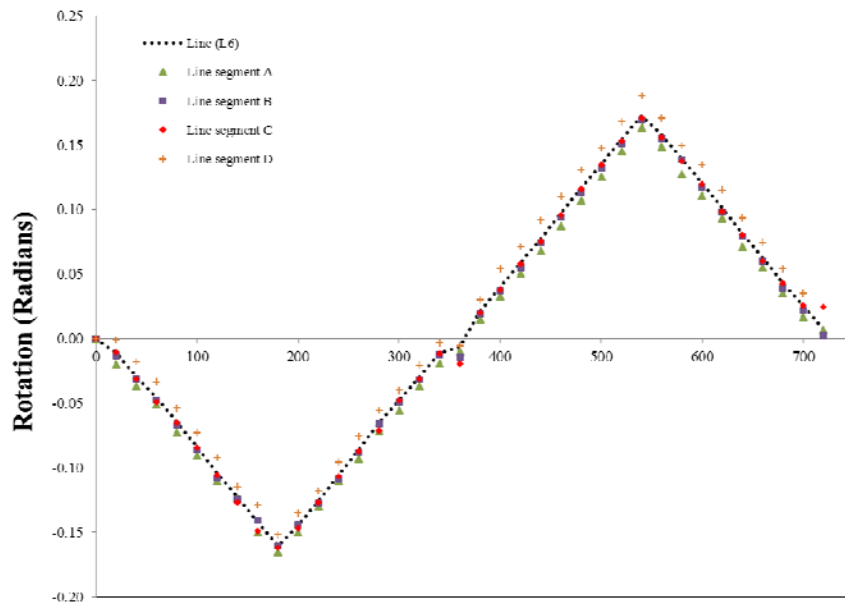
The relative twist was obtained from the difference between the two angular measurements and therefore the values of the shear modulus for each torsion specimen were calculated using Equation 5.1. Table 5-13 summarizes the values of shear modulus calculated from each segment of line L6. From the table, it can be seen that there are large degrees of variability in the calculated shear modulus values. The difference can be explained by the fact that the variability of glulam laminates affects the stiffness of the depth portion of the wood specimens. The repetition of the torsion tests conducted sequentially on the specimens yield slight differences in the values of shear modulus.

Figure 5-54 represents the average shear modulus of the glulam specimens calculated from all trial torsion tests. It can be seen that the shear modulus varies significantly across the depth of the torsion specimens. The test results show that segment C has the lowest shear modulus in comparison to other segments of the cross section in the long side direction. For most of the torsion specimens, the segments A and D have the highest values of shear modulus and they are very close to each other. This result is expected since the top and bottom of the glulam beams, which face compression and tension, were made of a high-strength class of timber



Time (sec)

(a)



Time (sec)

(b)

Figure 5-53: Rotations of Line L6 and its segments during maximum loading in a clockwise direction for a) the left photogrammetric pattern b) the right photogrammetric pattern.

Table 5-13: Shear modulus of torsion samples at each line segment.

Average shear modulus (MPa)						
		Section ID				
Specimen ID	Trial No.	A	B	C	D	L6
HT002	1	613	571	636	619	617
	2	604	630	481	599	618
	3	552	681	678	584	617
	4	608	556	642	566	598
HT003	1	709	671	596	702	693
	2	619	637	650	659	650
	3	639	599	657	559	625
	4	599	675	647	559	650
HT004	1	591	712	639	631	657
	2	650	621	610	663	632
	3	686	818	474	675	698
	4	507	759	618	664	774
HT005	1	575	681	650	579	642
	2	677	658	648	578	659
	3	561	650	603	568	628
	4	542	579	611	619	604
HT006	1	788	779	785	678	756
	2	775	758	715	763	752
	3	801	653	618	756	708
	4	714	775	681	677	729
HT007	1	645	579	635	635	643
	2	625	668	579	608	650
	3	537	626	450	551	590
	4	586	584	496	575	612
HT008	1	650	657	700	690	678
	2	696	706	747	687	702
	3	626	704	549	643	636
	4	669	762	494	637	650
HT009	1	553	666	598	591	615
	2	610	558	583	563	583
	3	564	545	691	622	577
	4	562	596	592	588	589

Average shear modulus (MPa)						
Section ID						
Specimen ID	Trial No.	A	B	C	D	L
HT010A	1	574	527	517	581	548
	2	542	560	510	576	568
	3	622	561	487	503	561
	4	575	590	464	593	567
HT010B	1	664	483	545	572	586
	2	618	522	484	584	580
	3	652	529	572	543	640
	4	625	644	480	578	629
HT011	1	622	621	564	610	624
	2	624	617	558	602	616
	3	603	668	562	586	623
	4	611	679	586	576	632
HT012	1	565	569	535	435	560
	2	607	607	527	500	599
	3	559	610	550	423	551
	4	541	623	683	412	568

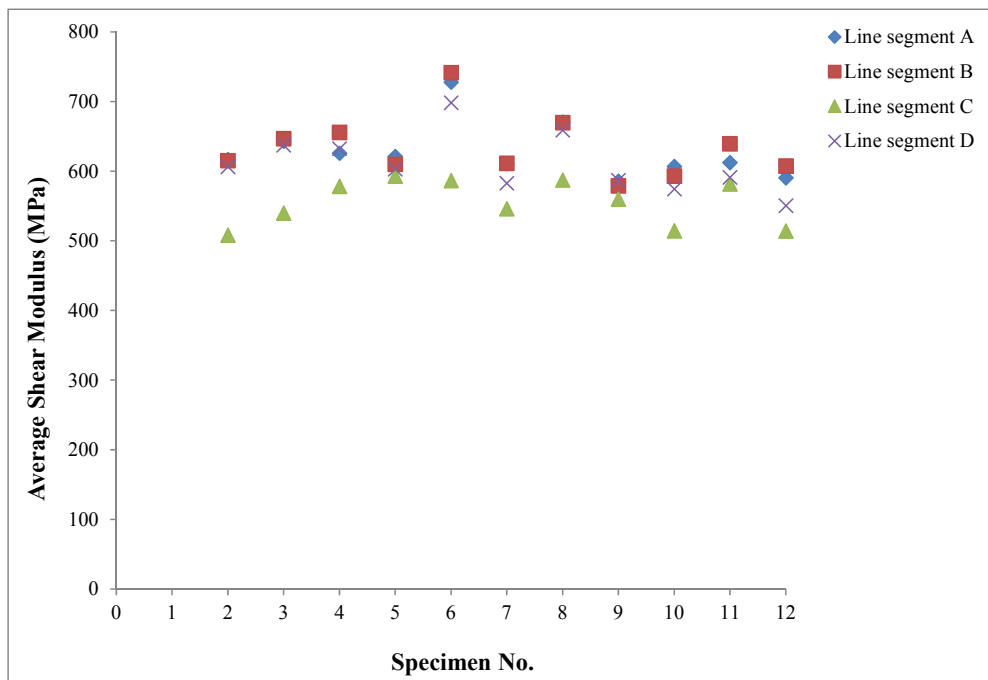


Figure 5-54: Variations of shear modulus along the long side of the cross section.

5.5 Summary

In this study, the new photogrammetric method has been employed to investigate the torsional behaviours of timber glulam beams. The powerful capability of the photogrammetric systems allowed more details of the torsion samples to be monitored. The accuracy of this method was validated by a comparison study which has been carried out between the photogrammetric method and the method of using conventional inclinometer sensors. Good agreement has been found between these two measuring systems. After confirming the accuracy of the proposed method, a further study on the shear displacement at cross-sectional level was carried out by tracking and measuring the displacement of the photogrammetric targets pre-painted on the sample surface. Significant non-linearity has been found from the measurement of the shear displacements along the long side of the cross-section. However, the average rotation shows clear agreements with the inclinometer readings.

The torsion experiments were designed to attempt to explore the effects of torque direction on the shear modulus. Torques of different magnitude were applied in loading and unloading cycles in both the clockwise and anticlockwise directions. The method of applying and releasing the torque in both directions was utilized so that both linearity and repeatability of the test results could be evaluated. The loading-unloading cycle was repeated four times and the final stiffness value is the average stiffness determined from the four loading cycles. Comparison of the loading and unloading phases revealed that applying torques to timber specimens in either a clockwise or anti-clockwise direction does not influence the torsional behaviour of the torsion specimens.

In order to further analyse and investigate how the direction of torque influence responses during the different phases of loadings, the shear modulus was calculated for the linear phase of the loading and unloading curves in both the clockwise and anti-clockwise directions. Comparison of the test results showed applying torques to timber specimens in either a clockwise or anti-clockwise direction does not influence the torque stiffness and hence the shear modulus. It was also observed

that loading and unloading in either of the two directions does cause only a little influence on the torque stiffness and hence the shear modulus of the glulam beams. The low variability in the test results is expected for engineered wood products such as glulam beams. The modulus of rigidity was determined to be 650 MPa which agrees well with the published values of G of the same strength grade of glulam beams.

One of the main advantages of using the photogrammetric approach developed in this research is the ability to monitor the torsional deformations at different locations, enabling the values of shear modulus at different cross-sections of the torsion specimens to be evaluated without the need to use more devices. By comparing shear modulus values of glulam beams measured based on different shear spans, it can be concluded that the larger the shear span the smaller the value of shear modulus. The comparison suggests that testing glulam beams in different shear spans is essential to evaluate the variations of shear modulus values at these different gauge lengths.

6. APPLICATION OF THE PROPOSED PHOTOGRAMMETRIC APPROACH TO STUDY THE PERFORMANCE OF DISPLACEMENT TRANSDUCERS

With the reliability of the results confirmed through the validation experiments presented in Chapters 4 and 5, the proposed photogrammetric method was also proposed and applied to monitor and evaluate the displacements of glulam timber specimens during the compression test. These measurements are essential to evaluate the values of modulus of elasticity (MOE) of glulam timber beams when considering the compression tests. Displacement transducers (LVDTs) are commonly used for assessing the deformation or displacement measurements of the compression specimens. However, limited research has been conducted to assess the performance of these devices on monitoring the deformation of the glulam timber samples, especially together with the system that attached them onto the sample surface during the compression test.

Experimental test series were conducted on nine timber samples in compression perpendicular to grain direction. The main objective of the experimental work presented in this chapter has been to assess the performance of LVDT displacement transducers during the compression test. After validating the proposed approach, its measurements were compared with the conventional measuring displacement transducers. The experimental work as well as the experimental results are provided in the following sections

6.1 Introduction

There are many different test methods that have been developed and adopted by different researchers to evaluate the mechanical properties of timber and timber-based composite materials. Among these methods and according to EN 408 standard (EN 408:2010, 2010), the compression test is used in timber as a method to determine modulus of elasticity (MOE) and some other elastic and strength properties of this material. The test results are of considerable importance as they are among those essential properties to be used to establish the product specifications or design. To understand the material characterizing the behaviour of glulam timber, it is essential to obtain accurate measurements of its material properties but this can be challenging, especially for commonly used properties such as the modulus of elasticity.

Measuring the deflections of the timber specimen accurately and effectively during the compression test plays an important role in evaluating the value and variations of the MOE. Displacement transducers are commonly used for assessing the deformation or displacement measurements of timber. These sensors have been widely used and proven to perform accurate, reliable, and immediate displacement measurements. However, the setup of these devices in timber during the compressive loading test is challenging and significantly more difficult. It requires applying a mounting system to accommodate the LVDTs and this system should be placed in contact with the surface of the specimen to be tested and this might affect their reading values. Moreover, limited research has been conducted to assess the performance of transducers on monitoring the deformation of timber samples, especially together with the system that is used to attach them onto the sample surface during the compression test. Therefore, an additional measurement technique that improves understanding the behaviour of these sensors during testing is the binocular stereo vision approach.

Monitoring tools using photogrammetry and image processing have been used in timber to measure mechanical properties, 3D displacements, or deformations at various points of the same specimen, as proposed in various experiments (Choi et

al., 1991, Dahl and Malo, 2009a, Dahl and Malo, 2009b, Franke et al., 2007, Garcia and Orteu, 2001, Maas and Hampel, 2006, Guindos and Ortiz). The binocular stereo vision approach is proposed and developed in this study for the deformation measurements. The binocular stereo vision is a non-contact measurement technique that can be used to extract reliable measurements of physical objects from stereo images. The main advantages of this technique compared to the traditional techniques are that it offers the capability to measure the three-dimensional (3D) location of any point located on the object's surface; in addition to that it can be used to monitor the deformations of the object at various locations without having to touch the object.

The main objective of the work presented has been to use the developed non-contact binocular stereo system for evaluating the performance of the LVDT displacement transducer during the compression test. Another objective of this project was to measure the displacements of the sample at various locations to understand its behaviour and give a basis for further studies. An experimental study was conducted to validate the proposed technique. After being validated, this technique was applied to an experimental study of timber specimens subjected to compressive loading perpendicular to grain in the elastic range. The contact-free technique is found to be promising as a method of determining the deflection of the timber specimens under loading. These measurements allowed evaluating the performance and reliability of the LVDT transducers as well as their mounting system which should be in contact with the timber specimen during compressive loadings. The methodology and measurement process performed in this study are discussed in the following sections and can be summarized in the workflow diagram shown in Figure 6-1.

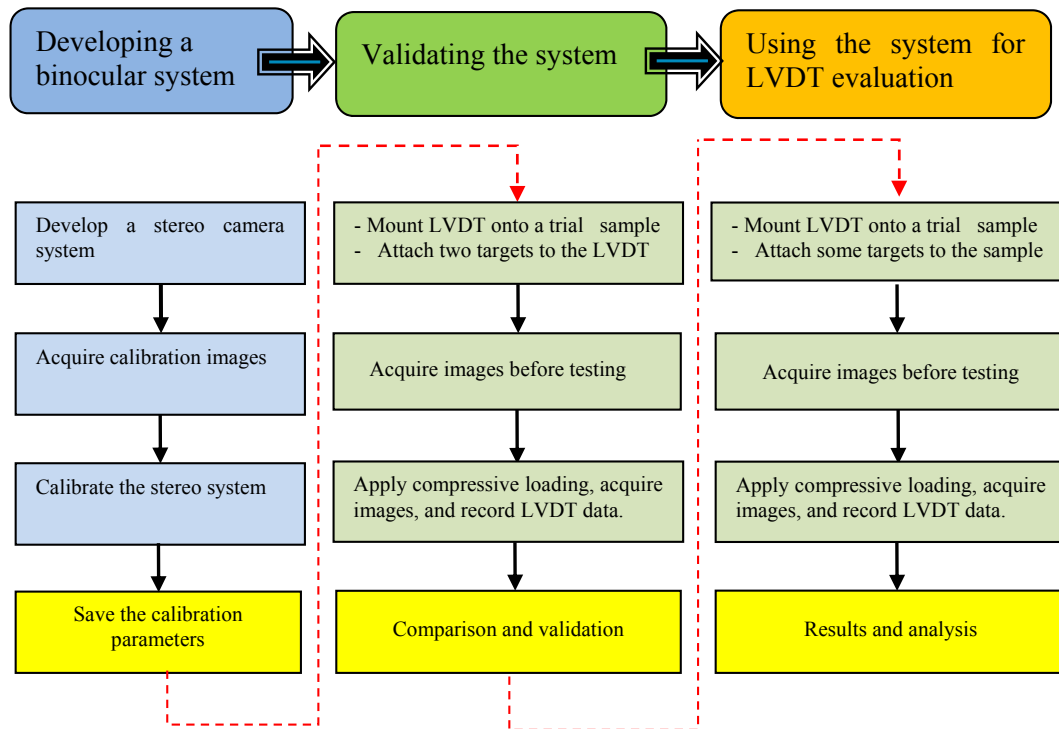


Figure 6-1: Workflow diagram of the experimental work.

6.2 Experimental Validation of the Approach

6.2.1 Materials and Methods

6.2.1.1 Materials and displacement measurement sensors

The material used in this study was a glulam timber beam which was employed during the preliminary torsion tests. The laminated beam was cut into cubic glulam blocks to provide samples to be used in the present study. A schematic diagram of the compression specimen with its dimensions is illustrated in Figure 6-2.

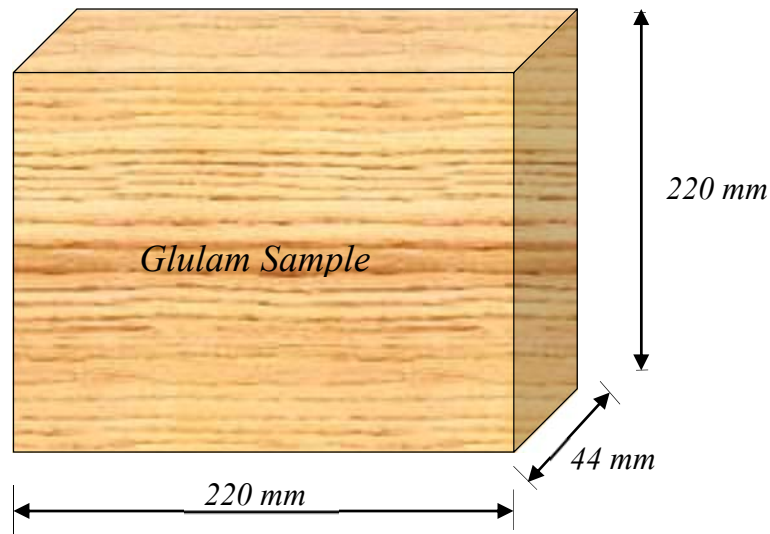


Figure 6-2: A Schematic diagram of a compression specimen with its dimensions.

In this study, two different measurement methods, LVDT displacement transducers and a non-contact deformation measurement system, were used to monitor the deformation of the glulam samples during testing. The LVDTs (model D5-200A GRA) (I RDP. Electronics Ltd) make accurate displacement measurements with a range of ± 5 mm and a sensitivity of ± 0.015 mm. This sensor needs a mounting system which should be in contact with the compressive load samples. In order to obtain more reliable and accurate measurements, the contact surfaces between the wood and the mounting system, which is used to accommodate the LVDT sensor, should be minimized. This was achieved by fabricating a mounting system, composed of a rectangular steel plate and an L-shape steel bracket. The steel plate was attach to the specimen by a single screw. A plastic fitting was fabricated and glued securely to this plate to clamp the LVDT body (the fixed end of the transducer). The L-shape bracket was mounted into the specimen by a single screw and attached to the moving end of the transducer. The displacement transducer together with its mounting system placed on the compression sample are shown in Figure 6-3.

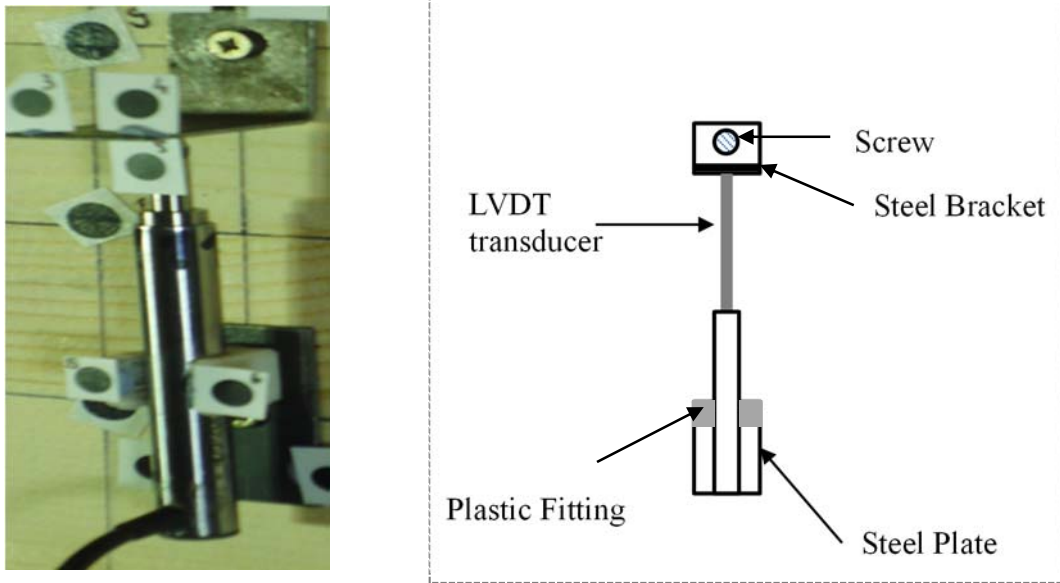


Figure 6-3: The LVDT transducer with its mounting system.

In addition to the LVDT sensor, a non-contact stereo camera system was also used to determine the relative displacements of the glulam samples. Figure 6-4 shows the optical system consisting of a pair of Basler Pilot piA2400-17gm cameras, two motorized pan tilt units to enable panning and tilting the cameras by using remote controls connected to them, and a tripod with a frame for adjusting the cameras. The two stereo cameras were fitted with a Computar (M2518-MPW 2/3" F1.8) Megapixel lenses with a constant focal length of 25mm and pixel size of 3.45 microns.

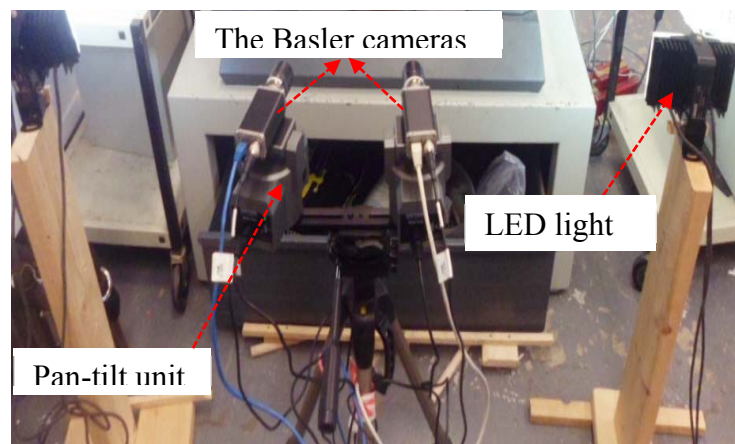


Figure 6-4: The image of the used Basler cameras.

6.2.1.2 Experimental Setup and Procedure

The validation and evaluation tests of the photogrammetric approach performed in this study were carried out at University of Edinburgh Napier. The proposed configuration, which enables the validation of the photogrammetric approach, is shown in Figure 6-5. In this setup, A Zwick/Roell Z050 (Zwick GmbH & Co, Germany) universal testing machine with maximum load capacity of 50 kN was used to test the specimens. Due to capacity limitation, the testing machine was only used to perform the compression tests perpendicular to the grain direction. This machine was equipped with a load cell connected, via a data acquisition system, to a desktop computer (PC1) which has its own software to be used for controlling and monitoring the experiments and collecting the data (time, load, deformations). The glulam timber sample was placed in the Zwick testing machine in front of the optical system. The LVDT sensor was mounted on the sample using the fabricated mounting system. The moving part of the sensor was attached to the L-shaped plate installed on the surface of the sample by a single screw. The fixed end of the sensor was clamped by a plastic fitting glued to a steel plate. The metal plate was connected to the sample surface by a screw. The LVDT transducer was then connected to a data acquisition system.

The Basler cameras were mounted on motorized pan tilt units fixed on a frame with a stereo baseline of approximately 30 cm. The stereo cameras were connected, via a Gigabit Netgear switch, to a desktop computer (PC2) with frame grabber and the image processing software installed. To produce images that cover the area of interest utilizing these lenses, the two-camera system was placed at approximately 74 cm from the location where the glulam specimens need to be inserted, resulting in a field of view covering an area of about 220 x 220 mm. Two black circular targets on a white background were attached to the LVDT transducer at two points representing the gauge length of the sensor. This configuration will allow the comparison between relative displacements measured by the LVDT and those determined by the optical system using the two targets. Two LED light sources were employed to assist in providing a homogenous illumination of the calibration plate during the calibration process.

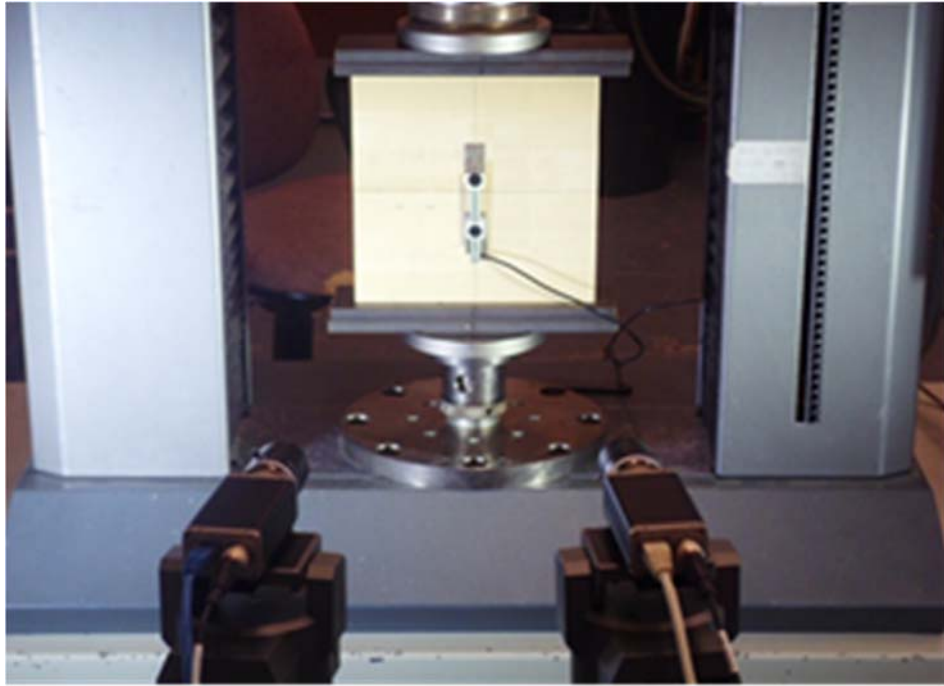
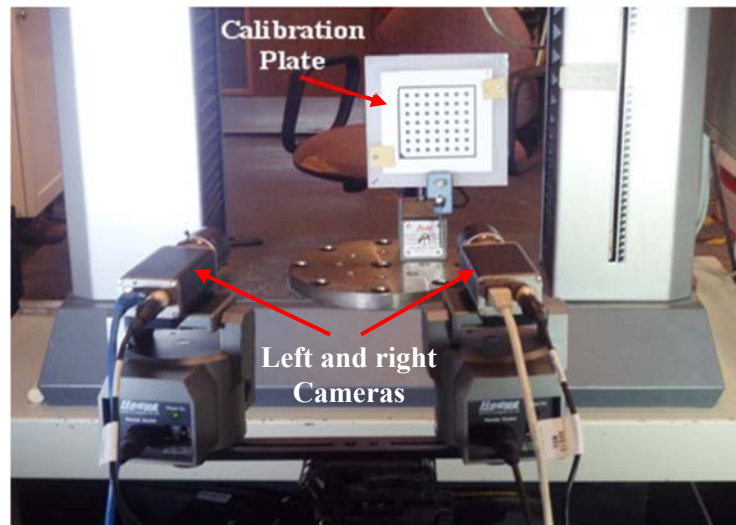


Figure 6-5: The test configuration for the validation of the photogrammetric approach.

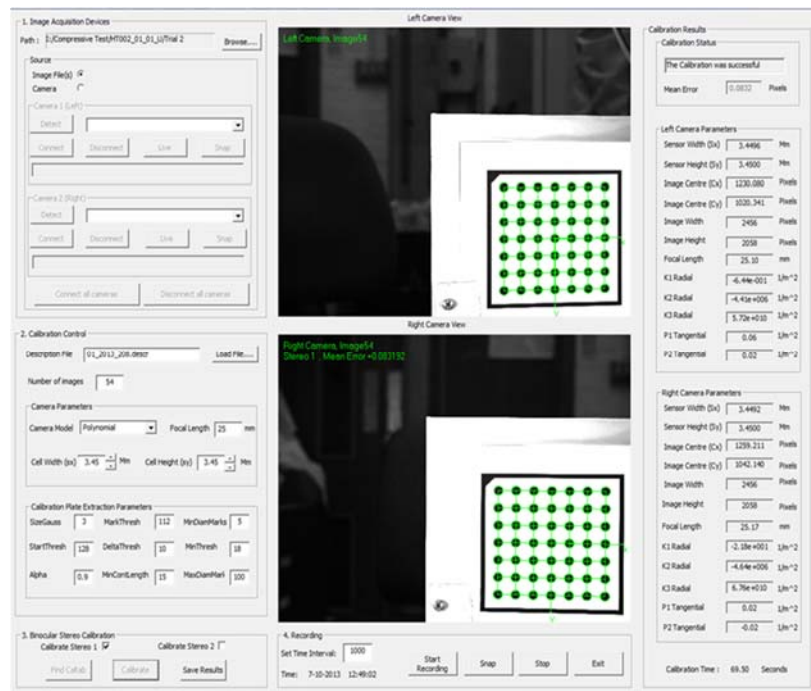
Prior to all the tests, the left and right cameras must be calibrated. In order to obtain highly accurate calibration results and hence highly accurate 3D measurements, a standard calibration plate was used to perform the binocular stereo calibration and the setup used in the calibration was carefully designed as described in (MVTech Software GmbH, 2011c.). A 100mm x 100 mm standard calibration plate, chosen according to the estimated dimensions of the region of interest to be captured as described in (MVTech Software GmbH, 2011c.), was placed in front of the two cameras as can be seen in Figure 6-6a. The plate was acquired from the left and right cameras in 54 different positions and orientations relative to the vision system. The image coordinates of the calibration images were extracted and the parameters of the stereo setup are determined via a least square solution with suitable chosen parameters of the cameras that can be determined from the specification of the camera sensor and the lens (MVTech Software GmbH., 2011c). A software package was developed based on visual C++ 2010 with the use of libraries from the image

processing software, HALCON version 11. This software provides all necessary tools required to easily and accurately perform the calibration of the binocular stereo system. Implemented in the Microsoft Foundation Classes (MFC), the graphical user interface (GUI) for this package provides the functions necessary to calibrate the binocular system and to record the image data during testing. Figure 6-6b shows an image of the GUI providing two calibration images of the calibration plate acquired from the two cameras in the process of calibrating the stereo camera system. This figure also shows the extracted calibration marks and calibration parameters for each camera. These parameters were then saved to be used in the calculation of the 3D positions of the photogrammetric targets from its stereo projections by triangulation (Hartley and Zisserman, 2003).

After conducting the calibration of the binocular system and before applying this system for evaluation purposes, it is important that the system should be validated. Four experimental evaluation tests were carried out according to the European standard procedures described in the EN 408 (2010). These tests were conducted in displacement control, with 0.02 mm/second cross-head displacement rate of the testing machine. The LVDT sensor and the calibrated binocular stereo system were both employed to monitor displacements between two points over the gauge length (8cm) on the glulam sample during the compressive loading. An initial pair of stereo images was captured by the two cameras before applying loads to the timber sample to allow comparison with the subsequent data. During the load application, the load and relative deformation which was measured from the LVDT were recorded through the data acquisition system and the GUI of the implemented software was used to automate recording the stereo images of the surface of the glulam sample with a time interval of about 1 second.



(a)



(b)

Figure 6-6: Stereo camera calibration

- a) Image of the stereo camera systems during the calibration process.
- b) Snapshot of the implemented GUI during the stereo camera calibration.

6.3 Performance Study of the Displacement Transducers

6.3.1 Materials and Methods

The materials used in this study were the glulam timber beams which were employed for the torsion tests. Image of these beams are shown in Figure 6-7. One of these beams was cut into cubic glulam blocks to provide samples to be used in the present study. The dimension of these samples is shown in the figure. As described in EN 408 standard (EN 408:2010, 2010), in order to ensure uniform loading, the test blocks were accurately prepared and their loaded surfaces were cut smoothly and accurately to be parallel to each other and perpendicular to the test piece axis. Prior to testing, all wood samples were stored in a controlled-temperature room with a temperature of approximately 20°C and a relative humidity of approximately 60 % in accordance to the mentioned standard.

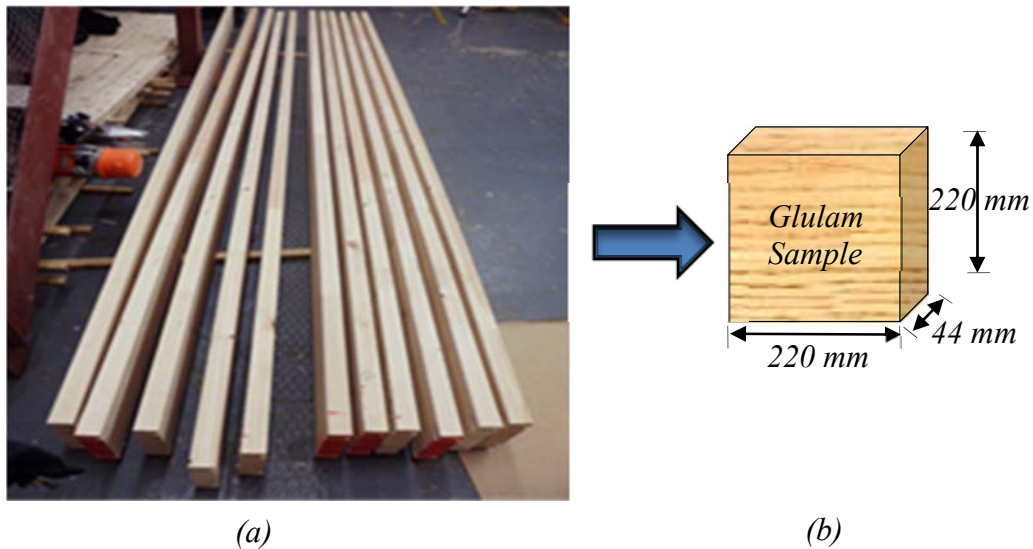


Figure 6-7: Materials used in the study

- Image of the glulam timber beams.
- Schematic view of a compression test sample with its dimensions.

6.3.2 Experimental Set-up and Procedure

All compression experiments carried out in this study followed the specification testing procedure as recommended in the EN 408 standard. Nine specimens which were cut from the same timber beam were selected to be tested with the compression tests performed in this study and carried out according to the procedure of the above-mentioned standard. The same configuration of the binocular stereo system which was used during the calibration process was also used during conducting the sample with compressive loading. Before performing the compression tests, a total of thirty targets were applied to the timber samples for optical deflection measurements. These targets (named as P1 to P30) represent black circular marks on a white background to be easily distinguished during the image processing stage. They were glued to one side of the timber sample as shown in Figure 6-8. Some of these targets (P9, P10, P21, and P22) were installed in accordance to LVDT and were intended to be used for comparing the LVDT readings with measurements of the optical system. The compression test sample was centred between two spherically seated loading heads. Two LVDTs (LVDT1 and LVDT2) with a gauge length of 8 cm were placed at the mid-height of the timber sample on two opposite sides, providing a local displacement measurement at both sides of the glulam specimen. To assess the performance of the LVDT1 mounting system, nine photogrammetric circular targets, shown in Figure 6-8c, were placed on the steel plate and bracket used to hold the transducer. These targets are shown in Figure 6-8a and indicated by a blue colour. Figure 6-9 shows a schematic plot of the experimental setup and equipment used during testing, including the Zwick testing machine and the binocular vision system. An Image of the experimental setup is shown in Figure 6-10.

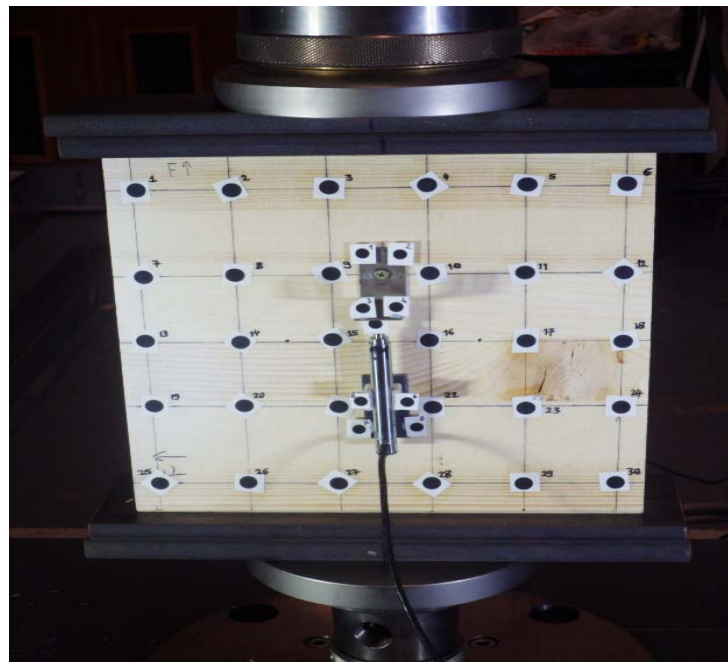
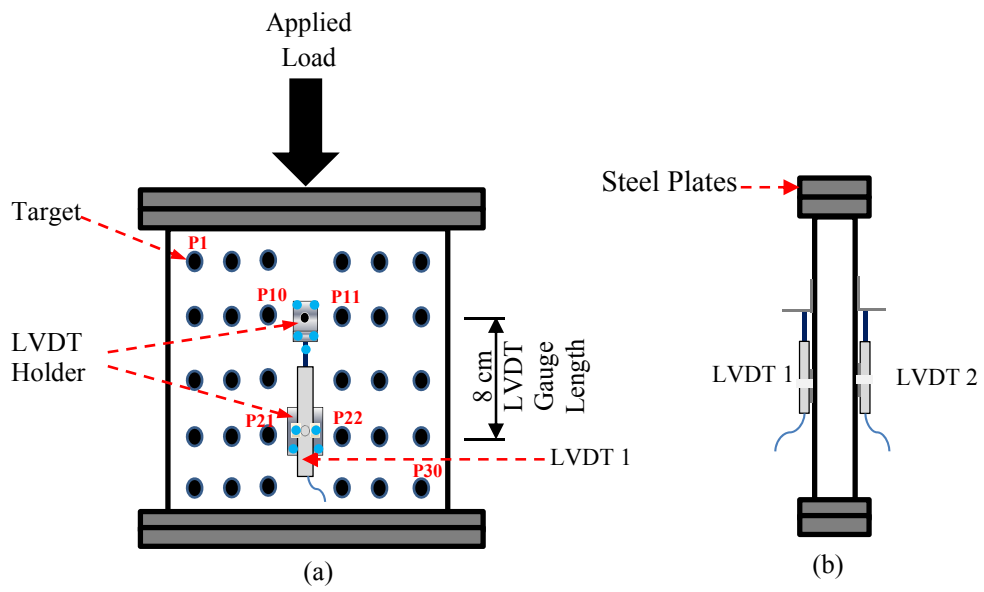


Figure 6-8: Schematic view of the test sample with LVDT instrumentation

- (a) Front view.
- (b) Side view.
- (c) Image of the installed targets and the LVDT on the specimen.

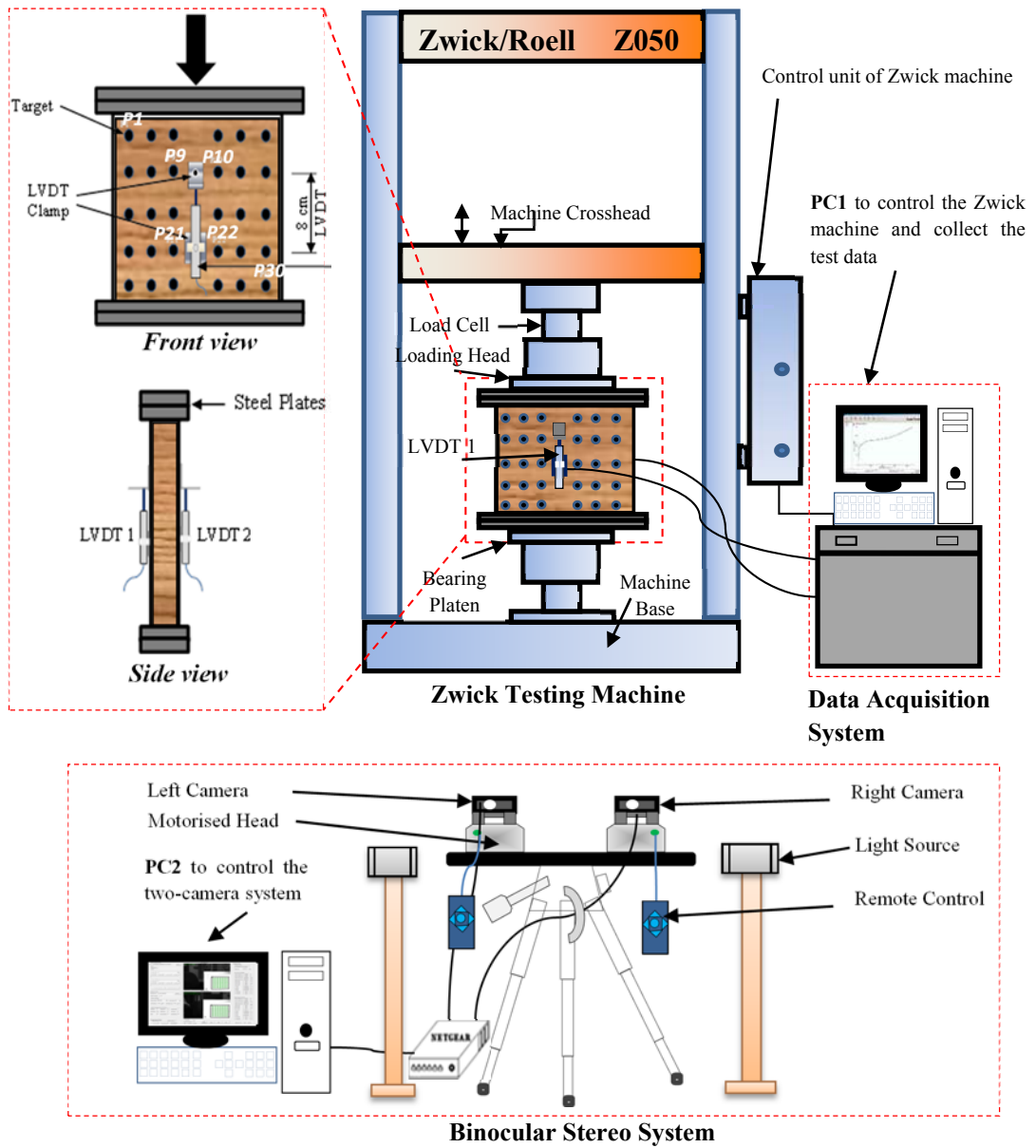


Figure 6-9: Image of experimental setup of compression test.

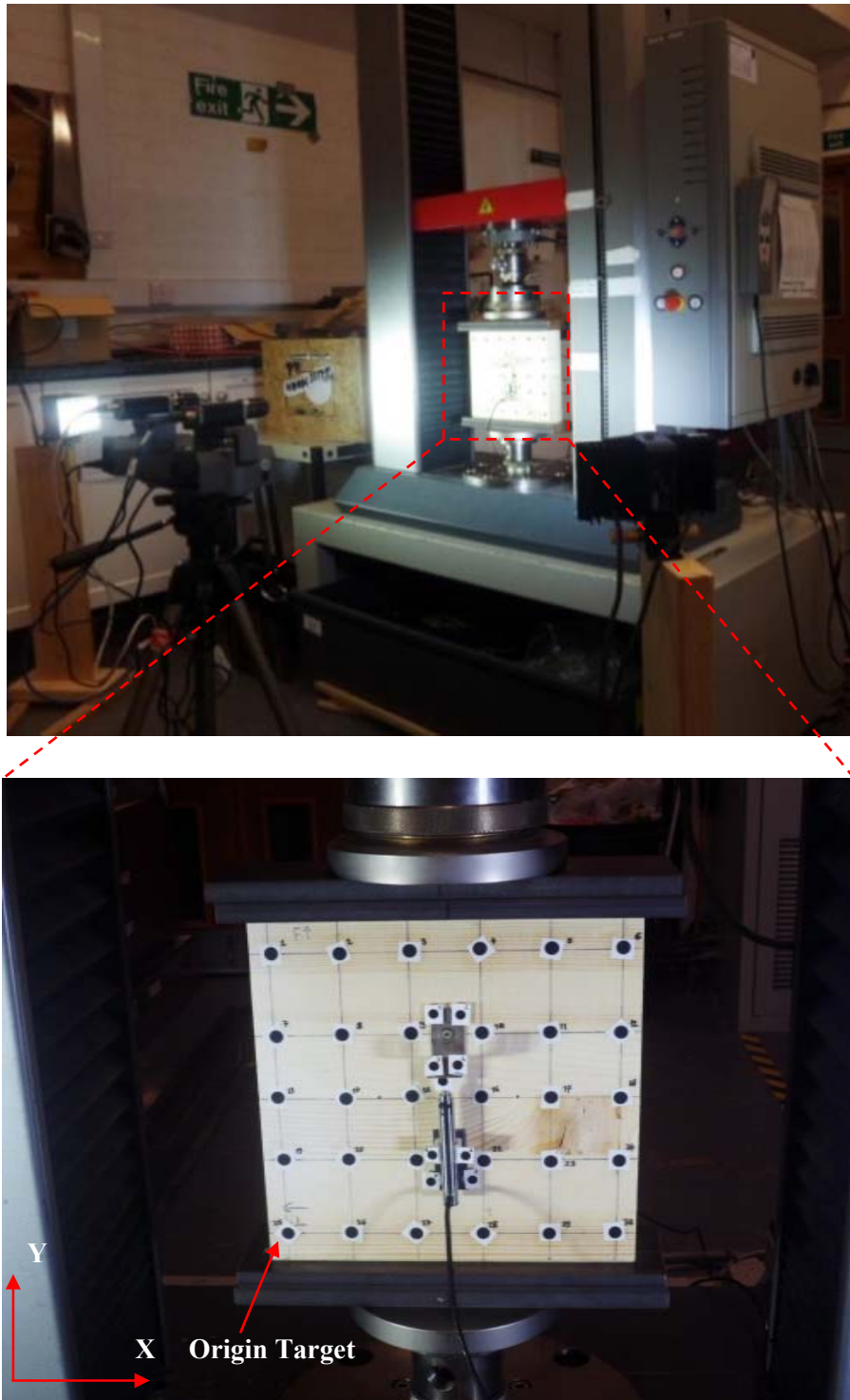


Figure 6-10: Schematic plot of the experimental setup of compression test with instrumentation (top), and more details of the specimen (bottom).

After calibrating the stereo camera system, the experimental tests were conducted on each timber sample in the direction perpendicular to the grain. The two-camera system was placed on one side in front of the testing machine. Before starting the actual compression tests, preliminary tests were conducted on a trial sample to determine the rate of loading and to estimate the elastic range of the sample in order to ensure that no permanent deformation occurred during the compression test and also to avoid any damage that might occur during testing. The deflection of the sample, rate of loading, and the maximum load to be applied to the system were then determined and a 12 kN was found to be appropriate to load the sample in the elastic range. The timber samples were tested based on these measurement data. Before applying the actual load, a pre-load with a force of 1kN was first applied to the wood test sample in order to enable it to be seated properly. The sample was then efficiently held to allow the two cameras to capture the initial state of the sample and the LVDTs were initialized to zero displacements through the data acquisition system. Using a displacement control of 0.02 mm/second, the samples were loaded constantly through the test. The loading and displacements were recorded simultaneously using a load cell and LVDT sensors connected to a data acquisition system at 0.1 second intervals. During loading, the implemented application software was used to automate recording images of the sample surface acquired by the two cameras with a time interval of about 1 second. At the end of loading the sample, the machine was set to let the crosshead displacement control stay in the same position to allow capturing the final state of the sample.

6.3.3 The Algorithm Developed for the Photogrammetric Deflection Measurements

In order to find the 3D information from the stereo images recorded during testing, it is necessary to utilize an image processing algorithm and stereo vision software. HALCON, a comprehensive and powerful software, provides the operators for image-based applications with image processing libraries and graphical user interface optimized for usability. As shown in Figure 6-11, an image processing algorithm was implemented in this software to process the stereo images. As well

as determining the presence of targets in each camera's image of the timber sample, the algorithm determines the 3D displacements of the circular targets to obtain their relative displacements from the stereo images of the timber sample recorded during testing. These 3D data will then be used to evaluate the performance of LVDT and to collect the sample displacements at various locations as mentioned before. The displacement measurements from these targets captured in stereo images involved several steps during image processing. The main steps involved in the algorithm are illustrated in Figure 6-12.

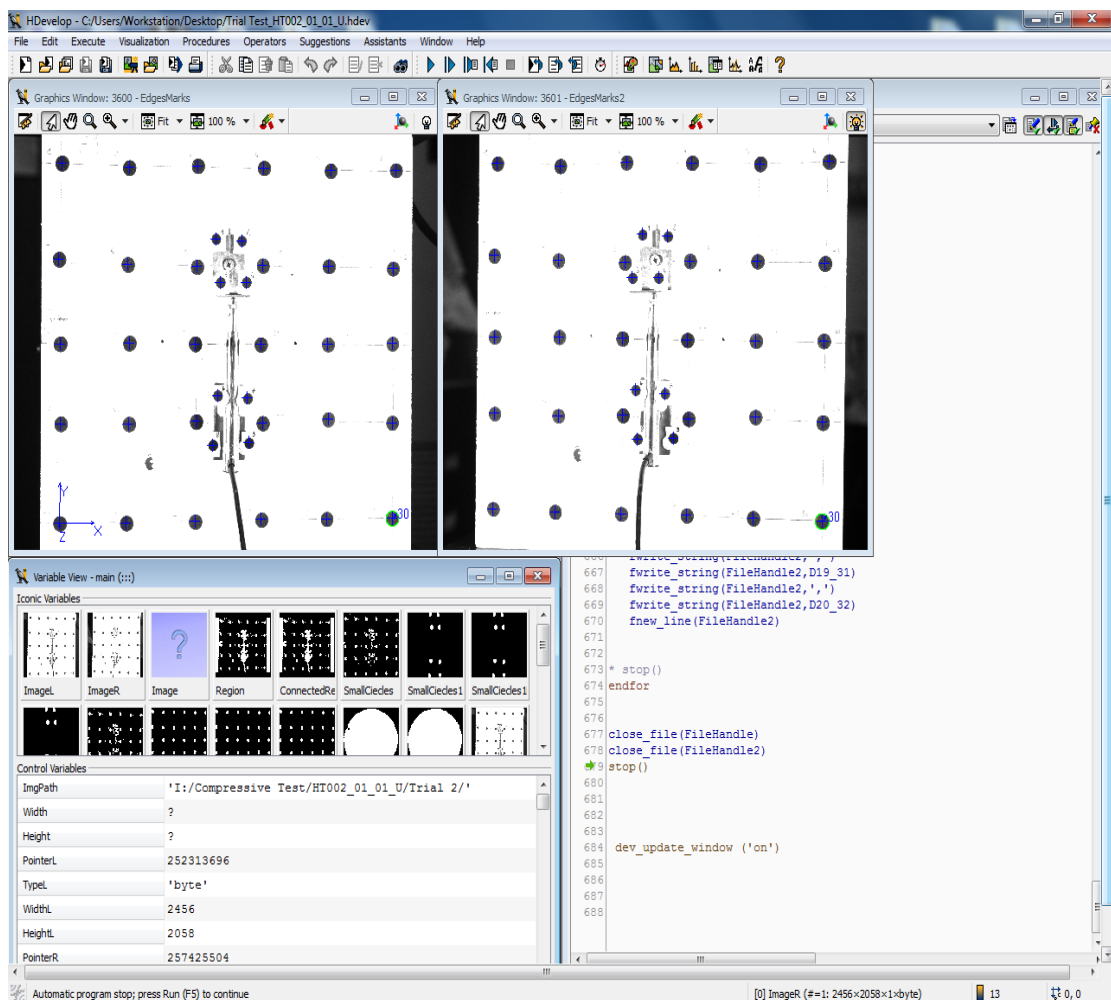


Figure 6-11: Screenshot of the implemented HALCON algorithm during stereo processing of the captured images.

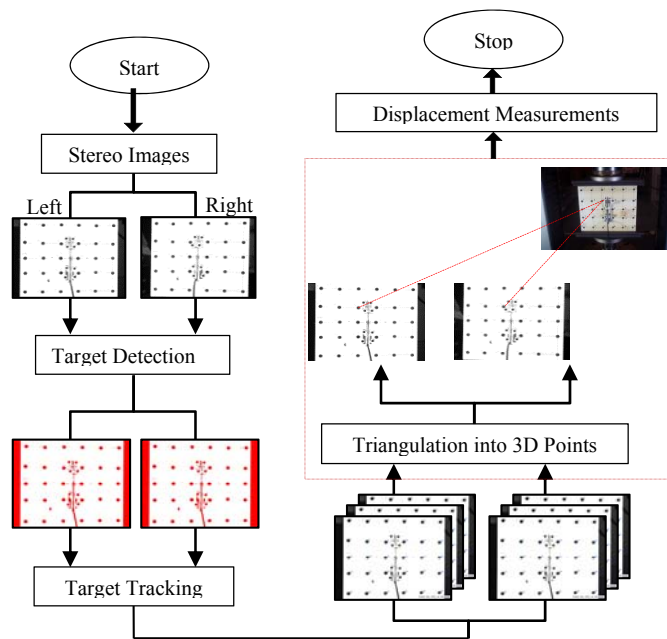
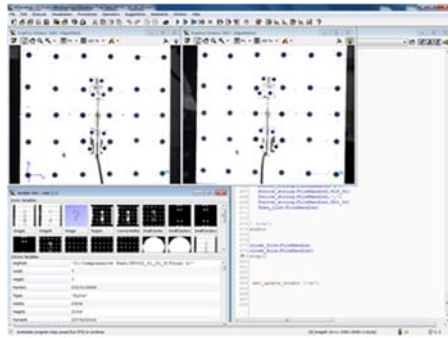
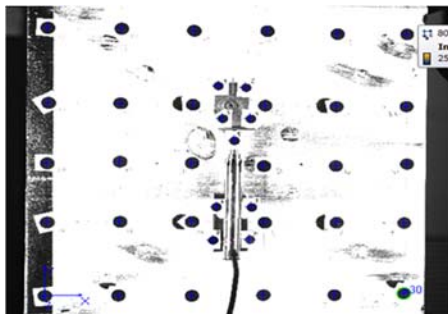


Figure 6-12: Flowchart of the algorithm.

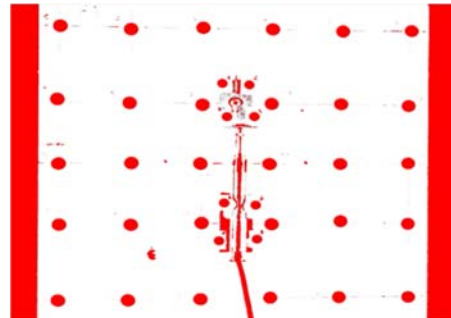
Figure 6-13 illustrates the concept and steps involved in the algorithm. The process starts with reading the calibration files, recorded during the calibration process, containing the internal and external parameters of the binocular stereo system. The stereo images of the timber sample recorded from the left and right cameras during testing were then displayed to be used in the image recognition process. The sub pixel-precise segmentation method provided by the software was used to reduce the area of interest by using the threshold values of the pixels to correspond to targets to separate the different regions and determine the black regions. The connected components of these regions are then calculated and all holes in these components were filled up. The stereo images were then reduced to these regions of interest and the potential targets that meet specific shape and size were selected. These targets were fitted to ellipse shapes and their image coordinates in both the left and right images were measured. The stereo-matching problem was then solved by sorting these targets in each of the left and right images according to their order in row and column coordinates from top to bottom. They were labelled and numbered to show how they match each other.



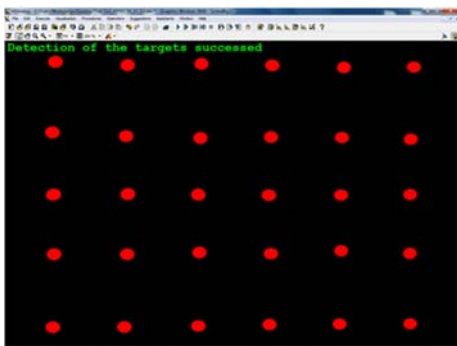
HALCON algorithm



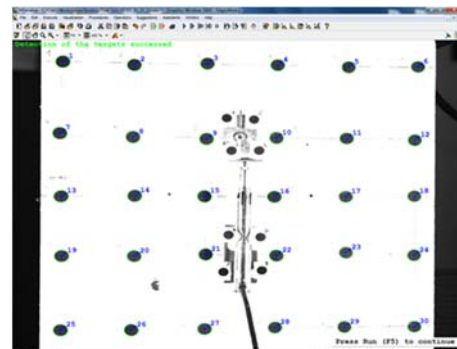
a) Original



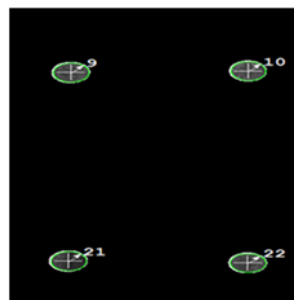
b) Image Segmentation



c) Target Detection



d) Target Ordering



e) The extracted targets

Figure 6-13: The image processing steps for extracting the targets.

After successful detection and matching of all targets in the stereo images, their 3D coordinates expressed in the camera coordinates of the left camera were determined using the theory of triangulation (Hartley and Zisserman, 2003). These 3D data were then transformed into the object coordinate system, as defined in Figure 6-10, and then used in the calculation of the displacement of the targets during the period of tests. The whole process was programmed in the software to be automated to reduce personnel time and effort. The recognized targets were displayed on the screen with their respective 3D coordinates and this data was saved on the computer to be used in the calculation of the displacements or relative displacement between the targets.

6.4 Validation Test Results

The validation tests were carried out with the purpose of validating the photogrammetric approach before using it to assess the performance of the LVDT sensor for measuring the displacements over a gauge length in the central part of the glulam specimens. The photogrammetric targets, P1 and P2, were placed at both the moving and fixed ends of the transducer to monitor the displacements over the gauge length (8cm). Using the 3D reconstruction algorithm presented previously, the 3D coordinates of the targets were obtained by processing all the stereo images captured by the calibrated stereo cameras during testing. The relative displacements in Y direction (the vertical direction) between the centroid of the two target points (P1 & P2) were then calculated. The corresponding relative displacement between the two points (gauge length) were measured by the LVDT. The relative displacements measured by the LVDT transducer and those determined by the photogrammetric approach are all plotted on the same figure in order to be compared with each other. Figure 6-14 shows some selected examples of these comparisons and indicates a remarkable correspondence. In this figure, the displacements obtained from the two-camera system describe very well the measured vertical displacement using the LVDT sensor which highlights the efficiency of the proposed approach.

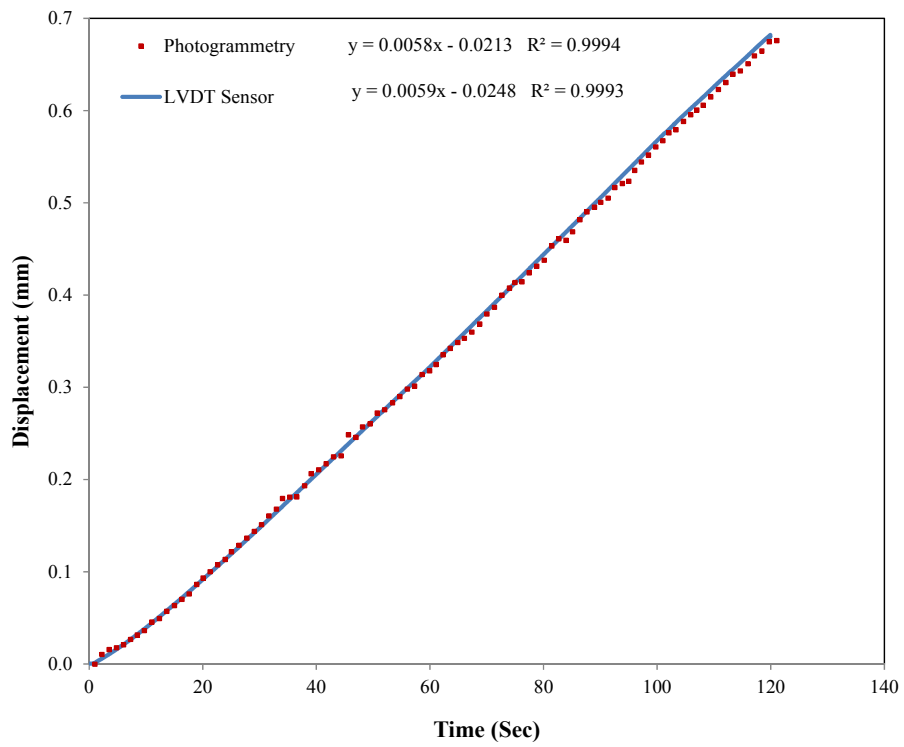
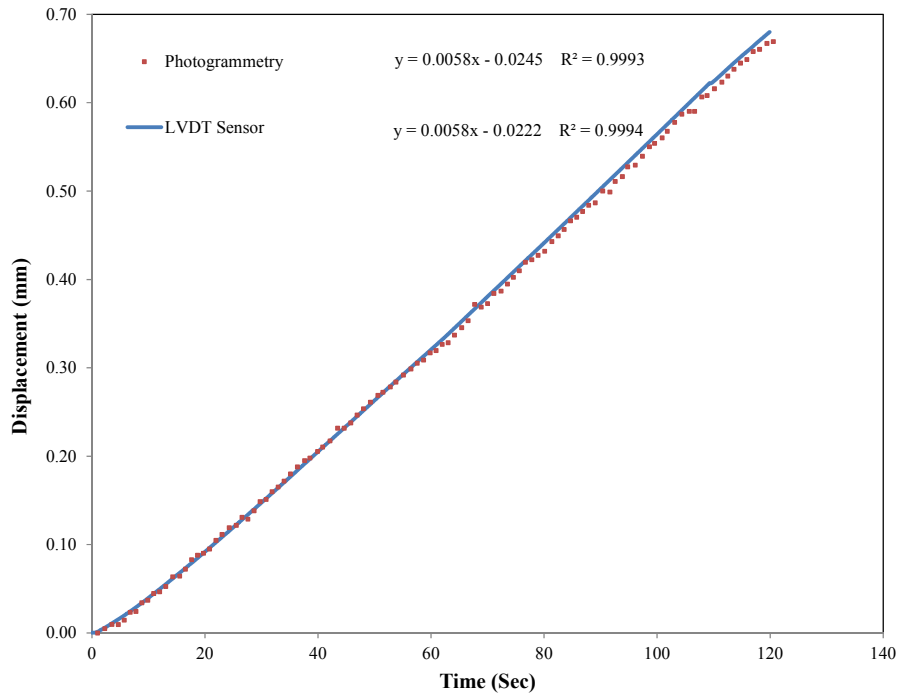


Figure 6-14: Comparison of measurements between the LVDT and the photogrammetric approach for trial test 2 (top) and trial test 3 (bottom).

6.5 Evaluation Test Results

The compression tests have been carried out in order to investigate the efficiency of using the LVDT transducer for measuring the relative displacements on the glulam specimens using the photogrammetric approach. The deformation of the mounting system used to attach the LVDT to the surface of the compression specimens was also investigated by the camera system. This was achieved by applying photogrammetric targets to both the surface of the glulam specimen in accordance with the setup of the LVDT and to the mounting system used to attach this device. The 3D coordinates of these targets were obtained by using the calibration parameters of the camera system and processing the stereo images in the developed 3D reconstruction algorithm described previously.

6.5.1 Comparison of the Test Results between the Photogrammetric Approach and the LVDT

As previously mentioned, the photogrammetric targets (P9, P10, P21, and P22) were installed in accordance with the LVDT and were intended to be used for comparing the LVDT readings with the stereo camera system. The locations of these targets are indicated in Figure 6-15 by the red-coloured circles. The setup of the investigated LVDT sensor is also shown. The 3D coordinates of the targets (P9, P10) and (P21, P22), were used to calculate the relative displacements over the two gauge lengths, l_1 and l_2 , respectively. The averages of these measurements in addition to the corresponding relative displacements measured by the LVDT were plotted in the same figure in order to be compared. Examples of these comparisons for samples 1 and 2 are shown, respectively, in Figures 6-16 and 6-17. It can be seen that the displacement graphs of the two sensors followed similar trends. However, there is a significant difference between the relative displacements measured by the transducer and those determined by the photogrammetric method. The maximum difference between the two methods was about 30%. This may be attributed to the fact that the setup of LVDT on timber will affect its reading values and the clamps used to attach this sensor might move during loading.

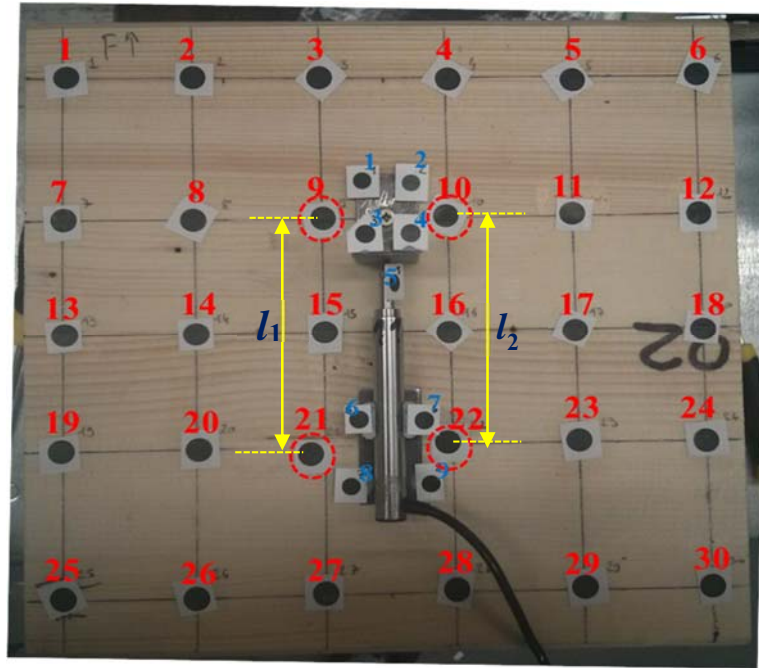


Figure 6-15: The selected targets to evaluate the performance of the LVDT.

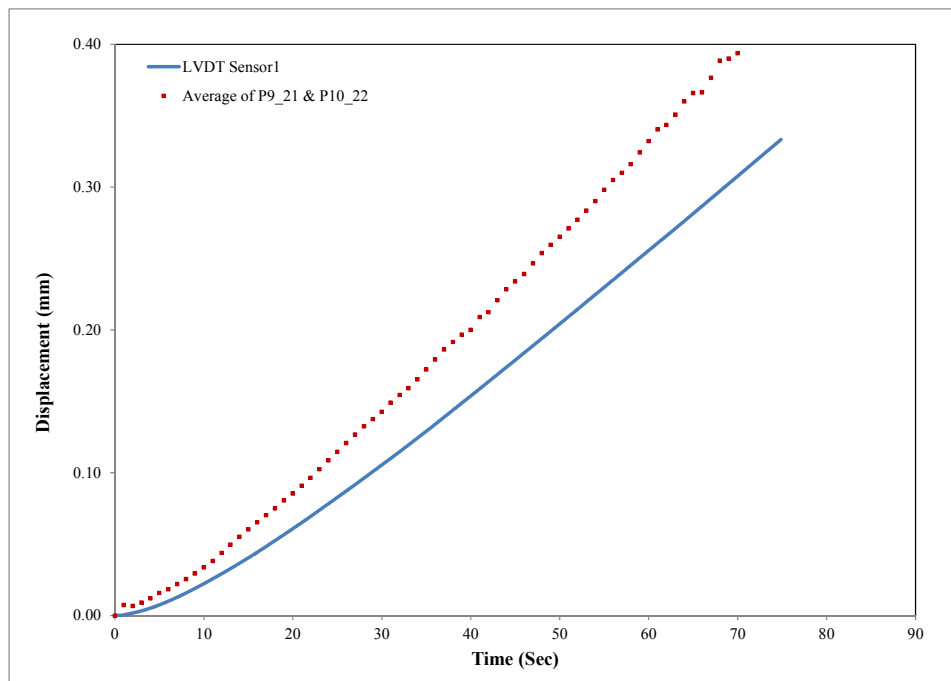


Figure 6-16: Comparison of the measurement results for sample 1.

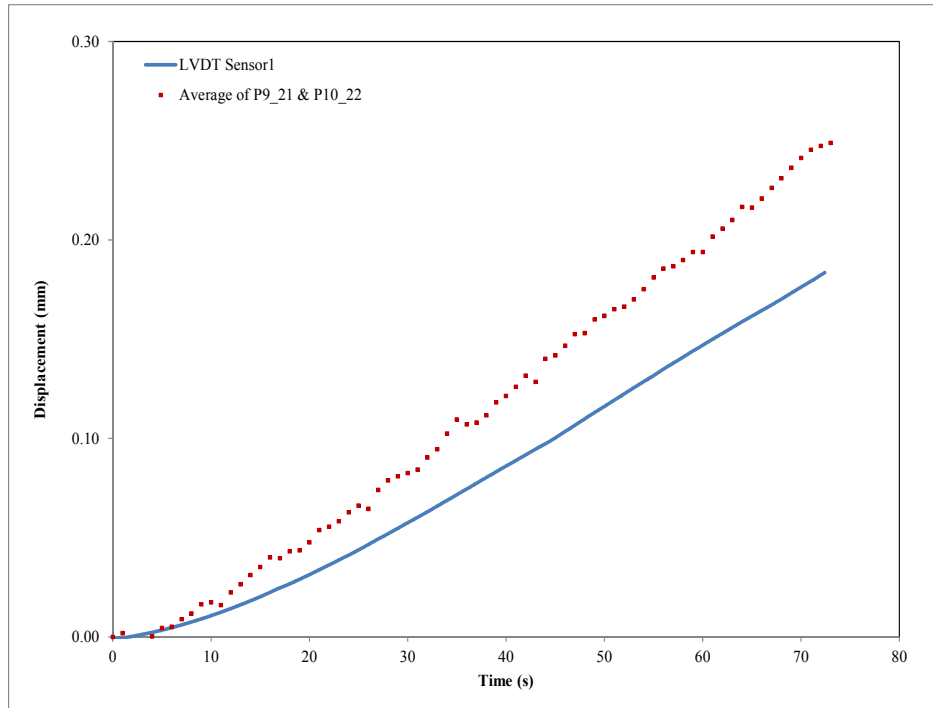


Figure 6-17: Comparison of the measurement results for sample 2.

The reading data of the transducer illustrates that the setup of this device was not stable and this could be explained by the fact that the wood surface, during the compression tests, does not remain stable since the wood is not a homogenous material. Therefore, the transducer holders might move, affecting the test results.

6.5.2 Investigation of the LVDT Mounting System

To further investigate the setup of the mounting system of the LVDT transducer, nine photogrammetric circular targets, shown in Figure 6-18, were glued on the steel plate and bracket of the mounting system used to hold the transducer. The targets 1, 2, 8, and 9 represent the marks, installed on the mounting system, far from the surface of the glulam specimen. The targets 3, 4, 6, and 7 represent the marks, installed on the mounting system, close to the surface of the test specimen. The target 5 represents the mark installed directly on the moving end of the LVDT transducer. The 3D coordinate of the photogrammetric marks were determined by the previously-mentioned 3D reconstruction algorithm and were used to calculate

the relative displacements of the targets. Figure 6-19 shows an example of the comparison of the test results. The LVDT readings and the displacements of the targets attached to the LVDT are in good agreement and close to each other. On the other hand, the relative displacements obtained from the targets glued to the surface of the glulam specimen and those obtained from the targets glued to the holder close to the wood surface are also close to each other, although there is a small difference between their readings. This can be attributed to the influence of the holder to the measurements since it can move differently from the movement of the wood surface.

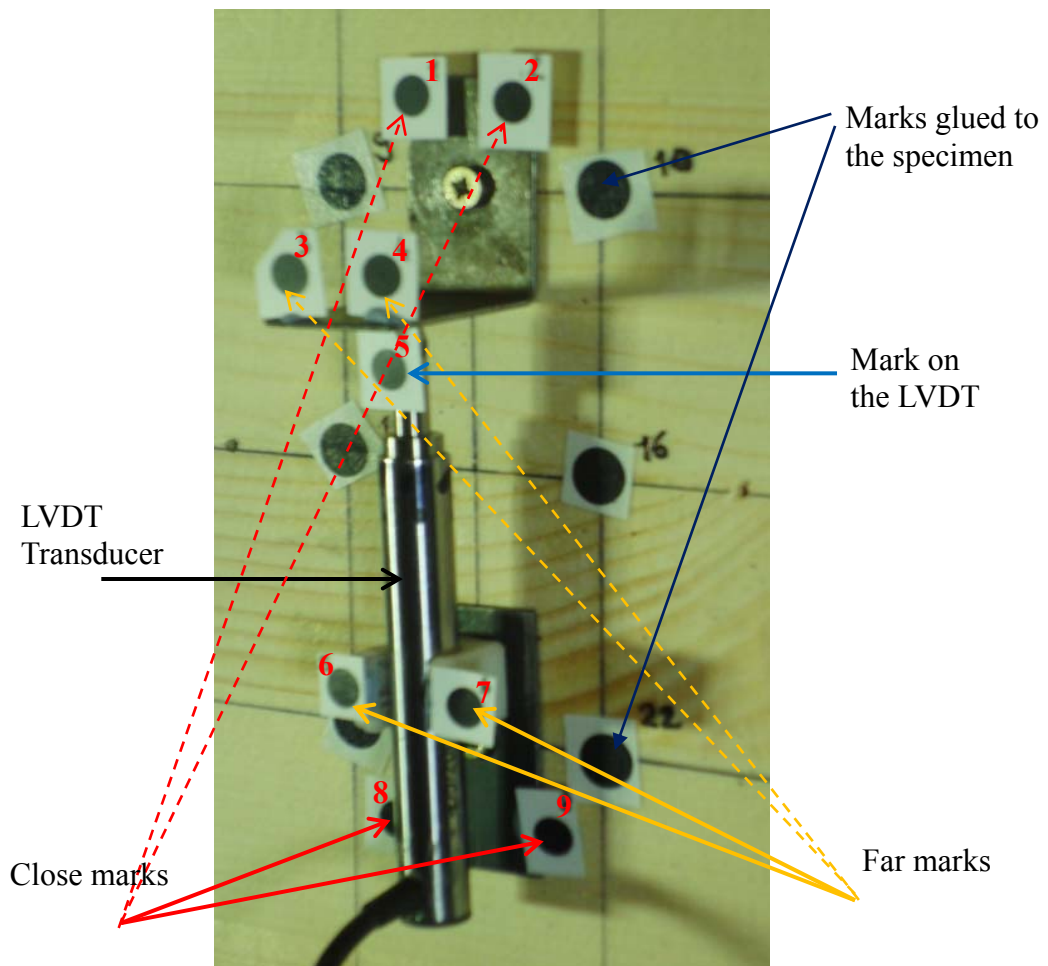


Figure 6-18: The setup used to investigate the mounting system of the LVDT.

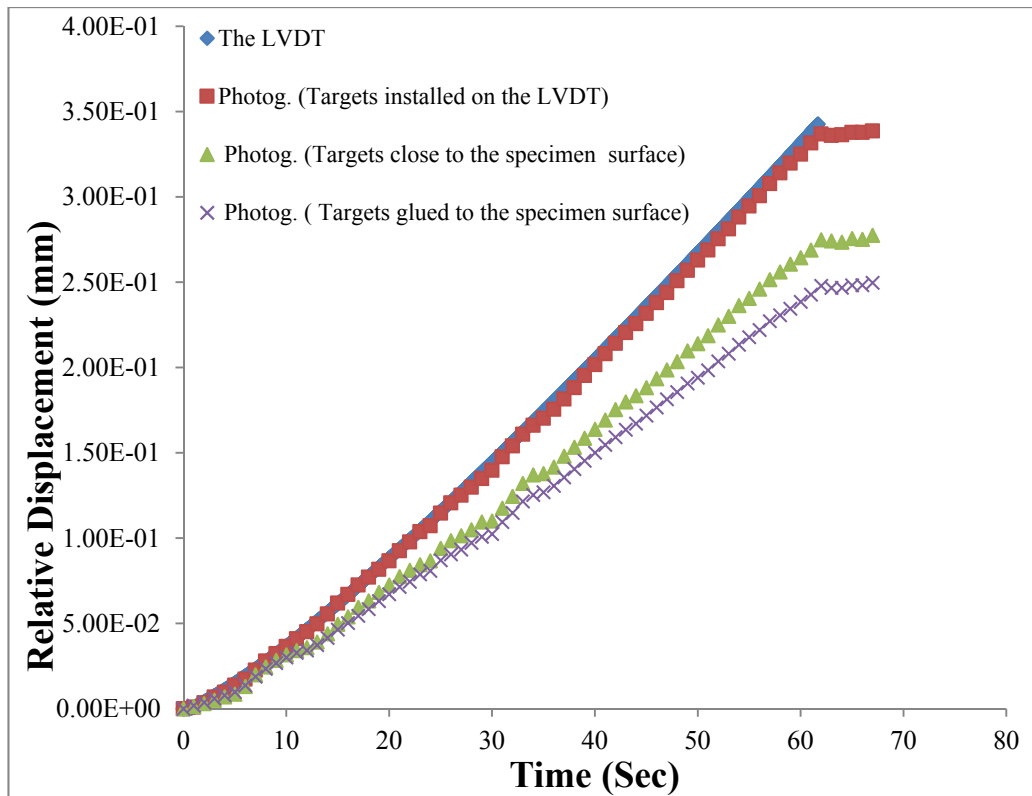


Figure 6-19: Comparison of the LVDT and the Photogrammetric measurements.

At the beginning of the applied loading and within the first 10 seconds, the relative displacements for both the LVDT and the considered targets were almost the same, but the magnitudes of those measured by the LVDT and the targets installed on them increased dramatically. This can be attributed to the influence of the holder on the measurements since it can move differently to the movement of the wood surface. This was confirmed with the different values of displacements obtained from the targets attached directly to wood and those placed on the holders but close to the surface of the specimen.

By comparing the results of the transducer efficiency tests, the difference between the measurements of the LVDT transducer and the photogrammetric method was higher than 30%. To figure out this big difference, the final maximum displacements measured by both methods were plotted in the same figure. Figure 6-20 shows an example of this comparison. The first column data represents the maximum displacement of the targets attached directly to the wood. The second

column data represents the maximum displacement of the targets glued to the holder near to the wood surface. The third column data, indicated by the blue colour, represents the maximum displacement of the targets attached directly to the LVDT transducer whereas the column data, indicated by the red and green colour, represents, respectively, the maximum displacement of the targets placed on the steel bracket and plate of the mounting system. They represent the holder's motion data. Finally, the last column data represents the maximum displacement measured by the LVDT transducer. The top bracket, which was close to the loading plate, had a higher displacement (0.054 mm) than that of the bottom plate (0.007mm), which was far from the loading plate. If the motion data of the transducer holder are added to the transducer data, this results in a displacement similar to that of the wood. These results show that the transducer results are not reliable since the setup is not stable due to the motion of the mounting system during the compressive test perpendicular to the grain.

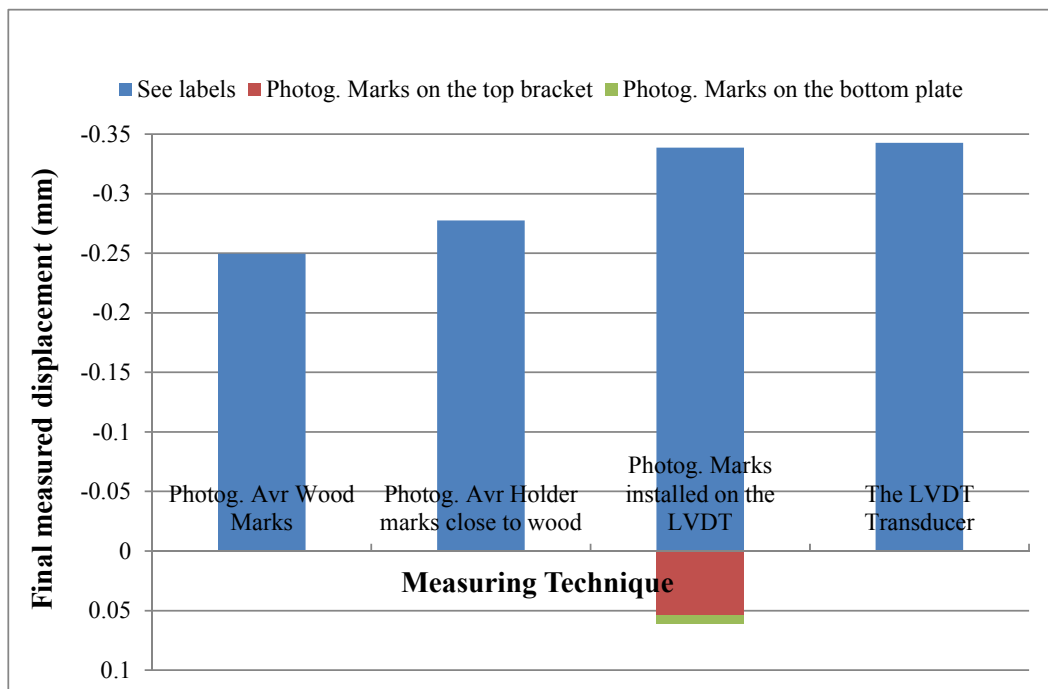


Figure 6-20: The test results for evaluating the LVDT mounting system.

6.5.2.1 Deformation of the surface of the glulam specimens

To investigate at different locations how the surface of the glulam specimens deform under the applied compressive loading, the relative displacement over the gauge lengths (L1 to L6), shown in Figure 6-21, were determined based on the above-mentioned 3D reconstruction algorithm. Typical results of these displacements for the glulam specimens, 1 and 9, are shown in Figure 6-22. It can be seen from these figures that the displacements determined between the two points placed in the middle of the specimens follow the same trend, but with different magnitude.

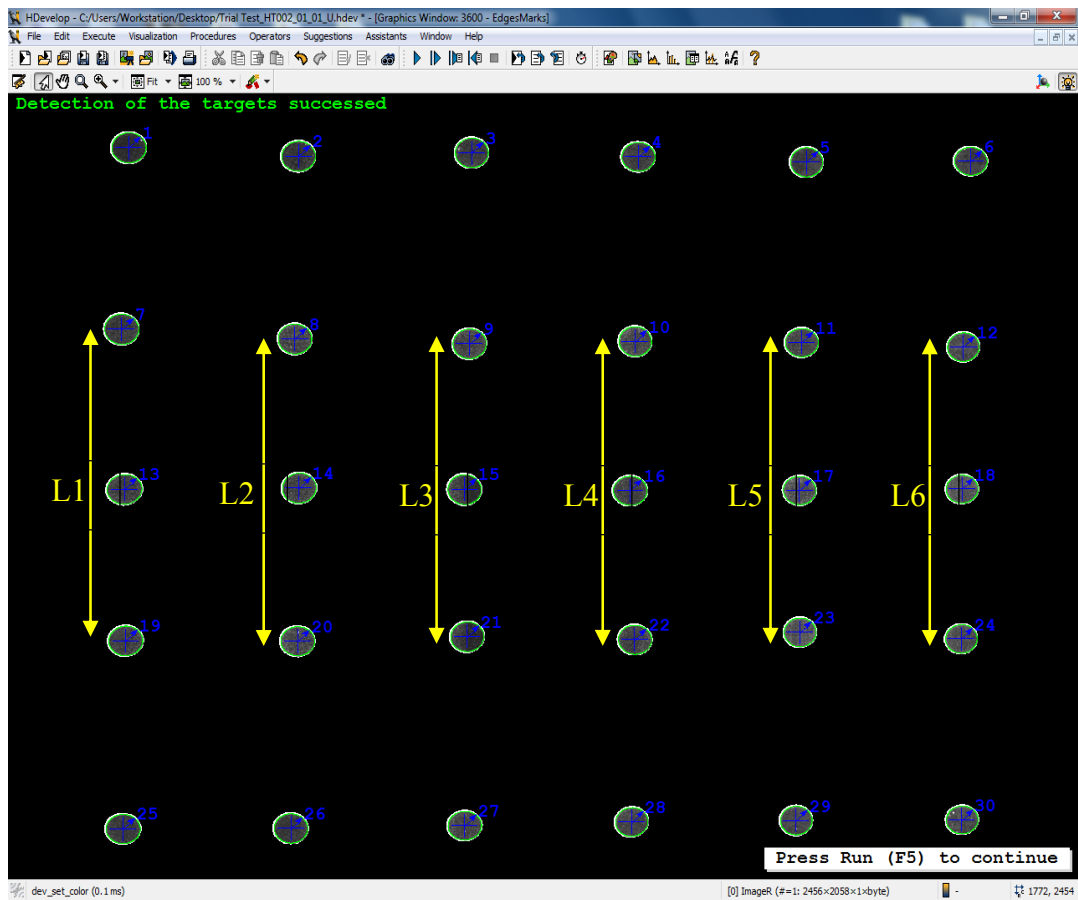


Figure 6-21: Screenshot of the target detection, showing the locations of the targets monitored with different gauge lengths.

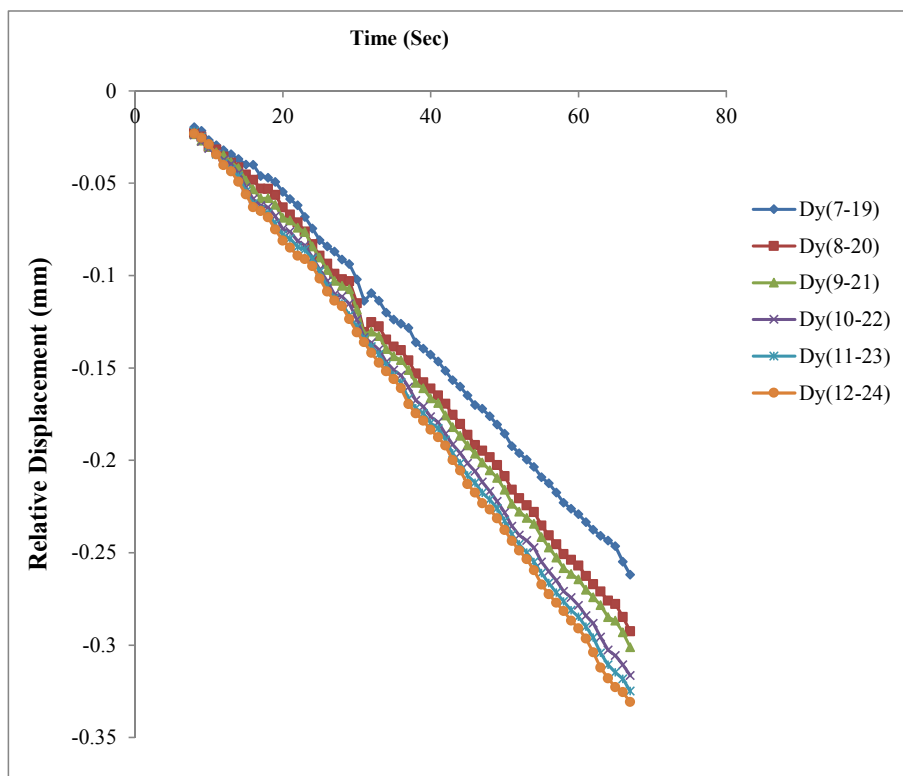
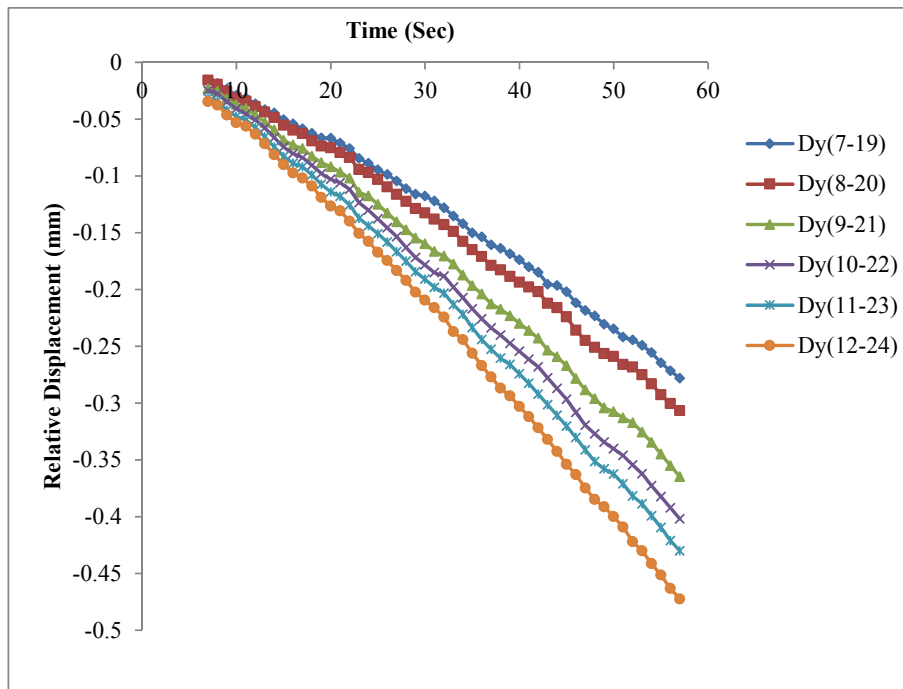


Figure 6-22: Comparison of the displacement results at the middle of sample 1 (top) and sample 9 (bottom).

6.6 Summary

In this study, a non-contact binocular stereo system developed in this project, was used to evaluate the performance of the LVDT displacement transducer on monitoring the deformation of the timber samples, especially together with the mounting system that is used to attach it onto the sample surface during the compression test. The non-contact photogrammetric approach has proved to be an efficient and accurate way of monitoring this performance. Several test series were conducted with nine timber samples in compression perpendicular to grain direction. After validating the proposed approach, its measurements were compared with the conventional measuring displacement transducers. The experimental results show that the readings measured by the LVDT sensor were mostly influenced by the setup of this device when mounted on timber. The results also showed that the optical system not only allowed assessing performance and reliability of this sensor but also allowed monitoring the deformation of the samples at various locations by providing more information which would not be possible to obtain using the traditional techniques. This will provide a better understanding of the deformation of the test sample and may assist in finding a proper way to mount this device on the surface of the timber sample when a high measuring accuracy is needed.

7. CONCLUSIONS AND RECOMMENDASIONS

7.1 Summary

This research describes the proposed non-contact photogrammetric approach and investigates its ability to evaluate the material properties of timber and timber-based composite beams. The photogrammetric technique provides the ability to measure the 3D coordinates of the photogrammetric targets, which can be applied to the surface of the timber specimens. These 3D measurements can then be used to calculate the displacements or the rotations of the samples, allowing the determination of the shear modulus (G) and modulus of elasticity (MOE) of the samples. This technique is based on close-range photogrammetry and stereo cameras which are required to capture images of the applied target before and after the deformations. It provides a good means to employ the stereo images and evaluate the displacements and deformations of the glulam surface in more detail, enabling the determination of the values and variations of G and MOE.

Compared to other experimental methods for determining the value of shear modulus, the torsion test is the only method which induces a pure state of shear on the test specimen. The torsion test method may be a better approach to determine the shear properties of structural-size timber-composite materials. Because of a lack of information available for proper use of the torsion test method torsion test, the torsion test has rarely been employed for the determination of G . This reason in addition to the difficulty in measuring reliable angular deformation of the torsion specimen using the torsion testing machines, such as the Tinius Olsen Machine, directed us to propose and develop the photogrammetric approach for these type of measurements, which aims to provide further understanding of the torsional behaviour of the glulam beams.

Before employing the proposed photogrammetric approach in the experimental work of this research for evaluating the material properties of the glulam beams, the stereo camera system was validated and evaluated. Therefore, the first experimental work of this research includes three different studies proposed with different objectives. The first study was conducted with the objective of

investigating the effect of several parameters, including the camera model, the number of calibration images, and the baseline length of the stereo cameras, on the efficiency of the stereo camera system.

The second study was intended to validate the proposed optical system combined with the photogrammetric targets. This was achieved by conducting experimental tests and comparing the displacement values of specific points determined by the photogrammetric approach with those measured by the other two different traditional devices, the digital micrometre and the LVDT transducer.

Finally, the last experimental study was conducted on the glulam timber specimens subjected to compressive loadings. The main objective of the study was to investigate and compare different target techniques which can be applied to the surface of the timber specimens. Three different marking techniques, the painted marks, the glued marks, and the pinned marks, were proposed to generate the photogrammetric targets. These targets were applied to the surface of the specimens which were prepared for the compression tests. Experimental compression tests were carried out on these specimens to evaluate the efficiency of the proposed targets for measuring the displacements on the surface of the samples. This was achieved by comparing the measurements results obtained by the LVDT with those obtained by the three different techniques using the binocular stereo camera system.

The research was mainly focused on the experimental study of torsion on structural-size glulam beams. Before being employed in the experimental work of this research to evaluate the adequacy of the torsion test for determining the values and variations of G , the photogrammetric approach has been used in preliminary torsion tests to validate its accuracy and evaluate its performance. The validation was accomplished by comparing the measurements of the photogrammetric targets acquired by a stereo camera system with those measured by the traditional sensor, the inclinometer. Preliminary torsion tests were first conducted on the trial specimen and to identify the elastic range of the specimens. A Tinius-Olsen torsion machine was used to conduct the experimental tests and apply torque, and the photogrammetric approaches as well as the inclinometers were employed to

measure, respectively, the twists on the long and short sides of the cross section of the glulam specimens. In addition, the powerful capability of the photogrammetric approach to monitor torsional deformations at different locations enables the warping displacements of the specimens to be investigated without the need to repeat the tests. Furthermore, the influence of using different shear spans on the shear modulus (G) as well as the variation of G along the cross sectional depth of the torsion specimens were also investigated.

The photogrammetric approach developed in this project was also employed in the compression test and the main objective of the experimental work was to investigate the ability of using the developed optical method in monitoring and evaluating displacement measurements during the compression test conducted on timber glulam beams. These measurements are essential to evaluate their modulus of elasticity (MOE). The non-contact photogrammetric approach based on the binocular stereo system was also used to evaluate the performance of the LVDT displacement transducer on monitoring the deformation of timber samples, especially together with the system that attached them onto the sample surface during compression testing. Several test series were conducted with nine timber samples in compression perpendicular to grain direction. After validating the proposed approach, its measurements were compared with the conventional measuring displacement transducers.

7.2 CONCLUSIONS

In contrast to the traditional techniques, the proposed photogrammetric approach assists in enhancing the torsion and compression tests by providing more details of the rotations and deformations of the laminated timber specimens. Based on the validation test results of the proposed photogrammetric system and the experimental work of this research, the following conclusions can be drawn:

1. The proposed method provides a cost-effective and non-contact method for determining reliable deformations at multi-locations of the tested specimen, which may assist in evaluating the values and variations of the G and the

MOE of the glulam timber beams. This technique overcomes the limitations of the traditional contact devices which only measure the angular deformation on a restricted number of points of the surface of the torsion specimens and can be destroyed during destructive tests.

2. The evaluation test results reveal that the number of calibration images highly influence the calibration results. The division model provides stable calibration results and hence accurate measurement of the calculated points when the number of the calibration images is two or more. On the other hand, four or more calibration images are required for the polynomial model to get the same stability of the results. The test results of the baseline study show that different lengths of the baseline produce different results of the calibration parameters of the stereo cameras and hence different 3D coordinates of the tracked targets. For the range of lengths examined by the cameras, it was found that the longer the baseline length the higher the accuracy of the camera system.
3. The validation of the proposed stereo camera system was achieved by performing validation tests and comparing the displacements obtained using the photogrammetric approach combined with the photogrammetric targets with those measured by two traditional devices, the LVDT sensor and the digital micrometre. The comparisons of the displacement data show that the photogrammetric results describe very well the results obtained from the other two traditional methods. Good agreement has been found between these two measuring systems.
4. The targeting techniques were proposed in this research to evaluate and compare the efficiency of applying them on the surface of the laminated glulam samples as photogrammetric targets to be tracked by the stereo camera system. The painted and glued targets, installed directly to the surface of the laminated timber specimen, had approximately the same displacement measurements. On the other hand, the pinned marks and the LVDT sensor, installed in contact with the surface of the test specimen, had

the same range of the displacement values. The significant difference between the displacement measurements of the contact and non-contact measuring techniques require developing a technique which can assist in finding a proper way to evaluate the performance of these sensors.

5. The first experimental work on the torsion test was conducted on 2m glulam timber beams graded to GL24 strength class with the objective of investigating the applicability of the proposed stereo camera system combined with the photogrammetric targets on measuring the rotations of the glulam timber beams. The proposed method was first validated by comparing the specimen's rotations obtained at a specific location from the photogrammetric method and those measured by the conventional inclinometer sensors. A good agreement was established between the two methods.
6. The photogrammetric method was also employed to measure the shear displacement along the long side of the cross-section. A significant warping along the long side of the cross-section has been observed even under a relatively low torque. The average rotation of the long side of the cross section, however, shows clear agreements with the inclinometer readings. The results showed that the contact-free measurement systems not only allowed evaluating the performance and reliability of inclinometers but also allowed monitoring the torsional deformations of the samples at various locations by providing more information which would not be possible to obtain using the traditional technique.
7. The second experimental work on the torsion test was conducted on the full-size glulam beams to determine their response to the torsional loading and unloading phase in clockwise and anticlockwise directions. The test results showed applying torques to timber specimens in either a clockwise or anticlockwise direction does not influence the torque stiffness and hence the shear modulus. It was also observed that loading and unloading in either of

the two directions does cause a significant change in the torque stiffness and hence the shear modulus of the glulam beams.

8. The average values of the shear modulus of the 11 laminated timber specimens ranged from 593 to 757 MPa. The difference can be attributed to the inhomogeneity and the variability of the wood specimens as well as the presence of defects such as knots which affect the overall stiffness of the wood specimens. The highest average values of shear modulus was found in specimen 06 and was about 742 MPa and the lowest values of the shear modulus of about 620 MPa was found in specimens HT007, HT009, HT010 and HT011.
9. The overall average G of all of the glulam beams tested in torsion is 649 MPa. This value agrees well with the published value of the same board of glulam beam GL24 and conforms to the requirements of BS EN 14080 (2009) which gives characteristic material properties for homogenous and combined glulam members.
10. To investigate the effects of inserting the torsion samples upside down on the torsional behaviour, sample HT010 was tested under torsional loads in two ways: the right way up and upside down. It was observed that mounting the torsion specimens the right way up during the torsion test yields higher values of shear modulus than those obtained when inserting the specimens upside down, although this finding was only based on a single piece of glulam beam, specimen HT010.
11. The photogrammetric approach allowed to investigate the influence of the shear span on the shear modulus of the tested glulam beams under the torsion tests. It was apparent that the shear modulus varied significantly with the different shear spans (12-17%). The test results of all the tested specimens revealed that the larger the shear span the smaller the value of shear modulus.

12. The photogrammetric approach enabled the investigation of the warping displacements of the longer side of the cross section. It was found that the applied torque causes the longer side of the sections, which were plane prior to twisting, to warp in the axial direction, meaning that the plane cross sections no longer remain plane after twisting. This warping deformations of the cross section will affect the torsional stiffness of the glulam specimens.
13. The photogrammetric camera system was utilized to examine if the shear modulus is constant or varies along the depth of the torsion specimens. Four segments along the long depth of the cross section were monitored by the stereo camera system. Using the rotations of these segments, their shear modulus was calculated and compared. It was clearly seen that the shear modulus varied significantly across the depth of the torsion specimens. The test results show that the top and bottom segments of the glulam timber specimens had the highest values of shear modulus than the segments in the middle. This result was expected since the top and bottom of the glulam beams, which face compression and tension, were made of a high-strength class of timber.
14. The photogrammetric approach has proved to be an efficient and accurate way of monitoring the performance of the LVDT transducer on measuring the displacements of the glulam specimens under the compression test. The experimental results showed that the readings measured by the LVDT sensor were mostly influenced by the setup of this device when mounted on timber.
15. The experimental results show that the optical system provides more deformations of the specimen's information at various locations, which would not be possible to obtain using the traditional techniques. This will provide a better understanding of the deformation of the compression sample and may assist in evaluating the modulus of elasticity (MOE) of the compression specimens.

7.3 RECOMMENDATIONS

This research quantifies values and variations of the shear modulus of the glulam specimens under the torsion test according to the EN 408 standard method with the help of the developed photogrammetric method. The application of the photogrammetric approach to evaluate the performance of the traditional device, the LVDT, was also considered in the course programme of this research. Future research efforts that could be investigated based upon the results of this research include the following:

1. The torsion test method is recommended by CEN standard (EN408:2009, 2009) to evaluate the shear modulus of structural-size specimens. However, this standard does not adequately address the test procedure in greater details. This investigation proved that the value and variations of the shear modulus can be obtained from the torsion tests by utilizing the photogrammetric technique. The inclusive findings provided by the optical system on the use of the torsion test to evaluate the shear properties of the laminated timber specimens could contribute to the experimental test procedure described in the above-mentioned standard.
2. The shear modulus is a fundamental mechanical property of wood that is used in the design of timber and engineered wood products. It would be of great interest to apply the photogrammetric approach in the bending test and investigate the correlation between the shear modulus and modulus of elasticity for the timber beams.
3. The targeting techniques proposed in this research included the painted, glued and pinned marks. The applicability of applying them on the surface of the glulam timber specimens was investigated. The significant difference between the test results of the contact and non-contact measuring techniques require developing a technique which can assist in finding a proper way to evaluate the performance of these sensors.

4. The torsion tests were carried out on structural-size glulam timber beams. Although clear wood may not be a better approach to determine the shear properties of the timber beams, it would be of high interest to further conduct the torsion tests on clear wood specimens and investigate the correlation between shear modulus values of the clear wood and full-size specimens.
5. This research work may assist in developing a suitable procedure to measure the size of knots and study their influence on the shear modulus of the specimens.
6. One of the main advantages of using the photogrammetric approach developed in this research is the ability to monitor the torsional deformations at different locations, enabling the values of shear modulus at different cross-sections of the torsion specimens to be evaluated without the need to use more devices. By comparing shear modulus values of glulam beams measured based on different shear spans, it was found that the larger the shear span the smaller the value of shear modulus. It was concluded that the shear span affects the value of shear modulus. The comparison suggests that testing glulam beams in different shear spans is essential to evaluate the variations of shear modulus values at these different gauge lengths.
7. Previous research projects paid less attention on evaluating the performance of the LVDT sensor on measuring the displacements of the laminated timber specimens under compressive loadings. Although the LVDT can be easily installed on a wide range of experiments, their installation in timber for the compressive loading test is challengeable and significantly more difficult since the setup of this sensor might affect its reading values during testing. Different setup of this device could lead to different displacement data. This research provides a performance study of the LVDT transducer and investigated the setup of the mounting system used to attach the sensor to the specimen. From the test results, it is recommended that the setup of the mounting system needs to be investigated before using it to hold the LVDT.

This might assist in finding a proper way to mount the sensor on the surface of the timber sample to minimize the error.

REFERENCES

Arias, P., et al. (2007). 3D modeling and section properties of ancient irregular timber structures by means of digital photogrammetry. *Computer-Aided Civil and Infrastructure Engineering* **22**(8): 597-611.

ASTM-D143-94 (1994). *Standards method for testing small clear specimen of timber*. American Society of Testing and Materials, West Conshohcken, PA, USA.

ASTM-D198-94 (1994). *Standard methods of static tests of lumber in structural size*. American Society of Testing and Materials, West Conshohcken, PA, USA.

Atkinson, K. B. (2001). Close range photogrammetry and machine vision., *Whittles Publishing*, Latheronwheel, Caithness, Scotland.

Bodig, J. and J. R. Goodman (1973). Prediction of elastic parameters for wood. *Wood Science* **5**(4): 249-264.

Bodig, J., & B. Jayne (1982). Mechanics of wood composites. *Von Nostrand Reinhold Company*, New York, Cincinnati, Toronto.

Bouguet, J.-Y. (2004). Camera calibration toolbox for Matlab. http://www.vision.caltech.edu/bouguetj/calib_doc. [Accessed on March 02, 2011].

Burdzik, W. and P. Nkwera (2003). The relationship between torsional rigidity and bending strength characteristics of SA pine. *The Southern African Forestry Journal* **198**(1): 17-21.

Cai, Z. and Ross, R.J. (2010). Mechanical properties of wood-based composite materials.

Choi, D., et al. (1991). Image analysis to measure strain in wood and paper. *Wood Science and Technology* **25**(4): 251-262.

Chounta, I., & Ioannidis, C. (2012). High Accuracy Deformation Monitoring of a Concrete Beam using Automatic Photogrammetric Techniques, Knowing to manage the territory, protect the environment. *Evaluate the Cultural Heritage*.

Chui, Y. (2002). Application of ribbed-plate theory of predict vibrational serviceability of timber floor systems. *The Proceedings of 7 th World Conference on Timber Engineering WCTE*, Vol 4: 87-93.

Clarke, T. A. (1994). Analysis of the properties of targets used in digital close-range photogrammetric measurement. *Videometrics III*. SPIE. Boston, 2350: 251- 262.

Cooper, M. and S. Robson (1996). Theory of close range photogrammetry. *Close range photogrammetry and machine vision*. Whittles Publishing, Caithness,UK: 9-51.

Dahl, K. and K. Malo (2009). Planar strain measurements on wood specimens. *Experimental mechanics* **49**(4): 575-586.

Dahl, K. B. and K. Malo (2009). Linear shear properties of spruce softwood. *Wood Science and Technology* **43**(5-6): 499-525.

Dahl, K. B. and K. Malo (2009). Nonlinear shear properties of spruce softwood: experimental results. *Wood Science and Technology* **43**(7-8): 539-558.

De Magistris, F. and L. Salmén (2004). Combined shear and compression analysis using the Iosipescu device: analytical and experimental studies of medium density fiberboard. *Wood Science and Technology* **37**(6): 509-521.

Detchev, I., Habib, A., & El-Badry, M. (2011). Estimation of vertical deflections in concrete beams through digital close range photogrammetry. *ISPRS Remote Sensing and Spatial Information Sciences*, 38, 5-W12.

Dias-da-Costa, D., Valença, J., Ranzi, G., & Albino, C. (2014). Monitoring of concrete members using photogrammetry and image processing.

Dumail, J.-F., et al. (2000). An analysis of rolling shear of spruce wood by the Iosipescu method. *Holzforschung* **54**(4): 420-426.

EN 338:2009 (2009). *Structural Timber - Strength Classes*. European Committee for Standardization, Brussels, Belgium.

EN 408:2003 (2003). *Timber structures-structural timber and glued laminated timber- determination of some physical and mechanical properties perpendicular to the grain*. European Committee for Standardization, Brussels, Belgium.

EN 408:2010 (2010). *Timber structures-structural timber and glued laminated timber- determination of some physical and mechanical properties perpendicular to the grain*. European Committee for Standardization, Brussels, Belgium.

EN 1995-1-1 (2004). *Eurocode 5-Design of Timber Structures-Part 1-1: General-Common Rules and Rules for Buildings*. European Committee for Standardization, Brussels, Belgium.

Fitzgibbon, A., et al. (1999). Direct least square fitting of ellipses. *Pattern Analysis and Machine Intelligence, IEEE Transactions on* **21**(5): 476-480.

Forest Products Laboratory (1987). *Wood handbook: wood as an engineering material*, United States Government Printing.

Foschi, R. O. (1982). Structural analysis of wood floor systems. *Journal of the Structural Division* **108**(7): 1557-1574.

Franke, S., et al. (2007). Strain analysis of wood components by close range photogrammetry. *Materials and structures* **40**(1): 37-46.

Franke, S., et al. (2006). Experimental verification of FE-Simulations of wood using photogrammetry. *WCTE 2006 Conference Proceedings, 9th World Conference on Timber Engineering*, Portland, USA.

Fraser, C.S. and Riedel, B. (2000). Monitoring the thermal deformation of steel beams via vision metrology. *ISPRS Journal of Photogrammetry & Remote Sensing*, 55: 268-276.

Fraser, C., et al. (2003). Photogrammetric monitoring of structural deformation: the federation square atrium project. *Proceedings of Optical 3D Measurement Techniques 1*: 22-25.

Galbiati Jr, L. J. (1990). *Machine vision and digital image processing fundamentals*, Prentice-Hall, Inc.

Garcia, D. and J.-J. Orteu (2001). 3D deformation measurement using stereo-correlation applied to experimental mechanics. *Proceedings of the 10th FIG International Symposium Deformation Measurements*.

Guindos, P. and J. Ortiz (2012). Low cost photogrammetry as a tool for stiffness analysis and finite element validation of timber with knots in bending.

Guindos, P. and J. Ortiz (2013). The utility of low-cost photogrammetry for stiffness analysis and finite-element validation of wood with knots in bending. *Biosystems Engineering* **114**(2): 86-96.

Gupta, R., et al. (2002). Experimental evaluation of the torsion test for determining shear strength of structural lumber. *Journal of testing and evaluation* **30** (4): 283-290.

Gupta, R., Siller, Tobias (2005). Shear strength of structural composite lumber using torsion tests. *Journal of testing and evaluation* **33** (2): 110-117.

Gupta, S. K. and S. J. Kosciol (2011). Measuring Angle of Twist in a Torsion Experiment. *American Society for Engineering Education*.

Gupta, S. K. and S. J. Kosciol (2012). Using a pair of iPods to Measure Angle of Twist in a Torsion Experiment. *American Society for Engineering Education*.

Harrison, S. K. (2006). Comparison of shear modulus test methods, *Master thesis*, Faculty of Virginia Polytechnic and State University, VA, USA.

Hartley, R. and A. Zisserman (2003). Multiple view geometry in computer vision, *Cambridge university press*.

Hecht, E. (1989). Optics, *Second Edition*, Addison Wesley Publishing Co.

Heikkila, J. (2000). Geometric camera calibration using circular control points. *Pattern Analysis and Machine Intelligence, IEEE Transactions on* **22**(10): 1066-1077.

Hindman, D., et al. (2005a). Torsional rigidity of rectangular wood composite materials. *Wood and fiber science* **37** (2): 283-291.

Hindman, D., et al. (2005b). Torsional rigidity of wood composite I-joists. *Wood and fiber science* **37** (2): 292-303.

Hornberg, A. (2007). Handbook of machine vision, *John Wiley & Sons*.

I RDP. Electronics Ltd (2012). <http://www.rdpe.com/>. [Accessed on May 10, 2012].

Jain, R., et al. (1995). Machine vision, *McGraw-Hill New York*.

Jáuregui, D.V., White, K.R., Woodward, C.B. and Leitch, K.R., (2003). Noncontact Photogrammetric Measurement of Vertical Bridge Deflection. *Journal of Bridge Engineering*, 8(4): 212-222.

Jáuregui, D., White, K., Woodward, C., & Leitch, K. (2002). Static measurement of beam deformations via close-range photogrammetry. *Transportation Research Record: Journal of the Transportation Research Board*, (1814), 3-8.

Jáuregui, D. V., White, K. R., Woodward, C. B., & Leitch, K. R. (2003). Noncontact photogrammetric measurement of vertical bridge deflection. *Journal of Bridge Engineering*, 8(4), 212-222.

Jiang, L., et al. (2004). Finite-element model for wood-based floors with lateral reinforcements. *Journal of Structural Engineering* **130**(7): 1097-1107.

Kang, H.-Y., et al. (2011). Preliminary Tests for Optically Measuring Drying Strains and Check Formation in Wood. *Journal of the Faculty of Agriculture, Kyushu University* **56**(2): 313-316.

Keenan, F. (1974). Shear strength of wood beams. *Forest Products Journal*, **24**(9): 63-70.

Khokhar, A., et al. (2010). The shear strength, and failure modes, of timber joists obtained from the torsion test method. *Proceedings of the 11th World Conference of Timber Engineering*, 20-24th June, Riva del Garda, Italy.

Khokhar, A. M. (2011). The Evaluation of Shear Properties of Timber Beams Using Torsion Test Method. *PhD Thesis*, Edinburgh Napier University, Edinburgh, UK.

Koken, A., Koroglu, M. A., Karabork, H., & Ceylan, A. (2014). PHOTOGRAMMETRIC APPROACH IN DETERMINING BEAM-COLUMN CONNECTION DEFORMATIONS. *Boletim de Ciências Geodésicas*, 20(3), 720-733.

Laboratory, F. P. (1987). Wood handbook: wood as an engineering material, *United States Government Printing*.

Laboratory, F. P. and U. D. o. Agriculture (2007). *The Encyclopedia of Wood*, Skyhorse Publishing Inc.

Luhmann, T. (2010). Close range photogrammetry for industrial applications. *ISPRS Journal of Photogrammetry and Remote Sensing* **65**(6): 558-569.

Maas, H.-G. and U. Hampel (2006). Photogrammetric techniques in civil engineering material testing and structure monitoring. *Photogrammetric Engineering & Remote Sensing* **72**(1): 39-45.

McGlone, C., et al. (2004). Manual of Photogrammetry, American Society for Photogrammetry and Remote Sensing. *Bethesda, MD*.

Mustaffar, M., et al. (2012). The measurement of full scale structural beam-column connection deformation using digital close range photogrammetry technique. *Malaysian Journal of Civil Engineering (MJCE)* **24**(2): 148-160.

MVTech Software HALCON GmbH (2010). The software for Machine Vision Applications. [http:// www.mvtech.com/halcon/](http://www.mvtech.com/halcon/). [Accessed on August 20, 2011].

MVTec Software GmbH (2011a). *Halcon 11.0 - the Power of Machine Vision - HDevelop User's Guide*. MVTec Software GmbH, München, Germany.

MVTec Software GmbH (2011b). *Halcon 11.0 - the Power of Machine Vision - Quick Guide*. MVTec Software GmbH, München, Germany.

MVTec Software GmbH (2011c). *Halcon 11.0 - the Power of Machine Vision - Reference Manual*. MVTec Software GmbH, München, Germany. NDS, A. F. A. P.

A. (2001). National Design Specification (NDS) for Wood Construction. *Washington, USA*.

Otepka, J. O. and C. S. Fraser (2004). Accuracy enhancement of vision metrology through automatic target plane determination, na.

Pease, B. J., Geiker, M. R., Stang, H., & Weiss, J. (2006). Photogrammetric assessment of flexure induced cracking of reinforced concrete beams under service loads. In *Second International RILEM Symposium: Advances in Concrete Through Science and Engineering*.

Radzuan, S., et al. (2011). Structural Beam Displacement Measurement Using DCRP Technique. *11th South East Asian Congress (SEASC) and 13th International Surveyor Congress (ISC)*. 22-24 June. PWTC Kuala Lumpur.

Rammer, D. R. and L. A. Soltis (1994). Experimental shear strength of glued-laminated beams, *Forest Products Laboratory*.

Rautenstrauch, K. (2003). Strain analysis of solid wood and glued laminated timber constructions by close range photogrammetry. *International Symposium: Non-Destructive Testing in Civil Engineering*, Berlin.

Reiterer, A. and S. E. Stanzl-Tschegg (2001). Compressive behaviour of softwood under uniaxial loading at different orientations to the grain. *Mechanics of materials* **33**(12): 705-715.

Riyanto, D. S., Gupta, Rakesh (1998). A comparison of test methods for evaluating shear strength of structural lumber. *Forest products journal* **48**(2): 83-90.

Serrano, E. and B. Enquist (2005). Contact-free measurement and non-linear finite element analyses of strain distribution along wood adhesive bonds. *Holzforschung* **59**(6): 641-646.

Shortis, M. R., et al. (1995). Practical testing of the precision and accuracy of target image centering algorithms. *Photonics East'95, International Society for Optics and Photonics*.

Sinha, A., et al. (2006). Strain profile in wood frame shear walls—preliminary results. *9th World Conference on Timber Engineering*, Portland USA.

Soltis, L. A., Rammer, Douglas R (1993). Shear strength of unchecked glued-laminated beams. *Forest Products Journal* **44** (1): 51-57.

Steger, C., et al. (2008). Machine vision algorithms and applications. *Handbook of machine vision*, Wiley-VCH, Weinheim.

Thelandersson, S. and H. J. Larsen (2003). Timber engineering, *John Wiley & Sons*, Chichester, UK.

Tsakiri, M., et al. (2004). Load testing measurements for structural assessment using geodetic and photogrammetric techniques. *Proceedings of the 1st International Symposium on Engineering Surveys for Construction Works and Structural Engineering*, Nottingham, UK.

Ukyo, S. and M. Masuda (2004). Investigation of the true stress-strain relation in shear using the digital image correlation method. *Journal of the Japan Wood Research Society*, Japan.

Ukyo, S. and M. Masuda (2006). A New Method for Measuring the True Shear Strength of Wood, *Proceedings of the 9th World conference on timber engineering*, Portland, USA.

USDA (1999). Wood handbook: Wood as an engineering material. *US Department of Agriculture and Forest Product Laboratory*, Madison, WI, USA.

Vafai, A. and G. Pincus (1973). Torsional and bending behavior of wood beams. *Journal of the Structural Engineering ASCE*, **99**(6): 1205-1221.

Valença, J., Júlio, E., & Araújo, H (2008). Application of Photogrammetry to Bridge Monitoring. In *Structural Faults & Repair, 12th International Conference* :10-12.

Whiteman, T., et al. (2002). Measurement of deflections in concrete beams by close-range digital photogrammetry. *Proceedings of the Symposium on Geospatial Theory, Processing and Applications, ISPRS Commission IV Ottawa, ON, Canada.*

Wolf, P. R., et al. (2000). *Elements of Photogrammetry: with applications in GIS, McGraw-Hill, New York.*

Xavier, J., et al. (2012). Stereovision measurements on evaluating the modulus of elasticity of wood by compression tests parallel to the grain. *Construction and Building Materials* **26**(1): 207-215.

Zhang, H., et al. (2011). Evaluation of shear constant of a timber beam using a photogrammetric approach. *Proceedings of the Thirteenth International Conference on Civil, Structural and Environmental Engineering Computing*. Crete, Greece.

Zhang, H., et al. (2012). Evaluation of shear constant of timber glulam composite with photogrammetric approach. *Proceedings of the Fourteenth International Conference on Computing in Civil and Building Engineering*, Moscow, Russia.

Zink, A. G., et al. (1995). Strain measurement in wood using a digital image correlation technique. *Wood and fiber science* **27**(4): 346-359.